



ATLAS Note

GROUP-2017-XX



29th April 2021

Draft version 0.1

1

2 **A Deep Learning Approach to Differential**
3 **Measurements of Higgs - Top Interactions in**
4 **Multilepton Final States**

5

The ATLAS Collaboration

6 Several theories Beyond the Standard Model modify the momentum spectrum of the Higgs
7 Boson, without significantly altering the overall rate of Higgs produced from top quark pairs.
8 A differential measurement of the Higgs transverse momentum provides a way to search for
9 these effects at the LHC. Because of the challenges inherent to reconstructing the Higgs in
10 multilepton final states, a deep learning approach is used to predict the momentum spectrum
11 of the Higgs for events where the Higgs Boson is produced from top quark pairs and decays
12 to final states that include multiple leptons. The regressed Higgs p_T is fit to data for events
13 with two or three leptons in the final state, and estimates of the sensitivity to variations in the
14 Higgs p_T spectrum are given.

© 2021 CERN for the benefit of the ATLAS Collaboration.

15 Reproduction of this article or parts of it is allowed as specified in the CC-BY-4.0 license.

16 **Contents**

17	I Introduction	7
18	1 Introduction	7
19	II Theoretical Motivation	10
20	2 The Standard Model and the Higgs Boson	10
21	2.1 The Forces and Particles of the Standard Model	10
22	2.2 The Higgs Mechanism	13
23	2.2.1 The Higgs Field	13
24	2.2.2 Electroweak Symmetry Breaking	15
25	2.3 $t\bar{t}H$ Production	18
26	2.4 WZ + Heavy Flavor Production	20
27	2.5 Extensions to the Standard Model	21
28	III The LHC and the ATLAS Detector	24
29	3 The LHC	24
30	4 The ATLAS Detector	27
31	4.1 Inner Detector	28
32	4.2 Calorimeters	30
33	4.3 Muon Spectrometer	31
34	4.4 Trigger System	32
35	IV Measurement of WZ + Heavy Flavor	33
36	5 Introduction	33
37	6 Data and Monte Carlo Samples	35
38	6.1 Data Samples	35
39	6.2 Monte Carlo Samples	35
40	7 Object Reconstruction	36
41	7.1 Trigger	37
42	7.2 Light leptons	37
43	7.3 Jets	38
44	7.4 B-tagged Jets	39
45	7.5 Missing transverse energy	41

46	7.6 Overlap removal	41
47	8 Event Selection and Signal Region Definitions	42
48	8.1 Event Preselection	42
49	8.2 Fit Regions	45
50	8.3 Non-Prompt Lepton Estimation	46
51	8.3.1 $t\bar{t}$ Validation	47
52	8.3.2 Z+jets Validation	48
53	9 tZ Interference Studies and Separation Multivariate Analysis	48
54	10 Data and Monte Carlo Samples	52
55	10.1 Data Samples	52
56	10.2 Monte Carlo Samples	52
57	11 Object Reconstruction	53
58	11.1 Trigger	54
59	11.2 Light leptons	54
60	11.3 Jets	55
61	11.4 B-tagged Jets	56
62	11.5 Missing transverse energy	58
63	11.6 Overlap removal	58
64	12 Event Selection and Signal Region Definitions	59
65	12.1 Event Preselection	59
66	12.2 Fit Regions	62
67	12.3 Non-Prompt Lepton Estimation	63
68	12.3.1 $t\bar{t}$ Validation	64
69	12.3.2 Z+jets Validation	65
70	13 tZ Interference Studies and Separation Multivariate Analysis	65
71	14 Systematic Uncertainties	69
72	15 Results	73
73	15.1 1-jet Fit Results	74
74	15.2 2-jet Fit Results	83
75	V Differential Studies of $t\bar{t}H$ Multilepton	92
76	16 Data and Monte Carlo Samples	92
77	16.1 Data Samples	93
78	16.2 Monte Carlo Samples	93

79	17 Object Reconstruction	95
80	17.1 Trigger Requirements	96
81	17.2 Light Leptons	96
82	17.3 Jets	97
83	17.4 B-tagged Jets	98
84	17.5 Missing Transverse Energy	98
85	17.6 Overlap removal	99
86	18 Higgs Momentum Reconstruction	99
87	18.1 Higgs Decay Product Identification	101
88	18.2 b-jet Identification	102
89	18.2.1 2lSS Channel	103
90	18.2.2 3l Channel	108
91	18.3 Higgs Reconstruction	111
92	18.3.1 2lSS Channel	112
93	18.3.2 3l Semi-leptonic Channel	116
94	18.3.3 3l Fully-leptonic Channel	120
95	18.4 p_T Prediction	124
96	18.4.1 2lSS Channel	125
97	18.4.2 3l Semi-leptonic Channel	128
98	18.4.3 3l Fully-leptonic Channel	132
99	18.5 3l Decay Mode	135
100	19 Signal Region Definitions	137
101	19.1 Pre-MVA Event Selection	138
102	19.2 Event MVA	143
103	19.3 Signal Region Definitions	151
104	20 Background Rejection MVA	154
105	20.1 Pre-MVA Event Selection	155
106	20.2 Event MVA	157
107	20.3 Signal Region Definitions	166
108	20.3.1 2lSS	167
109	20.3.2 3l – Semi – leptonic	167
110	20.3.3 3l – Fully – leptonic	167
111	21 Systematic Uncertainties	167
112	22 Results	172
113	22.1 Results - 80 fb^{-1}	173
114	22.2 Projected Results - 140 fb^{-1}	177

115	VI Conclusion	181
-----	----------------------	------------

116	Appendices	188
117	.1 Non-prompt lepton MVA	188
118	.2 Non-prompt CR Modelling	193
119	.3 tZ Interference Studies	198
120	.4 Alternate tZ Inclusive Fit	202
121	.4.1 tZ Inclusive Fit	203
122	.4.2 Floating tZ	204
123	.5 DSID list	205
124	A Machine Learning Models	228
125	A.1 Higgs Reconstruction Models	228
126	A.1.1 b-jet Identification Features - 2ISS	228
127	A.1.2 b-jet Identification Features - 3l	232
128	A.1.3 Higgs Reconstruction Features - 2ISS	237
129	A.1.4 Higgs Reconstruction Features - 3IS	242
130	A.1.5 Higgs Reconstruction Features - 3IF	247
131	A.2 Background Rejection MVAs	251
132	A.2.1 Background Rejection MVA Features - 2ISS	251
133	A.2.2 Background Rejection MVA Features - 3l	255
134	A.3 Alternate b-jet Identification Algorithm	260
135	A.4 Binary Classification of the Higgs p_T	261
136	A.5 Impact of Alternative Jet Selection	262

Part I**Introduction****1 Introduction**

140 Particle physics is an attempt to describe the fundamental building blocks of the universe and
141 their interactions. The Standard Model (SM) - our best current theory of fundamental particle
142 physics - does a remarkable job of that. All known fundamental particles and (almost) all of the
143 forces underlying their interactions can be explained by the SM, and the predictions from this
144 theory agree with experiment to an incredibly precise degree. This is especially true since the
145 Higgs Boson, the last piece of the SM predicted decades before, was finally discovered at the
146 Large Hadron Collider (LHC) in 2012.

147 Despite the success of the SM, there remains significant work to be done. For one, the
148 SM is incomplete: it fails to provide a description of gravity, to give an explanation for the
149 observation of Dark Matter, or to provide a mechanism for neutrinos to gain mass. Further, a
150 Higgs Boson with a mass of around 125 GeV, as observed at the LHC, gives rise to what is
151 known a hierarchy problem - such a low mass Higgs requires a seemingly unnatural level of “fine
152 tuning” that is unexplained by the SM.

153 A promising avenue for addressing these problems is to study the properties of the Higgs
154 Boson and the way it interacts with other particles, in part simply because these interactions

155 have not been measured before. Its interactions with the Top Quark are a particularly promising
156 place to look. Because the Higgs Field is responsible for allowing particle to acquire mass, the
157 strength of a particle's interaction with the Higgs Boson is proportional to its mass. As the most
158 massive of the fundamental particles, the Top Quark has the strongest coupling to the Higgs
159 Boson, meaning any new physics in the Higgs sector is likely to present itself most prominently
160 in its interaction with the Top Quark.

161 These interactions can be measured by directly by studying the production of a Higgs
162 Boson in association with a pair of Top Quarks ($t\bar{t}H$). While studies have been done measuring
163 the overall rate of $t\bar{t}H$ production, there are several theories of physics Beyond the Standard
164 Model (BSM) that would affect the kinematics of $t\bar{t}H$ production without altering its overall
165 rate. This dissertation attempts to make a differential measurement of the kinematics of the
166 Higgs Boson in $t\bar{t}H$ events in order to search for these BSM effects.

167 The proton-proton collision data collected by the ATLAS detector at the LHC from 2015-
168 2018 provides the opportunity to make this measurement for the first time. The unprecedented
169 energy achieved by the LHC during this period greatly increase the rate at which $t\bar{t}H$ events are
170 produced, and the large amount of data collected provides the necessary statistics for a differential
171 measurement to be performed.

172 A study of $t\bar{t}H$ events with multiple leptons in the final state is performed, using 139 fb^{-1}
173 of data from proton-proton collisions at an energy $\sqrt{s} = 13 \text{ TeV}$ collected by the ATLAS detector
174 from 2015-2018. Events are separated into channels based on the number of light leptons in the

175 final state - either two same-sign leptons, or three leptons. A deep neural network is used to
176 reconstruct the momentum of the Higgs Boson in each event. This momentum spectrum is fit to
177 data for each analysis channel in order to search for evidence of these BSM effects.

178 An additional study of WZ produced in association with a heavy flavor jet (including both
179 b-jets and charm jets) is also included. This process mimics the final state of $t\bar{t}H$ multilpjet
180 events, making it an irreducible background for that analysis. However, this process is poorly
181 understood, and difficult to simulate accurately, introducing large systematic uncertainties for
182 analyses that include it as a background. A measurement of WZ + heavy flavor in the fully
183 leptonic decay mode is performed in an attempt to reduce this uncertainty.

184 This dissertation begins with a brief explanation of the SM, its limitations, and the theor-
185 etical motivation behind this work in Part II. This is followed by a description of the LHC and
186 the ATLAS detector in Part III. Part IV details a measurement of WZ + heavy flavor. Studies
187 of differential measurements of $t\bar{t}H$ are then described in Part V, and preliminary results are
188 presented. Finally, the results of these studies are summarized in the conclusion, Part VI.

Part II**Theoretical Motivation****2 The Standard Model and the Higgs Boson**

The Standard Model of particle physics (SM) is a Quantum Field Theory (QFT) describing the known fundamental particles and their interactions. It accounts for three of the four known fundamental force - electromagnetism, the weak nuclear force, and the strong nuclear force, but not gravity. Further, the SM describes a mechanism for combining the weak and electromagnetic forces into a singular interaction, known as the electroweak force. It is a non-Abelian gauge theory, invariant under the Lie Group $SU(3)_C \otimes SU(2)_L \otimes U(1)_Y$, where C refers to color charge, L, the helicity of the particle, and Y, the hypercharge.

2.1 The Forces and Particles of the Standard Model

The SM particles, summarized in Figure 2.1, can be classified into two general categories based on their spin: fermions, and bosons.

Standard Model of Elementary Particles

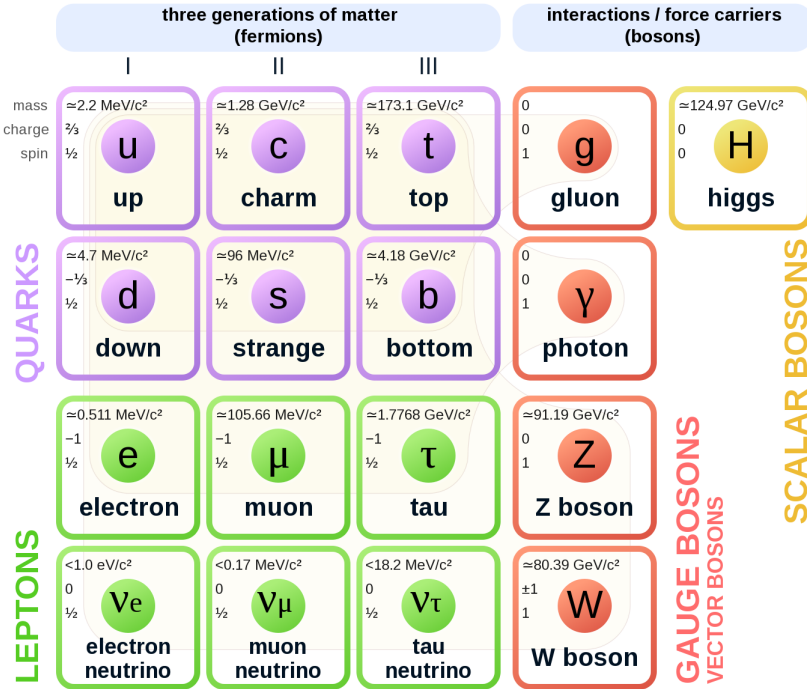


Figure 2.1: A summary of the particles of the Standard Model, including their mass, charge and spin, with the fermions listed on the left, and the bosons on the right. [1]

202 Fermions are particles with $\frac{1}{2}$ -integer spin, which according to the spin-statistics theorem,
 203 causes them to comply with the Pauli-exclusion principle. They can be separated into two groups,
 204 leptons and quarks, each of which consist of three generations of particles with increasing mass.

205 Leptons are fermions which interact via the electroweak force, but not the strong force.
 206 The three generation of leptons consist of the electron and electron neutrino, the muon and muon
 207 neutrino, the tau and tau neutrino. The quarks, by contrast, do interact via the strong force - which
 208 is to say they have color charge - in addition to the electroweak force. The three generations
 209 include the up and down quarks, the strange and charm quarks, and the top and bottom quarks.

210 Each of these generations form left-handed doublets invariant under SU(2) transfor-

211 mations. For the leptons these doublets are:

$$\begin{pmatrix} e^- \\ \nu_e \end{pmatrix}_L, \begin{pmatrix} \mu^- \\ \nu_\mu \end{pmatrix}_L, \begin{pmatrix} \tau^- \\ \nu_\tau \end{pmatrix}_L \quad (2.1)$$

212 And for the quarks:

$$\begin{pmatrix} u \\ d \end{pmatrix}_L, \begin{pmatrix} s \\ c \end{pmatrix}_L, \begin{pmatrix} t \\ b \end{pmatrix}_L \quad (2.2)$$

213 For both leptons and quarks, the heavier generations can decay into the lighter generation

214 of particles, while the first generation does not decay. Hence, ordinary matter generally consists

215 of this first generation of fermions - electrons, up quarks, and down quarks. Each of these

216 fermions has a corresponding anti-particle, which has an equal mass as its partner but opposite

217 charge. The fermions acquire their mass via the Higgs Mechanism, except for the neutrinos,

218 whose mass has been experimentally confirmed but is not accounted for in the SM.

219 Bosons, by contrast, have integer spin, and are therefore unconstrained by the Pauli-

220 exclusion principle. The SM includes two kinds of bosons: Gauge bosons, which are spin-1

221 particles that mediate the interactions between the fermions, and a single scalar, i.e. spin-0,

222 particle - the Higgs Boson. Of the gauge bosons, the W^+ , W^- and Z bosons - which are the

223 mass eigenstates of the electroweak bosons - mediate the weak interaction, while the photon

224 mediates the electric force, and the gluon mediates the strong force.

225 **2.2 The Higgs Mechanism**

226 A key feature of the SM is the gauge invariance of its Lagrangian. However, any terms added to

227 the Lagrangian giving mass to the the gauge bosons would violate this underlying symmetry of

228 the theory. This presents a clear problem with the theory: The experimental observation that the

229 W and Z bosons have mass seems to contradict the basic structure of the SM.

230 Rather than abandoning gauge invariance, an alternative way for particles to acquire mass

231 beyond adding a simple mass term to the Lagrangian was theorized by Higgs, Englert and Brout

232 in 1964 [2]. This procedure for introducing masses for the gauge bosons while preserving local

233 gauge invariance, known as the Higgs mechanism, was incorporated into the electroweak theory

234 by Weinberg in 1967 [3].

235 **2.2.1 The Higgs Field**

236 The Higgs mechanism introduces a complex scalar SU(2) doublet, Φ , with the form:

$$\Phi = \begin{pmatrix} \phi^+ \\ \phi^0 \end{pmatrix}_L \quad (2.3)$$

237 This field introduces a scalar potential to the Lagrangian of the form:

$$V(\Phi) = \mu^2 |\Phi^\dagger \Phi| + \lambda (|\Phi^\dagger \Phi|)^2 \quad (2.4)$$

238 Where μ and λ are free parameters of the new field. This represents the most general
239 potential allowed while preserving $SU(2)_L$ invariance and renormalizability. In the case that
240 $\mu^2 < 0$, this potential takes the form shown in Figure 2.2.

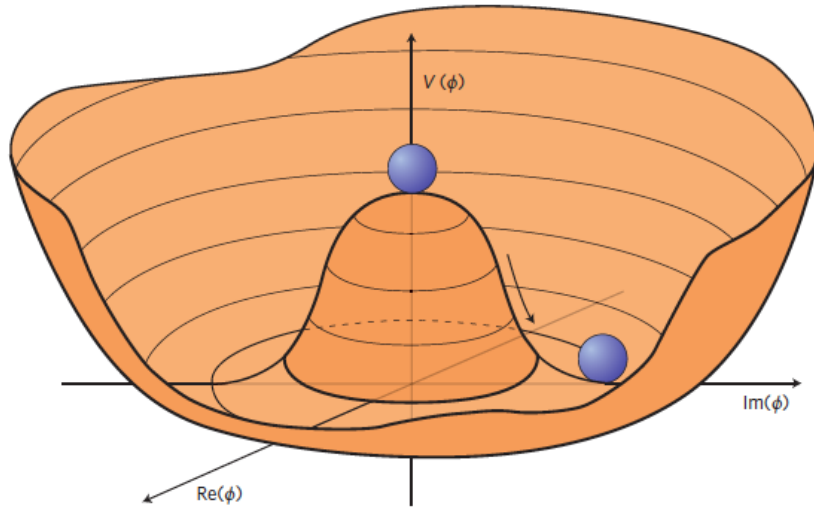


Figure 2.2: The value of the Higgs potential, $V(\Phi)$ as a function of Φ , for the case that $\mu^2 < 0$ [4].

241 The significant feature of this potential is that its minimum does not occur for a value of
242 $\Phi = 0$. Instead, it is minimized when $|\Phi^\dagger \Phi| = -\mu^2/\lambda$. This means that in its ground state, the
243 Higgs field takes on a non-zero value - referred to as a vacuum expectation value (VEV). So while
244 the Higgs potential is globally symmetric, about the minimum this symmetry is broken. Since

²⁴⁵ the minimum is determined only by $\Phi^\dagger \Phi$, there is some ambiguity in the particular definition of

²⁴⁶ the VEV, but it is generally represented as

$$\langle \Phi \rangle = \frac{1}{\sqrt{2}} \begin{pmatrix} 0 \\ v \end{pmatrix} \quad (2.5)$$

²⁴⁷ The full value of Φ can be written as

$$\langle \Phi \rangle = \frac{1}{\sqrt{2}} \begin{pmatrix} 0 \\ v + H/\sqrt{2} \end{pmatrix} \quad (2.6)$$

²⁴⁸ with v being the value of the VEV, and H being the real value of the scalar field.

²⁴⁹ 2.2.2 Electroweak Symmetry Breaking

²⁵⁰ The Electroweak (EWK) interaction is described in the SM by a $SU(2)_L \otimes U(1)_Y$ gauge theory.

²⁵¹ This theory predicts three $SU(2)_L$ gauge boson, $W_\mu^1, W_\mu^2, W_\mu^3$, and a single $U(1)_Y$ gauge boson,

²⁵² B_μ . The couplings of these bosons to the Higgs field show up in the kinetic terms of the scalar

²⁵³ field Φ in the Lagrangian:

$$(D_\mu \Phi)^\dagger (D^\mu \Phi) = |(\partial_\mu - \frac{i g}{2} W_\mu^a \sigma^a - \frac{i g'}{2} B_\mu Y) \phi|^2 \quad (2.7)$$

254 Here D_μ represents the covariant derivative required to preserve gauge invariance, g and
 255 g' represent coupling constant of the gauge bosons, σ^a denotes the Pauli matrices of $SU(2)$,
 256 and Y represents the hypercharge of $U(1)$. The terms in this interaction which contribute to the
 257 masses of the gauge bosons can be written as:

$$\frac{1}{2}(0, v) \left(\frac{g}{2} W_\mu^a \sigma^a - \frac{g'}{2} B_\mu \right)^2 \begin{pmatrix} 0 \\ v \end{pmatrix} \quad (2.8)$$

258 Expanding these terms into the mass eigenstates of the electroweak interaction yields four
 259 physical gauge bosons, two charged and two neutral, which are linear combinations of the fields
 260 W_μ^1 , W_μ^2 , W_μ^3 , and B_μ :

$$\begin{aligned} W_\mu^\pm &= \frac{1}{\sqrt{2}} (W_\mu^1 \pm i W_\mu^2) \\ Z^\mu &= \frac{1}{\sqrt{(g^2 + g'^2)}} (-g' B_\mu + g W_\mu^3) \\ A^\mu &= \frac{1}{\sqrt{(g^2 + g'^2)}} (g B_\mu + g' W_\mu^3) \end{aligned} \quad (2.9)$$

261 And the masses of these fields are given by:

$$\begin{aligned} M_W^2 &= \frac{1}{4} g^2 v^2 \\ M_Z^2 &= \frac{1}{4} (g^2 + g'^2) v^2 \\ M_A^2 &= 0 \end{aligned} \quad (2.10)$$

262 This produces exactly the particles we observe - three massive gauge bosons and a single
 263 massless photon. The massless photon represents the portion of the gauge symmetry, a single
 264 $U(1)$ of the electromagnetic force, that remains unbroken by the VEV.

265 Interactions with the Higgs field also lead to the generation of the fermion masses, which
 266 in the Lagrangian take the form:

$$-\lambda_\psi(\bar{\psi}_L \phi \psi_R + \bar{\psi}_R \phi^\dagger \psi_L) \quad (2.11)$$

267 After symmetry breaking has occurred and ϕ has taken on the value of the VEV as written
 268 in equation 2.5, the mass terms of the fermions become $\lambda_\psi v$. Written this way, the fermion
 269 masses are proportional to their Yukawa coupling to the VEV, λ_ψ .

270 Based on the equation 2.6, an additional mass term, $\mu^2 H^2$ arises from the potential $V(\Phi)$.
 271 This term can be understood as an excitation of the Higgs field, a scalar boson with mass $M_H = \mu$.
 272 This is the Higgs boson, which comes about as a natural prediction of electroweak symmetry
 273 breaking.

274 The fermions' Yukawa couplings to the VEV take the same form as the fermions' coupling
 275 to the Higgs boson - λ_ψ . Therefore, the strength of a fermion's interaction with the Higgs is
 276 directly proportional to its mass. We now have a model that predicts a Higgs boson with mass
 277 $M_H = \mu$, which interacts with the fermions with coupling strength λ_ψ . Because μ and λ_ψ are

²⁷⁸ free parameters of the theory, the mass of the Higgs boson and its interactions with the fermions

²⁷⁹ must be measured experimentally.

²⁸⁰ **2.3 $t\bar{t}H$ Production**

²⁸¹ The strength of a particles interaction with the Higgs, given by its Yukawa coupling, is propor-
²⁸² tionate to its mass. The top quark - as the heaviest known particle - has the strongest interaction,
²⁸³ making this interaction particularly interesting to study. While several processes involve interac-
²⁸⁴ tions between the Higgs and the top, some Higgs production modes include the top interaction
²⁸⁵ only as a part of a loop diagram, such as the gluon-gluon fusion diagram shown in Figure 2.3.

²⁸⁶ This process therefore only allows for an indirect probe of the Higgs-top Yukawa coupling, as
²⁸⁷ the flavor of the quark in this diagram is not unique.

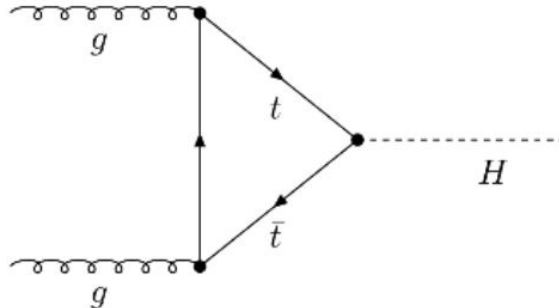


Figure 2.3: Diagram of a Higgs boson produced via gluon-gluon fusion.

²⁸⁸ Studying the Higgs produced in association with top quark pairs, $t\bar{t}H$, allows this interac-
²⁸⁹ tion to be measured directly. This process, as shown in Figure 2.4, involves a unique coupling
²⁹⁰ between the Higgs and the top, which can be identified by the top quark pair in the final state.

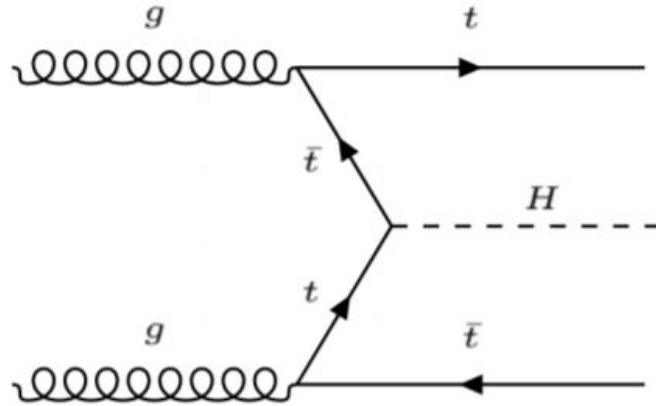


Figure 2.4: Diagram of a Higgs boson produced in association with a pair of top quarks.

291 The Higgs boson, as well as the top quarks, have very short lifetimes - on the order of
 292 10^{-22} s and 10^{-25} s respectively - meaning they can only be observed via their decay products.
 293 Measuring this process is therefore a matter of identifying events with final states consistent
 294 with $t\bar{t}H$ production. This thesis focuses on $t\bar{t}H$ events with multiple leptons in the final state,
 295 $t\bar{t}H - ML$. This includes $H \rightarrow W^+W^-$ events, where at least one of the W bosons decays
 296 leptonically.

297 While the branching ratio of $H \rightarrow W^+W^-$ is smaller than $H \rightarrow b\bar{b}$, it produces a clearer
 298 signal. On the other hand, $H \rightarrow \gamma\gamma$ produces the most easily identifiable signal, but has a much
 299 smaller branching ratio than $H \rightarrow W^+W^-$. Therefore, compared with other final states of $t\bar{t}H$,
 300 the $t\bar{t}H - ML$ channel is an attractive candidate for study, as it involves a good balance between
 301 statistical power and identifiability.

302 2.4 WZ + Heavy Flavor Production

303 Part IV is dedicated to a measurement of WZ produced in association with a heavy flavor jet
 304 - namely, a charm or b-jet - in the fully leptonic channel. In the instance that both the W
 305 and Z bosons decay leptonically, this process produces a final state similar to $t\bar{t}H$, making it
 306 an irreducible background for $t\bar{t}H$ – ML specifically, and any analysis that includes multiple
 307 leptons and b-tagged jets in the final state more broadly.

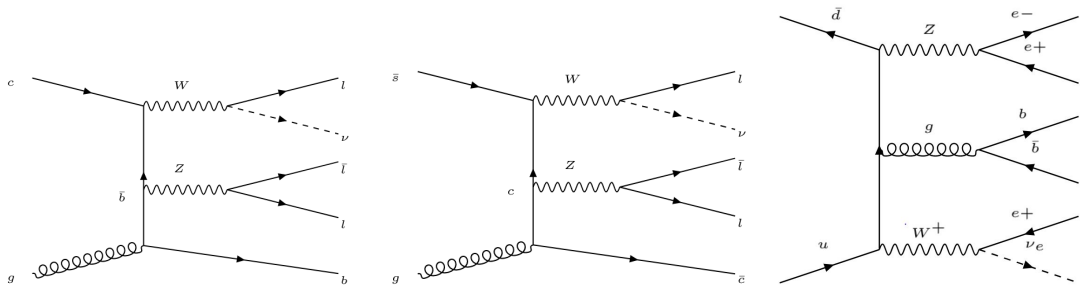


Figure 2.5: Example Feynman diagrams of WZ + heavy flavor production

308 The b-jets produced in this process can be thought of in two different ways: either as
 309 originating from the quark “sea” of the initial state hadrons, or as the result of a gluon from
 310 one the colliding protons splitting into $b\bar{b}$ pairs. However, the heavy flavor contribution to the
 311 parton distribution function (PDF) of the proton is uncertain, and simulations of this process
 312 disagree depending on which of these two approaches one considers. This makes WZ + heavy
 313 flavor difficult to accurately simulate, and introduces a large uncertainty for any analysis which
 314 includes it as a background, motivating a measurement of this process.

315 2.5 Extensions to the Standard Model

316 While the SM has been tested to great precision, particularly at the LHC, it is generally accepted
317 that it is only valid up to a certain energy scale. It is assumed that above a certain energy, at the
318 scale where something like a Grand Unified Theory (GUT) or quantum gravity become relevant,
319 the SM will not be applicable. Further, there are several experimental observations that the SM
320 fails to explain. For example, the SM predicts neutrinos to be massless, despite experimental
321 observation to the contrary, and fails to explain the observation of dark matter and dark energy.

322 Another example, relevant to the Higgs sector, is known as the hierarchy problem: large
323 quantum corrections to the Higgs mass from loop diagrams, such as those shown in Figure 2.6,
324 are many orders of magnitude larger than the Higgs mass itself. The observed value of the Higgs
325 mass therefore requires extremely precise cancellation between these corrections and the bare
326 mass of the Higgs, a cancellation which seems unnatural and suggests something missing in our
327 theoretical picture.

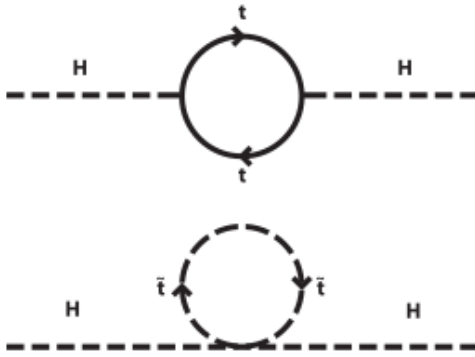


Figure 2.6: Above diagram is the leading order correction to the Higgs mass via a top quark loop, and below is the stop squark loop, coming from a supersymmetric extension of the SM, that provides a potential cancellation of the top diagram.

328 Because so many of the properties of the Higgs boson have not yet been studied, its
 329 interactions are a promising place to search for new physics that could resolve some of the
 330 limitations of the SM. As explained above, the interactions of the Higgs with the top quark, as in
 331 $t\bar{t}H$ production, are particularly interesting: As the most massive particle in the Standard Model,
 332 the top quark is the most strongly interacting with the Higgs. Therefore, any new physics effects
 333 are likely to be seen most prominently in this interaction.

334 These interactions can be measured directly by studying the production of a Higgs Boson
 335 in association with a pair of Top Quarks ($t\bar{t}H$). While this process has been observed by both
 336 the ATLAS [5] and CMS [6] collaborations, these analyses have focused on measuring the
 337 overall rate of $t\bar{t}H$ production. There are several theories of physics Beyond the Standard Model
 338 (BSM), however, that would affect the kinematics of $t\bar{t}H$ production without altering its overall
 339 rate [7].

340 An Effective Field Theory approach can be used to model the low energy effects of new,
 341 high energy physics, by parameterizing BSM effects as higher dimensional operators. These
 342 additional operators can then be added to the SM Lagrangian to write an effective Lagrangian
 343 that accounts for the effects of these higher energy physics. The lowest order of these that could
 344 contribute to Higgs-top couplings are dimension-six, as represented in Equation 2.12.

$$\mathcal{L}_{\text{eff}} = \mathcal{L}_{\text{SM}} + \frac{f}{\Lambda} O^6 \quad (2.12)$$

345 Here Λ represents the energy scale of the new physics, and f is a Wilson coefficient which
 346 represents the strength of the effective coupling. An experimental observation of any non-zero
 347 value of f would be a sign of BSM physics.

348 The addition of these operators can be shown to modify the transverse momentum (p_T)
 349 spectrum of the Higgs Boson in Higg-top interactions, without effecting the overall rate of $t\bar{t}H$
 350 production [8]. The possible impact of these higher order effects on the Higgs p_T spectrum are
 351 shown in Figure 2.7.

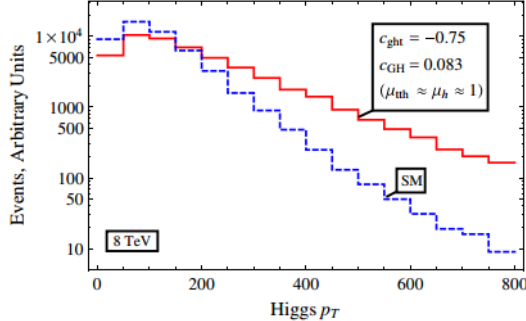


Figure 2.7: The momentum spectrum of the Higgs boson produced via top-quarks with (red) and without (blue) the presence of dimension-six operators.

352 This provides a clear, physics observable that could be used to search for evidence of
 353 BSM physics. The energy and luminosity produced by the LHC now make such a measurement
 354 possible. Reconstructing the momentum spectrum of the Higgs in $t\bar{t}H$ events therefore provides
 355 a means to search for new physics in the Higgs sector.

356 Part III

357 The LHC and the ATLAS Detector

358 3 The LHC

359 The Large Hadron Collider (LHC) is a particle accelerator consisting of a 27 km ring, designed
 360 to collide protons at high energy. Located outside of Geneva, Switzerland and buried about 100
 361 m underground, it consists of a ring of superconducting magnets which are used to accelerate

362 opposing beams of protons - or lead ions - which collide at the center of one of the various
363 detectors located around the LHC ring which record the result of these collisions. These
364 detectors include two general purpose detectors, ATLAS and CMS, which are designed to make
365 precision measurements of a broad range of physics phenomenon, and two more specialized
366 experiments, LHCb and ALICE, which are optimized to study b-quarks and heavy-ion physics,
367 respectively.

368 The LHC first began running in 2009 at a proton-proton center of mass energy of $\sqrt{s} = 8$
369 TeV. It operated at this energy from 2009 to 2012, known as Run 1, and data collected during
370 this period was used in discovering the Higgs Boson. The LHC began running again in 2015,
371 and collected data at an increased energy of $\sqrt{s} = 13$ TeV until 2018, a period referred to as Run
372 2.

373 The LHC consists of a chain of accelerators, which accelerate the protons to higher and
374 higher energies until they are injected into the main ring. This process is summarized in figure
375 3.1. Protons extracted from a tank of ionized hydrogen are fed into a linear accelerator, LINAC2,
376 where they reach an energy of 50 MeV. From there, they enter a series of three separate circular
377 accelerators, before being injected into the main accelerator ring at an energy of 450 GeV. Within
378 the main ring protons are separated into two separate beams moving in opposite directions,
379 and their energy is increased to their full collision energy. Radiofrequency cavities are used to
380 accelerate these particles and sort them into bunches. From 2015-2018, these bunches consisted
381 of around 100 billion protons each with an energy of 6.5 TeV per proton, which collided at a rate
382 of 40 MHz, or every 25 ns.

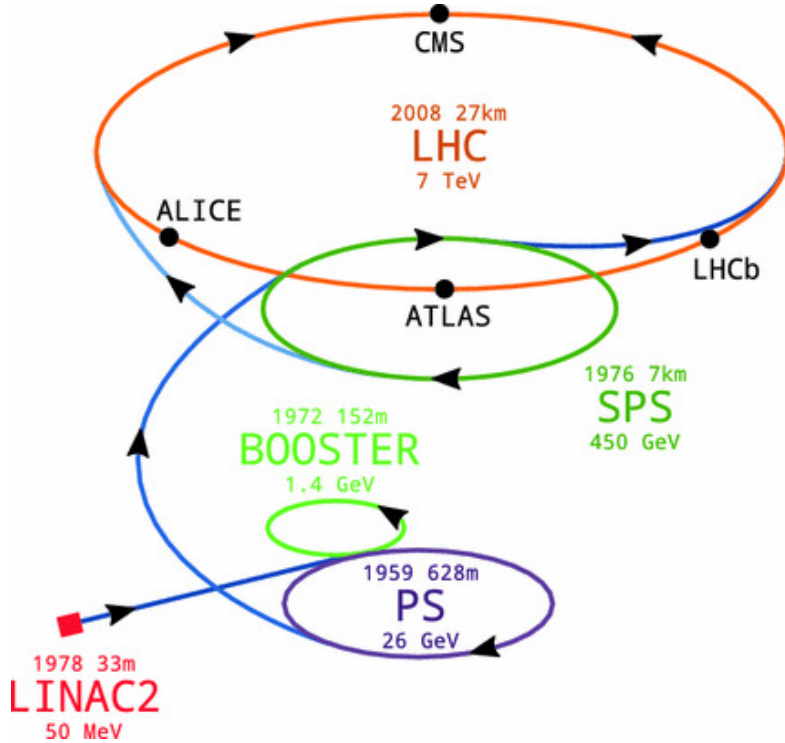


Figure 3.1: A summary of the accelerator chain used to feed protons into the LHC [9].

Because these proton bunches consist of a large number of particles, each bunch crossing consists of not just one, but several direct proton-proton collisions. The number of interactions that occur per bunch crossing, μ , is known as pileup. During Run 2, the average pileup for bunch crossings was around $\langle \mu \rangle = 35$, with values typically ranging between 10 and 70.

The amount of data collected by the LHC is measured in terms of luminosity, which is the ratio of the number of events detected per unit time, $\frac{dN}{dt}$, and the interaction cross-section, σ .

$$\mathcal{L} = \frac{1}{\sigma} \frac{dN}{dt} \quad (3.1)$$

389 The design luminosity of the LHC is $10^{34} \text{ cm}^{-2}\text{s}^{-1}$, however the LHC has achieved a
390 luminosity of over $2 \times 10^{34} \text{ cm}^{-2}\text{s}^{-1}$. The total luminosity is then this instantaneous luminosity
391 integrated over time.

$$\mathcal{L}_{\text{int}} = \int \mathcal{L} dt \quad (3.2)$$

392 The integrated luminosity collected by the ATLAS detector as of the end of 2018 is around
393 140 fb^{-1} , exceeding the expected integrated luminosity of 100 fb^{-1} .

394 4 The ATLAS Detector

395 ATLAS (a not terribly natural acronym for “A Toroidal LHC Apparatus”) is a general purpose
396 detector designed to maximize the detection efficiency of all physics objects, including leptons,
397 jets, and photons. This means it is capable of measuring all SM particles, with the exception of
398 neutrinos, the presence of which can be inferred based on missing transverse momentum. The
399 detector measures 44 m long, and 25 m tall.

400 The ATLAS detector consists of multiple concentric layers, each of which serves a different
401 purpose in reconstructing collisions. At the very center of the detector is the interaction point
402 where the proton beams of the LHC collide.

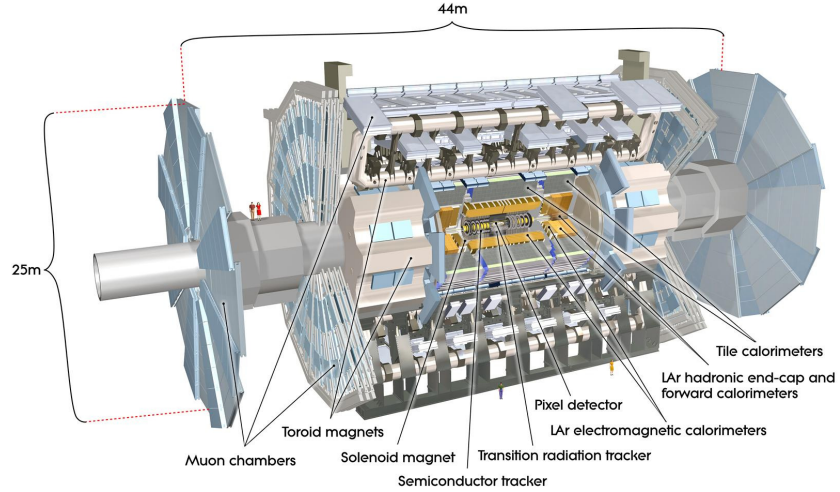


Figure 4.1: Cutaway view of the ATLAS detector, with labels of its major components [10].

403 4.1 Inner Detector

404 Just surrounding the interaction point is the Inner Detector, designed to track the path of charged
 405 particles moving through the detector. An inner solenoid surrounding the Innder Detector is
 406 used to produces a magnetic field of 2 T. This large magnetic field causes the path of charged
 407 particles moving through the Inner Detector to bend. Because this magnetic field is uniform and
 408 well known, it can be used in conjunction with the curvature of a particles path to measure its
 409 charge and momentum.

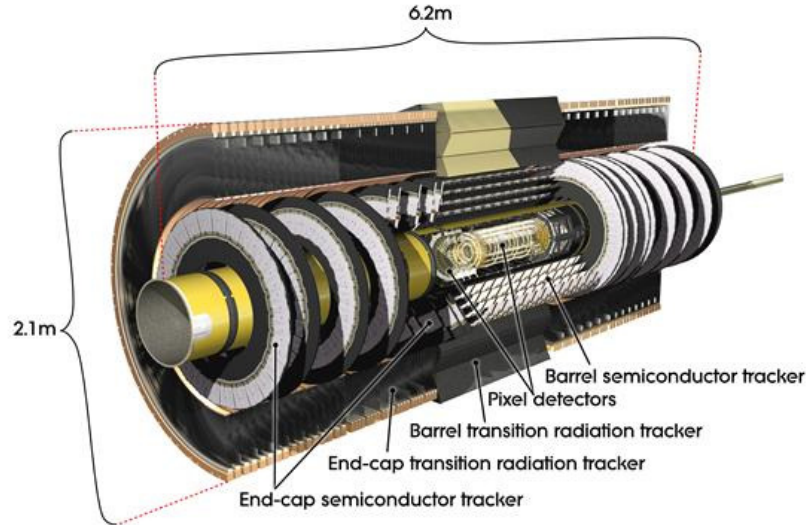


Figure 4.2: Cutaway view of the Inner Detector [11].

410 The Inner Detector consists of three components - the Pixel Detector, the Semi-Conductor
 411 Tracker (SCT), and the Transition Radiation Tracker (TRT). The Pixel Detector is the innermost
 412 of these, beginning just 33.25 mm away from the beam line. It consists of three silicon layers
 413 along the barrel, as well as three endcap layers, covering a range of $|\eta| < 2.5$.

414 The Semiconductor Tracker (SCT) is similar to the Pixel detector, but uses long strips of
 415 silicon rather than small pixels to cover a larger spatial area. It includes over 6 million readout
 416 strips, allowing the position of charged particles to be measured to an accuracy of $17 \mu\text{m}$.

417 The outermost component of the inner detector, the TRT consists of around 300,000 straw
 418 tubes filled with ionizable gas, which produces current through a wire in the center of each tube
 419 when a charged particle passes through. Between these staws are layers of material designed
 420 to produce transition radiation from ultrarelativistic particles as they pass through each material

421 boundary, amplifying the signal. The position uncertainty in the TRT is higher than the other
 422 two, on the order of 200 μm , but covering a much larger area.

423 **4.2 Calorimeters**

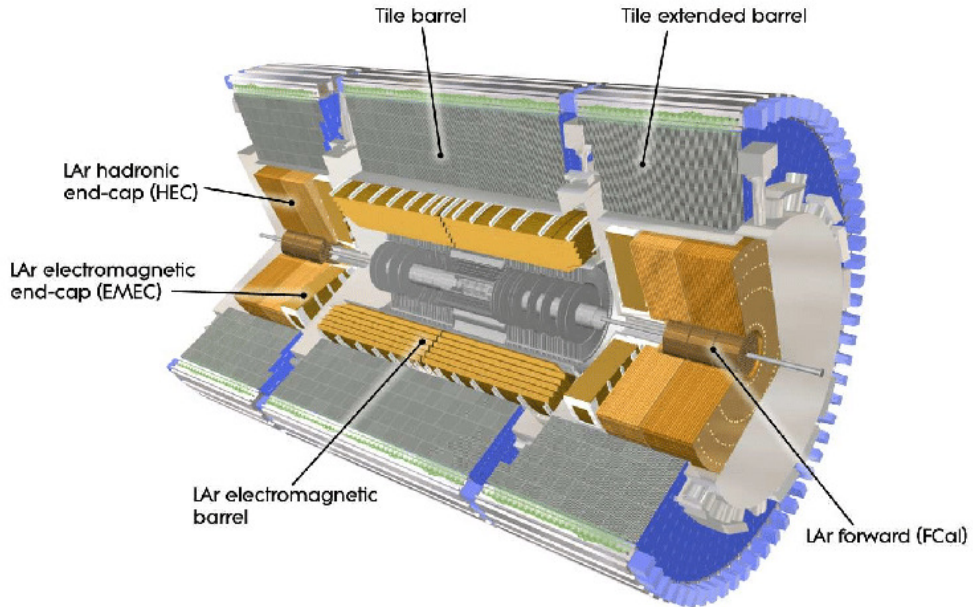


Figure 4.3: Cutaway view of the calorimeter system of the ATLAS detector [11].

424 Situated outside the Inner Detector are two concentric calorimeters. The inner calorimeter
 425 uses liquid argon (LAr) to measure the energy of particles that interact electromagnetically,
 426 which includes photons and any charged particle. The LAr calorimeter is made of heavy metals,
 427 primarily lead and copper, which causes electromagnetically interacting particles to shower,
 428 depositing their energy in the detector. The showering of the high energy particles that pass

429 through the calorimeter cause the liquid argon to ionize, and the ionized electrons are detected
430 by electronic readouts. The LAr calorimeter consists of around 180,000 readout channels.

431 The outer calorimeter measures the energy from particles that pass through the EM
432 calorimeter, and measures the energy of particles that interact via the strong force. This is
433 primarily hadrons. It is composed of steel plates designed to cause hadronic showering and
434 around 500,000 scintillating tiles as the active material. The signals from the hadronic calorimeter
435 are read out by photomultiplier tubes (PMTs).

436 **4.3 Muon Spectrometer**

437 Because muons are heavier than electrons and photons, and do not interact via the strong force,
438 they generally pass through the detector without being stopped by the calorimeters. The outermost
439 components of the detector are designed specifically to measure the energy and momentum of
440 muons produced in the LHC. The muon spectrometer consists of tracking and triggering systems.

441 The largest of the subdetectors, it extends from the outside of the calorimeter system, about a
442 4.25 m radius from the beam line, to a radius of 11 m. This large detector system is necessary
443 to accurately measure the momentum of muons, which is essential not only for measurements
444 involving the muons themselves, but also to accurately estimate the missing energy in each
445 event.

446 Two large toroidal magnets within the muon system generate a large magnetic field which
447 covers an area 26 m long with a radius of 10 m. Because the area covered by this magnet system

448 is so large, a uniform magnetic field like the one produced in the Inner Detector is impractical.
449 Instead, the magnetic field that exists in the muon spectrometer ranges between 2 T and 8 T, and
450 is much less uniform. The path of the muons passing through the spectrometer is bent by this
451 field, allowing their charge to be determined.

452 1200 tracking chambers are placed in the muon system in order to precisely measure the
453 tracks of muons with high spatial resolution. The path of the muons are tracked by Monitored
454 Drift Tubes, which are drift chambers formed by aluminum tubes and filled with ionizing gas.
455 These tubes produce a multi-layer spatial resolution on the order of 50 μm .

456 **4.4 Trigger System**

457 Because of the high collision rate and large amount of data collected by the various subdetectors,
458 ATLAS produces far more data than can actually be stored. Each event produces around 25 Mb
459 of raw data, which multiplied by the bunch crossing rate of 40 MHz, comes out to around a
460 petabyte of data every second. The information from every event cannot practically be stored,
461 therefore a sophisticated trigger system is employed in real time to determine whether events are
462 sufficiently interesting to be worth storing.

463 The trigger system in ATLAS involves multiple levels, each of which select out which
464 events move on to the next level of scrutiny. The level-1 trigger uses hardware information from
465 the calorimeters and muon spectrometer to select events that contain candidates for particles

⁴⁶⁶ commonly used in analysis, such as energetic leptons and jets. The level-1 trigger reduces the
⁴⁶⁷ rate of events from 40 MHz to around 100 kHz.

⁴⁶⁸ Events that pass the level-1 trigger move to the High-Level Trigger (HLT). The HLT takes
⁴⁶⁹ place outside of the detector in software, and looks for properties such as a large amount of
⁴⁷⁰ missing transverse energy, well defined leptons, and multiple high energy jets. Events that pass
⁴⁷¹ the HLT are stored and used for analysis. Because the specifics of the HLT are determined by
⁴⁷² software rather than hardware, the thresholds can be changed throughout the run of the detector
⁴⁷³ in response to run conditions such as changes to pileup and luminosity. After the HLT is applied,
⁴⁷⁴ the event rate is reduced to around 1000 per second, which are recorded for analysis.

⁴⁷⁵ **Part IV**

⁴⁷⁶ **Measurement of WZ + Heavy Flavor**

⁴⁷⁷ **5 Introduction**

⁴⁷⁸ The production of WZ in association with a heavy flavor jet represents an important background
⁴⁷⁹ for many major analyses. This includes any process with leptons and b-jets in the final state,
⁴⁸⁰ such as $t\bar{t}H$, $t\bar{t}W$, and $t\bar{t}Z$. While precise measurements have been made of WZ production
⁴⁸¹ [12], WZ + heavy flavor remains poorly understood. This is largely because the QCD processes

482 involved in the production of the b-jet make it difficult to simulate accurately. This introduces a
483 large uncertainty for analyses that include this process as a background.

484 Motivated by its relevance to the $t\bar{t}H$ multilepton analysis, we perform a study of the fully
485 leptonic decay mode of this channel; that is, events where both the W and Z decay leptonically.
486 Because WZ has no associated jets at leading order, while the major backgrounds for this channel
487 tend to have high jet multiplicity, events with more than two jets are rejected. This gives a final
488 state signature of three leptons and one or two jets.

489 Events that meet this selection criteria are sorted into pseudo-continuous b-tagging regions
490 based on the DL1r b-tag score of their associated jets. This is done to separate WZ + b-jet events
491 from WZ + charm and WZ + light jets. These regions are fit to data in order to make a more
492 accurate estimate of the contribution of WZ + heavy-flavor, where heavy-flavor jets include
493 b-jets and charm jets. The full Run-2 dataset collected by the ATLAS detector, representing 139
494 fb^{-1} of data from pp collisions at $\sqrt{s} = 13 \text{ TeV}$, is used for this study.

495 Section 10 details the data and Monte Carlo (MC) samples used in the analysis. The
496 reconstruction of various physics objects is described in Section 11. Section 12 describes the
497 event selection applied to these samples, along the definitions of the various regions used in
498 the fit. The multivariate analysis techniques used to separate the tZ background from WZ +
499 heavy flavor are described in Section 13. Section 21 describes the various sources of systematic
500 uncertainties considered in the fit. Finally, the results of the analysis are summarized in Section
501 22, followed by a brief conclusion in Section ??.

502 **The current state of the analysis shows blinded results for the full 2018 dataset.**
503 **Regions containing >5% WZ+b events are blinded, and results are from Asimov, MC only**
504 **fits.**

505 **6 Data and Monte Carlo Samples**

506 **6.1 Data Samples**

507 This study uses a sample of proton-proton collision data collected by the ATLAS detector from
508 2015 through 2018 at an energy of $\sqrt{s} = 13$ TeV, which represents an integrated luminosity of
509 139 fb^{-1} . This data set was collected with a bunch crossing rate of 25 ns. All data used in this
510 analysis was verified by data quality checks.

511 **6.2 Monte Carlo Samples**

512 Several different generators were used to produce Monte Carlo simulations of the signal and
513 background processes. For all samples, the response of the ATLAS detector is simulated using
514 Geant4. The WZ signal samples are simulated using Sherpa 2.2.2 [13]. Specific information
515 about the Monte Carlo samples being used can be found in Table 23.

Table 1: The configurations used for event generation of signal and background processes, including the event generator, matrix element (ME) order, parton shower algorithm, and parton distribution function (PDF).

Process	Event generator	ME order	Parton Shower	PDF
WZ, VV	SHERPA 2.2.2	MEPS NLO	SHERPA	CT10
tZ	MG5_AMC	NLO	PYTHIA 8	CTEQ6L1
t̄tW	MG5_AMC (SHERPA 2.1.1)	NLO (LO multileg)	PYTHIA 8 (SHERPA)	NNPDF 3.0 NLO (NNPDF 3.0 NLO)
t̄t(Z/γ* → ll)	MG5_AMC	NLO	PYTHIA 8	NNPDF 3.0 NLO
t̄tH	MG5_AMC (MG5_AMC)	NLO (NLO)	PYTHIA 8 (HERWIG++)	NNPDF 3.0 NLO [14] (CT10 [15])
tHqb	MG5_AMC	LO	PYTHIA 8	CT10
tHW	MG5_AMC (SHERPA 2.1.1)	NLO (LO multileg)	HERWIG++ (SHERPA)	CT10 (NNPDF 3.0 NLO)
tWZ	MG5_AMC	NLO	PYTHIA 8	NNPDF 2.3 LO
t̄t̄, t̄t̄t̄	MG5_AMC	LO	PYTHIA 8	NNPDF 2.3 LO
t̄tW+W-	MG5_AMC	LO	PYTHIA 8	NNPDF 2.3 LO
t̄t	POWHEG-BOX v2 [16]	NLO	PYTHIA 8	NNPDF 3.0 NLO
t̄t̄γ	MG5_AMC	LO	PYTHIA 8	NNPDF 2.3 LO
s-, t-channel, Wt single top	POWHEG-BOX v1 [17]	NLO	PYTHIA 6	CT10
qqVV, VVV				
Z → l+l-	SHERPA 2.2.1	MEPS NLO	SHERPA	NNPDF 3.0 NLO

516 7 Object Reconstruction

517 All regions defined in this analysis share a common lepton, jet, and overall event preselection.

518 The selection applied to each physics object is detailed here; the event preselection, and the
519 selection used to define the various fit regions, is described in Section 12.

520 All events are required to be selected by dilepton triggers. The p_T thresholds of the
521 dilepton trigger on two electrons were 12 GeV in 2015, 17 GeV in 2016, and 24 GeV in 2017 and
522 2018, while for the dimuon triggers the p_T thresholds on the leading (sub-leading) muon were

523 18 GeV (8 GeV) in 2015, and 22 GeV (8 GeV) in 2016-2018. For the electron+muon triggers,
 524 the p_T thresholds on the electron (muon) were 17 GeV (14 GeV) for all datasets.

525 **7.1 Light leptons**

526 Electron candidates are reconstructed from energy clusters in the electromagnetic calorimeter
 527 that are associated with charged particle tracks reconstructed in the inner detector [18]. Electron
 528 candidates are required to have $p_T > 10$ GeV and $|\eta_{\text{cluster}}| < 2.47$. Muon candidates are
 529 reconstructed by combining inner detector tracks with track segments or full tracks in the muon
 530 spectrometer [19]. Muon candidates are required to have $p_T > 10$ GeV and $|\eta| < 2.5$. Candidates
 531 in the transition region between different electromagnetic calorimeter components, $1.37 <$
 532 $|\eta_{\text{cluster}}| < 1.52$, are rejected. A multivariate likelihood discriminant combining shower shape
 533 and track information is used to distinguish real electrons from hadronic showers (fake electrons).
 534 To further reduce the non-prompt electron contribution, the track is required to be consistent
 535 with originating from the primary vertex; requirements are imposed on the transverse impact
 536 parameter significance ($|d_0|/\sigma_{d_0} < 5$) and the longitudinal impact parameter ($|\Delta z_0 \sin \theta_\ell| < 0.5$
 537 mm). Electron candidates are required to pass TightLH identification.

538 Muon candidates are reconstructed by combining inner detector tracks with track segments
 539 or full tracks in the muon spectrometer [19]. Muon candidates are required to have $p_T > 10$ GeV
 540 and $|\eta| < 2.5$. The longitudinal impact parameter is the same for both electrons and muons, while

541 muons are required to pass a slightly tighter transverse impact parameter, $|d_0|/\sigma_{d_0} < 3$. Muons
 542 are also required to pass Medium ID requirements.

543 Leptons are additionally required to pass a non-prompt BDT selection developed by the
 544 $t\bar{t}H$ multilepton/ $t\bar{t}W$ analysis group. This BDT and the WPs used are summarized in Appendix
 545 .1, and described in detail in [20]. Optimized working points and scale factors for this BDT are
 546 taken from that analysis.

547 7.2 Jets

548 Jets are reconstructed from calibrated topological clusters built from energy deposits in the
 549 calorimeters [21], using the anti- k_t algorithm with a radius parameter $R = 0.4$. Particle Flow, or
 550 PFlow, jets are used in the analysis, which are hadronic objects reconstructed using information
 551 from both the tracker and the calorimeter. Jets with energy contributions likely arising from noise
 552 or detector effects are removed from consideration [22], and only jets satisfying $p_T > 25$ GeV
 553 and $|\eta| < 2.5$ are used in this analysis. For jets with $p_T < 60$ GeV and $|\eta| < 2.4$, a jet-track
 554 association algorithm is used to confirm that the jet originates from the selected primary vertex,
 555 in order to reject jets arising from pileup collisions [23].

556 7.3 B-tagged Jets

557 In order to make a measurement of $WZ +$ heavy flavor it is necessary to distinguish these events
 558 from $WZ +$ light jets. For this purpose, the DL1r b-tagging algorithm is used to distinguish

559 heavy flavor jets from lighter ones. The DL1r algorithm uses jet kinematics, particularly jet
 560 vertex information, as input for a neural network which assigns each jet a score designed to
 561 reflect how likely that jet is to have originated from a b-quark.

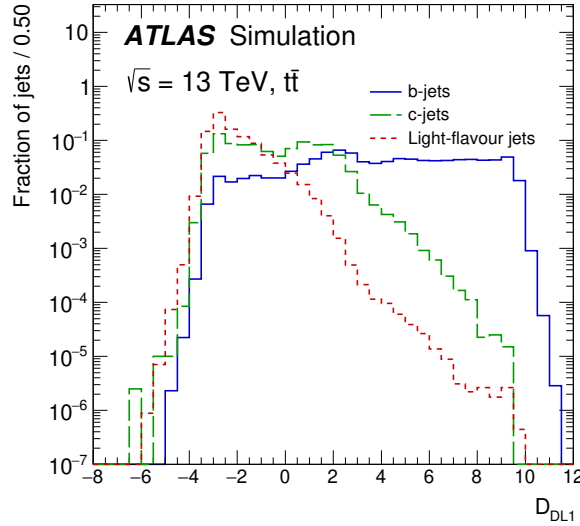


Figure 7.1: Output distribution of the DL1r algorithm for b-jets, charm jets, and light jets

562 From the output of the BDT, calibrated working points (WPs) are developed based on the
 563 efficiency of truth b-jets at particular values of the DL1r algorithm. The working points used in
 564 this analysis are summarized in Table 10.

WP	none	loose	medium	tight	tightest
b eff.	-	85%	77%	70%	60%

Table 2: B-tagging Working Points by tightness and b-jet efficiency

565 A tighter WP will accept fewer b-jets, but reject a higher fraction of charm and light jets.
 566 Generally, analyses that include b-jets will use a fixed working point, for example, requiring that

567 a jet pass the 70% threshold. By instead treating these working point as bins, e.g. events with
568 jets that fall between the 85% and 77% WPs fall into one bin, while events with jets passing the
569 60% WP fall into another, and looking at the full psuedo-continuous DL1r spectrum of the jets,
570 additional information can be gained. The psuedo-continuous b-tag spectrum is used in this case
571 to separate out $WZ + b$, $WZ + \text{charm}$, and $WZ + \text{light}$.

572 **7.4 Missing transverse energy**

573 Missing transverse momentum (E_T^{miss}) is used as part of the event selection. The missing
574 transverse momentum vector is defined as the inverse of the sum of the transverse momenta of
575 all reconstructed physics objects as well as remaining unclustered energy, the latter of which is
576 estimated from low- p_T tracks associated with the primary vertex but not assigned to a hard object,
577 with object definitions taken from [24]. Light leptons considered in the E_T^{miss} reconstruction are
578 required to have $p_T > 10$ GeV, while jets are required to have $p_T > 20$ GeV.

579 **7.5 Overlap removal**

580 To avoid double counting objects and remove leptons originating from decays of hadrons, overlap
581 removal is performed in the following order: any electron candidate within $\Delta R = 0.1$ of another
582 electron candidate with higher p_T is removed; any electron candidate within $\Delta R = 0.1$ of a muon
583 candidate is removed; any jet within $\Delta R = 0.3$ of an electron candidate is removed; if a muon

584 candidate and a jet lie within $\Delta R = \min(0.4, 0.04 + 10[\text{GeV}]/p_T(\text{muon}))$ of each other, the jet
 585 is kept and the muon is removed.

586 This algorithm is applied to the preselected objects. The overlap removal procedure is
 587 summarized in Table 26.

Keep	Remove	Cone size (ΔR)
electron	electron (low p_T)	0.1
muon	electron	0.1
electron	jet	0.3
jet	muon	$\min(0.4, 0.04 + 10[\text{GeV}]/p_T(\text{muon}))$
electron	tau	0.2

Table 3: Summary of the overlap removal procedure between electrons, muons, and jets.

588 8 Event Selection and Signal Region Definitions

589 Event are required to pass a preselection described in Section 12.1 and summarized in Table 12.
 590 Those that pass this preselection are divided into various fit regions described in Section 12.2,
 591 based on the number of jets in the event, and the b-tag score of those jets.

592 8.1 Event Preselection

593 Events are required to include exactly three reconstructed light leptons passing the requirement
 594 described in 11.2, which have a total charge of ± 1 .

595 The leptons are ordered in the analysis code as 0, 1, and 2. Lepton 0 is the lepton whose
 596 charge is opposite the other two. Lepton 1 is the lepton closest to the opposite charge lepton, i.e.
 597 the smallest ΔR , leaving lepton 2 as the lepton further from the opposite charge lepton. Lepton
 598 0 is required to have $p_T > 10$ GeV, while the same sign leptons, 1 and 2, are required to have
 599 $p_T > 20$ GeV to reduce the contribution of non-prompt leptons.

600 The invariant mass of at least one pair of opposite sign, same flavor leptons is required
 601 to fall within 10 GeV of the mass of the Z boson, 91.2 GeV. Events where one of the opposite
 602 sign pairs have an invariant mass less than 12 GeV are rejected in order to suppress low mass
 603 resonances.

604 An additional requirement is placed on the missing transverse energy, $E_T^{\text{miss}} > 20$ GeV,
 605 and the transverse mass of the W candidate, $m(E_T^{\text{miss}} + l_{\text{other}}) > 30$ GeV, where E_T^{miss} is the
 606 missing transverse energy, and l_{other} is the lepton not included in the Z-candidate.

607 Events are required to have one or two reconstructed jets passing the selection described
 608 in Section 11.3. Events with more than two jets are rejected in order to reduce the contribution
 609 of backgrounds such as $t\bar{t}Z$ and $t\bar{t}W$, which tend to have higher jet multiplicity.

Event Selection

- Exactly three leptons with charge ± 1
 - Two same-charge leptons with $p_T > 20$ GeV
 - One opposite charge lepton with $p_T > 10$ GeV
 - $m(l^+l^-)$ within 10 GeV of 91.2 GeV
 - Transverse mass of W-candidate, $m_T(E_T^{\text{miss}} + \text{lep}_{\text{other}}) > 30$ GeV
 - Missing transverse energy, $E_T^{\text{miss}} > 20$ GeV
 - One or two jets with $p_T > 25$ GeV
-

Table 4: Summary of the selection applied to events for inclusion in the fit

610 The event yields in the preselection region for both data and Monte Carlo are summarized
 611 in Table 12.1, which shows good agreement between data and Monte Carlo, and demonstrates
 612 that this region consists primarily of WZ events. The WZ events are split into WZ + b, WZ +
 613 c, and WZ + l based on the truth flavor of the associated jet in the event. In this ordering b-jet
 614 supersede charm, which supersides light. That is, WZ + l events contain no charm and no b jets
 615 at truth level, WZ + c contain at least one truth charm and no b-jets, and WZ + b contains at least
 616 one truth b-jet.

Process	Events
WZ + b	167.6 ± 6.5
WZ + c	1080 ± 40
WZ + l	7220 ± 310
Other VV	850 ± 140
$t\bar{t}W$	16.8 ± 2.3
$t\bar{t}Z$	115 ± 17
rare Top	2.2 ± 0.1
Single top	0.10 ± 0.45
Three top	0.01 ± 0.01
Four top	0.02 ± 0.01
$t\bar{t}WW$	0.23 ± 0.05
Z + jets	600 ± 260
V + γ	37 ± 54
tZ	190 ± 70
tW	5.5 ± 1.2
WtZ	25.8 ± 1.1
VVV	26.2 ± 0.9
VH	94 ± 7
t \bar{t}	108.68 ± 8
t $\bar{t}H$	4.3 ± 0.5
Total	10600 ± 530
Data	10574

Table 5: Event yields in the preselection region at 139.0 fb^{-1}

617 Here Other VV represents diboson processes other than WZ, and consists predominantly

618 of $ZZ \rightarrow ll\bar{l}\bar{l}$ events where one of the leptons is not reconstructed.

619 8.2 Fit Regions

620 Once preselection has been applied, the remaining events are categorized into one of twelve
621 orthogonal regions. The regions used in the fit are summarized in Table 14.

Table 6: A list of the regions used in the fit and the selection used for each.

Region	Selection
1j, <85%	$N_{\text{jets}} = 1, n\text{Jets}_{\text{DL1r}_85} = 0$
1j, 85%-77%	$N_{\text{jets}} = 1, n\text{Jets}_{\text{DL1r}_85} = 1, n\text{Jets}_{\text{DL1r}_77} = 0$
1j, 77%-70%	$N_{\text{jets}} = 1, n\text{Jets}_{\text{DL1r}_77} = 1, n\text{Jets}_{\text{DL1r}_70} = 0$
1j, 70%-60%	$N_{\text{jets}} = 1, n\text{Jets}_{\text{DL1r}_70} = 1, n\text{Jets}_{\text{DL1r}_60} = 0$
1j, >60%	$N_{\text{jets}} = 1, n\text{Jets}_{\text{DL1r}_60} = 1, tZ \text{ BDT} > 0.725$
1j tZ CR	$N_{\text{jets}} = 1, n\text{Jets}_{\text{DL1r}_60} = 1, tZ \text{ BDT} < 0.725$
2j, <85%	$N_{\text{jets}} = 2, n\text{Jets}_{\text{DL1r}_85} = 0$
2j, 85%-77%	$N_{\text{jets}} = 2, n\text{Jets}_{\text{DL1r}_85} \geq 1, n\text{Jets}_{\text{DL1r}_77} = 0$
2j, 77%-70%	$N_{\text{jets}} = 2, n\text{Jets}_{\text{DL1r}_77} \geq 1, n\text{Jets}_{\text{DL1r}_70} = 0$
2j, 70%-60%	$N_{\text{jets}} = 2, n\text{Jets}_{\text{DL1r}_70} \geq 1, n\text{Jets}_{\text{DL1r}_60} = 0$
2j, >60%	$N_{\text{jets}} = 2, n\text{Jets}_{\text{DL1r}_60} \geq 1, tZ \text{ BDT} > 0.725$
2j tZ CR	$N_{\text{jets}} = 2, n\text{Jets}_{\text{DL1r}_60} \geq 1, tZ \text{ BDT} < 0.725$

622 The working points discussed in Section 11.4 are used to separate events into fit regions
623 based on the highest working point reached by a jet in each event. Because the background
624 composition differs significantly based on the number of b-jets, events are further subdivided
625 into 1-jet and 2-jet regions in order to minimize the impact of background uncertainties.

626 An unfolding procedure is performed to account for differences in the number of recon-
627 structed jets compared to the number of truth jets in each event. In order to account for migration

628 of WZ+1-jet and WZ+2-jet events between the 1-jet and 2-jet bins at reco level, the signal
 629 samples are separated based on the number of truth jets. Events with 0 jets or more than 3 jets at
 630 truth level, yet fall within one of the categories listed in Table 14, are categorized as WZ + other,
 631 and treated as a background. The composition of the number of truth jets in each reco jet bin is
 632 taken from MC, with uncertainties in these estimates described in detail in Section 21.

633 An additional tZ control region is created based on the BDT described in Section 13. The
 634 region with 1-jet passing the 60% working point is split in two - a signal enriched region of
 635 events with a BDT score greater than 0.03, and a tZ control region including events with less
 636 than 0.03. This cutoff is arrived at by performing an Asimov fit with a variety of cutoffs, and
 637 selecting the value that produces the highest significance for the measurement of WZ + b.

638 **8.3 Non-Prompt Lepton Estimation**

639 Two processes act as sources of non-prompt leptons appear in the analysis: $t\bar{t}$ and Z+jet
 640 production both produce two prompt leptons, and each contribute to the 31 region when an
 641 additional non-prompt lepton appears in the event. The contribution of these processes is
 642 estimated with Monte Carlo simulations, which are validated using enriched control regions.

643 The modelling in the Z+jets and $t\bar{t}$ CRs is further validated for each of the pseudo-
 644 continuous b-tag regions used in the analysis. The relevant lepton p_T spectrum in each b-tag
 645 region is shown in Appendix .2 for these CRs after the correction factors derived below have
 646 been applied.

647 **8.3.1 $t\bar{t}$ Validation**

648 $t\bar{t}$ events can produce two prompt leptons from the decay of each of the tops. These top decays
 649 produce two b-quarks, the decay of which can produce additional non-prompt leptons, which
 650 occasionally pass the event preselection. In order to validate that the Monte Carlo accurately
 651 simulates this process accurately, the MC prediction in a non-prompt $t\bar{t}$ enriched control region
 652 is compared to data.

653 The $t\bar{t}$ control region is similar to the preselection region - three leptons meeting the
 654 criteria described in Section 12 are required, and the requirements on E_T^{miss} remain the same.
 655 However, the selection requiring a lepton pair form a Z-candidate are reversed. Events where the
 656 invariant mass of any two opposite sign, same flavor leptons falls within 10 GeV of 91.2 GeV are
 657 rejected. This ensures the $t\bar{t}$ control region is orthogonal to the preselection region.

658 Further, because the jet multiplicity of $t\bar{t}$ events tends to be higher than WZ, the number
 659 of jets in each event is required to be greater than 1. As b-jets are almost invariably produced
 660 from top decays, at least one b-tagged jet passing the 70% DL1r WP in each event is required.

661 Data is compared to MC predictions in the region for a variety of kinematic variable, as well
 662 as various b-tag WPs. A constant normalization discrepancy between data and MC predictions
 663 of approximately 10% is found, which is accounted for by applying a constant correction factor
 664 of 0.9 to the $t\bar{t}$ MC prediction. As data and MC are found to agree within 20% for each of
 665 the b-tag WPs considered, a 20% systematic uncertainty on the $t\bar{t}$ prediction is included for the
 666 analysis.

667 **8.3.2 Z+jets Validation**

668 Similar to $t\bar{t}$, a non-prompt Z +jets control region is produced in order to validate the MC
 669 predictions. The lepton requirements remain the same as the preselection region. Because no
 670 neutrinos are present for this process, the E_T^{miss} cut is reversed, requiring $E_T^{\text{miss}} < 30 \text{ GeV}$. This
 671 also ensures this control region is orthogonal to the preselection region. Further, the number of
 672 jets in each event is required to be greater than or equal to one.

673 While there is general agreement between data and MC within statistical uncertainty, the
 674 shape of the p_T spectrum of the lepton from the W is found to differ. To account for this
 675 discrepancy, a variable correction factor is applied to Z +jets. χ^2 minimization of the W lepton
 676 p_T spectrum is performed to derive a correction factor of $1.53 - 6.6 * 10^{-6}(\text{lep}_\text{Pt}_W)$.

677 The uncertainty in the $Z + \text{jets}$ prediction is evaluated by comparing data to MC for each
 678 of the continuous b-tag WPs. For each of the regions considered, the data falls within 25% of
 679 the MC prediction once this correction factor has been applied. Therefore, a 25% systematic
 680 uncertainty is applied to $Z + \text{jets}$ in the analysis.

681 **9 tZ Interference Studies and Separation Multivariate Analysis**

682 An important process to consider in this analysis is tZ : the top almost always decays into a W
 683 boson and b-quark, and when both the W and Z decay leptonically, this gives three leptons and
 684 a heavy flavor jet in the final state. Because tZ can produce a final state identical to the signal,

685 it represents a predominant background in the most signal enriched regions. That is, the region
686 with one jet passing the 60% DL1r WP. Therefore, a boosted decision tree (BDT) algorithm is
687 trained using XGBoost [28] to separate WZ + heavy flavor from tZ. The result of this BDT is
688 used to create a tZ enriched region in the fit, reducing its impact on the measurement of WZ +
689 heavy flavor.

690 The following kinematic variables are used as inputs to train this BDT:

- 691 • The invariant mass of the reconstructed top candidate
- 692 • p_T of each of the leptons, jet
- 693 • The invariant mass of each combination of lepton pairs, $M(l\bar{l})$
- 694 • E_T^{miss}
- 695 • Distance between each combination of leptons, $\Delta R(l\bar{l})$
- 696 • Distance between each lepton and the jet, $\Delta R(lj)$

697 Here the top candidate is reconstructed based on the procedure described in section 6.1 of
698 [27]. Broadly, the mass of the top quark candidate is reconstructed from the jet, the lepton not
699 included in the Z-candidate, and a reconstructed neutrino. In the case that there is one jet in the
700 event, there is only possible b-jet candidate. For events with two jets, the jet with the highest
701 DL1r score is used.

702 The training samples included only events meeting the requirements of the 1-jet, >60%
703 region, i.e. passing all the selection described in section 12 and having exactly one jet which
704 passes the tightest (60%) DL1r working point. A sample of 20,000 background (tZ) and signal
705 (WZ+b) Monte Carlo events are used to train the BDT. And additional 5,000 events are reserved
706 for testing the model, in order to prevent over-fitting. A total of 750 decision trees with a
707 maximum depth of 6 branches are used to build the model. These parameters are chosen
708 empirically, by training several models with different parameters and selecting the one that gave
709 the best separation for the test sample.

710 The results of the BDT training are shown in figure 13.1. The output scores for both signal
711 and background events is shown on the left. The right shows the receiving operating characteristic
712 (ROC) curve that results from the MVA. The ROC curve represents the background rejection
713 as a function of signal efficiency, where each point on the curve represents a different response
714 score. The ROC curve of the BDT is compared to the performance of using an optimal set of flat
715 selections on the same set of input variables.

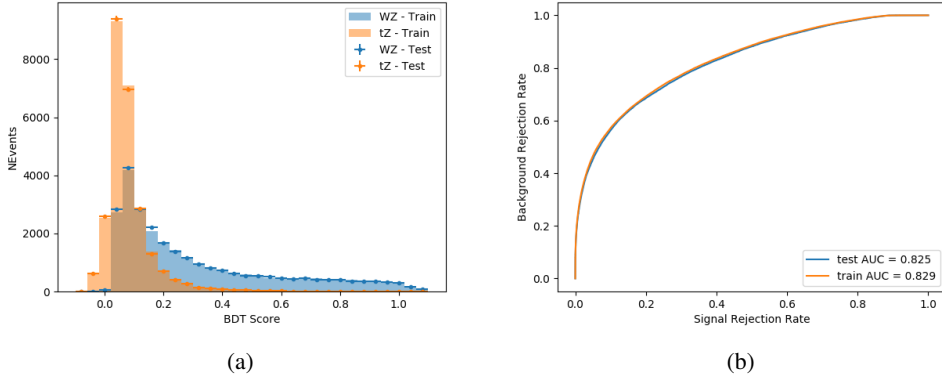


Figure 9.1: Distribution of the BDT response for signal and background events on the left, the ROC curve for the BDT on the right.

716 The relative important of each input feature in the model, measured by how often they
 717 appeared in the decision trees, is shown in figure 13.2.

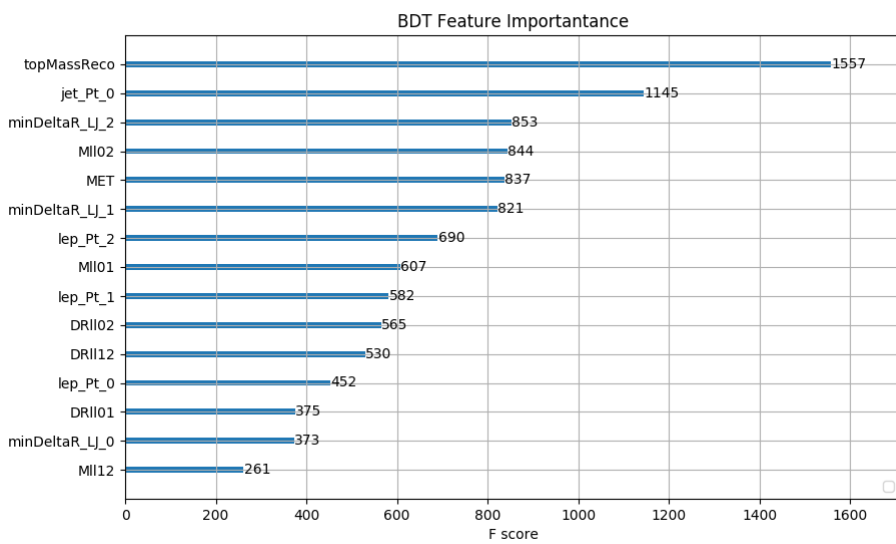


Figure 9.2: Relative importance of each input feature in the model.

718 These results suggest that some amount of separation can be achieved between these two
719 processes, with a high BDT score selecting a set of events that is pure in $WZ + b$. A BDT score
720 of 0.725 is selected as a cutoff, where events with scores higher than this form a signal enriched
721 region, and events with scores lower than this form a $t\bar{Z}$ control region. This cutoff is selected by
722 varying the value of this cutoff in stat-only Asimov fits, and selecting the value that minimizes
723 the statistical uncertainty on $WZ + b$.

724 **10 Data and Monte Carlo Samples**

725 **10.1 Data Samples**

726 This study uses a sample of proton-proton collision data collected by the ATLAS detector from
727 2015 through 2018 at an energy of $\sqrt{s} = 13$ TeV, which represents an integrated luminosity of
728 139 fb^{-1} . This data set was collected with a bunch crossing rate of 25 ns. All data used in this
729 analysis was verified by data quality checks.

730 **10.2 Monte Carlo Samples**

731 Several different generators were used to produce Monte Carlo simulations of the signal and
732 background processes. For all samples, the response of the ATLAS detector is simulated using
733 Geant4. The WZ signal samples are simulated using Sherpa 2.2.2 [13]. Specific information
734 about the Monte Carlo samples being used can be found in Table 23.

Table 7: The configurations used for event generation of signal and background processes, including the event generator, matrix element (ME) order, parton shower algorithm, and parton distribution function (PDF).

Process	Event generator	ME order	Parton Shower	PDF
WZ, VV	SHERPA 2.2.2	MEPS NLO	SHERPA	CT10
tZ	MG5_AMC	NLO	PYTHIA 8	CTEQ6L1
t̄tW	MG5_AMC (SHERPA 2.1.1)	NLO (LO multileg)	PYTHIA 8 (SHERPA)	NNPDF 3.0 NLO (NNPDF 3.0 NLO)
t̄t(Z/γ* → ll)	MG5_AMC	NLO	PYTHIA 8	NNPDF 3.0 NLO
t̄tH	MG5_AMC (MG5_AMC)	NLO (NLO)	PYTHIA 8 (HERWIG++)	NNPDF 3.0 NLO [14] (CT10 [15])
tHqb	MG5_AMC	LO	PYTHIA 8	CT10
tHW	MG5_AMC (SHERPA 2.1.1)	NLO (LO multileg)	HERWIG++ (SHERPA)	CT10 (NNPDF 3.0 NLO)
tWZ	MG5_AMC	NLO	PYTHIA 8	NNPDF 2.3 LO
t̄t̄t, t̄t̄t̄t	MG5_AMC	LO	PYTHIA 8	NNPDF 2.3 LO
t̄tW+W-	MG5_AMC	LO	PYTHIA 8	NNPDF 2.3 LO
t̄t	POWHEG-BOX v2 [16]	NLO	PYTHIA 8	NNPDF 3.0 NLO
t̄tγ	MG5_AMC	LO	PYTHIA 8	NNPDF 2.3 LO
s-, t-channel, Wt single top	POWHEG-BOX v1 [17]	NLO	PYTHIA 6	CT10
qqVV, VVV				
Z → l+l-	SHERPA 2.2.1	MEPS NLO	SHERPA	NNPDF 3.0 NLO

11 Object Reconstruction

All regions defined in this analysis share a common lepton, jet, and overall event preselection.

737 The selection applied to each physics object is detailed here; the event preselection, and the

⁷³⁸ selection used to define the various fit regions, is described in Section 12.

All events are required to be selected by dilepton triggers. The p_T thresholds of the

dilepton trigger on two electrons were 12 GeV in 2015, 17 GeV in 2016, and 24 GeV in 2017 and

741 2018, while for the dimuon triggers the p_T thresholds on the leading (sub-leading) muon were

⁷⁴² 18 GeV (8 GeV) in 2015, and 22 GeV (8 GeV) in 2016-2018. For the electron+muon triggers,
⁷⁴³ the p_T thresholds on the electron (muon) were 17 GeV (14 GeV) for all datasets.

⁷⁴⁴ **11.1 Light leptons**

⁷⁴⁵ Electron candidates are reconstructed from energy clusters in the electromagnetic calorimeter
⁷⁴⁶ that are associated with charged particle tracks reconstructed in the inner detector [18]. Electron
⁷⁴⁷ candidates are required to have $p_T > 10$ GeV and $|\eta_{\text{cluster}}| < 2.47$. Muon candidates are
⁷⁴⁸ reconstructed by combining inner detector tracks with track segments or full tracks in the muon
⁷⁴⁹ spectrometer [19]. Muon candidates are required to have $p_T > 10$ GeV and $|\eta| < 2.5$. Candidates
⁷⁵⁰ in the transition region between different electromagnetic calorimeter components, $1.37 <$
⁷⁵¹ $|\eta_{\text{cluster}}| < 1.52$, are rejected. A multivariate likelihood discriminant combining shower shape
⁷⁵² and track information is used to distinguish real electrons from hadronic showers (fake electrons).
⁷⁵³ To further reduce the non-prompt electron contribution, the track is required to be consistent
⁷⁵⁴ with originating from the primary vertex; requirements are imposed on the transverse impact
⁷⁵⁵ parameter significance ($|d_0|/\sigma_{d_0} < 5$) and the longitudinal impact parameter ($|\Delta z_0 \sin \theta_\ell| < 0.5$
⁷⁵⁶ mm). Electron candidates are required to pass TightLH identification.

⁷⁵⁷ Muon candidates are reconstructed by combining inner detector tracks with track segments
⁷⁵⁸ or full tracks in the muon spectrometer [19]. Muon candidates are required to have $p_T > 10$ GeV
⁷⁵⁹ and $|\eta| < 2.5$. The longitudinal impact parameter is the same for both electrons and muons, while

760 muons are required to pass a slightly tighter transverse impact parameter, $|d_0|/\sigma_{d_0} < 3$. Muons
761 are also required to pass Medium ID requirements.

762 Leptons are additionally required to pass a non-prompt BDT selection developed by the
763 $t\bar{t}H$ multilepton/ $t\bar{t}W$ analysis group. This BDT and the WPs used are summarized in Appendix
764 [.1](#), and described in detail in [\[20\]](#). Optimized working points and scale factors for this BDT are
765 taken from that analysis.

766 **11.2 Jets**

767 Jets are reconstructed from calibrated topological clusters built from energy deposits in the
768 calorimeters [\[21\]](#), using the anti- k_t algorithm with a radius parameter $R = 0.4$. Particle Flow, or
769 PFlow, jets are used in the analysis, which are hadronic objects reconstructed using information
770 from both the tracker and the calorimeter. Jets with energy contributions likely arising from noise
771 or detector effects are removed from consideration [\[22\]](#), and only jets satisfying $p_T > 25$ GeV
772 and $|\eta| < 2.5$ are used in this analysis. For jets with $p_T < 60$ GeV and $|\eta| < 2.4$, a jet-track
773 association algorithm is used to confirm that the jet originates from the selected primary vertex,
774 in order to reject jets arising from pileup collisions [\[23\]](#).

775 **11.3 B-tagged Jets**

776 In order to make a measurement of $WZ +$ heavy flavor it is necessary to distinguish these events
777 from $WZ +$ light jets. For this purpose, the DL1r b-tagging algorithm is used to distinguish

778 heavy flavor jets from lighter ones. The DL1r algorithm uses jet kinematics, particularly jet
 779 vertex information, as input for a neural network which assigns each jet a score designed to
 780 reflect how likely that jet is to have originated from a b-quark.

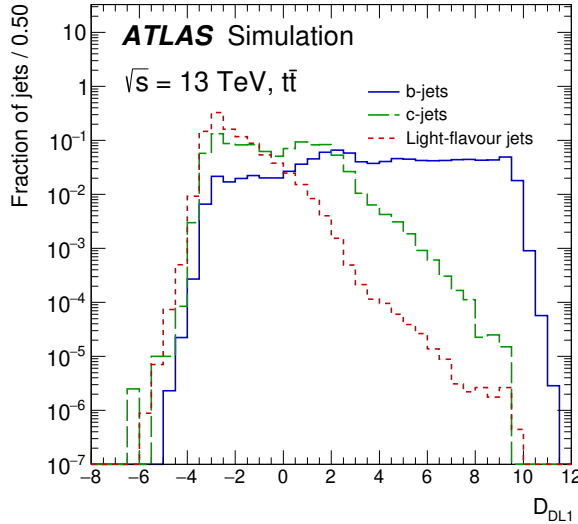


Figure 11.1: Output distribution of the DL1r algorithm for b-jets, charm jets, and light jets

781 From the output of the BDT, calibrated working points (WPs) are developed based on the
 782 efficiency of truth b-jets at particular values of the DL1r algorithm. The working points used in
 783 this analysis are summarized in Table 10.

WP	none	loose	medium	tight	tightest
b eff.	-	85%	77%	70%	60%

Table 8: B-tagging Working Points by tightness and b-jet efficiency

784 A tighter WP will accept fewer b-jets, but reject a higher fraction of charm and light jets.
 785 Generally, analyses that include b-jets will use a fixed working point, for example, requiring that

786 a jet pass the 70% threshold. By instead treating these working point as bins, e.g. events with
787 jets that fall between the 85% and 77% WPs fall into one bin, while events with jets passing the
788 60% WP fall into another, and looking at the full psuedo-continuous DL1r spectrum of the jets,
789 additional information can be gained. The psuedo-continuous b-tag spectrum is used in this case
790 to separate out WZ + b, WZ + charm, and WZ + light.

791 **11.4 Missing transverse energy**

792 Missing transverse momentum (E_T^{miss}) is used as part of the event selection. The missing
793 transverse momentum vector is defined as the inverse of the sum of the transverse momenta of
794 all reconstructed physics objects as well as remaining unclustered energy, the latter of which is
795 estimated from low- p_T tracks associated with the primary vertex but not assigned to a hard object,
796 with object definitions taken from [24]. Light leptons considered in the E_T^{miss} reconstruction are
797 required to have $p_T > 10$ GeV, while jets are required to have $p_T > 20$ GeV.

798 **11.5 Overlap removal**

799 To avoid double counting objects and remove leptons originating from decays of hadrons, overlap
800 removal is performed in the following order: any electron candidate within $\Delta R = 0.1$ of another
801 electron candidate with higher p_T is removed; any electron candidate within $\Delta R = 0.1$ of a muon
802 candidate is removed; any jet within $\Delta R = 0.3$ of an electron candidate is removed; if a muon

803 candidate and a jet lie within $\Delta R = \min(0.4, 0.04 + 10[\text{GeV}]/p_T(\text{muon}))$ of each other, the jet
 804 is kept and the muon is removed.

805 This algorithm is applied to the preselected objects. The overlap removal procedure is
 806 summarized in Table 26.

Keep	Remove	Cone size (ΔR)
electron	electron (low p_T)	0.1
muon	electron	0.1
electron	jet	0.3
jet	muon	$\min(0.4, 0.04 + 10[\text{GeV}]/p_T(\text{muon}))$
electron	tau	0.2

Table 9: Summary of the overlap removal procedure between electrons, muons, and jets.

807 12 Event Selection and Signal Region Definitions

808 Event are required to pass a preselection described in Section 12.1 and summarized in Table 12.
 809 Those that pass this preselection are divided into various fit regions described in Section 12.2,
 810 based on the number of jets in the event, and the b-tag score of those jets.

811 12.1 Event Preselection

812 Events are required to include exactly three reconstructed light leptons passing the requirement
 813 described in 11.2, which have a total charge of ± 1 .

814 The leptons are ordered in the analysis code as 0, 1, and 2. Lepton 0 is the lepton whose
 815 charge is opposite the other two. Lepton 1 is the lepton closest to the opposite charge lepton, i.e.
 816 the smallest ΔR , leaving lepton 2 as the lepton further from the opposite charge lepton. Lepton
 817 0 is required to have $p_T > 10$ GeV, while the same sign leptons, 1 and 2, are required to have
 818 $p_T > 20$ GeV to reduce the contribution of non-prompt leptons.

819 The invariant mass of at least one pair of opposite sign, same flavor leptons is required
 820 to fall within 10 GeV of the mass of the Z boson, 91.2 GeV. Events where one of the opposite
 821 sign pairs have an invariant mass less than 12 GeV are rejected in order to suppress low mass
 822 resonances.

823 An additional requirement is placed on the missing transverse energy, $E_T^{\text{miss}} > 20$ GeV,
 824 and the transverse mass of the W candidate, $m(E_T^{\text{miss}} + l_{\text{other}}) > 30$ GeV, where E_T^{miss} is the
 825 missing transverse energy, and l_{other} is the lepton not included in the Z-candidate.

826 Events are required to have one or two reconstructed jets passing the selection described
 827 in Section 11.3. Events with more than two jets are rejected in order to reduce the contribution
 828 of backgrounds such as $t\bar{t}Z$ and $t\bar{t}W$, which tend to have higher jet multiplicity.

Event Selection

- Exactly three leptons with charge ± 1
 - Two same-charge leptons with $p_T > 20$ GeV
 - One opposite charge lepton with $p_T > 10$ GeV
 - $m(l^+l^-)$ within 10 GeV of 91.2 GeV
 - Transverse mass of W-candidate, $m_T(E_T^{\text{miss}} + \text{lep}_{\text{other}}) > 30$ GeV
 - Missing transverse energy, $E_T^{\text{miss}} > 20$ GeV
 - One or two jets with $p_T > 25$ GeV
-

Table 10: Summary of the selection applied to events for inclusion in the fit

829 The event yields in the preselection region for both data and Monte Carlo are summarized
 830 in Table 12.1, which shows good agreement between data and Monte Carlo, and demonstrates
 831 that this region consists primarily of WZ events. The WZ events are split into WZ + b, WZ +
 832 c, and WZ + l based on the truth flavor of the associated jet in the event. In this ordering b-jet
 833 supersede charm, which supersides light. That is, WZ + l events contain no charm and no b jets
 834 at truth level, WZ + c contain at least one truth charm and no b-jets, and WZ + b contains at least
 835 one truth b-jet.

Process	Events
WZ + b	167.6 ± 6.5
WZ + c	1080 ± 40
WZ + l	7220 ± 310
Other VV	850 ± 140
$t\bar{t}W$	16.8 ± 2.3
$t\bar{t}Z$	115 ± 17
rare Top	2.2 ± 0.1
Single top	0.10 ± 0.45
Three top	0.01 ± 0.01
Four top	0.02 ± 0.01
$t\bar{t}WW$	0.23 ± 0.05
Z + jets	600 ± 260
V + γ	37 ± 54
tZ	190 ± 70
tW	5.5 ± 1.2
WtZ	25.8 ± 1.1
VVV	26.2 ± 0.9
VH	94 ± 7
t \bar{t}	108.68 ± 8
t $\bar{t}H$	4.3 ± 0.5
Total	10600 ± 530
Data	10574

Table 11: Event yields in the preselection region at 139.0 fb^{-1}

836 Here Other VV represents diboson processes other than WZ, and consists predominantly

⁸³⁷ of $ZZ \rightarrow ll\bar{l}\bar{l}$ events where one of the leptons is not reconstructed.

⁸³⁸ 12.2 Fit Regions

⁸³⁹ Once preselection has been applied, the remaining events are categorized into one of twelve
⁸⁴⁰ orthogonal regions. The regions used in the fit are summarized in Table 14.

Table 12: A list of the regions used in the fit and the selection used for each.

Region	Selection
1j, <85%	$N_{\text{jets}} = 1, n\text{Jets_DL1r_85} = 0$
1j, 85%-77%	$N_{\text{jets}} = 1, n\text{Jets_DL1r_85} = 1, n\text{Jets_DL1r_77}=0$
1j, 77%-70%	$N_{\text{jets}} = 1, n\text{Jets_DL1r_77} = 1, n\text{Jets_DL1r_70}=0$
1j, 70%-60%	$N_{\text{jets}} = 1, n\text{Jets_DL1r_70} = 1, n\text{Jets_DL1r_60}=0$
1j, >60%	$N_{\text{jets}} = 1, n\text{Jets_DL1r_60} = 1, tZ \text{ BDT} > 0.725$
1j tZ CR	$N_{\text{jets}} = 1, n\text{Jets_DL1r_60} = 1, tZ \text{ BDT} < 0.725$
2j, <85%	$N_{\text{jets}} = 2, n\text{Jets_DL1r_85} = 0$
2j, 85%-77%	$N_{\text{jets}} = 2, n\text{Jets_DL1r_85} >= 1, n\text{Jets_DL1r_77}=0$
2j, 77%-70%	$N_{\text{jets}} = 2, n\text{Jets_DL1r_77} >= 1, n\text{Jets_DL1r_70}=0$
2j, 70%-60%	$N_{\text{jets}} = 2, n\text{Jets_DL1r_70} >= 1, n\text{Jets_DL1r_60}=0$
2j, >60%	$N_{\text{jets}} = 2, n\text{Jets_DL1r_60} >= 1, tZ \text{ BDT} > 0.725$
2j tZ CR	$N_{\text{jets}} = 2, n\text{Jets_DL1r_60} >= 1, tZ \text{ BDT} < 0.725$

⁸⁴¹ The working points discussed in Section 11.4 are used to separate events into fit regions
⁸⁴² based on the highest working point reached by a jet in each event. Because the background
⁸⁴³ composition differs significantly based on the number of b-jets, events are further subdivided
⁸⁴⁴ into 1-jet and 2-jet regions in order to minimize the impact of background uncertainties.

⁸⁴⁵ An unfolding procedure is performed to account for differences in the number of recon-
⁸⁴⁶ structed jets compared to the number of truth jets in each event. In order to account for migration

847 of WZ+1-jet and WZ+2-jet events between the 1-jet and 2-jet bins at reco level, the signal
 848 samples are separated based on the number of truth jets. Events with 0 jets or more than 3 jets at
 849 truth level, yet fall within one of the categories listed in Table 14, are categorized as WZ + other,
 850 and treated as a background. The composition of the number of truth jets in each reco jet bin is
 851 taken from MC, with uncertainties in these estimates described in detail in Section 21.

852 An additional tZ control region is created based on the BDT described in Section 13. The
 853 region with 1-jet passing the 60% working point is split in two - a signal enriched region of
 854 events with a BDT score greater than 0.03, and a tZ control region including events with less
 855 than 0.03. This cutoff is arrived at by performing an Asimov fit with a variety of cutoffs, and
 856 selecting the value that produces the highest significance for the measurement of WZ + b.

857 **12.3 Non-Prompt Lepton Estimation**

858 Two processes act as sources of non-prompt leptons appear in the analysis: $t\bar{t}$ and Z+jet
 859 production both produce two prompt leptons, and each contribute to the 31 region when an
 860 additional non-prompt lepton appears in the event. The contribution of these processes is
 861 estimated with Monte Carlo simulations, which are validated using enriched control regions.

862 The modelling in the Z+jets and $t\bar{t}$ CRs is further validated for each of the pseudo-
 863 continuous b-tag regions used in the analysis. The relevant lepton p_T spectrum in each b-tag
 864 region is shown in Appendix .2 for these CRs after the correction factors derived below have
 865 been applied.

866 **12.3.1 $t\bar{t}$ Validation**

867 $t\bar{t}$ events can produce two prompt leptons from the decay of each of the tops. These top decays
 868 produce two b-quarks, the decay of which can produce additional non-prompt leptons, which
 869 occasionally pass the event preselection. In order to validate that the Monte Carlo accurately
 870 simulates this process accurately, the MC prediction in a non-prompt $t\bar{t}$ enriched control region
 871 is compared to data.

872 The $t\bar{t}$ control region is similar to the preselection region - three leptons meeting the
 873 criteria described in Section 12 are required, and the requirements on E_T^{miss} remain the same.
 874 However, the selection requiring a lepton pair form a Z-candidate are reversed. Events where the
 875 invariant mass of any two opposite sign, same flavor leptons falls within 10 GeV of 91.2 GeV are
 876 rejected. This ensures the $t\bar{t}$ control region is orthogonal to the preselection region.

877 Further, because the jet multiplicity of $t\bar{t}$ events tends to be higher than WZ, the number
 878 of jets in each event is required to be greater than 1. As b-jets are almost invariably produced
 879 from top decays, at least one b-tagged jet passing the 70% DL1r WP in each event is required.

880 Data is compared to MC predictions in the region for a variety of kinematic variable, as well
 881 as various b-tag WPs. A constant normalization discrepancy between data and MC predictions
 882 of approximately 10% is found, which is accounted for by applying a constant correction factor
 883 of 0.9 to the $t\bar{t}$ MC prediction. As data and MC are found to agree within 20% for each of
 884 the b-tag WPs considered, a 20% systematic uncertainty on the $t\bar{t}$ prediction is included for the
 885 analysis.

886 12.3.2 Z+jets Validation

887 Similar to $t\bar{t}$, a non-prompt Z +jets control region is produced in order to validate the MC
 888 predictions. The lepton requirements remain the same as the preselection region. Because no
 889 neutrinos are present for this process, the E_T^{miss} cut is reversed, requiring $E_T^{\text{miss}} < 30 \text{ GeV}$. This
 890 also ensures this control region is orthogonal to the preselection region. Further, the number of
 891 jets in each event is required to be greater than or equal to one.

892 While there is general agreement between data and MC within statistical uncertainty, the
 893 shape of the p_T spectrum of the lepton from the W is found to differ. To account for this
 894 discrepancy, a variable correction factor is applied to Z +jets. χ^2 minimization of the W lepton
 895 p_T spectrum is performed to derive a correction factor of $1.53 - 6.6 * 10^{-6}(\text{lep}_\text{Pt}_W)$.

896 The uncertainty in the $Z + \text{jets}$ prediction is evaluated by comparing data to MC for each
 897 of the continuous b-tag WPs. For each of the regions considered, the data falls within 25% of
 898 the MC prediction once this correction factor has been applied. Therefore, a 25% systematic
 899 uncertainty is applied to $Z + \text{jets}$ in the analysis.

900 13 tZ Interference Studies and Separation Multivariate Analysis

901 An important process to consider in this analysis is tZ : the top almost always decays into a W
 902 boson and b-quark, and when both the W and Z decay leptonically, this gives three leptons and
 903 a heavy flavor jet in the final state. Because tZ can produce a final state identical to the signal,

904 it represents a predominant background in the most signal enriched regions. That is, the region
 905 with one jet passing the 60% DL1r WP. Therefore, a boosted decision tree (BDT) algorithm is
 906 trained using XGBoost [28] to separate WZ + heavy flavor from tZ. The result of this BDT is
 907 used to create a tZ enriched region in the fit, reducing its impact on the measurement of WZ +
 908 heavy flavor.

909 The following kinematic variables are used as inputs to train this BDT:

- 910 • The invariant mass of the reconstructed top candidate
- 911 • p_T of each of the leptons, jet
- 912 • The invariant mass of each combination of lepton pairs, $M(l\bar{l})$
- 913 • E_T^{miss}
- 914 • Distance between each combination of leptons, $\Delta R(l\bar{l})$
- 915 • Distance between each lepton and the jet, $\Delta R(lj)$

916 Here the top candidate is reconstructed based on the procedure described in section 6.1 of
 917 [27]. Broadly, the mass of the top quark candidate is reconstructed from the jet, the lepton not
 918 included in the Z-candidate, and a reconstructed neutrino. In the case that there is one jet in the
 919 event, there is only possible b-jet candidate. For events with two jets, the jet with the highest
 920 DL1r score is used.

921 The training samples included only events meeting the requirements of the 1-jet, >60%
922 region, i.e. passing all the selection described in section 12 and having exactly one jet which
923 passes the tightest (60%) DL1r working point. A sample of 20,000 background (tZ) and signal
924 (WZ+b) Monte Carlo events are used to train the BDT. And additional 5,000 events are reserved
925 for testing the model, in order to prevent over-fitting. A total of 750 decision trees with a
926 maximum depth of 6 branches are used to build the model. These parameters are chosen
927 empirically, by training several models with different parameters and selecting the one that gave
928 the best separation for the test sample.

929 The results of the BDT training are shown in figure 13.1. The output scores for both signal
930 and background events is shown on the left. The right shows the receiving operating characteristic
931 (ROC) curve that results from the MVA. The ROC curve represents the background rejection
932 as a function of signal efficiency, where each point on the curve represents a different response
933 score. The ROC curve of the BDT is compared to the performance of using an optimal set of flat
934 selections on the same set of input variables.

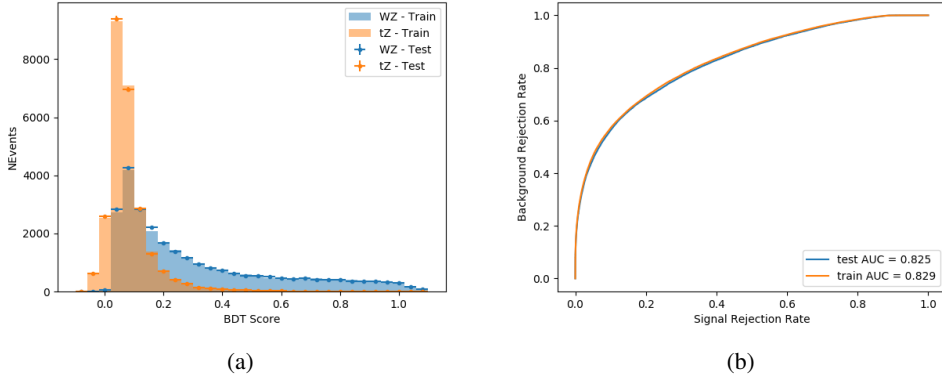


Figure 13.1: Distribution of the BDT response for signal and background events on the left, the ROC curve for the BDT on the right.

935 The relative important of each input feature in the model, measured by how often they
 936 appeared in the decision trees, is shown in figure 13.2.

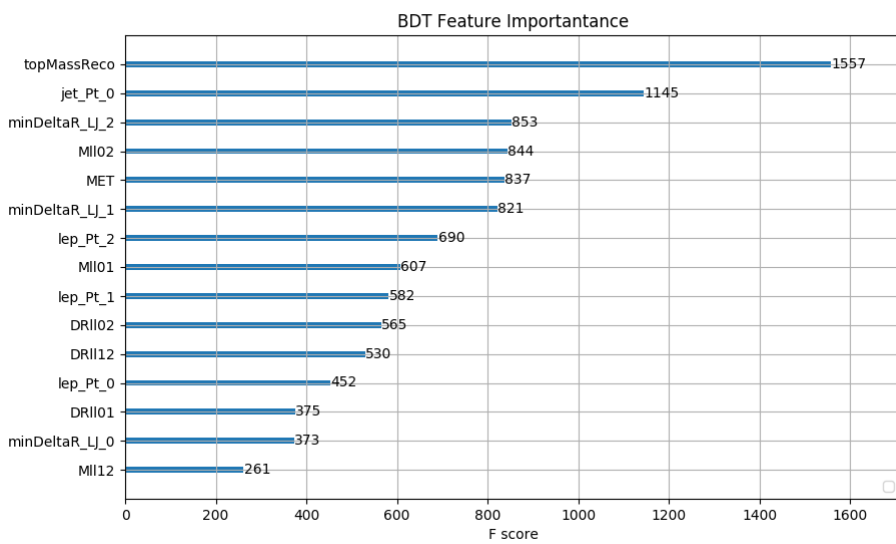


Figure 13.2: Relative importance of each input feature in the model.

937 These results suggest that some amount of separation can be achieved between these two
938 processes, with a high BDT score selecting a set of events that is pure in $WZ + b$. A BDT score
939 of 0.725 is selected as a cutoff, where events with scores higher than this form a signal enriched
940 region, and events with scores lower than this form a $t\bar{Z}$ control region. This cutoff is selected by
941 varying the value of this cutoff in stat-only Asimov fits, and selecting the value that minimizes
942 the statistical uncertainty on $WZ + b$.

943 **14 Systematic Uncertainties**

944 The systematic uncertainties that are considered are summarized in Table 46. These are imple-
945 mented in the fit either as a normalization factors or as a shape variation or both in the signal
946 and background estimations. The numerical impact of each of these uncertainties is outlined in
947 Section 22.

Table 13: Sources of systematic uncertainty considered in the analysis.

Systematic uncertainty	Components
Luminosity	1
Pileup reweighting	1
Physics Objects	
Electron	6
Muon	15
Jet energy scale	28
Jet energy resolution	8
Jet vertex fraction	1
Jet flavor tagging	131
E_T^{miss}	3
Total (Experimental)	194
Signal Modeling	
Shape modelling	3
Renormalization and factorization scales	5
nJet Migration	5
Background Modeling	
Cross section	15
Renormalization and factorization scales	12
Total (Signal and background modeling)	35
Total (Overall)	230

948 The uncertainty in the combined integrated luminosity is derived from a calibration of the

949 luminosity scale performed for 13 TeV proton-proton collisions [29], [30].

950 The experimental uncertainties are related to the reconstruction and identification of light

951 leptons and b-tagging of jets, and to the reconstruction of E_T^{miss} . The sources which contribute to

952 the uncertainty in the jet energy scale (JES) [31] are decomposed into uncorrelated components

953 and treated as independent sources of uncertainty in the analysis. These are treated as 30

954 nuisance parameters included in the fit. A similar approach is used for the jet energy resolution

955 (JER) uncertainty, which is decomposed into 8 JER uncertainty components included as NPs in
956 the fit.

957 The uncertainties in the b-tagging efficiencies measured in dedicated calibration analyses
958 [32] are also decomposed into uncorrelated components. The large number of components for
959 b-tagging is due to the calibration of the distribution of the MVA discriminant.

960 Theoretical uncertainties applied to MC predictions, including cross section, PDF, and scale
961 uncertainties are taken from theory calculations, with the exception of non-prompt and dibo-
962 son backgrounds. The cross-section uncertainty on tZ is taken from [33]. Derivation of the
963 non-prompt background uncertainties, Z+jets and tt>, are explained in Section 12.3. These
964 normalization uncertainties are chosen so as to account for the complete uncertainty in the
965 non-prompt contribution, and therefore no additional modelling uncertainties are considered for
966 Z+jets and tt>.

967 The other VV + heavy flavor processes (namely VV+b and VV+charm, which primarily
968 consist of ZZ events) are also poorly understood, because these processes involve the same
969 physics as WZ + heavy flavor, and have also not been measured. Therefore, a conservative 50%
970 uncertainty is applied to those samples. While this uncertainty is large, it is found to have little
971 impact on the significance of the final result.

972 The theory uncertainties applied to the predominate background estimates are summarized
973 in Table 50.

Process	X-section [%]
tZ	X-sec: ± 15.2 QCD Scale: $^{+5.2}_{-1.3}$ PDF($+\alpha_S$): ± 1.2
t̄t H (aMC@NLO+Pythia8)	QCD Scale: $^{+5.8}_{-9.2}$ PDF($+\alpha_S$): ± 3.6
t̄t Z (aMC@NLO+Pythia8)	QCD Scale: $^{+9.6}_{-11.3}$ PDF($+\alpha_S$): ± 4
t̄t W (aMC@NLO+Pythia8)	QCD Scale: $^{+12.9}_{-11.5}$ PDF($+\alpha_S$): ± 3.4
VV + b/charm (Sherpa 2.2.1)	± 50
VV + light (Sherpa 2.2.1)	± 6
t̄t	± 20
Z + jets	± 25
Others	± 50

Table 14: Summary of theoretical uncertainties for MC predictions in the analysis.

974 Additional signal uncertainties are estimated by comparing estimates from the nominal Sherpa
 975 WZ samples with alternate WZ samples generated with Powheg+PYTHIA8. Separate systemat-
 976 ics are included in the fit for WZ + b, WZ + charm and WZ + light, where the distribution among
 977 each of the fit regions is varied based on the prediction of the Powheg sample.

978 A similar approach is taken to account for uncertainties in migrations between the number of
 979 reco and truth jets. The fraction of events with 1 truth jet which fall into the 1 jet bin versus the
 980 2 jet bin at reco level is compared for Sherpa and Powheg. The same is done for events with 2
 981 truth jets. A systematic is included where events are shifted between the 1-jet and 2-jet regions
 982 based on the differences between these two shapes. This is done independently for each of the
 983 WZ + b, WZ + charm, and WZ + light templates.

984 Additional systematics are included to account for the uncertainty in the contamination of
 985 0 jet and 3 or more jet events (as defined at truth level) in the 1 and 2 reco jet bins. Because these
 986 events fall outside the scope of this measurement, these events are included as a background.
 987 As such, a normalization, rather than a shape, uncertainty is applied for this background. The
 988 number of WZ events with 0-jets and $>=3$ -jets in the reconstructed 1-jet and 2-jet regions are
 989 compared for Sherpa and Powheg, and these differences are taken as separate normalization
 990 systematics on the yield of WZ+0-jet and WZ+ $>=3$ -jet events.

991 15 Results

992 A separate maximum-likelihood fit is performed over the 1-jet and 2-jet fit regions in order to
 993 extract the best-fit value of the WZ + b-jet and WZ + charm jet contributions. The WZ + b,
 994 WZ + charm and WZ + light contributions are allowed to float, with the remaining background
 995 contributions are held fixed. **The current fit strategy treats the WZ + b-jet contribution as**
 996 **the parameter of interest, with the normalization of the WZ + charm and the WZ + light**
 997 **contributions taken as systematic uncertainties. This could however be adjusted, depending**
 998 **on whether it is decided the goal of the analysis should be to measure WZ+b specifically or**
 999 **WZ + heavy flavor overall.** The result of the fit is used to extract the cross-section of WZ +
 1000 heavy-flavor production.

1001 A maximum likelihood fit to data is performed simultaneously in the regions described
 1002 in Section 12. The parameters μ_{WZ+b} , $\mu_{WZ+charm}$, $\mu_{WZ+light}$, where $\mu = \sigma_{\text{observed}}/\sigma_{\text{SM}}$, are

1003 extracted from the fit.

1004 The Asimov fit for 1-jet events gives an expected μ value of $1.00^{+0.37}_{-0.35}(\text{stat})^{+0.24}_{-0.22}(\text{sys})$ for
 1005 WZ + b. The fitted cross-section modifiers for WZ + charm and WZ + light are $1.00 \pm 0.17 \pm 0.15$
 1006 and $1.00 \pm 0.04 \pm 0.07$, respectively.

1007 The expected cross-section of WZ+b with 1 associated jet obtained from the fit is
 1008 $1.74^{+0.65}_{-0.61}(\text{stat})^{+0.42}_{-0.37}(\text{sys})$ fb with an expected significance of 2.2σ . The expected cross-sectin
 1009 of WZ + charm is measured to be $14.6 \pm 2.5(\text{stat}) \pm 2.1(\text{sys})$ fb, with a correlation of -0.23.

1010 For 2-jet events, the fit gives an expected μ value of $1.00^{+0.34}_{-0.33}(\text{stat})^{+0.29}_{-0.28}(\text{sys})$ for WZ +
 1011 b. The fitted cross-section modifiers for WZ + charm and WZ + light are $1.00 \pm 0.17 \pm 0.15$ and
 1012 $1.00 \pm 0.04 \pm 0.08$, respectively.

1013 The expected WZ + b cross-section in the 2-jet region is $2.46^{+0.83}_{-0.81}(\text{stat})^{+0.073}_{-0.68}(\text{sys})$ fb
 1014 with an expected significance of 2.6σ . The 2-jet expected cross-section of WZ + charm is
 1015 $12.7 \pm 2.2(\text{stat}) \pm 2.0(\text{sys})$ fb, and the correlation between WZ + charm and WZ + b is -0.26.

1016 **15.1 1-jet Fit Results**

1017 **The results of the fit are currently blinded.**

1018 The pre-fit yields in each of the regions used in the fit are shown in Table 15.1, and
 1019 summarized in Figure 15.1.

Sample	1j, <85% WP	1j, 77%-85% WP	1j, 70%-77% WP	1j, 60%-70% WP	1j, >60% WP	tZ CR
WZ + b - 1j	8.1 ± 1.6	4.7 ± 0.5	4.6 ± 0.4	5.1 ± 0.4	18.2 ± 2.4	4.8 ± 0.6
WZ + c - 1j	260 ± 22	81 ± 6	43.1 ± 3.6	25.8 ± 2.6	9.4 ± 1.8	2.9 ± 0.6
WZ + l - 1j	3090 ± 250	91 ± 13	17 ± 3	4.9 ± 1.6	1.3 ± 0.4	0.2 ± 0.1
WZ + b - 2j	1.10 ± 0.37	0.44 ± 0.11	0.39 ± 0.06	0.62 ± 0.14	2.1 ± 0.5	0.59 ± 0.14
WZ + c - 2j	21 ± 5	5.6 ± 1.2	3.0 ± 0.7	2.0 ± 0.5	0.70 ± 0.20	0.30 ± 0.08
WZ + l - 2j	250 ± 60	5.7 ± 1.6	0.73 ± 0.53	0.31 ± 0.15	0.07 ± 0.06	0.01 ± 0.01
WZ - Other	13 ± 5	1.4 ± 0.4	0.42 ± 0.08	0.2 ± 0.01	0.30 ± 0.05	0.67 ± 0.15
Other VV	6.2 ± 0.6	0.2 ± 0.4	0.2 ± 0.04	0.07 ± 0.1	0.1 ± 0.1	0.1 ± 0.2
ZZ	336 ± 26	17.8 ± 2.1	4.3 ± 0.6	1.7 ± 0.5	0.36 ± 0.08	0.10 ± 0.03
t̄W	1.1 ± 0.2	0.2 ± 0.1	0.3 ± 0.1	0.4 ± 0.1	1.5 ± 0.3	0.7 ± 0.2
t̄Z	6.8 ± 1.2	1.4 ± 0.3	1.0 ± 0.2	1.2 ± 0.2	4.4 ± 0.8	3.2 ± 0.6
Z + jets	169 ± 38	8.9 ± 1.9	3.7 ± 0.8	3.3 ± 0.7	3.2 ± 0.7	0.8 ± 0.17
V + γ	45 ± 28	1.9 ± 2.4	0.1 ± 0.1	0.02 ± 0.01	1.0 ± 0.9	0.02 ± 0.03
tZ	24.3 ± 4.3	5.5 ± 1.1	4.1 ± 0.8	5.9 ± 1.1	10.7 ± 2.0	23 ± 4
tW	1.4 ± 0.8	0.2 ± 0.5	0.0 ± 0.2	0.7 ± 0.6	0.26 ± 0.42	0.39 ± 0.41
WtZ	2.3 ± 1.2	0.6 ± 0.3	0.3 ± 0.21	0.27 ± 0.2	1.1 ± 0.7	0.6 ± 0.5
VVV	12.4 ± 0.5	0.93 ± 0.06	0.35 ± 0.03	0.13 ± 0.02	0.14 ± 0.03	0.02 ± 0.01
VH	40 ± 6	2.6 ± 1.4	0.9 ± 0.8	0.7 ± 0.8	0.5 ± 0.6	0.0 ± 0.0
t̄t	12.1 ± 1.6	2.9 ± 0.6	2.5 ± 0.5	2.8 ± 0.5	11.2 ± 1.4	10.9 ± 1.5
t̄tH	0.24 ± 0.03	0.05 ± 0.01	0.04 ± 0.01	0.06 ± 0.01	0.20 ± 0.03	0.13 ± 0.02
Total	5010 ± 260	227 ± 24	88 ± 12	57 ± 8	76 ± 16	53 ± 8

Table 15: Pre-fit yields in each of the 1-jet fit regions.

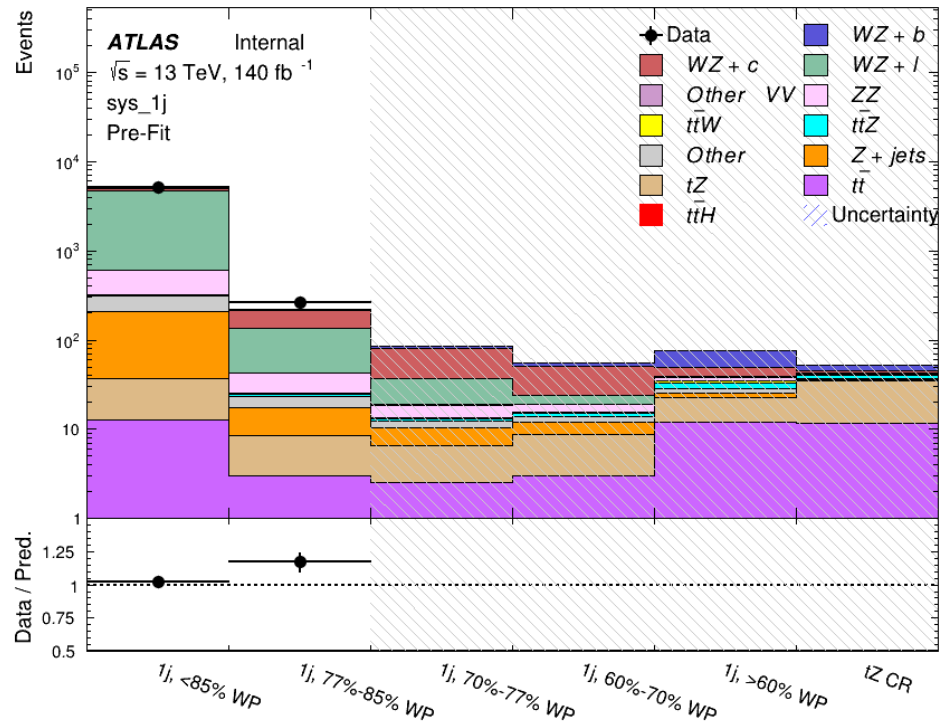


Figure 15.1: Pre-fit summary of the 1-jet fit regions.

1021

The post-fit yields in each region are summarized in Figure 15.1.

1022

	1j, <85% WP	1j, 77%-85% WP	1j, 70%-77% WP	1j, 60%-70% WP	1j, >60% WP	tZ CR
WZ + b	8.1 ± 4.9	4.7 ± 2.0	4.6 ± 2.0	5.1 ± 2.1	18 ± 10	5.0 ± 2.5
WZ + c	260 ± 60	80 ± 14	43 ± 7	26 ± 5	9.4 ± 2.3	2.9 ± 0.7
WZ + l	3090 ± 130	90 ± 11	17.3 ± 2.8	4.9 ± 1.6	1.3 ± 0.4	0.23 ± 0.1
WZ + b - 2j	1.10 ± 0.37	0.44 ± 0.11	0.39 ± 0.06	0.62 ± 0.14	2.1 ± 0.5	0.59 ± 0.1
WZ + c - 2j	21 ± 5	5.6 ± 1.2	3.0 ± 0.7	2.0 ± 0.5	0.70 ± 0.20	0.30 ± 0.0
WZ + l - 2j	250 ± 60	5.7 ± 1.6	0.73 ± 0.53	0.31 ± 0.15	0.07 ± 0.06	0.01 ± 0.0
WZ - Other	13 ± 5	1.4 ± 0.4	0.42 ± 0.08	0.2 ± 0.01	0.30 ± 0.05	0.67 ± 0.1
Other VV	6.2 ± 0.6	0.92 ± 0.07	0.02 ± 0.01	0.01 ± 0.01	0.01 ± 0.01	0.01 ± 0.0
ZZ	346 ± 57	19 ± 5	4.3 ± 0.8	2.7 ± 0.5	2.4 ± 0.1	2.1 ± 0.6
t̄tW	1.09 ± 0.21	0.2 ± 0.1	0.1 ± 0.1	0.4 ± 0.1	1.5 ± 0.3	0.1 ± 0.2
t̄tZ	6.8 ± 1.2	1.4 ± 0.3	1.0 ± 0.2	1.2 ± 0.2	4.4 ± 0.7	3.2 ± 0.5
rare Top	0.14 ± 0.04	0.04 ± 0.02	0.04 ± 0.0	0.1 ± 0.03	0.14 ± 0.04	0.15 ± 0.0
t̄tWW	0.04 ± 0.03	0.01 ± 0.02	0.01 ± 0.01	0.01 ± 0.01	0.01 ± 0.02	0.01 ± 0.0
Z + jets	169 ± 37	8.9 ± 1.9	3.7 ± 0.8	3.3 ± 0.7	3.2 ± 0.7	0.8 ± 0.2
W + jets	0.01 ± 0.01	0.01 ± 0.0				
V + γ	46 ± 28	1.9 ± 2.4	0.1 ± 0.1	0.0 ± 0.2	1.0 ± 0.9	0.0 ± 0.0
tZ	24 ± 4	5.5 ± 1.0	4.1 ± 0.8	5.9 ± 1.1	10.7 ± 1.8	23.3 ± 3.7
tW	1.37 ± 0.82	0.18 ± 0.26	0.01 ± 0.12	0.67 ± 0.64	0.26 ± 0.42	0.39 ± 0.4
WtZ	2.3 ± 1.2	0.6 ± 0.3	0.3 ± 0.2	0.3 ± 0.2	1.1 ± 0.6	0.6 ± 0.3
VVV	12.4 ± 0.4	0.9 ± 0.1	0.4 ± 0.1	0.13 ± 0.02	0.14 ± 0.03	0.02 ± 0.0
VH	40 ± 6	2.6 ± 1.4	0.9 ± 0.8	0.7 ± 0.8	0.4 ± 0.6	0.01 ± 0.0
t̄t	12.1 ± 1.6	2.9 ± 0.6	2.5 ± 0.5	2.8 ± 0.5	11.2 ± 1.5	10.9 ± 1.4
t̄tH	0.24 ± 0.03	0.05 ± 0.01	0.04 ± 0.01	0.06 ± 0.01	0.20 ± 0.03	0.13 ± 0.0
Total	5100 ± 110	227 ± 12	87 ± 6	56.7 ± 4.4	76 ± 9	52.5 ± 4.2

Table 16: Post-fit yields in each of the 1-jet fit regions.

1023

A post-fit summary plot of the 1-jet fitted regions is shown in Figure 15.2:

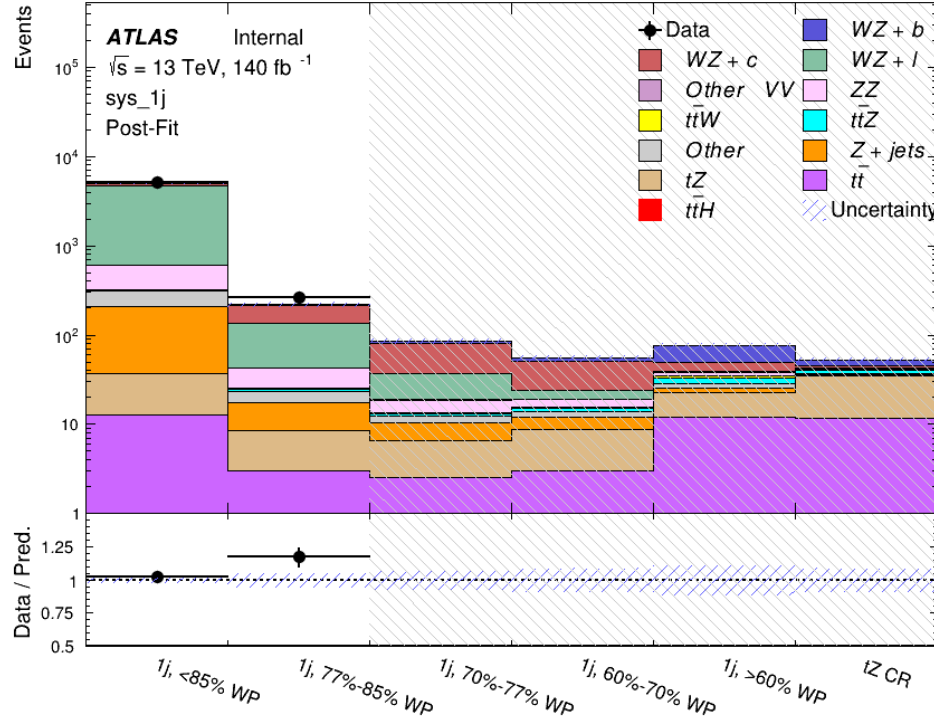


Figure 15.2: Post-fit summary of the 1-jet fit regions.

1024 As described in Section 21, there are 226 systematic uncertainties that are considered
 1025 as NPs in the fit. These NPs are constrained by Gaussian or log-normal probability density
 1026 functions. The latter are used for normalisation factors to ensure that they are always positive.
 1027 The expected number of signal and background events are functions of the likelihood. The prior
 1028 for each NP is added as a penalty term, decreasing the likelihood as it is shifted away from its
 1029 nominal value.

1030 The impact of each NP is calculated by performing the fit with the parameter of interest held
 1031 fixed, varied from its fitted value by its uncertainty, and calculating $\Delta\mu$ relative to the baseline

¹⁰³² fit. The impact of the most significant sources of systematic uncertainties is summarized in Table

¹⁰³³ [19.](#)

Uncertainty Source	$\Delta\mu$	
WZ + light cross-section	0.13	-0.12
WZ + charm cross-section	-0.10	0.12
Jet Energy Scale	0.08	0.13
tZ cross-section	-0.10	0.10
Jet Energy Resolution	-0.10	0.10
Luminosity	-0.08	0.09
Other Diboson + b cross-section	-0.07	0.07
Flavor tagging	0.05	0.05
t <bar>t</bar>	-0.05	0.05
WZ cross-section - QCD scale	-0.04	0.03
Total Systematic Uncertainty	0.28	0.32

Table 17: Summary of the most significant sources of systematic uncertainty on the measurement of WZ + b with exactly one associated jet.

¹⁰³⁴ The ranking and impact of those nuisance parameters with the largest contribution to the

¹⁰³⁵ overall uncertainty is shown in Figure [15.3](#).

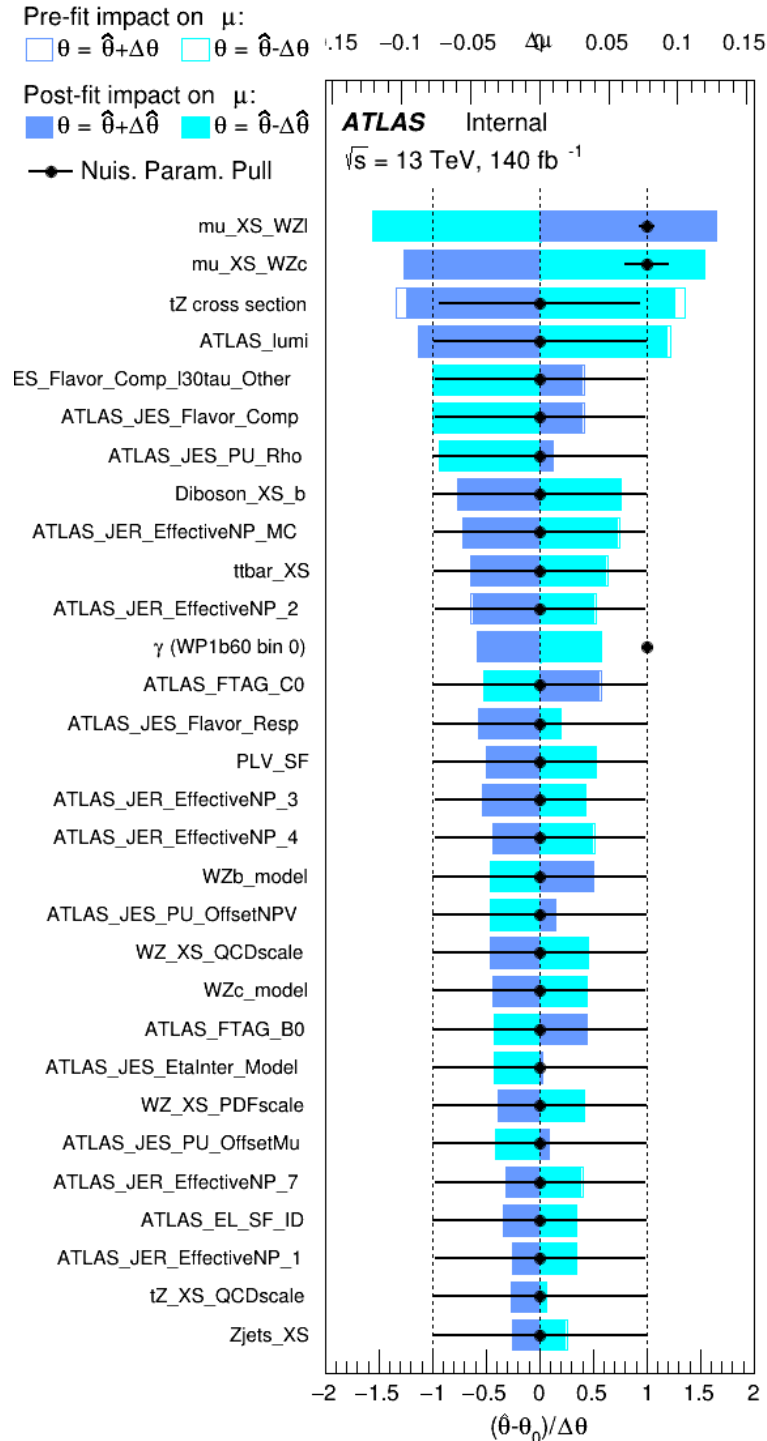


Figure 15.3: Impact of systematic uncertainties on the signal-strength of $WZ + b$ for events with exactly one jet

1036 The large impact of the Jet Energy Scale and Jet Flavor Tagging is unsurprising, as the
 1037 shape of the fit regions depends heavily on the modeling of the jets. The other major sources
 1038 of uncertainty come from background modelling and cross-section uncertainty. The pie charts
 1039 in Figure 15.4 show that for the modelling uncertainties that contribute most correspond to the
 1040 most significant backgrounds.

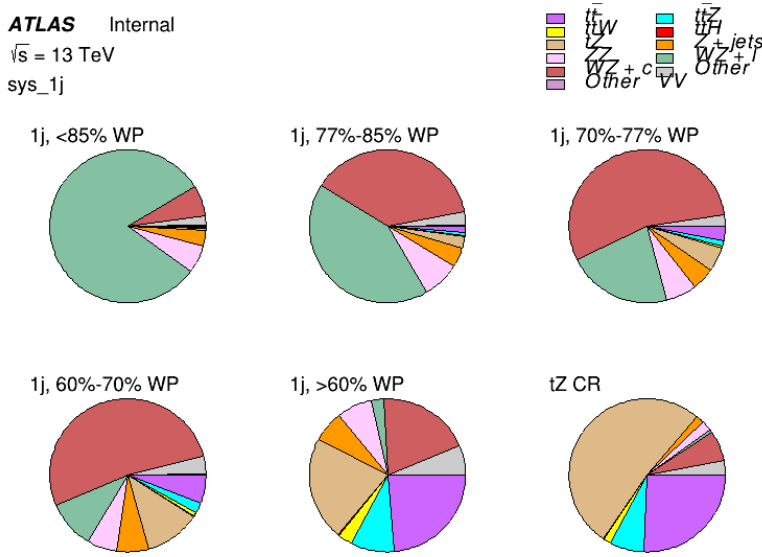


Figure 15.4: Post-fit background composition of the fit regions.

1041 The correlations between these nuisance parameters are summarized in Figure 15.5.

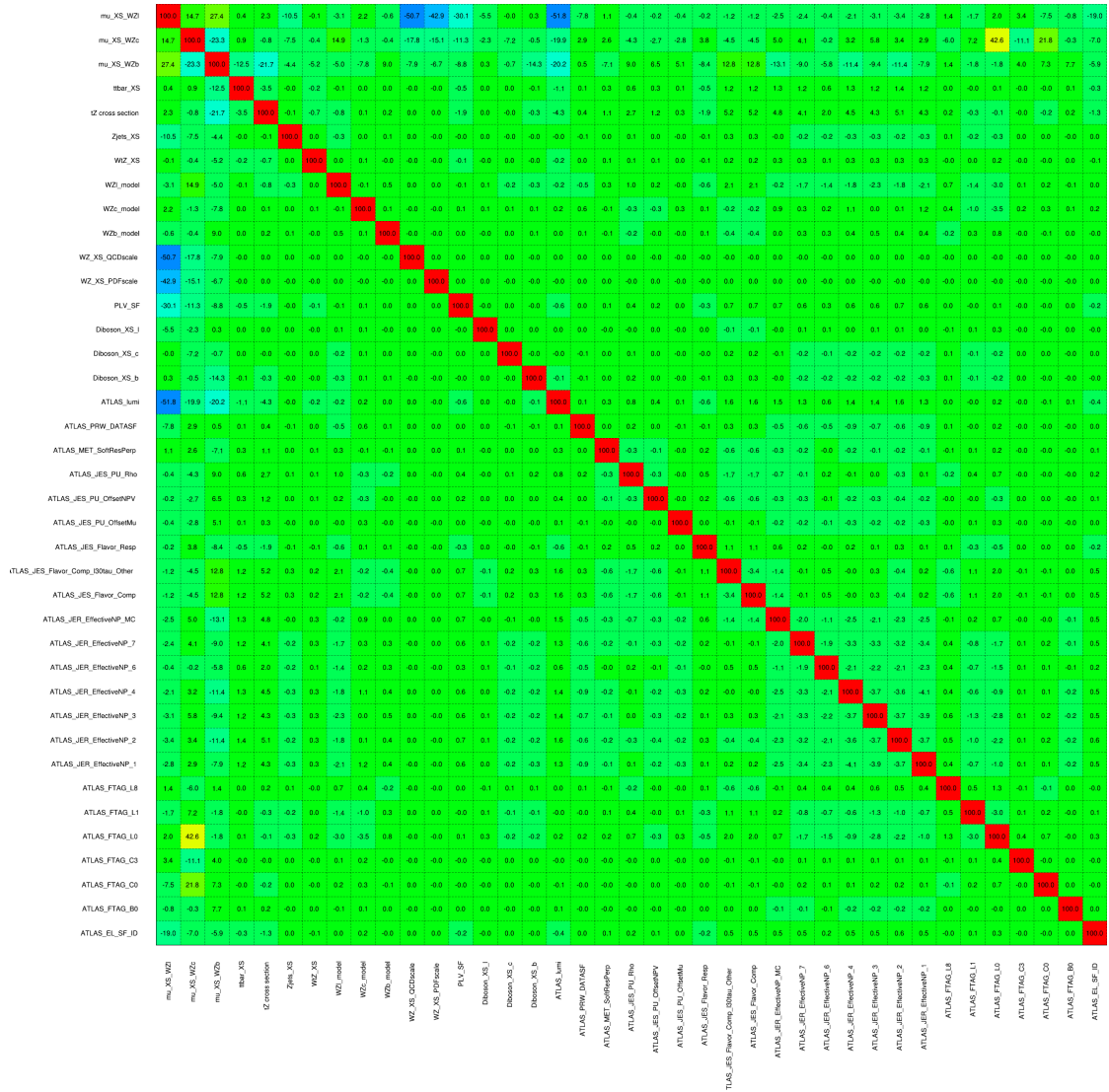


Figure 15.5: Correlations between nuisance parameters

1042 The negative correlations between $\mu_{WZ+\text{charm}}$ and μ_{WZ+b} and $\mu_{WZ+\text{light}}$ are expected:
 1043 WZ + charm is present in both the WZ + b and WZ + light enriched regions, therefore increasing
 1044 the fraction of charm requires increasing the fraction of WZ + b and WZ + light. This reasoning
 1045 also explains the positive correlation between μ_{WZ+b} and $\mu_{WZ+\text{light}}$.

1046 Two of the major backgrounds in the region with the highest purity of WZ + b are tZ and
1047 Other VV + b, explaining the negative correlations between μ_{WZ+b} and the tZ cross section, and
1048 the VV + b cross section.

1049 The high correlation between the luminosity and $\mu_{WZ+light}$ arises from the fact that the
1050 uncertainty on $\mu_{WZ+light}$ is very low (around 4%). Small changes in luminosity cause a change
1051 in the yield of WZ + light that is large compared to its uncertainty, producing a large correlation
1052 between these two parameters.

1053 **15.2 2-jet Fit Results**

1054 **The results of the fit are currently blinded.**

1055 Pre-fit yields in each of the 2-jet fit regions are shown in Figure 15.2.

	2j, <85% WP	2j, 77%-85% WP	2j, 70%-77% WP	2j, 60%-70% WP	2j, >60% WP	tZ CR 2j
WZ + b - 2j	3.1 ± 1.6	6.7 ± 0.5	5.6 ± 0.4	8.0 ± 0.6	31 ± 2	14 ± 1
WZ + c - 2j	180 ± 20	54 ± 6	41 ± 3	24 ± 3	11 ± 2	4.8 ± 0.6
WZ + l - 2j	1250 ± 150	90 ± 14	18 ± 3	5.8 ± 1.4	1.4 ± 0.4	0.25 ± 0.1
WZ + b - 1j	3.4 ± 0.6	1.52 ± 0.35	1.58 ± 0.23	1.95 ± 0.39	6.7 ± 1.1	1.9 ± 0.6
WZ + c - 1j	56 ± 14	17.6 ± 4.0	8.6 ± 2.2	6.3 ± 1.8	3.0 ± 0.9	0.7 ± 0.2
WZ + l - 1j	427 ± 120	24 ± 7	4.7 ± 2.3	1.6 ± 0.7	0.3 ± 0.2	0.01 ± 0.0
WZ - Other	129 ± 29	6.1 ± 4.6	1.2 ± 0.3	0.3 ± 0.2	2.9 ± 0.5	3.6 ± 0.6
Other VV	7.63 ± 0.63	0.6 ± 0.5	0.16 ± 0.03	0.01 ± 0.01	0.1 ± 0.1	0.1 ± 0.1
ZZ	135 ± 20	14.1 ± 3.2	4.7 ± 0.8	4.0 ± 0.6	4.1 ± 0.7	3.1 ± 0.5
t̄tW	0.8 ± 0.2	0.4 ± 0.1	0.5 ± 0.1	0.7 ± 0.2	4.3 ± 0.6	3.9 ± 0.6
t̄tZ	14.7 ± 2.2	5.6 ± 0.8	4.5 ± 0.7	6.5 ± 1.1	25.4 ± 4.0	21.9 ± 3.4
rare Top	0.14 ± 0.04	0.07 ± 0.03	0.03 ± 0.02	0.09 ± 0.03	0.37 ± 0.07	0.6 ± 0.1
t̄tWW	0.04 ± 0.03	0.02 ± 0.02	0.01 ± 0.01	0.01 ± 0.00	0.03 ± 0.03	0.01 ± 0.0
Z + jets	110.0 ± 22.9	9.6 ± 2.0	2.1 ± 0.50	1.6 ± 0.4	5.1 ± 1.1	1.5 ± 0.3
W + jets	0.0 ± 0.0	0.0 ± 0.0	0.0 ± 0.0	0.0 ± 0.0	0.0 ± 0.0	0.0 ± 0.0
V + γ	25 ± 18	0.5 ± 0.2	0.1 ± 0.1	0.1 ± 0.1	0.0 ± 0.02	0.05 ± 0.0
tZ	15.9 ± 2.9	6.9 ± 1.3	5.1 ± 1.0	8.0 ± 1.5	18.7 ± 3.2	36.4 ± 6.1
tW	0.9 ± 0.7	0.2 ± 0.3	0.0 ± 0.1	0.0 ± 0.0	0.8 ± 0.6	0.2 ± 0.2
WtZ	4.9 ± 2.5	1.5 ± 0.8	1.1 ± 0.6	1.3 ± 0.7	4.6 ± 2.4	3.3 ± 1.7
VVV	7.4 ± 0.3	1.0 ± 0.1	0.4 ± 0.1	0.2 ± 0.1	0.13 ± 0.03	0.04 ± 0.0
VH	19.5 ± 4.2	2.8 ± 1.6	0.7 ± 0.7	0.1 ± 0.2	0.0 ± 0.0	0.0 ± 0.0
t̄t	0.7 ± 0.4	0.1 ± 0.1	0.05 ± 0.06	0.15 ± 0.13	0.8 ± 0.5	2.3 ± 1.2
t̄t	6.8 ± 1.0	2.4 ± 0.5	1.8 ± 0.4	3.3 ± 0.6	8.4 ± 1.2	13.6 ± 1.1
t̄tH	0.4 ± 0.1	0.2 ± 0.1	0.16 ± 0.02	0.23 ± 0.03	0.94 ± 0.11	1.03 ± 0.1
Total	2580 ± 160	229 ± 24	89 ± 13	69 ± 11	120 ± 15	108 ± 11

Table 18: Pre-fit yields in each of the 2-jet fit regions.

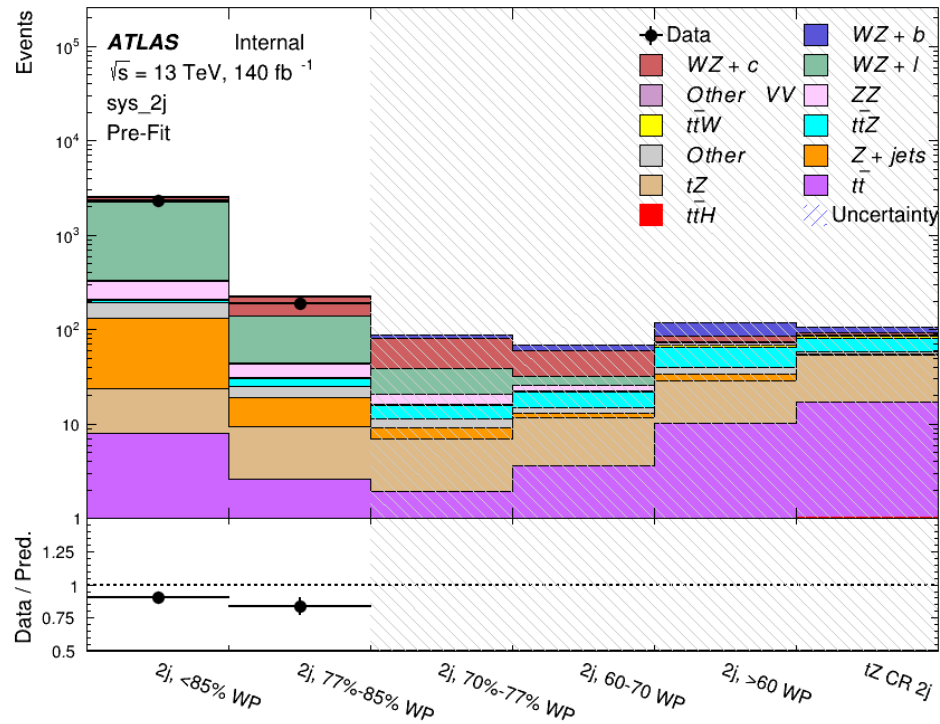


Figure 15.6: Pre-fit summary of the 2-jet fit regions.

1056

The post-fit yields in each region are summarized in Figure 15.2.

	2j, <85% WP	2j, 77%-85% WP	2j, 70%-77% WP	2j, 60%-70% WP	2j, >60% WP	tZ CR 2j
WZ + b	13 ± 6	6.7 ± 2.9	5.8 ± 2.5	8.0 ± 3.5	31 ± 13	14 ± 5
WZ + c	260 ± 60	77 ± 15	41 ± 8	26 ± 5	10.9 ± 2.4	4.8 ± 1.1
WZ + l	1860 ± 90	90 ± 12	17.6 ± 2.8	5.8 ± 1.3	1.4 ± 0.4	0.3 ± 0.2
WZ + b - 1j	3.4 ± 0.6	1.52 ± 0.35	1.58 ± 0.23	1.95 ± 0.39	6.7 ± 1.1	1.9 ± 0.6
WZ + c - 1j	56 ± 14	17.6 ± 4.0	8.6 ± 2.2	6.3 ± 1.8	3.0 ± 0.9	0.7 ± 0.2
WZ + l - 1j	427 ± 120	24 ± 7	4.7 ± 2.3	1.6 ± 0.7	0.3 ± 0.2	0.01 ± 0.0
WZ - Other	129 ± 29	6.1 ± 4.6	1.2 ± 0.3	0.3 ± 0.2	2.9 ± 0.5	3.6 ± 0.6
Other VV	7.6 ± 0.6	0.3 ± 0.3	0.3 ± 0.1	0.1 ± 0.06	0.03 ± 0.02	0.1 ± 0.1
ZZ	145 ± 30	11.3 ± 4.4	2.7 ± 1.6	1.0 ± 0.3	4.0 ± 0.1	2.4 ± 0.1
t̄tW	0.8 ± 0.2	0.4 ± 0.1	0.54 ± 0.12	0.74 ± 0.15	4.3 ± 0.6	3.9 ± 0.6
t̄tZ	14.7 ± 2.2	5.6 ± 0.8	4.5 ± 0.7	6.5 ± 1.0	25.4 ± 3.9	21.9 ± 3.0
rare Top	0.14 ± 0.04	0.07 ± 0.03	0.03 ± 0.02	0.09 ± 0.03	0.4 ± 0.1	0.6 ± 0.1
t̄tWW	0.04 ± 0.03	0.02 ± 0.02	0.01 ± 0.01	0.01 ± 0.01	0.03 ± 0.03	0.01 ± 0.0
Z + jets	110 ± 23	9.6 ± 2.0	2.1 ± 0.5	1.6 ± 0.4	5.1 ± 1.1	1.5 ± 0.3
W + jets	0.0 ± 0.0	0.0 ± 0.0				
V + γ	25 ± 19	0.5 ± 0.2	0.1 ± 0.1	0.13 ± 0.14	0.0 ± 0.02	0.05 ± 0.0
tZ	15.9 ± 2.7	6.9 ± 1.2	5.1 ± 0.9	8.0 ± 1.4	18.7 ± 3.0	36 ± 6
tW	0.1 ± 0.7	0.2 ± 0.3	0.0 ± 0.1	0.0 ± 0.0	0.8 ± 0.6	0.2 ± 0.2
WtZ	4.9 ± 2.5	1.5 ± 0.8	1.1 ± 0.6	1.3 ± 0.7	4.6 ± 2.3	3.3 ± 1.7
VVV	7.4 ± 0.3	1.0 ± 0.1	0.36 ± 0.03	0.19 ± 0.03	0.13 ± 0.03	0.04 ± 0.0
VH	19 ± 4	2.8 ± 1.6	0.7 ± 0.7	0.1 ± 0.2	0.0 ± 0.0	0.0 ± 0.0
t̄t	6.8 ± 1.0	2.4 ± 0.5	1.8 ± 0.4	3.3 ± 0.6	8.4 ± 1.2	13.6 ± 1.7
t̄tH	0.40 ± 0.05	0.19 ± 0.03	0.16 ± 0.02	0.23 ± 0.03	0.94 ± 0.11	1.03 ± 0.1
Total	2580 ± 60	229 ± 11	89 ± 6	69.1 ± 4.1	120 ± 10	108 ± 6

Table 19: Post-fit yields in each of the 2-jet fit regions.

1057

A post-fit summary of the fitted regions is shown in Figure 15.7:

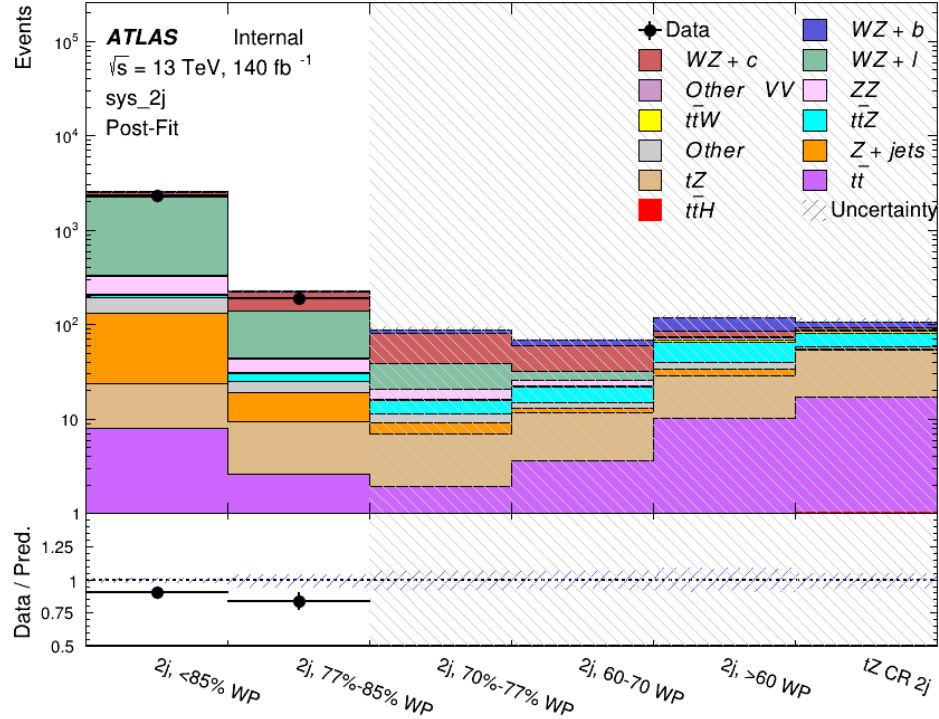


Figure 15.7: Post-fit summary of the fit over 2-jet regions.

1058 The same set of systematic uncertainties consider for the 1-jet fit are included in the 2-jet
 1059 fit as well. The impact of the most significant systematic uncertainties is summarized in Table
 1060 [22](#).

Uncertainty Source	$\Delta\mu$	
WZ + c cross-section	-0.1	0.14
Luminosity	-0.11	0.12
tZ cross-section	-0.11	0.11
Jet Energy Scale	-0.11	0.11
ttZ cross-section - QCD scale	-0.08	0.09
WZ + l cross-section	0.08	-0.07
WtZ cross-section	-0.07	0.07
Flavor tagging	0.05	0.05
Other VV + b cross-section	-0.05	0.05
Jet Energy Resolution	-0.04	0.04
Total	0.29	0.31

Table 20: Summary of the most significant sources of systematic uncertainty on the measurement of WZ + b 2-jet events.

1061 The ranking and impact of those nuisance parameters with the largest contribution to the
 1062 overall uncertainty is shown in Figure 15.8.

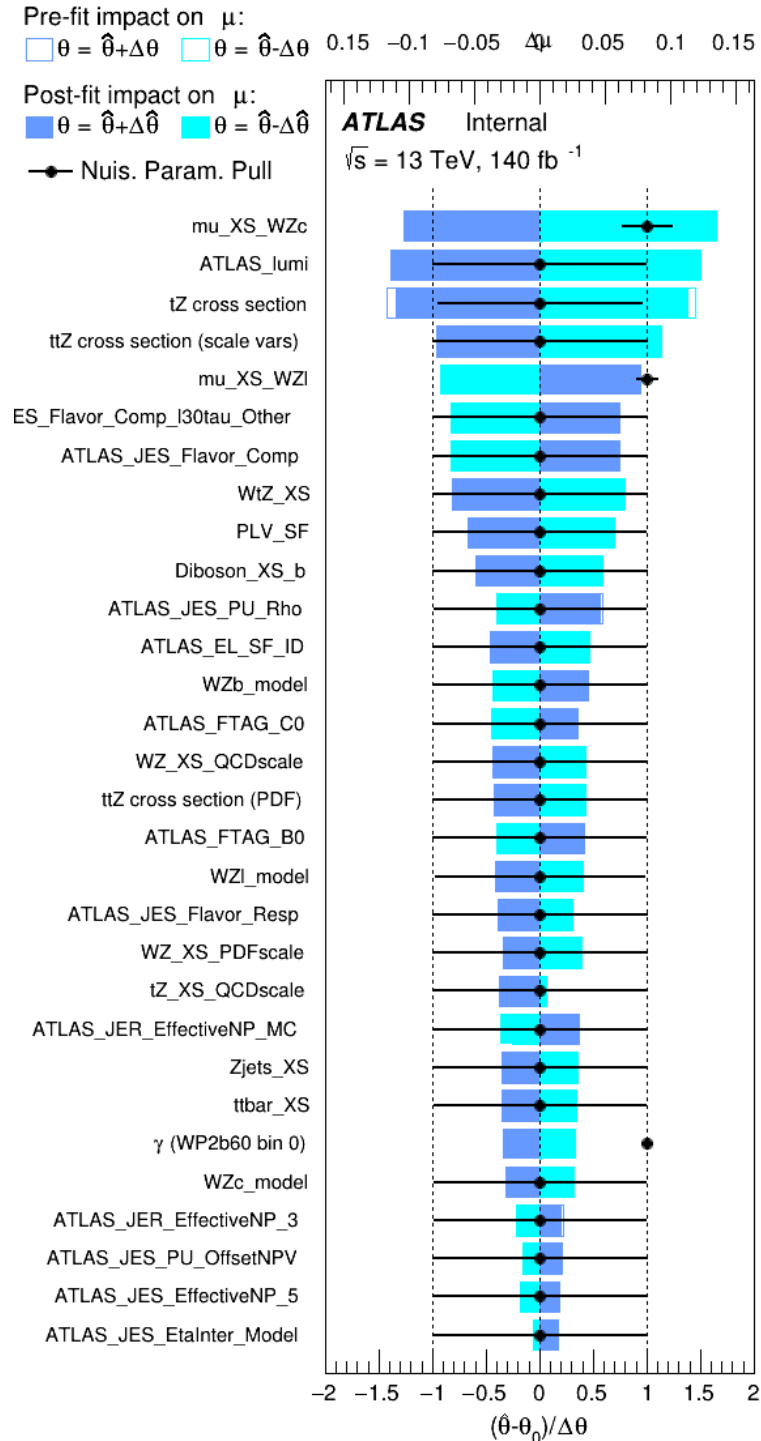


Figure 15.8: Impact of systematic uncertainties on the signal-strength of $WZ + b$ in 2-jet events.

1063 The large impact of the Jet Energy Scale and Jet Flavor Tagging is unsurprising, as the
 1064 shape of the fit regions depends heavily on the modeling of the jets. The other major sources
 1065 of uncertainty come from background modelling and cross-section uncertainty. The pie charts
 1066 in Figure 15.9 show that for the modelling uncertainties that contribute most correspond to the
 1067 most significant backgrounds.

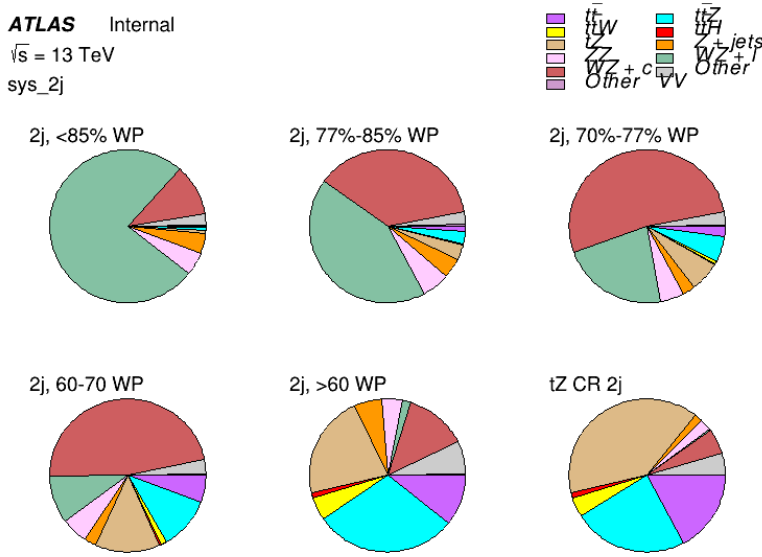


Figure 15.9: Post-fit background composition of the 2-jet fit regions.

1068 The correlations between these nuisance parameters are summarized in Figure 15.10.



Figure 15.10: Correlations between nuisance parameters in the 2-jet fit

1069

As in the 1-jet case, no significant, unexpected correlations are found between nuisance

1070 parameters.

Part V**1072 Differential Studies of $t\bar{t}H$ Multilepton****1073 16 Data and Monte Carlo Samples**

1074 For both data and Monte Carlo (MC) simulations, samples were prepared in the `xAOD` format,
1075 which was used to produce a `xAOD` based on the `HIGG8D1` derivation framework. This framework
1076 was designed for the main $t\bar{t}H$ multi-lepton analysis. Because this analysis targets events with
1077 multiple light leptons, as well as tau hadrons, this framework skims the dataset of any events that
1078 do not meet at least one of the following requirements:

- 1079 • at least two light leptons within a range $|\eta| < 2.6$, with leading lepton $p_T > 15$ GeV and
1080 subleading lepton $p_T > 5$ GeV
- 1081 • at least one light lepton with $p_T > 15$ GeV within a range $|\eta| < 2.6$, and at least two hadronic
1082 taus with $p_T > 15$ GeV.

1083 Samples were then generated from these `HIGG8D1` derivations using `AnalysisBase` version
1084 21.2.127. A ptag of `p4133` was used for MC samples, and `p4134` for data.

1085 **16.1 Data Samples**

1086 The study uses proton-proton collision data collected by the ATLAS detector from 2015 through
 1087 2018, which represents an integrated luminosity of 139 fb^{-1} and an energy of $\sqrt{s} = 13 \text{ TeV}$. All
 1088 data used in this analysis was included in one of the following Good Run Lists:

- 1089 • data15_13TeV.periodAllYear_DetStatus-v79-repro20-02_DQDefects-00-02-02
 1090 _PHYS_StandardGRL_All_Good_25ns.xml
- 1091 • data16_13TeV.periodAllYear_DetStatus-v88-pro20-21_DQDefects-00-02-04
 1092 _PHYS_StandardGRL_All_Good_25ns.xml
- 1093 • data17_13TeV.periodAllYear_DetStatus-v97-pro21-13_Unknown_PHYS_StandardGRL
 1094 _All_Good_25ns_Triggerno17e33prim.xml
- 1095 • data18_13TeV.periodAllYear_DetStatus-v102-pro22-04_Unknown_PHYS_StandardGRL
 1096 _All_Good_25ns_Triggerno17e33prim.xml

1097 **16.2 Monte Carlo Samples**

1098 Several Monte Carlo (MC) generators were used to simulate both signal and background pro-
 1099 cesses. For all of these, the effects of the ATLAS detector are simulated in Geant4. The specific
 1100 event generator used for each of these MC samples is listed in Table 23.

Table 21: The configurations used for event generation of signal and background processes, including the event generator, matrix element (ME) order, parton shower algorithm, and parton distribution function (PDF).

Process	Event generator	ME order	Parton Shower	PDF
t̄H	MG5_AMC (MG5_AMC)	NLO (NLO)	PYTHIA 8 (HERWIG++)	NNPDF 3.0 NLO [14] (CT10 [15])
t̄W	MG5_AMC (SHERPA 2.1.1)	NLO (LO multileg)	PYTHIA 8 (SHERPA)	NNPDF 3.0 NLO (NNPDF 3.0 NLO)
t̄(Z/γ* → ll)	MG5_AMC	NLO	PYTHIA 8	NNPDF 3.0 NLO
VV	SHERPA 2.2.2	MEPS NLO	SHERPA	CT10
t̄t	POWHEG-BOX v2 [16]	NLO	PYTHIA 8	NNPDF 3.0 NLO
t̄γ	MG5_AMC	LO	PYTHIA 8	NNPDF 2.3 LO
tZ	MG5_AMC	LO	PYTHIA 6	CTEQ6L1
tHqb	MG5_AMC	LO	PYTHIA 8	CT10
tHW	MG5_AMC (SHERPA 2.1.1)	NLO (LO multileg)	HERWIG++ (SHERPA)	CT10 (NNPDF 3.0 NLO)
tWZ	MG5_AMC	NLO	PYTHIA 8	NNPDF 2.3 LO
t̄t̄, t̄t̄t̄	MG5_AMC	LO	PYTHIA 8	NNPDF 2.3 LO
t̄W+W-	MG5_AMC	LO	PYTHIA 8	NNPDF 2.3 LO
s-, t-channel, Wt single top	POWHEG-BOX v1 [17]	NLO	PYTHIA 6	CT10
qqVV, VVV				
Z → l+l-	SHERPA 2.2.1	MEPS NLO	SHERPA	NNPDF 3.0 NLO

1101 As explained in detail in [5], the t̄W contribution predicted by MC is found disagree
 1102 significantly with what is observed in data. While an effort is currently being undertaken to
 1103 measure t̄W more accurately, the approach used by the 80 fb⁻¹ t̄H analysis is used for this
 1104 analysis: A normalization factor of 1.68 is applied to the MC estimate of t̄W. Additionally,
 1105 systematic uncertainties are applied to account for this modelling discrepancy, as outlined in
 1106 Section 21.

1107 While the main t̄H analysis uses a more sophisticated data-driven approach to estimating
 1108 the contribution of events with non-prompt leptons (or "fakes"), at the time of this note this

1109 strategy has not been completely developed for the full Run-2 dataset. Therefore, the non-prompt
1110 contribution is estimated with MC, while applying normalization corrections and systematic
1111 uncertainties derived from data driven techniques developed for the 80 fb^{-1} $t\bar{t}H/t\bar{t}W$ analysis
1112 [5]. The primary contribution to the non-prompt lepton background is from $t\bar{t}$ production, with
1113 $V+jets$ and single-top as much smaller sources. Likelihood fits over several control regions
1114 enriched with these non-prompt backgrounds are fit to data in order to derive normalization
1115 factors for these backgrounds. The specific normalization factors and uncertainties applied to
1116 the non-prompt contributions are listed in Section 21.

1117 The specific DSIDs used in the analysis are listed below:

Sample	DSID
tH	345873-5, 346343-5
VV	364250-364254, 364255, 363355-60, 364890
tW	413008
tZ	410156, 410157, 410218-20
low mass tZ	410276-8
Rare Top	410397, 410398, 410399
single Top	410658-9, 410644-5
three Top	304014
four Top	410080
tWW	410081
Z + jets	364100-41
low mass Z + jets	364198-215
W + jets	364156-97
V γ	364500-35
tZ	410560
tW	410013-4
WtZ	410408
VVV	364242-9
VH	342284-5
WtH	341998
t $\bar{\gamma}$	410389
t \bar{t}	410470

Table 22: List of Monte Carlo samples by data set ID used in the analysis.

1118 17 Object Reconstruction

1119 All analysis channels considered in this note share a common object selection for leptons and

1120 jets, as well as a shared trigger selection.

¹¹²¹ **17.1 Trigger Requirements**

¹¹²² Events are required to be selected by dilepton triggers, as summarized in Table 25.

Dilepton triggers (2015)	
$\mu\mu$ (asymm.)	HLT_mu18_mu8noL1
ee (symm.)	HLT_2e12_lhloose_L12EM10VH
$e\mu, \mu e$ (\sim symm.)	HLT_e17_lhloose_mu14
Dilepton triggers (2016)	
$\mu\mu$ (asymm.)	HLT_mu22_mu8noL1
ee (symm.)	HLT_2e17_lhvloose_nod0
$e\mu, \mu e$ (\sim symm.)	HLT_e17_lhloose_nod0_mu14
Dilepton triggers (2017)	
$\mu\mu$ (asymm.)	HLT_mu22_mu8noL1
ee (symm.)	HLT_2e24_lhvloose_nod0
$e\mu, \mu e$ (\sim symm.)	HLT_e17_lhloose_nod0_mu14
Dilepton triggers (2018)	
$\mu\mu$ (asymm.)	HLT_mu22_mu8noL1
ee (symm.)	HLT_2e24_lhvloose_nod0
$e\mu, \mu e$ (\sim symm.)	HLT_e17_lhloose_nod0_mu14

Table 23: List of lowest p_T -threshold, un-prescaled dilepton triggers used for 2015-2018 data taking.

¹¹²³ **17.2 Light Leptons**

¹¹²⁴ Electron candidates are reconstructed from energy clusters in the electromagnetic calorimeter
¹¹²⁵ that are associated with charged particle tracks reconstructed in the inner detector [18]. Electron
¹¹²⁶ candidates are required to have $p_T > 10$ GeV and $|\eta_{\text{cluster}}| < 2.47$. Candidates in the transition
¹¹²⁷ region between different electromagnetic calorimeter components, $1.37 < |\eta_{\text{cluster}}| < 1.52$, are
¹¹²⁸ rejected. A multivariate likelihood discriminant combining shower shape and track information

1129 is used to distinguish prompt electrons from nonprompt leptons, such as those originating from
1130 hadronic showers. Electron candidate are also required to pass TightLH identification.

1131 To further reduce the non-prompt contribution, the track of each electron is required to
1132 originate from the primary vertex; requirements are imposed on the transverse impact parameter
1133 significance ($|d_0|/\sigma_{d_0}$) and the longitudinal impact parameter ($|\Delta z_0 \sin \theta_\ell|$).

1134 Muon candidates are reconstructed by combining inner detector tracks with track segments
1135 or full tracks in the muon spectrometer [19]. Muon candidates are required to have $p_T > 10$ GeV
1136 and $|\eta| < 2.5$. Muons are required to Medium ID requirements.

1137 All leptons are required to pass a non-prompt BDT selection developed by the main
1138 $t\bar{t}H - ML/t\bar{t}W$ analysis, described in detail in [5]. Optimized working points and scale factors
1139 for this BDT are taken from that analysis. This BDT and the WPs used are summarized in
1140 Appendix .1,

1141 17.3 Jets

1142 Jets are reconstructed from calibrated topological clusters built from energy deposits in the
1143 calorimeters [21], using the anti- k_t algorithm with a radius parameter $R = 0.4$. Particle Flow, or
1144 PFlow, jets are used in the analysis, which are hadronic objects reconstructed using information
1145 from both the tracker and the calorimeter. Jets with energy contributions likely arising from noise
1146 or detector effects are removed from consideration [22], and only jets satisfying $p_T > 25$ GeV

1147 and $|\eta| < 2.5$ are used in this analysis. For jets with $p_T < 60$ GeV and $|\eta| < 2.4$, a jet-track
1148 association algorithm is used to confirm that the jet originates from the selected primary vertex,
1149 in order to reject jets arising from pileup collisions [23].

1150 17.4 B-tagged Jets

1151 Each analysis channel used in this analysis includes b-jets in the final state. These are identified
1152 using the DL1r b-tagging algorithm, which uses jet vertex and kinematic information to distin-
1153 guish heavy and light flavored jets. These features are used as inputs to a neural network, the
1154 output of which is used to form calibrated working points (WPs) based on how likely a jet is to
1155 have originated from a b-quark. This analysis uses the 70% DL1r WP - implying an efficiency of
1156 70% for truth b-jets - for selecting b-tagged jets.

1157 17.5 Missing Transverse Energy

1158 Because all $t\bar{t}H - ML$ channels considered include multiple neutrinos, missing transverse
1159 energy (E_T^{miss}) is present in each event. The missing transverse momentum vector is defined as
1160 the inverse of the sum of the transverse momenta of all reconstructed physics objects as well
1161 as remaining unclustered energy, the latter of which is estimated from low- p_T tracks associated
1162 with the primary vertex but not assigned to a hard object [24].

1163 17.6 Overlap removal

1164 To avoid double counting objects and remove leptons originating from decays of hadrons, overlap
 1165 removal is performed in the following order: any electron candidate within $\Delta R = 0.1$ of another
 1166 electron candidate with higher p_T is removed; any electron candidate within $\Delta R = 0.1$ of a muon
 1167 candidate is removed; any jet within $\Delta R = 0.3$ of an electron candidate is removed; if a muon
 1168 candidate and a jet lie within $\Delta R = \min(0.4, 0.04 + 10[\text{GeV}]/p_T(\text{muon}))$ of each other, the jet
 1169 is kept and the muon is removed.

1170 This algorithm is applied to the preselected objects. The overlap removal procedure is
 1171 summarized in Table 26.

Keep	Remove	Cone size (ΔR)
electron	electron (low p_T)	0.1
muon	electron	0.1
electron	jet	0.3
jet	muon	$\min(0.4, 0.04 + 10[\text{GeV}]/p_T(\text{muon}))$
electron	tau	0.2

Table 24: Summary of the overlap removal procedure between electrons, muons, and jets.

1172 18 Higgs Momentum Reconstruction

1173 Reconstructing the momentum of the Higgs boson is a particular challenge for channels with
 1174 leptons in the final state: Because all channels include at least two neutrinos in the final state, the
 1175 Higgs can never be fully reconstructed. However, the momentum spectrum can be well predicted
 1176 by a neural network when provided with the four-vectors of the Higgs Boson decay products, as

1177 shown in Section 18.1. With this in mind, several layers of MVAs are used to reconstruction the
1178 Higgs momentum.

1179 The first layer is a model designed to select which jets are most likely to be the b-jets that
1180 came from the top decay, detailed in Section 18.2. As described in Section 18.3, the kinematics
1181 of these jets and possible Higgs decay products are fed into the second layer, which is designed
1182 to identify the decay products of the Higgs Boson itself. The kinematics of the particles this
1183 layer identifies as most likely to have originated from the Higgs decay are then fed into yet
1184 another neural-network, which predicts the momentum of the Higgs (18.4). For the 3l channel,
1185 an additional MVA is used to determine the decay mode of the Higgs boson in the 3l channel
1186 (18.5).

1187 Models are trained on Monte Carlo simulations of $t\bar{t}H$ events generated using MG5_AMC.
1188 Specifically, events DSIDs 346343-5, 345873-5, and 345672-4 are used for training in order to
1189 increase the statistics of the training sample.

1190 For all of these models, the Keras neural network framework, with Tensorflow 2.0 as the
1191 backend, is used, and the number of hidden layers and nodes are determined using grid search
1192 optimization. Each neural network uses the LeakyReLU activation function, a learning rate of
1193 0.01, and the Adam optimization algorithm, as alternatives are found to either decrease or have
1194 no impact on performance. Batch normalization is applied after each layer in order to stabilize
1195 the model and decrease training time. For the classification algorithms (b-jet matching, Higgs
1196 reconstruction, and 3l decay identification) binary-cross entropy is used as the loss function,

1197 while the p_T reconstruction algorithm uses MSE.

1198 The specific inputs features used for each model are arrived at through a process of trial
1199 and error - features considered potentially useful are tried, and those that are found to increase
1200 performance are included. While each model includes a relatively large number of features,
1201 some using upwards of 30, this inclusive approach is found to maximize the performance of each
1202 model while decreasing the variance compared to a reduced number of inputs. Each input feature
1203 is validated by comparing MC simulations to 80 fb^{-1} of data, as shown in the sections below.

1204 **18.1 Higgs Decay Product Identification**

1205 Machine Learning algorithms are trained to identify the decay products of the Higgs Boson using
1206 MC simulations of $t\bar{t}H$ events. The kinematics of the reconstructed physics objects, as well as
1207 event level variables, are used as inputs, with the parent ID taken from the truth record used to
1208 label the data. The objects considered include light leptons and jets.

1209 Reconstructed physics objects are matched to particle level objects, in order to identify the
1210 parent particle of these reconstructed objects. Reconstructed jets are matched to truth jets based
1211 on the requirements that the reco jet and truth jet fall within $\Delta R < 0.4$, and the two objects have
1212 a p_T that agrees within 10%. Truth level and reco level leptons are required to have the same
1213 flavor, a $\Delta R < 0.1$, and p_T that agree within 10%. Events where no match can be found between
1214 the particle level decay products of the Higgs and the reconstructed objects are not included in
1215 training.

1216 Leptons considered as possible Higgs and top decay candidates are required to pass the
1217 selection described in Section 17.2. For jets, however, it is found that a large fraction that
1218 originate from either the top decay or the Higgs decay fall outside the selection described in
1219 Section 17.3. Specifically, jets from the Higgs decay tend to be soft, with 32% having $p_T <$
1220 25 GeV. Therefore jets with $p_T < 15$ GeV are considered as possible candidates in the models
1221 described below. By contrast, less than 5% of the jets originating from the Higgs fall below
1222 this p_T threshold. The jets are found to be well modeled even down to this low p_T threshold,
1223 as shown in Section 20.1. The impact of using different p_T selection for the jet candidates is
1224 considered in detail in Section A.5. As they are expected to originate from the primary vertex,
1225 jets are also required to pass a JVT cut.

1226 18.2 b-jet Identification

1227 Including the kinematics of the b-jets that originate from the top decay is found to improve the
1228 identification of the Higgs decay products, and improve the accuracy with which the Higgs
1229 momentum can be reconstructed. Because these b-jets are reconstructed by the detector with
1230 high efficiency (just over 90% of the time), and can be identified relatively consistently, the first
1231 step in reconstructing the Higgs is selecting the b-jets from the top decay.

1232 Exactly two b-jets are expected in the final state of $t\bar{t}H - \text{ML}$ events. However, in both
1233 the 3l and 2lSS channels, only one or more b-tagged jets are required (where the 70% DL1r b-tag
1234 working point is used). Therefore, for events which have exactly one, or more than two, b-tagged

1235 jets, deciding which combination of jets correspond to the top decay is non-trivial. Further,
1236 events with 1 b-tagged jet represent just over half of all $t\bar{t}H - ML$ events. Of those, both b-jets
1237 are reconstructed by the detector 75% of the time. Therefore, rather than adjusting the selection
1238 to require exactly 2 b-tagged jets, and losing more than half of the signal events, a neural network
1239 is used to predict which pair of jets is most likely to correspond to truth b-jets.

1240 Once the network is trained, all possible pairings of jets are fed into the model, and the pair
1241 of jets with the highest output score are taken to be b-jets in successive steps of the analysis.

1242 **18.2.1 2lSS Channel**

1243 For the 2lSS channel, the input features shown in Table 27 are used for training. Here j_0 and j_1
1244 are the two jet candidates, while l_0 and l_1 are the two leptons in the event, both ordered by p_T . jet
1245 DL1r is an integer corresponding to the calibrated b-tagging working points reached by each jet,
1246 where 5 represents the tightest working point and 1 represents the loosest. The variables nJets
1247 DL1r 60% and nJets DL1r 85% represent the number of jets in the event passing the 60% and
1248 85% b-tag working points, respectively.

jet p_T 0	jet p_T 1	Lepton p_T 0
Lepton p_T 1	jet η 0	jet η 1
$\Delta R(j_0)(j_1)$	$M(j_0 j_1)$	$\Delta R(l_0)(j_0)$
$\Delta R(l_0)(j_1)$	$\Delta R(l_1)(j_0)$	$\Delta R(l_1)(j_1)$
$M(l_0 j_0)$	$M(l_0 j_1)$	$M(l_1 j_0)$
$M(l_1 j_1)$	jet DL1r 0	jet DL1r 1
nJets OR DL1r 85	nJets OR DL1r 60	$\Delta R(j_0 l_0)(j_1 l_1)$
$\Delta R(j_0 l_1)(j_1 l_0)$	$p_T(j_0 j_1 l_0 l_1 E_T^{\text{miss}})$	$M(j_0 j_1 l_0 l_1 E_T^{\text{miss}})$
$\Delta\phi(j_0)(E_T^{\text{miss}})$	$\Delta\phi(j_1)(E_T^{\text{miss}})$	HT jets
nJets	E_T^{miss}	

Table 25: Input features used in the b-jet identification algorithm for the 2lSS channel

1249 As there are far more incorrect combinations than correct ones, by a factor of more than
 1250 20:1, the training set is resampled to reduce the fraction of incorrect combinations. A random
 1251 sample of 5 million incorrect entries are used for training, along with close 1 million correct
 1252 entries. 10% of the dataset is set aside for testing, leaving around 5 million datapoints for
 1253 training.

1254 The difference between the distributions for a few of these features for the "correct" (i.e.
 1255 both jets are truth b-jets), and "incorrect" combinations are shown in Figure 18.1. The correct and
 1256 incorrect contributions are scaled to the same integral, so as to better demonstrate the differences
 1257 in the distributions.

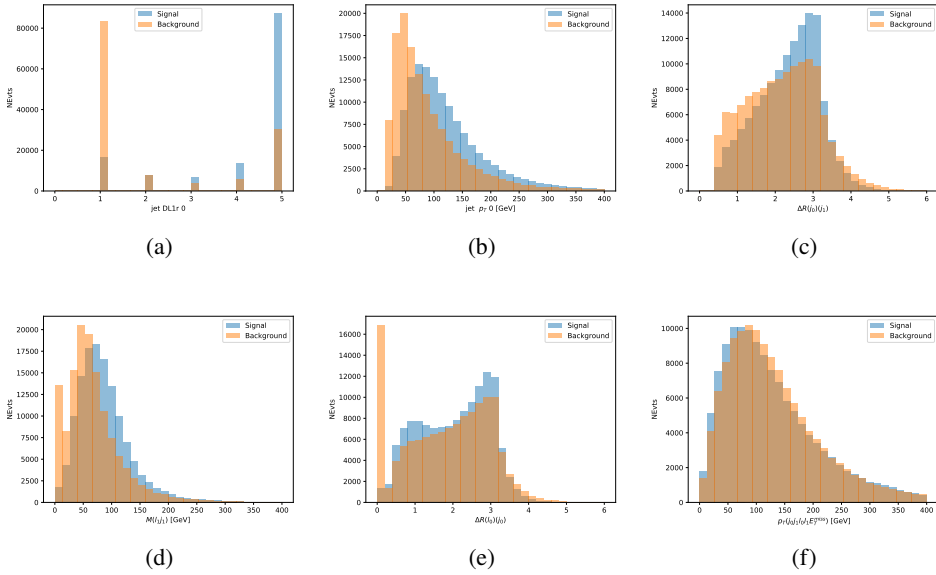


Figure 18.1: Input features for top2lSS training. The signal in blue represents events where both jet candidates are truth b-jets from top decays, and the orange is all other combinations. Each are scaled to the same number of events. (a) shows the DL1r working point of leading jet, (b) shows the p_T of the leading jet, (c) shows the ΔR of the two jets, (d) the invariant mass of lepton 1 and jet 1, (e) the ΔR of lepton 0 and jet 0, and (f) the p_T of both jets, both leptons, and the E_T^{miss} .

1258 The modeling of these inputs is validated against data, with Figure 18.2 showing good
 1259 general agreement between data and MC. Plots for the complete list of features can found in
 1260 Section A.

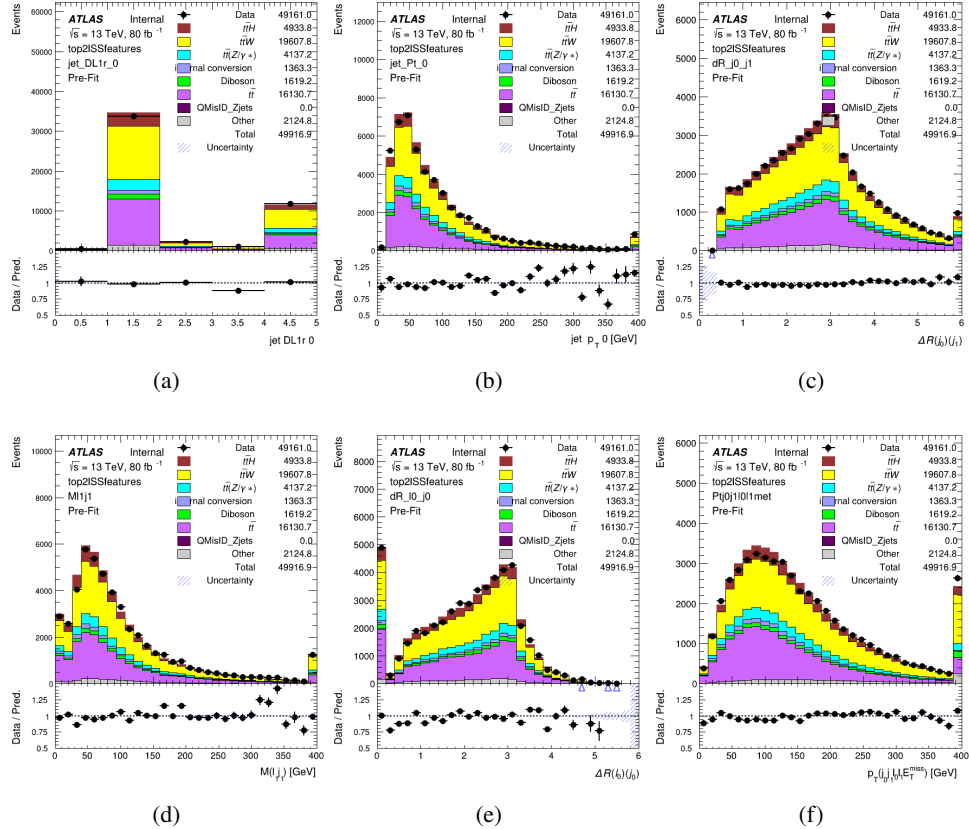


Figure 18.2: Data/MC comparisons of input features for top2ISS training for 80 fb^{-1} of data. (a) shows the DL1r working point of leading jet, (b) shows the p_T of the leading jet, (c) shows the ΔR of the two jets, (d) the invariant mass of lepton 1 and jet 1, (e) the ΔR of lepton 0 and jet 0, and (f) the p_T of both jets, both leptons, and the E_T^{miss} .

1261 Based on the results of grid search evaluation, the optimal architecture is found to include
 1262 5 hidden layers with 40 nodes each. No regularizer or dropout is added to the network, as
 1263 overfitting is found to not be an issue. The output score distribution as well as the ROC curve for
 1264 the trained model are shown in Figure 18.2.1. The model is found to identify the correct pairing
 1265 of jets for 73% of 2lSS signal events on test data.

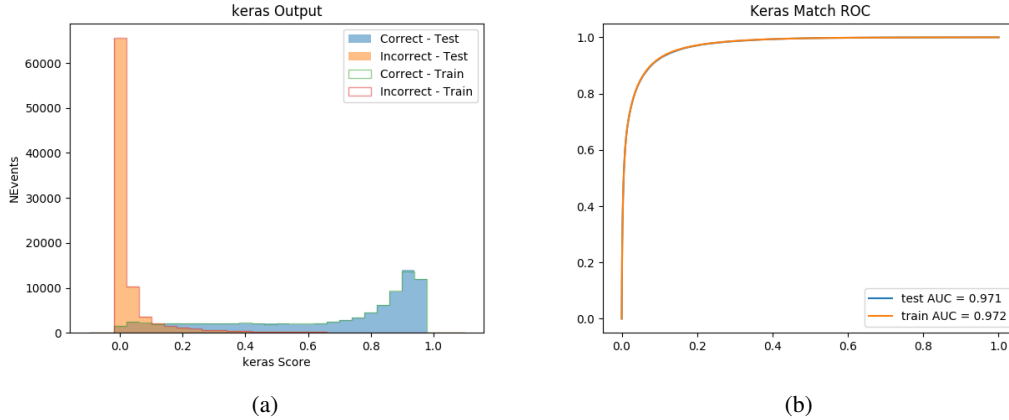


Figure 18.3: Results of the b-jet identification algorithm for the 2lSS channel, showing (a) the output score of the NN for correct and incorrect combinations of jets. (b) the ROC curve of the output, showing background rejection as a function of signal efficiency

1266 For point of comparison, a "naive" approach to identify b-jets is used as well: The two
 1267 jets which pass the highest DL1r b-tag working point are assumed to be the b-jets from the top
 1268 decay. In the case that multiple jets meet the same b-tag working point, the jet with higher p_T is
 1269 used. This method identifies the correct jet pair 65% of the time.

1270 The accuracy of the model for different values of n-bjets, compared to this naive approach,
 1271 is shown in Table 28.

b-jet Selection	Neural Network	Naive
1 b-jet	58.6%	42.1%
2 b-jets	88.4%	87.1%
≥ 3 b-jets	61.7%	53.3%
Overall	73.9%	67.2%

Table 26: Accuracy of the NN in identifying b-jets from tops in 2lSS events, overall and split by the number of b-tagged jets in the event, compared to the accuracy of taking the two highest b-tagged jets.

1272 18.2.2 3l Channel

¹²⁷³ The input features used in the 3l channel are listed in Table 29, with the same naming convention
¹²⁷⁴ as the 2lSS channel.

jet p_T 0	jet p_T 1	jet η 0
jet η 1	Lepton p_T 0	Lepton p_T 1
Lepton p_T 2	$\Delta R(j_0)(j_1)$	$M(j_0 j_1)$
$\Delta R(l_0)(j_0)$	$\Delta R(l_1)(j_0)$	$\Delta R(l_2)(j_0)$
$\Delta R(l_0)(j_1)$	$\Delta R(l_1)(j_1)$	$\Delta R(l_2)(j_1)$
$M(l_0 j_0)$	$M(l_1 j_0)$	$M(l_2 j_0)$
$M(l_0 j_1)$	$M(l_1 j_1)$	$M(l_2 j_1)$
$\Delta R(j_0 l_0)(j_1 l_1)$	$\Delta R(j_0 l_0)(j_1 l_2)$	$\Delta R(j_0 l_1)(j_1 l_0)$
$\Delta R(j_0 l_2)(j_1 l_0)$	jet DL1r 0	jet DL1r 1
$p_T(j_0 j_1 l_0 l_1 l_2 E_T^{\text{miss}})$	$M(t j_0 j_1 l_0 l_1 l_2 E_T^{\text{miss}})$	$\Delta\phi(j_0)(E_T^{\text{miss}})$
$\Delta\phi(j_1)(E_T^{\text{miss}})$	HT Lepton	HT jets
nJets	E_T^{miss}	nJets OR DL1r 85
nJets OR DL1r 60		

Table 27: Input features for the b-jet identification algorithm in the 3l channel.

¹²⁷⁵ A few of these features are shown in Figure 18.4, comparing the distributions for correct
¹²⁷⁶ and incorrect combinations of jets.

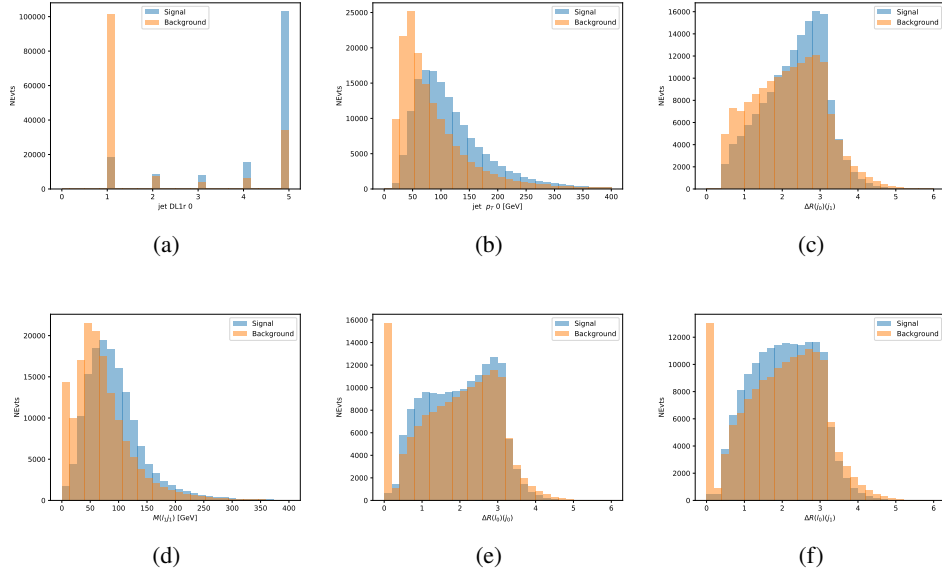


Figure 18.4: Input features for top3l training. The signal in blue represents events where both jet candidates are truth b-jets from top decays, and the orange is all other combinations. Scaled to the same number of events. (a) show the DL1r WP of jet 0, (b) the p_T of jet 0, (c) ΔR between jet 0 and jet 1, (d) the invariant mass of lepton 1 and jet 1, (e) ΔR between lepton 0 and jet 0, and (f) ΔR between lepton 0 and jet 1

1277 The modeling of these inputs is validated against data, with Figure 18.5 showing good
1278 general agreement between data and MC. Plots for the complete list of features can found in
1279 Section A.

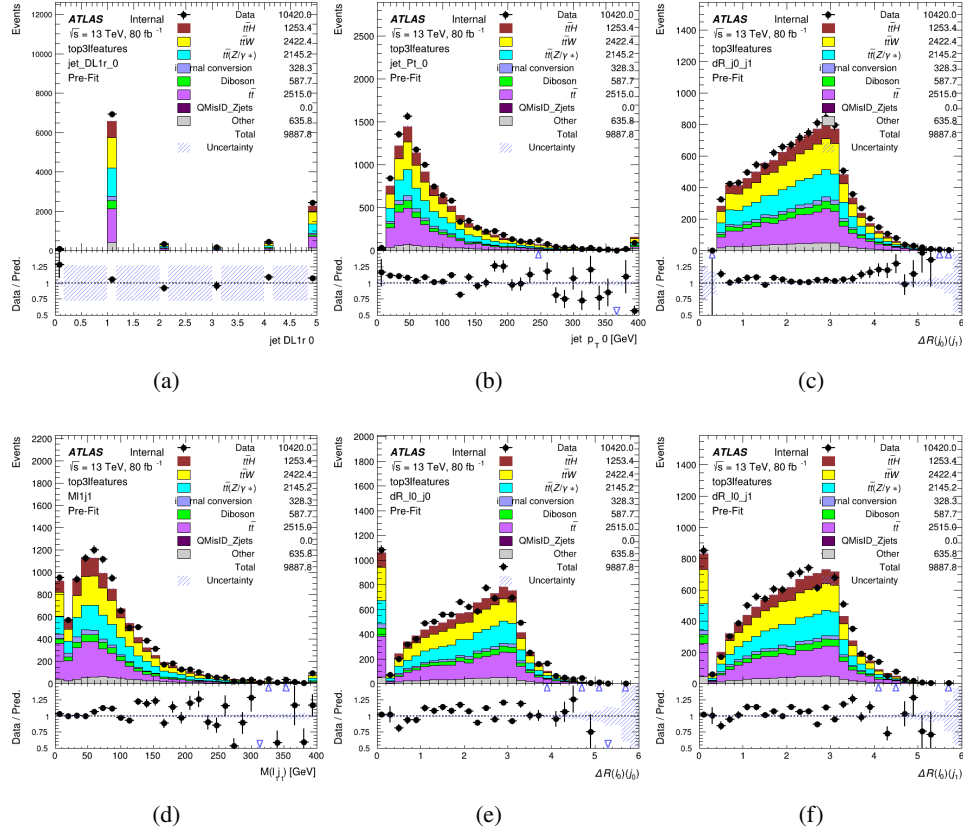


Figure 18.5: Data/MC comparisons of input features for top3l training for 80 fb^{-1} of data. (a) show the DL1r WP of jet 0, (b) the p_T of jet 0, (c) ΔR between jet 0 and jet 1, (d) the invariant mass of lepton 1 and jet 1, (e) ΔR between lepton 0 and jet 0, and (f) ΔR between lepton 0 and jet 1

Again, the dataset is downsized to reduce the ratio of correct and incorrect combination from 20:1, to 5:1. Around 7 million events are used for training, with 10% set aside for testing. Based on the results of grid search evaluation, the optimal architecture is found to include 5 hidden layers with 60 nodes each. The output score distribution as well as the ROC curve for the trained model are shown in Figure 18.2.2.

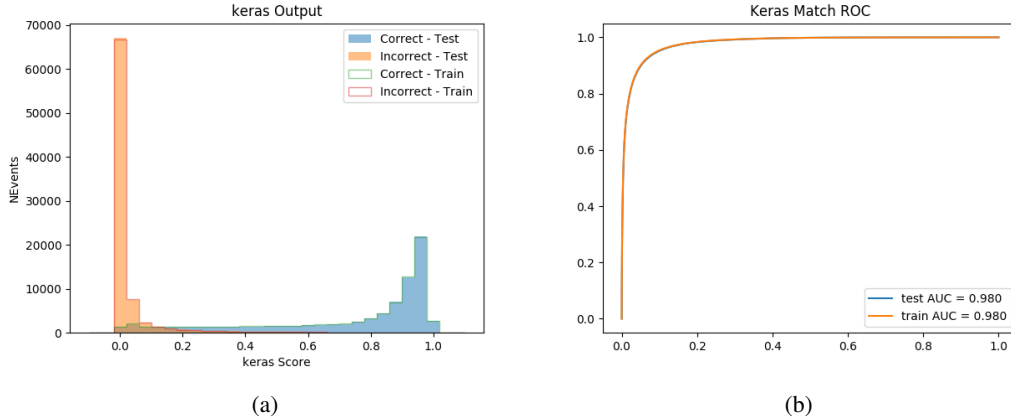


Figure 18.6: Results of the b-jet identification algorithm for the 3l channel, showing (a) the output score of the NN for correct and incorrect combinations of jets. (b) the ROC curve of the output, showing background rejection as a function of signal efficiency

1285 This procedure is found to identify the correct pairing of jets for nearly 80% of 3l signal
 1286 events. The accuracy of the model is summarized in Table 30.

Table 28: Accuracy of the NN in identifying b-jets from tops, compared to the naive method of taking the highest b-tagged jets.

	NN	Naive
1 b-jet	69.0%	48.9%
2 b-jets	89.6%	88.3%
≥ 3 b-jets	55.7%	52.3%
Overall	79.8%	70.2%

1287 18.3 Higgs Reconstruction

1288 Techniques similar to the b-jet identification algorithms are employed to select the decay products
 1289 of the Higgs: kinematics of all possible combinations of reconstructed objects are fed into a neural
 1290 network to determine which of those is most likely to be the decay products of the Higgs.

1291 Again separate models are used for the 2lSS and 3l channels, while the 3l channel has now
1292 been split into two: $t\bar{t}H$ events with three leptons in the final state include both instances where
1293 the Higgs decays into a lepton (and a neutrino) and a pair of jets, and instances where the Higgs
1294 decays to two leptons.

1295 3l events are therefore categorized as either semi-leptonic (3lS) or fully-leptonic (3lF). In
1296 the semi-leptonic case the reconstructed decay products consist of two jets and a single lepton.
1297 For the fully-leptonic case, the decay products include 2 of the three leptons associated with the
1298 event. For training the models, events are separated into these two categories using truth level
1299 information. A separate MVA, described in Section 18.5, is used to make this distinction at reco
1300 level and determine which model to use.

1301 For all channels, the models described in Section 18.2 are used to identify b-jet candidates,
1302 whose kinematics are used to identify the Higgs decay products. These jets are not considered
1303 as possible candidates for the Higgs decay, justified by the fact that these models are found to
1304 misidentify jets from the Higgs decay as jets from the top decay less than 1% of the time.

1305 18.3.1 2lSS Channel

1306 For the 2lSS channel, the Higgs decay products include one light lepton and two jets. The neural
1307 network is trained on the kinematics of different combinations of leptons and jets, as well as the
1308 b-jets identified in Section 18.2, with the specific input features listed in Table 9.

Lepton p_T H	Lepton p_T T	jet p_T 0
jet p_T 1	top p_T 0	top p_T 1
top η 0	top η 1	jet η 0
jet η 1	jet Phi 0	jet Phi 1
Lepton η H	Lepton heta T	$\Delta R(j_0)(j_1)$
$\Delta R(l_H)(j_0)$	$\Delta R(l_H)(j_1)$	$M(j_0 j_1)$
$M(l_H j_0)$	$M(l_H j_1)$	$\Delta R(l_H)(b_0)$
$\Delta R(l_H)(b_1)$	$\Delta R(l_T)(b_0)$	$\Delta R(l_T)(b_1)$
$\Delta R(j_0 j_1)(l_H)$	$\Delta R(j_0 j_1)(l_T)$	$\Delta R(j_0 j_1)(b_0)$
$\Delta R(j_0 j_1)(b_1)$	$\Delta R(j_0)(b_0)$	$\Delta R(j_0)(b_1)$
$\Delta R(j_1)(b_0)$	$\Delta R(j_1)(b_1)$	$M(j_0 j_1 l_H)$
$p_T(j_0 j_1 l_H l_T b_0 b_1 E_T^{\text{miss}})$	topScore	E_T^{miss}
nJets	HT jets	

Table 29: Input features used to identify the Higgs decay products in 2ISS events

1309 Here j_0 and j_1 , and l_H are the jet and lepton decay candidates, respectively. The other
 1310 lepton in the event is labeled l_T , as it is assumed to have come from the decay of one of the top
 1311 quarks. b_0 and b_1 are the two b-jets identified by the b-jet identification algorithm. The b-jet
 1312 Reco Score is the output of the b-jet reconstruction algorithm.

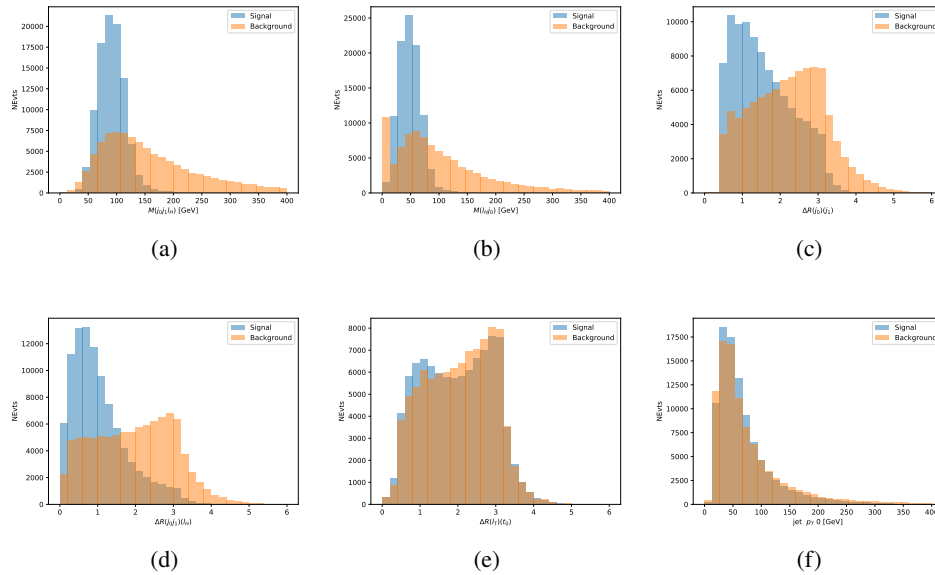


Figure 18.7: Input features for higgs2lSS training. The signal in blue represents events where both jet candidates are truth b-jets from top decays, and the orange is all other combinations. Scaled to the same number of events. (a) shows the invariant mass of the two jet candidates and the lepton candidate, (b) the invariant mass of jet 0 and the lepton candidate, (c) ΔR between the jet candidates, (d) ΔR between jet 0 + jet 1 and the lepton candidate, (e) ΔR between the lepton from the top and the leading b-jet, (f) the p_T of jet 0.

1313 The modeling of these inputs is validated against data, with Figure 18.2 showing good
 1314 general agreement between data and MC. Plots for the complete list of features can found in
 1315 Section A.

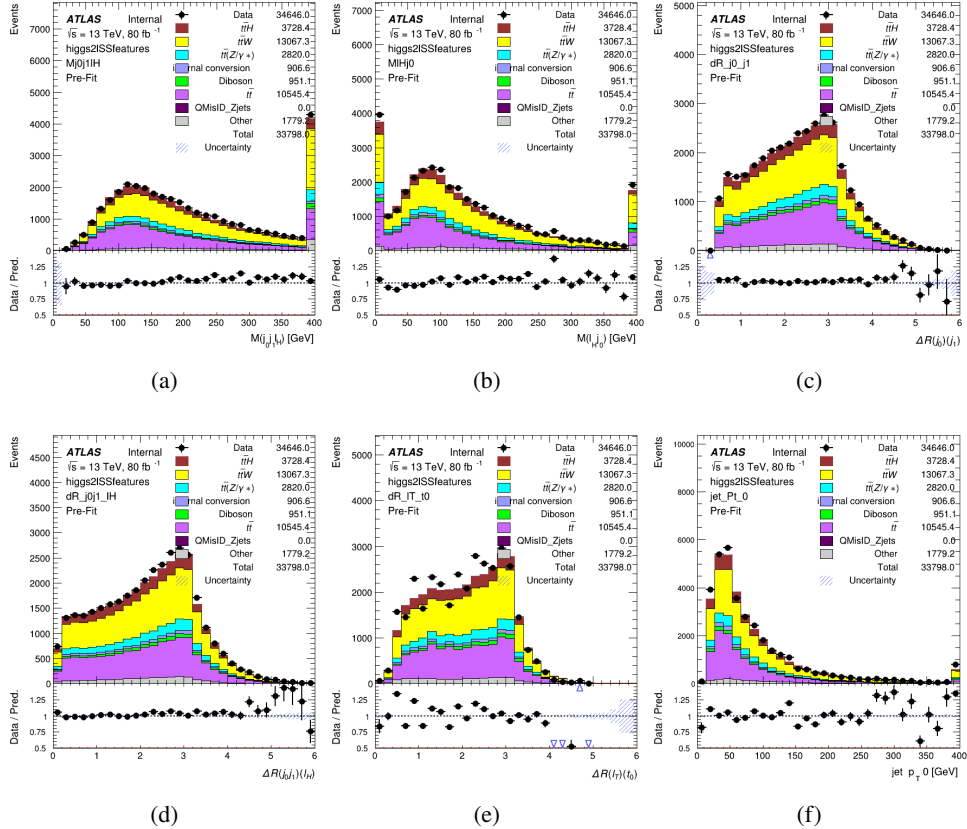


Figure 18.8: Data/MC comparisons of input features for higgs2lSS training for 80 fb^{-1} of data. (a) shows the invariant mass of the two jet candidates and the lepton candidate, (b) the invariant mass of jet 0 and the lepton candidate, (c) ΔR between the jet candidates, (d) ΔR between jet 0 + jet 1 and the lepton candidate, (e) ΔR between the lepton from the top and the leading b-jet, (f) the p_T of jet 0.

1316 A neural network consisting of 7 hidden layers with 60 nodes each is trained on around 2
 1317 million events, with an additional 200,000 reserved for testing the model. In order to compensate
 1318 for large number of incorrect combinations, these have been downsampled such that the correct
 1319 combinations represent over 10% of the training set. The output of the NN is summarized in
 1320 Figure 18.3.1.

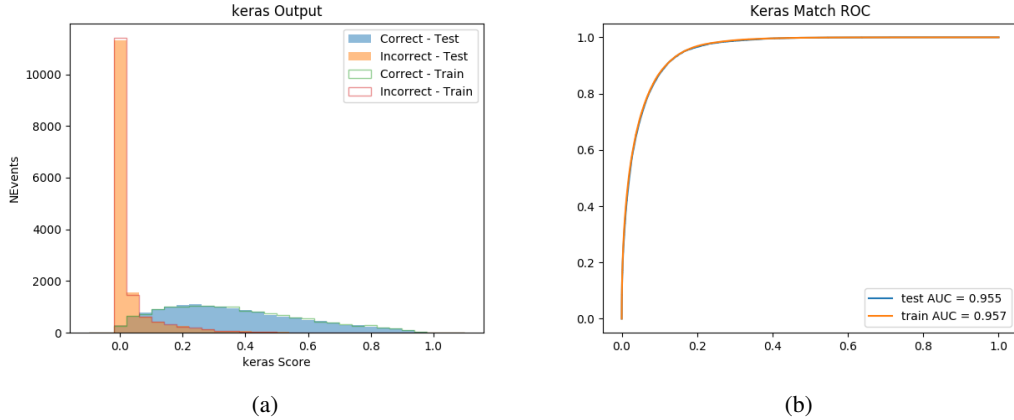


Figure 18.9: Result of the Higgs reconstruction algorithm in the 2lSS channel, showing (a) the output score of the NN for correct and incorrect combinations of jets scaled to an equal number of events, and (b) the ROC curve of the output, showing background rejection as a function of signal efficiency

1321 The neural network identifies the correct combination 55% of the time. It identifies the
 1322 correct lepton 85% of the time, and selects the correct lepton and at least one of the correct jets
 1323 81% of the time.

1324 18.3.2 3l Semi-leptonic Channel

1325 For 3l $t\bar{t}H$ where the Higgs decay semi-leptonically, the decay products include one of the three
 1326 leptons and two jets. In this case, the other two leptons originated from the decay of the tops,
 1327 meaning the opposite-sign (OS) lepton cannot have come from the Higgs. This leaves only the two
 1328 same-sign (SS) leptons as possible Higgs decay products.

Lepton $p_T H$	Lepton $p_T T_0$	Lepton $p_T T_1$
jet $p_T 0$	jet $p_T 1$	top $p_T 0$
top $p_T 1$	jet $\eta 0$	jet $\eta 1$
jet $\phi 0$	jet $\phi 1$	$\Delta R(j_0)(j_1)$
$M(j_0 j_1)$	$\Delta R(l_H)(j_0)$	$\Delta R(l_H)(j_1)$
$\Delta R(j_0 j_1)(l_H)$	$\Delta R(j_0 j_1)(l_{T_1})$	$\Delta R(l_{T_0})(l_{T_1})$
$\Delta R(l_H)(l_{T_1})$	$M(j_0 j_1 l_{T_0})$	$M(j_0 j_1 l_{T_1})$
$M(j_0 j_1 l_H)$	$\Delta R(j_0 j_1 l_H)(l_{T_0})$	$\Delta R(j_0 j_1 l_H)(l_{T_1})$
$\Delta\phi(j_0 j_1 l_H)(E_T^{\text{miss}})$	$p_T(j_0 j_1 l_H l_{T_0} l_{T_1} b_0 b_1 E_T^{\text{miss}})$	$M(j_0 j_1 b_0)$
$M(j_0 j_1 b_1)$	$\Delta R(l_{T_0})(b_0)$	$\Delta R(l_{T_0})(b_1)$
$\Delta R(l_{T_1})(b_0)$	$\Delta R(l_{T_1})(b_1)$	$\Delta R(j_0)(b_0)$
$\Delta R(j_0)(b_1)$	$\Delta R(j_1)(b_0)$	$\Delta R(j_1)(b_1)$
topScore	MET	HT jets
nJets		

Table 30: Input features used to identify the Higgs decay products in 3lS events

1329 Here j_0 and j_1 , and l_H are the jet and lepton decay candidates, respectively. The other
 1330 two leptons in the event are labeled as l_{T0} and l_{T1} . b_0 and b_1 are the two b-jets identified by
 1331 the b-jet identification algorithm. The b-jet Reco Score is the output of the Higgs reconstruction
 1332 algorithm.

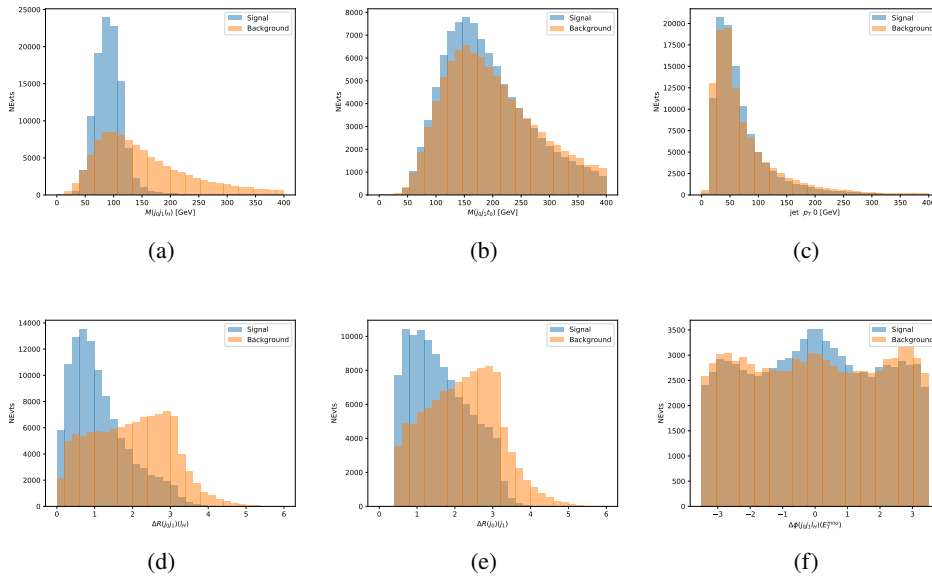


Figure 18.10: Input features for higgs3lS training. The signal in blue represents events where both jet candidates are truth b-jets from top decays, and the orange is all other combinations. Scaled to the same number of events.

1333 The modeling of these inputs is validated against data, with Figure 18.11 showing good
 1334 general agreement between data and MC. Plots for the complete list of features can found in
 1335 appendix A.1.

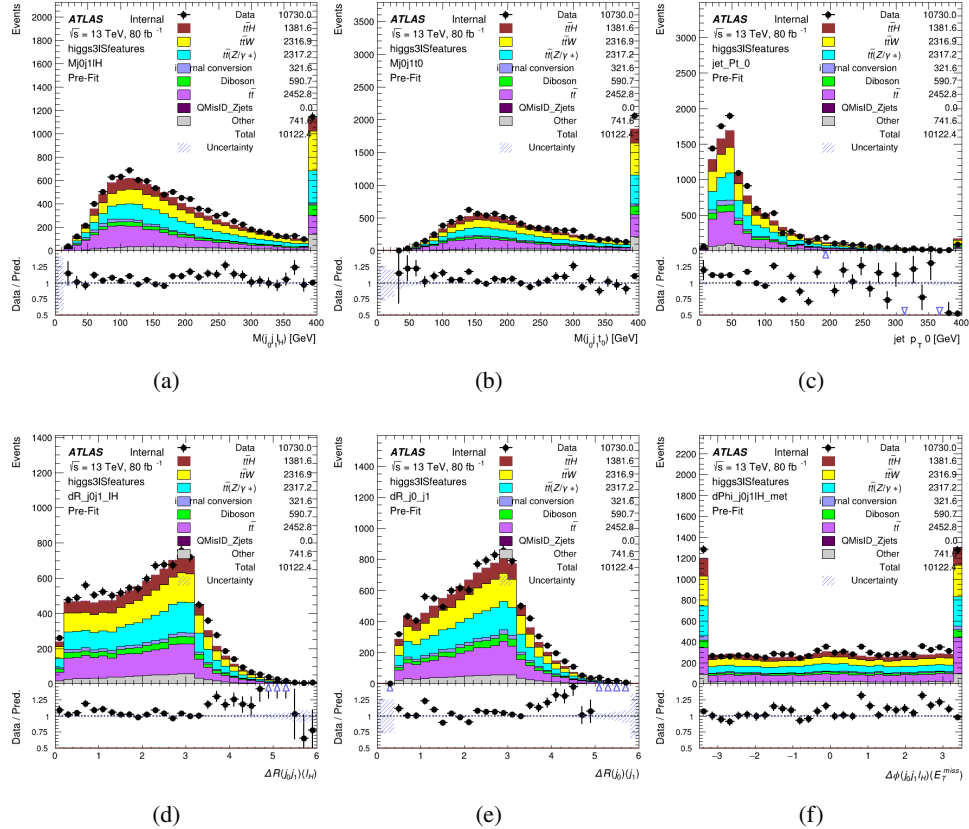


Figure 18.11: Data/MC comparisons of input features for higgs3IS training for 80 fb^{-1} of data.

1336 A neural network of 7 hidden layers with 70 nodes each is trained on 1.8 million events.

1337 Once again, incorrect combinations are downsampled, such that the correct combinations are
 1338 around 10% of the training set. 10% of the dataset is reserved for testing. The output of the NN
 1339 is summarized in Figure 18.3.2.

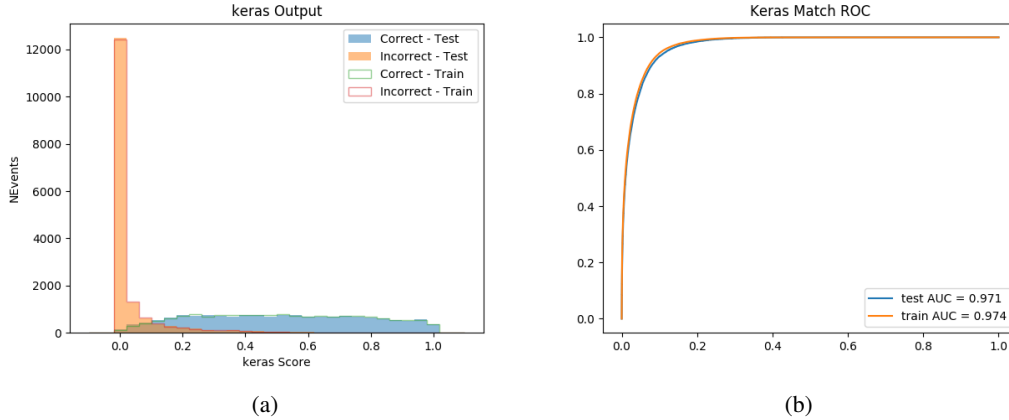


Figure 18.12: Results of the Higgs reconstruction algorithm in the 3lS channel, showing (a) the output score of the NN for correct and incorrect combinations of jets, scaled to an equal number of entries.,. (b) the ROC curve of the output, showing background rejection as a function of signal efficiency

1340 The neural network identifies the correct combination 64% of the time. It identifies the
 1341 correct lepton 85% of the time, and selects the correct lepton and at least one of the correct jets
 1342 83% of the time.

1343 **18.3.3 3l Fully-leptonic Channel**

1344 In the fully-leptonic 3l case, the goal is identify which two of the three leptons originated from
 1345 the Higgs decay. Since one of these two must be the OS lepton, this problem is reduced to
 1346 determining which of the two SS leptons originated from the Higgs. The kinematics of both
 1347 possibilities are used for training, one where the SS lepton from the Higgs is correctly labeled,
 1348 and one where it is not.

Lepton $p_T H_1$	Lepton $p_T H_0$	Lepton $p_T T$
top $p_T 0$	top $p_T 1$	$\Delta\phi(l_{H_1})(E_T^{\text{miss}})$
$\Delta\phi(l_T)(E_T^{\text{miss}})$	$M(l_{H_0}l_{H_1})$	$M(l_{H_1}l_T)$
$M(l_{H_0}l_T)$	$\Delta R(l_{H_0})(l_{H_1})$	$\Delta R(l_{H_1})(l_T)$
$\Delta R(l_{H_0})(l_T)$	$\Delta R(l_{H_0}l_{H_1})(l_T)$	$\Delta R(l_{H_0}l_T)(l_{H_1})$
$\Delta R(l_{H_0}l_{H_1})(b_0)$	$\Delta R(l_{H_0}l_{H_1})(b_1)$	$\Delta R(l_{H_0}b_0)$
$M(l_{H_0}b_0)$	$\Delta R(l_{H_0}b_1)$	$M(l_{H_0}b_1)$
$\Delta R(l_{H_1}b_0)$	$M(l_{H_1}b_0)$	$\Delta R(l_{H_1}b_1)$
$M(l_{H_1}b_1)$	E_T^{miss}	topScore

Table 31: Input features used to identify the Higgs decay products in 3lF events

1349 Here l_{H0} and l_{H1} are the Higgs decay candidates. The other lepton in the event is labeled
 1350 l_T . b_0 and b_1 are the two b-jets identified by the b-jet identification algorithm. The b-jet Reco
 1351 Score is the output of the Higgs reconstruction algorithm.

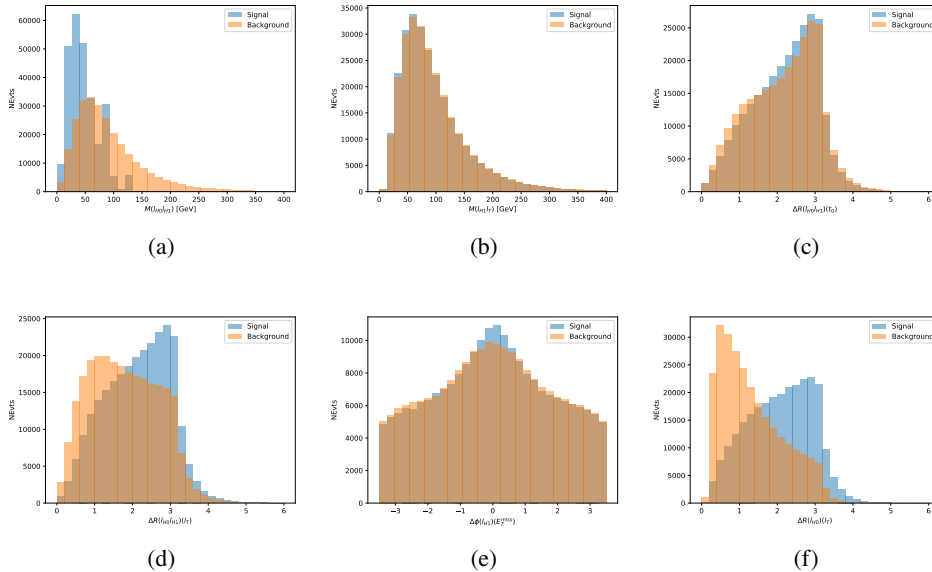


Figure 18.13: Input features for higgs3IF training. The signal in blue represents events where both jet candidates are truth b-jets from top decays, and the orange is all other combinations. Scaled to the same number of events.

1352 The modeling of these inputs is validated against data, with Figure 18.14 showing good
 1353 general agreement between data and MC. Plots for the complete list of features can found in
 1354 Section A.

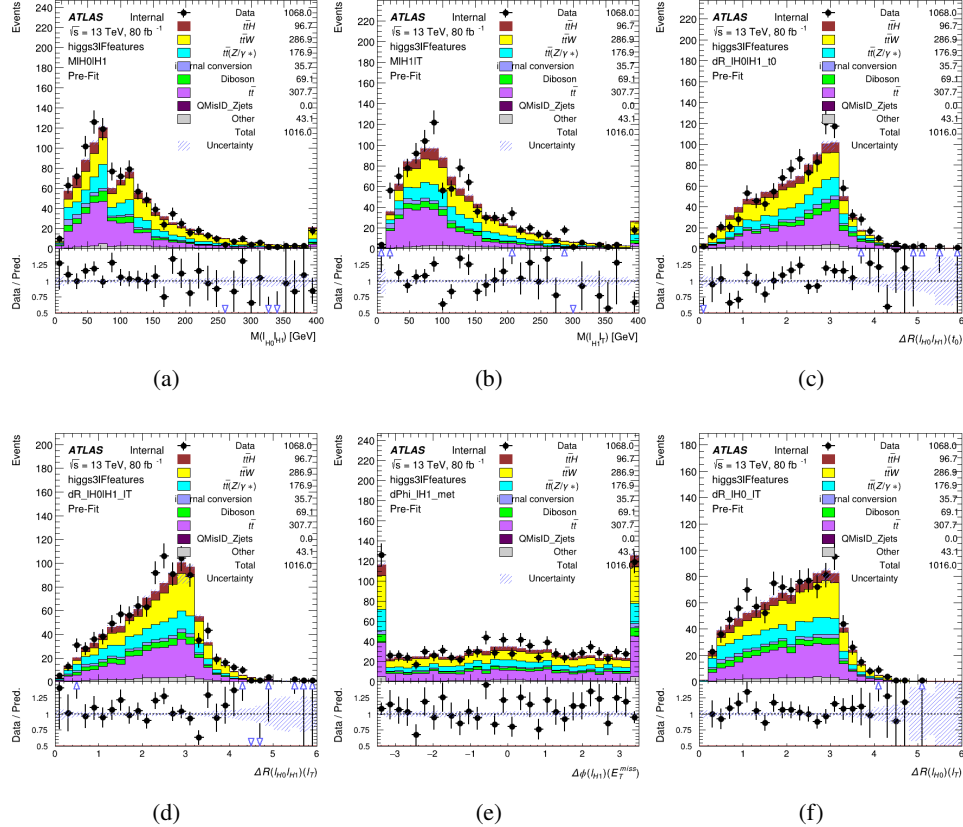


Figure 18.14: Data/MC comparisons of input features for higgs3IF training for 80 fb^{-1} of data.

1355 A neural network consisting of 5 nodes and 60 hidden units is trained on 800,000 events,
 1356 with 10% of the dataset reserved for testing. The output of the model is summarized in Figure
 1357 [18.3.3.](#)

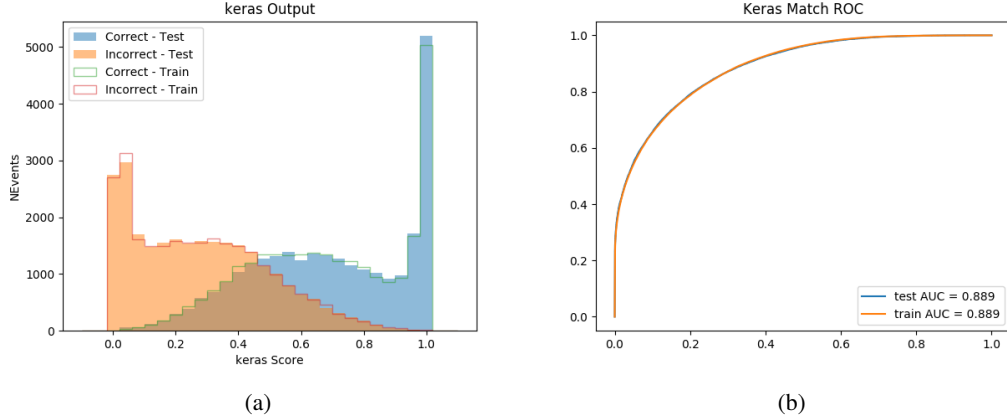


Figure 18.15: (a) the output score of the NN for correct and incorrect combinations of jets. (a) the ROC curve of the output, showing background rejection as a function of signal efficiency

1358 The correct lepton is identified by the model for 80% of events in the testing data set.

1359 18.4 p_T Prediction

1360 Once the most probable decay products have been identified, their kinematics are used as inputs
 1361 to a regression model which attempts to predict the momentum of the Higgs Boson. Once again,
 1362 a DNN is used. Input variables representing the b-jets and leptons not from the Higgs decay
 1363 are included as well, as these are found to improve performance. The truth p_T of the Higgs,
 1364 as predicted by MC, are used as labels. Separate models are built for each channel - 2lSS, 3l
 1365 Semi-leptonic and 3l Fully-leptonic.

1366 As a two-bin fit is targeted for the final result, some metrics evaluating the performance
 1367 of the models aim to show how well it distinguished between "high p_T " and "low p_T " events. A

1368 cutoff point of 150 GeV is used to define these two categories.

1369 Because the analysis uses a two bin fit of the Higgs p_T , the momentum reconstruction
1370 could be treated as a binary classification problem, rather than a regression problem. This
1371 approach is explored in detail in Section A.4, and is found not to provide any significant increase
1372 in sensitivity. The regression approach is used because it provides more flexibility for future
1373 analyses, as it is independent of the cutoff between high and low p_T , as well as the number of
1374 bins. Further, a regression allows the output of the neural network to be more clearly understood,
1375 as it can be directly compared to a physics observable.

1376 **18.4.1 2lSS Channel**

1377 The input variables listed in Table 12 are used to predict the Higgs p_T in the 2lSS channel. Here
1378 j_0 and j_1 are the two jets identified as Higgs decay products. The lepton identified as originating
1379 from the Higgs is labeled l_H , while the other lepton is labeled l_T , as it is assumed to have come
1380 from the decay of one of the top quarks. b_0 and b_1 are the two b-jets identified by the b-jet
1381 identification algorithm. The Higgs Reco Score and b-jet Reco Score are the outputs of the Higgs
1382 reconstruction algorithm, and the b-jet identification algorithm, respectively.

HT	$M(j_0 j_1)$	$M(j_0 j_1 l_H)$
$M(l_H j_0)$	$M(l_H j_1)$	$p_T(b_0 b_1)$
$p_T(j_0 j_1 l_H)$	$\Delta\phi(j_0 j_1 l_H)(E_T^{\text{miss}})$	$\Delta R(j_0)(j_1)$
$\Delta R(j_0 j_1)(l_H)$	$\Delta R(j_0 j_1 l_H)(l_T)$	$\Delta R(j_0 j_1 l_H)(b_0)$
$\Delta R(j_0 j_1 l_H)(b_1)$	$\Delta R(l_H)(j_0)$	$\Delta R(l_H)(b_0)$
$\Delta R(l_H)(b_1)$	$\Delta R(l_T)(b_0)$	$\Delta R(l_T)(b_1)$
$\Delta R(b_0)(b_1)$	Higgs Reco Score	jet η 0
jet η 1	jet Phi 0	jet Phi 1
jet p_T 0	jet p_T 1	Lepton η H
Lepton ϕ H	Lepton p_T H	Lepton p_T T
E_T^{miss}	nJets	b-jet Reco Score
b-jet p_T 0	b-jet p_T 1	

Table 32: Input features for reconstructing the Higgs p_T spectrum for 2lSS events

1383 The optimal neural network architecture for this channel is found to consist of 7 hidden
 1384 layers with 60 nodes each. The inputdata set includes 1.2 million events, 10% of which is used
 1385 for testing, the other 90% for training. Training is found to converge after around 150 epochs.

1386 To evaluate the performance of the model, the predicted p_T spectrum is compared to the
 1387 truth Higgs p_T in Figure 18.16. In order to visualize the model performance more clearly, in (a)
 1388 of that figure, the color of each point is determined by Kernal Density Estimation (KDE). The
 1389 color shown represents the logarithm of the output from KDE, to counteract the large number of
 1390 low p_T events. For that same reason, each column of the histogram shown in (b) of Figure 18.16
 1391 is normalized to unity. This plot therefore demonstrates what the model predicts for each slice
 1392 of truth p_T .

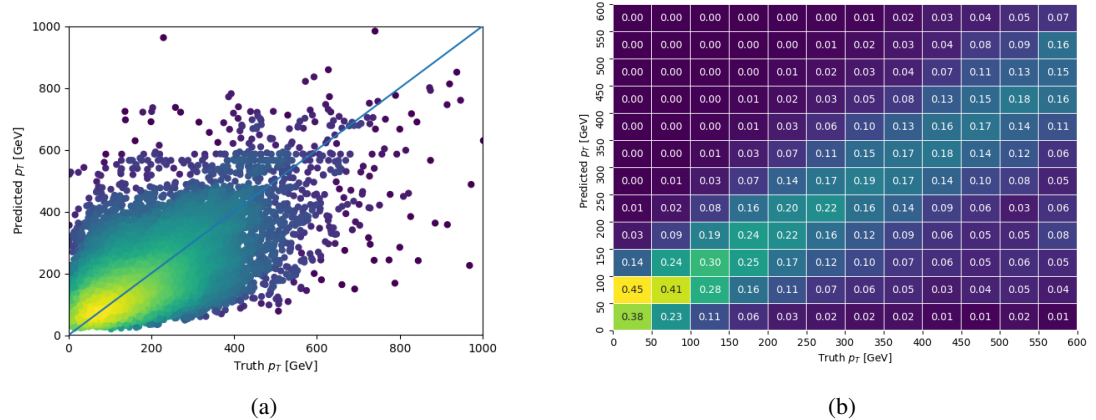


Figure 18.16: The regressed Higgs momentum spectrum as a function of the truth p_T for 2ISS $t\bar{t}H$ events in (a) a scatterplot, where the color of each point represents the log of the point density, based on Gaussian Kernel Density Estimation, and (b) a histogram where each column has been normalized to one.

1393 We are also interested in how well the model distinguishes between events with $p_T < 150$

1394 GeV and >150 GeV. Figure 18.17 demonstrates the NN output for high and low p_T events based

1395 on this cutoff.

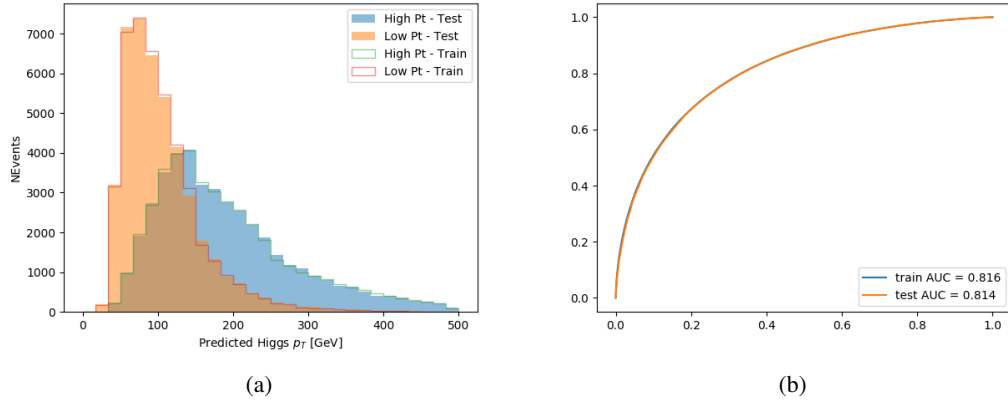


Figure 18.17: (a) shows the reconstructed Higgs p_T for 2lSS events with truth $p_T > 150$ GeV and < 150 GeV, while (b) shows the ROC curve for those two sets of events.

1396 **18.4.2 3l Semi-leptonic Channel**

1397 The following input features are used to predict the Higgs p_T for events in the 3lS channel:

HT jets	MET	$M(j_0 j_1)$
$M(j_0 j_1 l_H)$	$M(j_0 j_1 l_{T0})$	$M(j_0 j_1 l_{T1})$
$M(j_0 j_1 b_0)$	$M(j_0 j_1 b_1)$	$M(b_0 l_{T0})$
$M(b_0 l_{T1})$	$M(b_1 l_{T0})$	$M(b_1 l_{T1})$
$\Delta\phi(j_0 j_1 l_H)(E_T^{\text{miss}})$	$\Delta R(j_0)(j_1)$	$\Delta R(j_0 j_1)(l_H)$
$\Delta R(j_0 j_1)(l_{T1})$	$\Delta R(j_0 j_1)(b_0)$	$\Delta R(j_0 j_1)(b_1)$
$\Delta R(j_0 j_1 l_H)(l_{T0})$	$\Delta R(j_0 j_1 l_H)(l_{T1})$	$\Delta R(j_0 j_1 l_H)(b_0)$
$\Delta R(j_0 j_1 l_H)(b_1)$	$\Delta R(l_H)(j_0)$	$\Delta R(l_H)(j_1)$
$\Delta R(l_H)(l_{T1})$	$\Delta R(l_{T0})(l_{T1})$	$\Delta R(l_{T0})(b_0)$
$\Delta R(l_{T0})(b_1)$	$\Delta R(l_{T1})(b_0)$	$\Delta R(l_{T1})(b_1)$
higgsScore	jet η 0	jet η 1
jet ϕ 0	jet ϕ 1	jet p_T 0
jet p_T 1	Lepton η H	Lepton ϕ H
Lepton p_T H	Lepton p_T T0	Lepton p_T T1
nJets	topScore	b-jet p_T 0
b-jet p_T 1		

Table 33: Input features for reconstructing the Higgs p_T spectrum for 3lS events

Again, j_0 and j_1 are the two jets identified as Higgs decay products, ordered by p_T . The lepton identified as originating from the Higgs is labeled l_H , while the other two leptons are labeled l_{T0} and l_{T1} . b_0 and b_1 are the two b-jets identified by the b-jet identification algorithm. The Higgs Reco Score and b-jet Reco Score are the outputs of the Higgs reconstruction algorithm, and the b-jet identification algorithm, respectively.

The optimal neural network architecture for this channel is found to consist of 7 hidden layers with 80 nodes each. The inputdata set includes one million events, 10% of which is used for testing, the other 90% for training. Training is found to converge after around 150 epochs.

To evaluate the performance of the model, the predicted p_T spectrum is compared to the truth Higgs p_T in Figure 18.18. Once again, (a) of 18.18 shows a scatterplots of predicted vs truth p_T , where the color of each point corresponds to the log of the relative KDE at that point. Each column of the the histogram in (b) is normalized to unity, to better demonstrate the output of the NN for each slice of truth p_T .

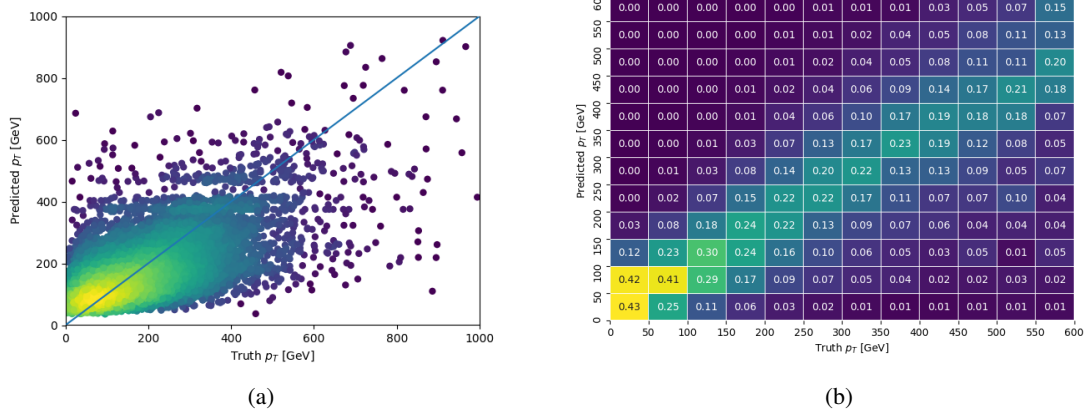


Figure 18.18: The regressed Higgs momentum spectrum as a function of the truth p_T for 3lS $t\bar{t}H$ events in (a) a scatterplot, where the color of each point represents the log of the point density, based on Gaussian Kernal Density Estimation, and (b) a histogram where each column has been normalized to one.

1411 Figure 18.19 shows (a) the output of the NN for events with truth p_T less than and greater
 1412 than 150 GeV and (b) the ROC curve demonstrating how well the NN distinguishes high and low
 1413 p_T events.

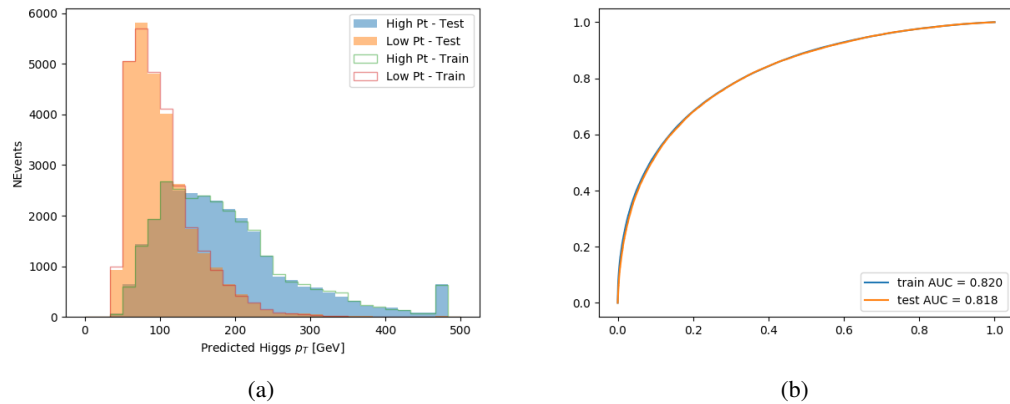


Figure 18.19: (a) shows the reconstructed Higgs p_T for 3lS events with truth $p_T > 150$ GeV and < 150 GeV, while (b) shows the ROC curve for those two sets of events.

¹⁴¹⁴ **18.4.3 3l Fully-leptonic Channel**

¹⁴¹⁵ The features listed in 14 are used to construct a model for predictin the Higgs p_T for 3lF events.

HT	$M(l_{H0}l_{H1})$	$M(l_{H0}l_T)$
$M(l_{H0}b_0)$	$M(l_{H0}b_1)$	$M(l_{H1}l_T)$
$M(l_{H1}b_0)$	$M(l_{H1}b_1)$	$\Delta R(l_{H0})(l_{H1})$
$\Delta R(l_{H0})(l_T)$	$\Delta R(l_{H0}l_{H1})(l_T)$	$\Delta R(l_{H0}l_T)(l_{H1})$
$\Delta R(l_{H1})(l_T)$	$\Delta R(l_{H0}b_0)$	$\Delta R(l_{H0}b_1)$
$\Delta R(l_{H1}b_1)$	$\Delta R(l_{H1}b_0)$	higgsScore
Lepton η H_0	Lepton η H_1	Lepton η T
Lepton p_T H_0	Lepton p_T H_1	Lepton p_T T
E_T^{miss}	topScore	b-jet p_T 0
b-jet p_T 1		

Table 34: Input features for reconstructing the Higgs p_T spectrum for 3lF events

1416 l_{H0} and l_{H1} represent the two leptons identified by the Higgs reconstruction model as
 1417 originating from the Higgs, while l_T is the other lepton in the event. The Higgs Reco Score and
 1418 b-jet Reco Score are the outputs of the Higgs reconstruction algorithm, and b-jet identification
 1419 algorithm, respectively.

1420 The optimal neural network architecture for this channel is found to consist of 5 hidden
 1421 layers with 40 nodes each. The input data set includes 400,000 events, 10% of which is used for
 1422 testing, the other 90% for training. Training is found to converge after around 150 epochs.

1423 The predicted transverse momentum, as a function of the truth p_T , is shown in Figure
 1424 [18.20](#).

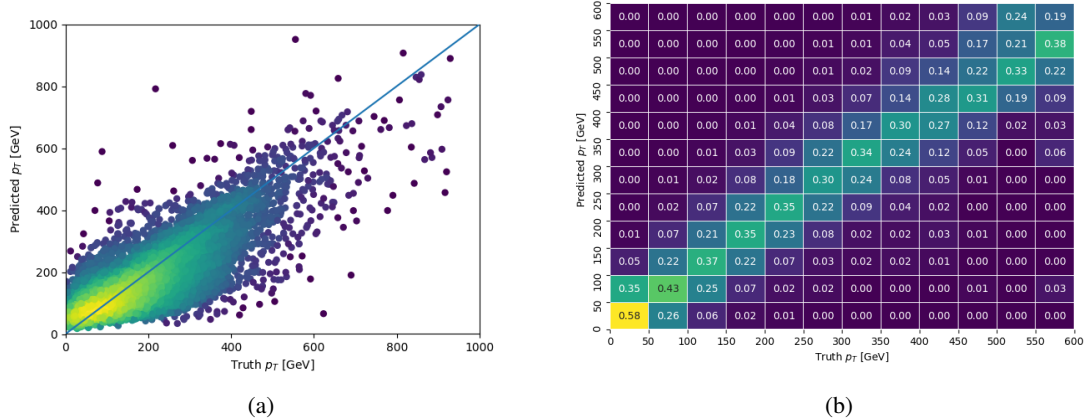


Figure 18.20: The regressed Higgs momentum spectrum as a function of the truth p_T for 3lF $t\bar{t}H$ events in (a) a scatterplot, where the color of each point represents the log of the point density, based on Gaussian Kernel Density Estimation, and (b) a histogram where each column has been normalized to one.

1425 When split into high and low p_T , based on a cutoff of 150 GeV, the

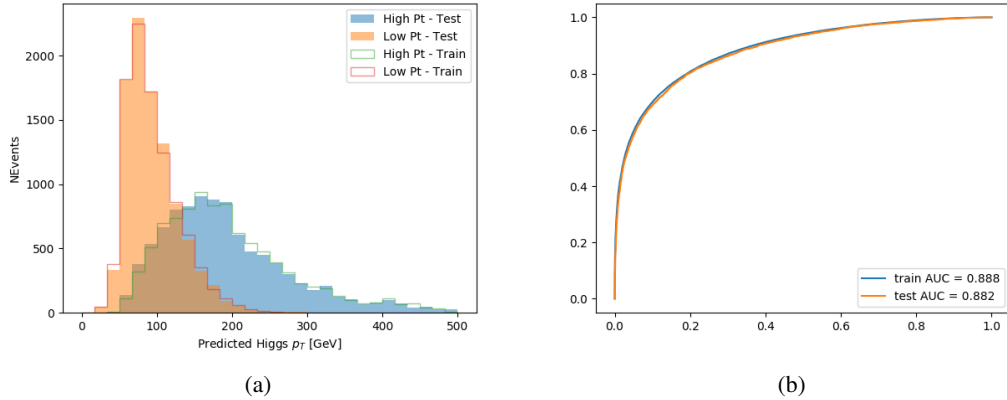


Figure 18.21: (a) shows the reconstructed Higgs p_T for 3lF events with truth $p_T > 150$ GeV and < 150 GeV, while (b) shows the ROC curve for those two sets of events.

18.5 3l Decay Mode

In the 3l channel, there are two possible ways for the Higgs to decay, both involving intermediate W boson pairs: Either both W bosons decay leptonically, in which case the reconstructed decay consists of two leptons (referred as the fully-leptonic 3l channel), or one W decays leptonically and the other hadronically, giving two jets and one lepton in the final state (referred to as the semi-leptonic 3l channel). In order to accurately reconstruct the Higgs, it is necessary to identify which of these decays took place for each 3l event.

The kinematics of each event, along with the output scores of the Higgs and top reconstruction algorithms, are used to distinguish these two possible decay modes. The particular inputs used are listed in Table 15.

HT jets	$M(l_0 t_0)$	$M(l_0 t_1)$
$M(l_1 t_0)$	$M(l_1 t_1)$	$M(l_0 l_1)$
$M(l_0 l_2)$	$M(l_1 l_2)$	$\Delta R(l_0 t_0)$
$\Delta R(l_0 t_1)$	$\Delta R(l_1 t_0)$	$\Delta R(l_1 t_1)$
$\Delta R(l l_0 1)$	$\Delta R(l l_0 2)$	$\Delta R(l l_1 2)$
Lepton η 0	Lepton η 1	Lepton η 2
Lepton ϕ 0	Lepton ϕ 1	Lepton ϕ 2
Lepton p_T 0	Lepton p_T 1	Lepton p_T 2
E_T^{miss}	nJets	nJets OR DL1r 60
nJets OR DL1r 85	score3lF	score3lS
topScore	total charge	

Table 35: Input features used to distinguish semi-leptonic and fully-leptonic Higgs decays in the 3l channel.

1436 Here l_0 is the opposite charge lepton, l_1 and l_2 are the two SS leptons order by ΔR
 1437 from lepton 0. score3lF and score3lS are the outputs of the 3lS and 3lF Higgs reconstruction
 1438 algorithms, while topScore is the output of the b-jet identification algorithm.

1439 A neural network with 5 hidden layers, each with 50 nodes, is trained to distinguish these
 1440 two decay modes. The output of the model is summarized in Figure 18.22.

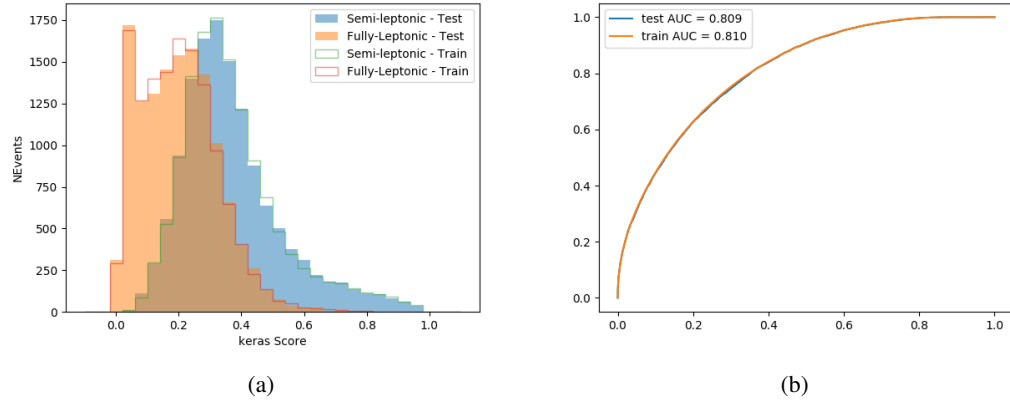


Figure 18.22: (a) shows the output of the decay separation NN for Semi-leptonic (blue) and Fully-leptonic (orange) 3l events, scaled to equal area. (b) shows the ROC curve for those two sets of events.

1441 A cutoff of 0.23 is determined to be optimal for separating 3lS and 3lF in the fit.

19 Signal Region Definitions

1443 Events are divided into two channels based on the number of leptons in the final state: one with
 1444 two same-sign leptons, the other with three leptons. The 3l channel includes events where both
 1445 leptons originated from the Higgs boson as well as events where only one of the leptons

1446 19.1 Pre-MVA Event Selection

1447 A preselection is applied to define orthogonal analysis channels based on the number of leptons

1448 in each event. For the 2lSS channel, the following preselection is used:

- 1449
- Two very tight, same-charge, light leptons with $p_T > 20 \text{ GeV}$

- 1450
- ≥ 4 reconstructed jets, ≥ 1 b-tagged jets

- 1451
- No reconstructed tau candidates

1452 The event yield after the 2lSS preselection has been applied, for MC and data at 80 fb^{-1} ,

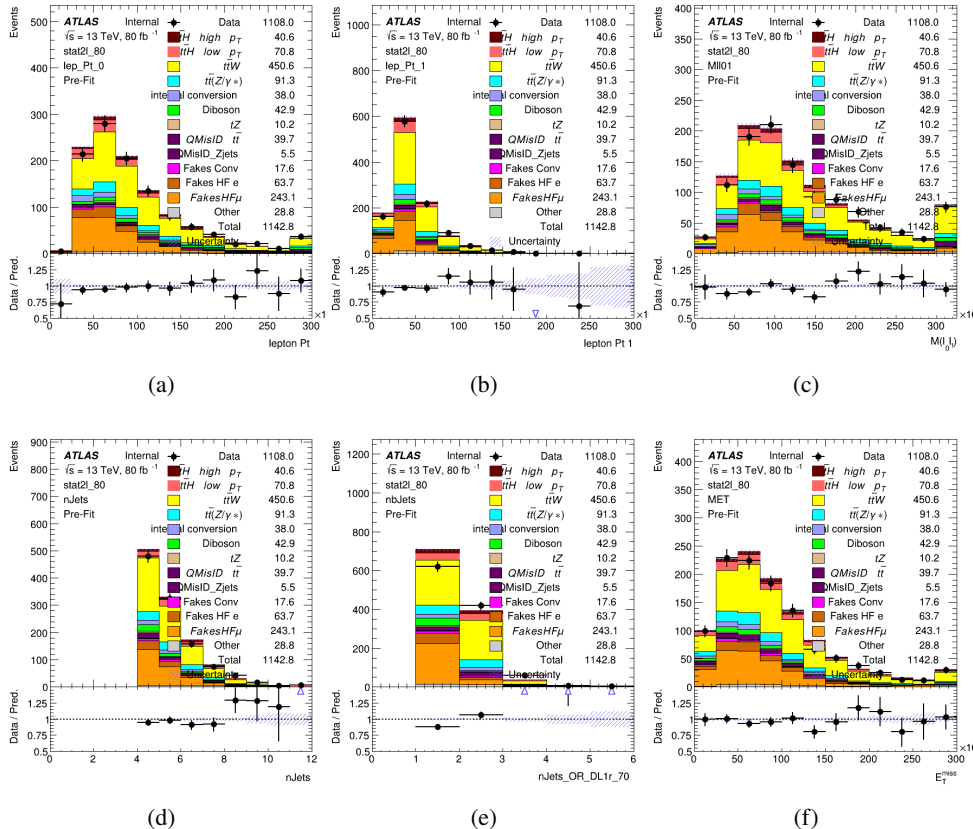
1453 is shown in Table 16.

	Yields
t̄H high p _T	36.19 ± 0.23
t̄H low p _T	63.58 ± 0.31
t̄W	440.64 ± 2.32
t̄Z/γ	91.84 ± 0.79
t̄lllowmass	8.47 ± 0.28
rareTop	24.2099 ± 0.40
VV	38.7927 ± 0.55
tZ	3e-05 ± 5.47-06
QMISID t̄	39.90 ± 2.36
QMISID Zjets	5.49 ± 0.67
t̄ int. conv.	12.74 ± 1.40
t̄ + γ int. conv.	12.09 ± 0.58
t̄ Conv.	13.55 ± 1.43
t̄ + γ Conv.	5.35 ± 0.38
t̄ HF e	59.92 ± 2.89
t̄ + γ HF e	0.51 ± 0.15
t̄ HF μ	224.57 ± 5.62
t̄ + γ HF μ	1.60 ± 0.23
Z + jets internal conv	3e-05 ± 5.47e-06
Z + jets conv	0.62 ± 0.21
Z + jets HF e	0.14 ± 0.13
Z + jets HF μ	0.82 ± 0.26
Single top Conv	2.27 ± 0.53
Single top HF e	2.33 ± 0.50
Single top HF μ	11.12 ± 1.07
Three top	2.22 ± 0.02
Four top	13.09 ± 0.16
t̄WW	10.985 ± 0.30
tW	3e-05 ± 5.47-06
WtZ	9.07 ± 0.44
VVV	0.30 ± 0.04
VH	0.59 ± 1.55
Total	1133.11 ± 7.69
Data	1108

Table 36: Event yield in the 2ISS preselection region.

1454

Figure 20.1. Good general agreement is found.

Figure 19.1: Data/MC comparisons of the 2lSS pre-selection region. (a) and (b) show the p_T of leptons 0 and 1, (c) shows the invariant mass of lepton 0 and 1, (d) shows the jet multiplicity, (e) the b-tagged jet multiplicity, and (f) the missing transverse energy.

1455

For the 3l channel, the following selection is applied:

1456

- Three light leptons with total charge ± 1
- Same charge leptons are required to be very tight, with $p_T > 20 \text{ GeV}$
- Opposite charge lepton must be loose, with $p_T > 10 \text{ GeV}$

1457

1459 • ≥ 2 reconstructed jets, ≥ 1 b-tagged jets

1460 • No reconstructed tau candidates

1461 • $|M(l^+l^-) - 91.2 \text{ GeV}| > 10 \text{ GeV}$ for all opposite-charge, same-flavor lepton pairs

1462 The event yield after the 3l preselection has been applied, for MC and data at 80 fb^{-1} , is

1463 shown in Table 6.1.

	Yields
t̄H high p _T	18.40 ± 0.13
t̄H low p _T	29.91 ± 0.16
t̄W	134.22 ± 1.25
t̄Z/γ	88.47 ± 0.73
t̄lllowmass	2.77 ± 0.16
rareTop	15.05 ± 0.32
VV	34.54 ± 0.54
tZ	2e-05 ± 4.47-06
QMisID t̄t	1.80 ± 0.59
QMisID Zjets	0.02 ± 0.02
t̄t internal conversion	4.34 ± 0.43
t̄t + γ internal conversion	5.83 ± 0.42
t̄t Conv.	4.71 ± 0.45
t̄t + γ Conv.	2.64 ± 0.27
t̄t HF e	27.44 ± 1.05
t̄t + γ HF e	0.27 ± 0.11
t̄t HF μ	89.21 ± 1.92
t̄t + γ HF μ	0.94 ± 0.16
Z + jets conv	0.09 ± 0.19
Z + jets HF e	0.25 ± 0.15
Z + jets HF μ	2.41 ± 0.95
Single top Conv	0.58 ± 0.61
Single top HF e	1.50 ± 0.43
Single top HF μ	4.62 ± 0.85
Three top	0.96 ± 0.02
Four top	5.58 ± 0.10
t̄WW	5.45 ± 0.21
WtZ	8.71 ± 0.42
VVV	0.81 ± 0.02
Total	492.14 ± 3.22
Data	535

Table 37: Yields of the analysis

1464

Comparisons of kinematic distributions for data and MC in this region are shown in Figure

1465 20.2.

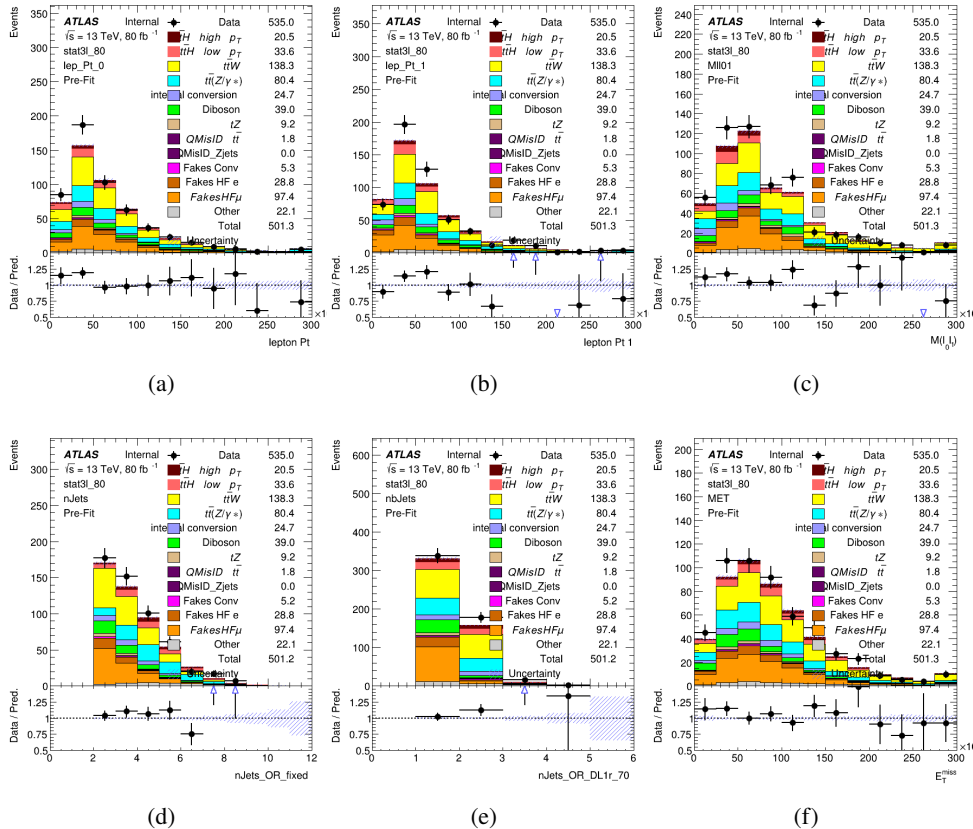


Figure 19.2: Data/MC comparisons of the 3l pre-selection region. (a) and (b) show the p_T of leptons 0 and 1, (c) shows the invariant mass of lepton 0 and 1, (d) shows the jet multiplicity, (e) the b-tagged jet multiplicity, and (f) the missing transverse energy.

1466

19.2 Event MVA

1467

Separate multi-variate analysis techniques (MVAs) are used in order to distinguish signal events

1468

from background for each analysis channel - 2lSS, 3l semi-leptonic (3lS), and 3l fully leptonic

1469

(3lF). In particular, Boosted Decision Tree (BDT) algorithms are produced with XGBoost

1470 [xgboost] are trained using the kinematics of signal and background events derived from Monte
1471 Carlo simulations. Events are weighted in the BDT training by the weight of each Monte Carlo
1472 event.

1473 Because the background composition differs for events with a high reconstructed Higgs p_T
1474 compared to events with low reconstructed Higgs p_T , separate MVAs are produced for high and
1475 low p_T regions. This is found to provide better significance than attempting to build an inclusive
1476 model, as demonstrated in appendix A.2. A cutoff of 150 GeV is used. This gives a total of 6
1477 background rejection MVAs - explicitly, 2lSS high p_T , 2lSS low p_T , 3lS high p_T , 3lS low p_T ,
1478 3lF high p_T , and 3lF low p_T .

1479 The following features are used in both the high and low p_T 2lSS BDTs:

HT	$M(\text{lep}, E_T^{\text{miss}})$	$M(l_0 l_1)$
binHiggs p_T 2ISS	$\Delta R(l_0)(l_1)$	diLepton type
higgsRecoScore	jet η 0	jet η 1
jet ϕ 0	jet ϕ 1	jet p_T 0
jet p_T 1	Lepton η 0	Lepton η 1
Lepton ϕ 0	Lepton ϕ 1	Lepton p_T 0
Lepton p_T 1	E_T^{miss}	$\min \Delta R(l_0)(\text{jet})$
$\min \Delta R(l_1)(\text{jet})$	$\min \Delta R(\text{Lepton})(\text{bjet})$	mjjMax frwdJet
nJets	nJets OR DL1r 60	nJets OR DL1r 70
nJets OR DL1r 85	topRecoScore	

Table 38: Input features used to distinguish signal and background events in the 2ISS channel.

1480

While for each of the 31 BDTs, the features listed below are used for training:

$M(\text{lep}, E_T^{\text{miss}})$	$M(l_0 l_1)$	$M(l_0 l_1 l_2)$
$M(l_0 l_2)$	$M(l_1 l_2)$	$\text{binHiggs } p_T \text{ 3lF}$
$\text{binHiggs } p_T \text{ 3lS}$	$\Delta R(l_0)(l_1)$	$\Delta R(l_0)(l_2)$
$\Delta R(l_1)(l_2)$	decayScore	higgsRecoScore3lF
higgsRecoScore3lS	$\text{jet } \eta \text{ 0}$	$\text{jet } \eta \text{ 1}$
$\text{jet } \phi \text{ 0}$	$\text{jet } \phi \text{ 1}$	$\text{jet } p_T \text{ 0}$
$\text{jet } p_T \text{ 1}$	$\text{Lepton } \eta \text{ 0}$	$\text{Lepton } \eta \text{ 1}$
$\text{Lepton } \eta \text{ 2}$	$\text{Lepton } \phi \text{ 0}$	$\text{Lepton } \phi \text{ 1}$
$\text{Lepton } \phi \text{ 2}$	$\text{Lepton } p_T \text{ 0}$	$\text{Lepton } p_T \text{ 1}$
$\text{Lepton } p_T \text{ 2}$	E_T^{miss}	$\min \Delta R(l_0)(\text{jet})$
$\min \Delta R(l_1)(\text{jet})$	$\min \Delta R(l_2)(\text{jet})$	$\min \Delta R(\text{Lepton})(\text{bjet})$
$mjj\text{Max frwdJet}$	$n\text{Jets}$	$n\text{Jets OR DL1r 60}$
$n\text{Jets OR DL1r 70}$	$n\text{Jets OR DL1r 85}$	topScore

Table 39: Input features used to distinguish signal and background events in the 3l channel.

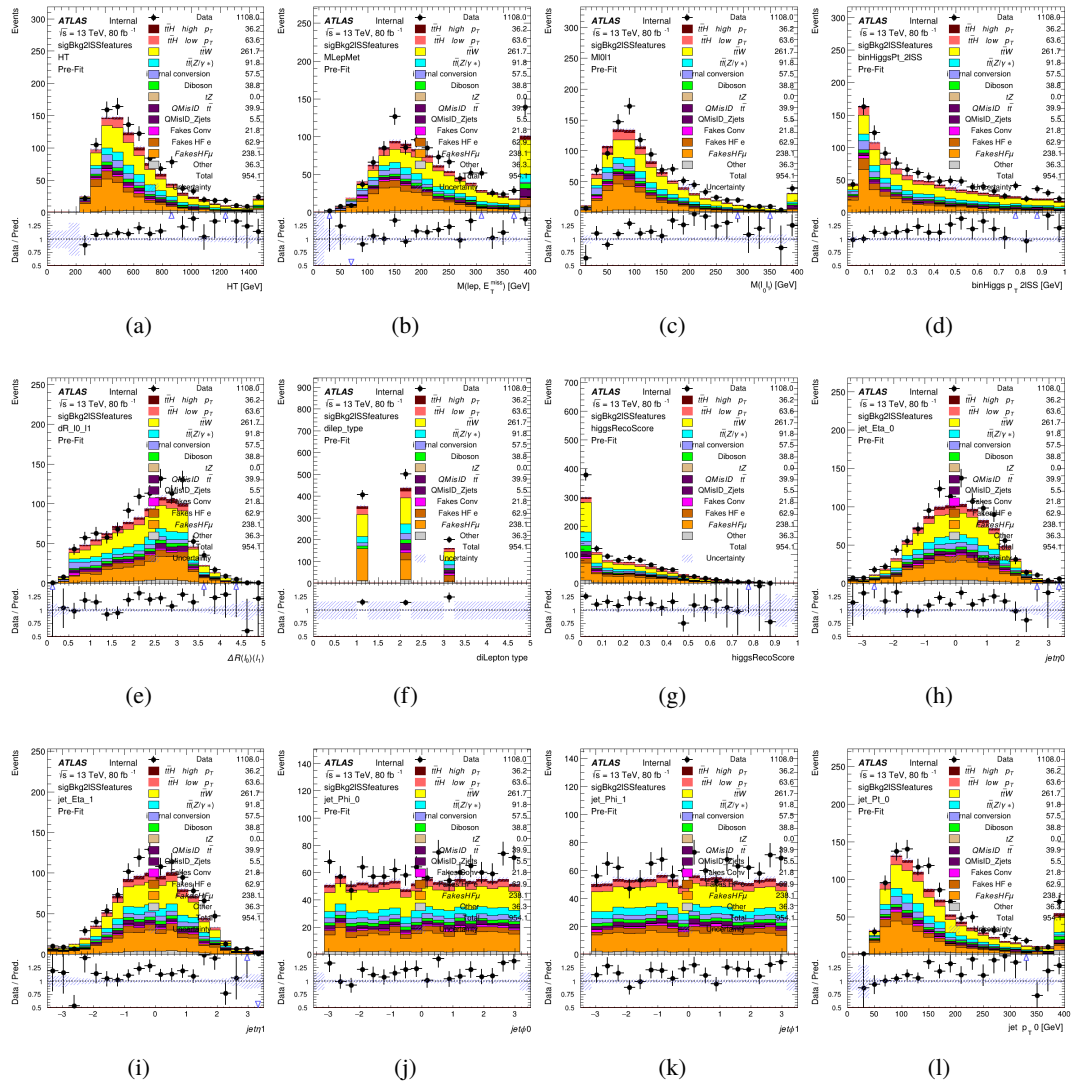


Figure 19.3:

1481

The BDTs are produced with a maximum tree depth of 6, using AUC as the target loss

1482

function.

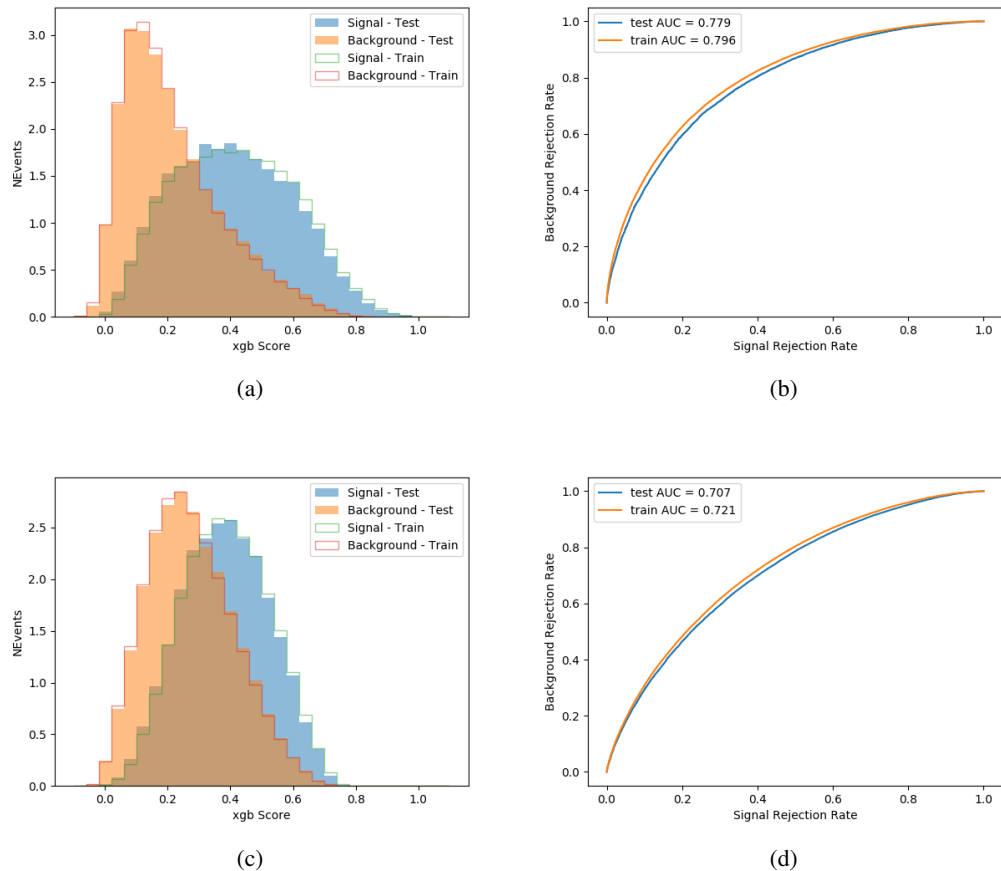


Figure 19.4:

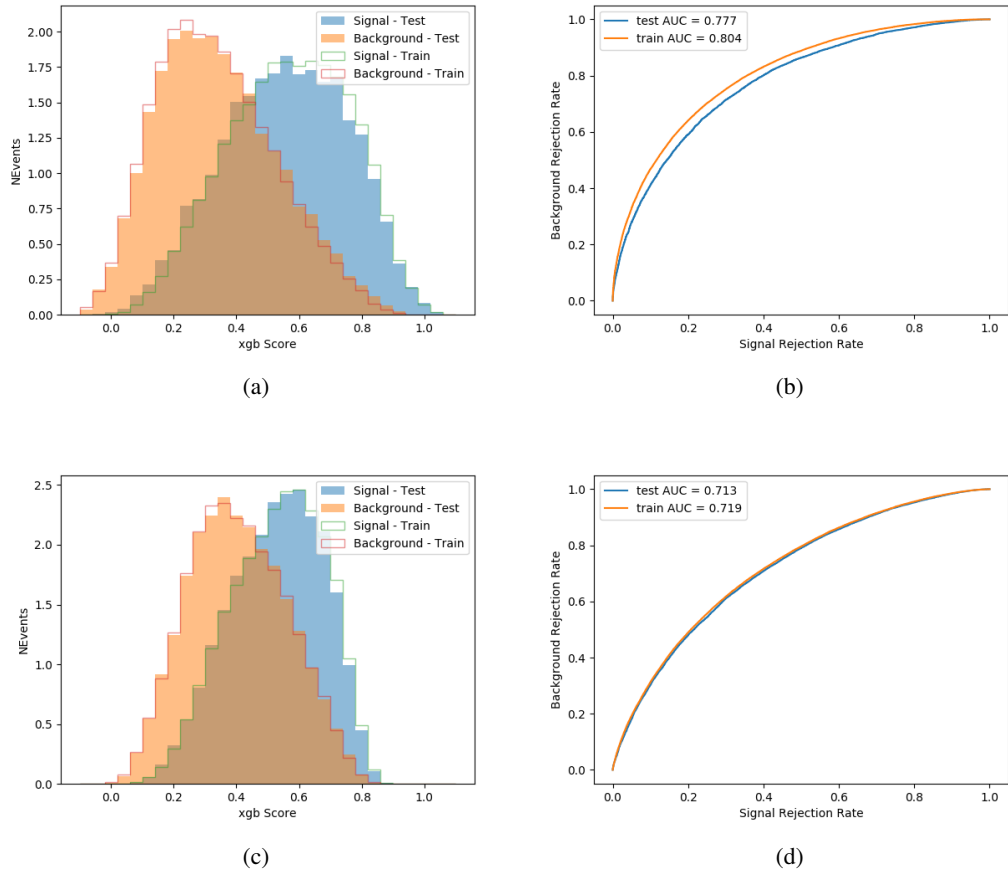


Figure 19.5:

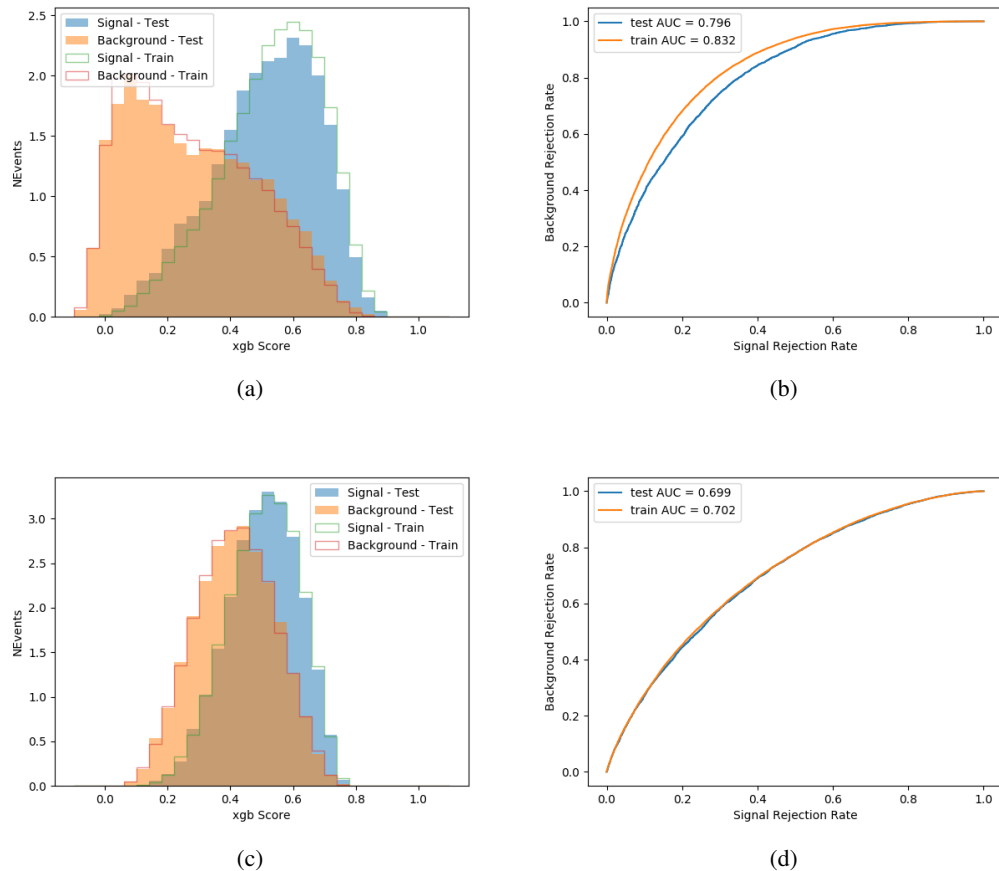


Figure 19.6:

1483 Output distributions of each MVA comparing MC prediction to data at 80 fb^{-1} are shown
 1484 in figures 19.7-19.2.

1485 19.3 Signal Region Definitions

1486 Once pre-selection has been applied, channels are further refined based on the MVAs described
 1487 above. The output of the model described in Section 18.5 is used to separate the three channel

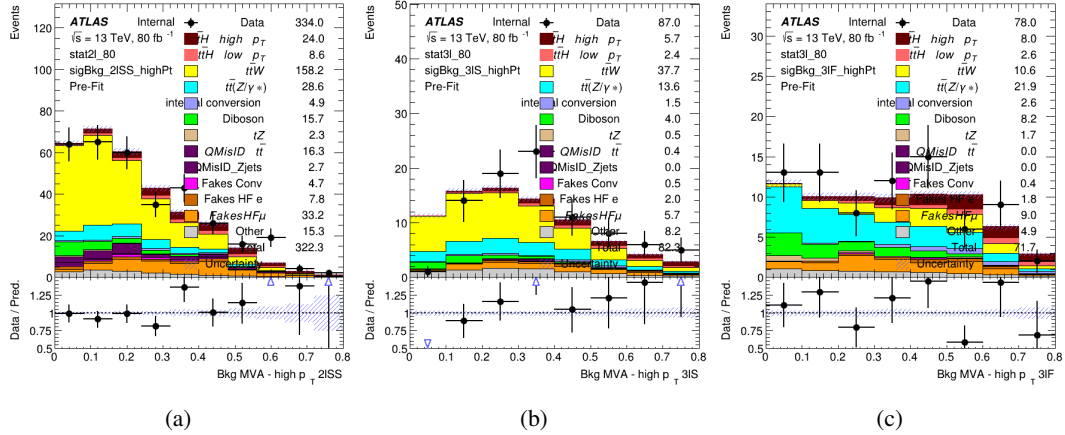


Figure 19.7: Output score of the high p_T BDTs in the (a) 2ISS, (b) 3IS, and (c) 3IF channels

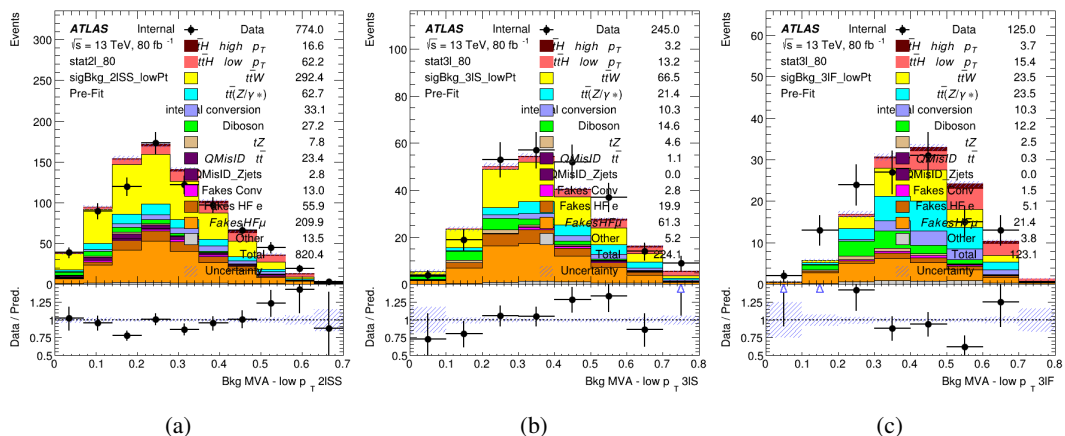


Figure 19.8: Output score of the low p_T BDTs in the (a) 2ISS, (b) 3IS, and (c) 3IF channels

1488 into two - Semi-leptonic and Fully-leptonic - based on the predicted decay mode of the Higgs
 1489 boson. This leaves three orthogonal signal regions - 2lSS, 3lS, and 3lF.

1490 For each event, depending on the number of leptons as well as whether the p_T of the Higgs
 1491 is predicted to be high (> 150 GeV) or low (< 150 GeV), a cut on the appropriate background
 1492 rejection MVA is applied. The particular cut values, listed in Table 42, are determined by
 1493 maximizing S/\sqrt{B} in each region.

Channel	BDT Score
2lSS high p_T	0.36
2lSS low p_T	0.34
3lS high p_T	0.51
3lS low p_T	0.43
3lF high p_T	0.33
3lF low p_T	0.41

Table 40: Cutoff values on background rejection MVA score applied to signal regions.

1494 The event preselection and MVA selection define the three signal regions. These signal
 1495 region definitions are summarized in Table 43.

Region	Selection
2ISS	Two same charge tight leptons with $p_T > 20 \text{ GeV}$ $N_{\text{jets}} \geq 4, N_{\text{b-jets}} \geq 1$ b-tagged jets Zero τ_{had} $H_{p_T}^{\text{pred}} > 150 \text{ GeV}$ and BDT score > 0.36 or $H_{p_T}^{\text{pred}} < 150 \text{ GeV}$ and BDT score > 0.34
3IS	Three light leptons with total charge ± 1 Two tight SS leptons, $p_T > 20 \text{ GeV}$ One loose OS lepton, $p_T > 10 \text{ GeV}$ $N_{\text{jets}} \geq 2, N_{\text{b-jets}} \geq 1$ b-tagged jets Zero τ_{had} $ M(l^+l^-) - 91.2 \text{ GeV} > 10 \text{ GeV}$ for all OSSF lepton pairs Decay NN Score < 0.23 $H_{p_T}^{\text{pred}} > 150 \text{ GeV}$ and BDT score > 0.51 or $H_{p_T}^{\text{pred}} > 150 \text{ GeV}$ and BDT score > 0.43
3IF	Three light leptons with total charge ± 1 Two tight SS leptons, $p_T > 20 \text{ GeV}$ One loose OS lepton, $p_T > 10 \text{ GeV}$ $N_{\text{jets}} \geq 2, N_{\text{b-jets}} \geq 1$ b-tagged jets Zero τ_{had} $ M(l^+l^-) - 91.2 \text{ GeV} > 10 \text{ GeV}$ for all OSSF lepton pairs Decay NN Score > 0.23 $H_{p_T}^{\text{pred}} > 150 \text{ GeV}$ and BDT score > 0.33 or $H_{p_T}^{\text{pred}} > 150 \text{ GeV}$ and BDT score > 0.41

Table 41: Selection applied to define the three signal regions used in the fit.

20 Background Rejection MVA

1496 Events are divided into two channels based on the number of leptons in the final state: one with
 1497 two same-sign leptons, the other with three leptons. The 3l channel includes events where both
 1498 leptons originated from the Higgs boson as well as events where only one of the leptons

1500 20.1 Pre-MVA Event Selection

1501 A preselection is applied to define orthogonal analysis channels based on the number of leptons
 1502 in each event. For the 2lSS channel, the following preselection is used:

- 1503 • Two very tight, same-charge, light leptons with $p_T > 20$ GeV

- 1504 • ≥ 4 reconstructed jets, ≥ 1 b-tagged jets

- 1505 • No reconstructed tau candidates

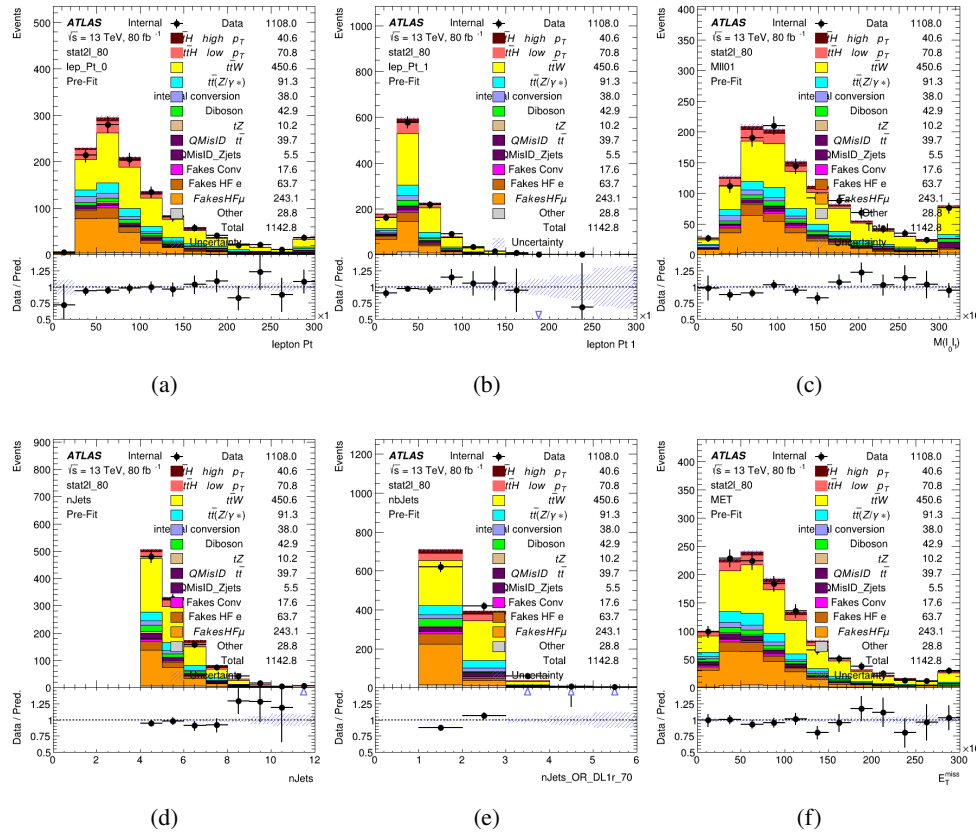


Figure 20.1:

1506 For the 31 channel, the following selection is applied:

- 1507 • Three light leptons with total charge ± 1
- 1508 • Same charge leptons are required to be very tight, with $p_T > 20 \text{ GeV}$
- 1509 • Opposite charge lepton must be loose, with $p_T > 10 \text{ GeV}$
- 1510 • $>= 2$ reconstructed jets, $>= 1$ b-tagged jets
- 1511 • No reconstructed tau candidates
- 1512 • $|M(l^+l^-) - 91.2 \text{ GeV}| > 10 \text{ GeV}$ for all opposite-charge, same-flavor lepton pairs

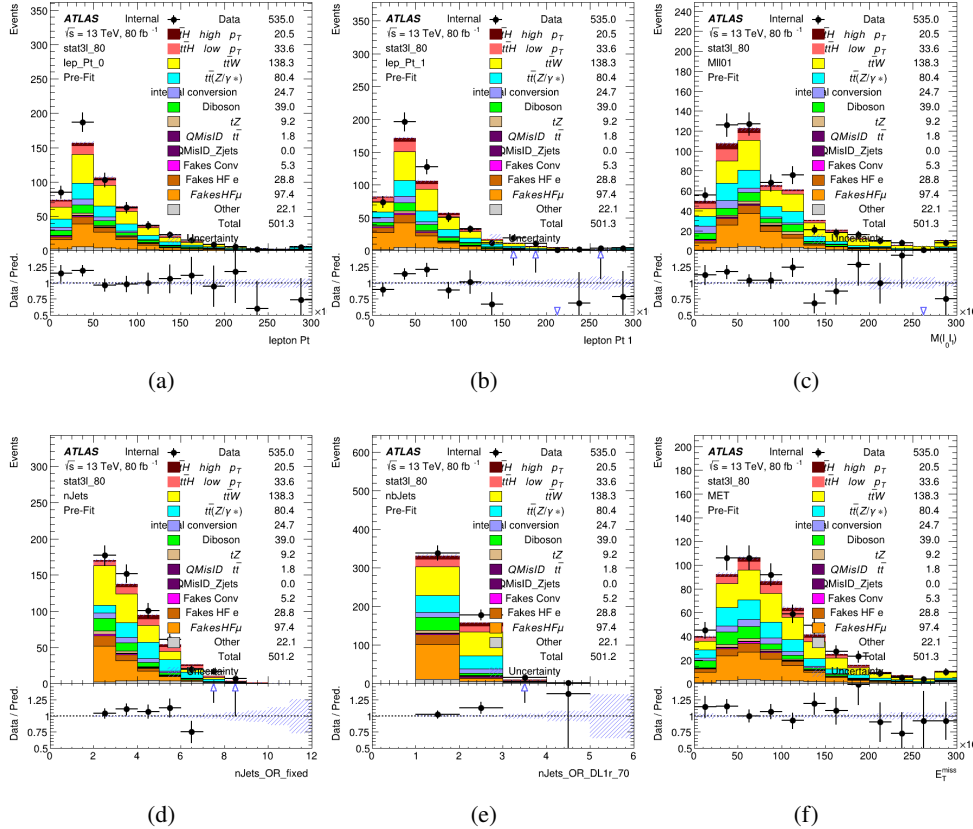


Figure 20.2:

1513 20.2 Event MVA

1514 Separate multi-variate analysis techniques (MVAs) are used in order to distinguish signal events
 1515 from background for each analysis channel - 2lSS, 3l semi-leptonic (3lS), and 3l fully leptonic
 1516 (3lF). In particular, Boosted Decision Tree (BDT) algorithms are produced with XGBoost
 1517 [[xgboost](#)] are trained using the kinematics of signal and background events derived from Monte
 1518 Carlo simulations. Events are weighted in the BDT training by the weight of each Monte Carlo

1519 event.

1520 Because the background composition differs for events with a high reconstructed Higgs p_T
1521 compared to events with low reconstructed Higgs p_T , separate MVAs are produced for high and
1522 low p_T regions. This is found to provide better significance than attempting to build an inclusive
1523 model, as demonstrated in appendix A.2. A cutoff of 150 GeV is used. This gives a total of 6
1524 background rejection MVAs - explicitly, 2lSS high p_T , 2lSS low p_T , 3lS high p_T , 3lS low p_T ,
1525 3lF high p_T , and 3lF low p_T .

1526 The following features are used in both the high and low p_T 2lSS BDTs:

HT	$M(\text{lep}, E_T^{\text{miss}})$	$M(l_0 l_1)$
binHiggs p_T 2ISS	$\Delta R(l_0)(l_1)$	diLepton type
higgsRecoScore	jet η 0	jet η 1
jet ϕ 0	jet ϕ 1	jet p_T 0
jet p_T 1	Lepton η 0	Lepton η 1
Lepton ϕ 0	Lepton ϕ 1	Lepton p_T 0
Lepton p_T 1	E_T^{miss}	$\min \Delta R(l_0)(\text{jet})$
$\min \Delta R(l_1)(\text{jet})$	$\min \Delta R(\text{Lepton})(\text{bjet})$	mjjMax frwdJet
nJets	nJets OR DL1r 60	nJets OR DL1r 70
nJets OR DL1r 85	topRecoScore	

Table 42: Input features used to distinguish signal and background events in the 2ISS channel.

1527

While for each of the 31 BDTs, the features listed below are used for training:

$M(\text{lep}, E_T^{\text{miss}})$	$M(l_0 l_1)$	$M(l_0 l_1 l_2)$
$M(l_0 l_2)$	$M(l_1 l_2)$	$\text{binHiggs } p_T \text{ 3lF}$
$\text{binHiggs } p_T \text{ 3lS}$	$\Delta R(l_0)(l_1)$	$\Delta R(l_0)(l_2)$
$\Delta R(l_1)(l_2)$	decayScore	higgsRecoScore3lF
higgsRecoScore3lS	$\text{jet } \eta \text{ 0}$	$\text{jet } \eta \text{ 1}$
$\text{jet } \phi \text{ 0}$	$\text{jet } \phi \text{ 1}$	$\text{jet } p_T \text{ 0}$
$\text{jet } p_T \text{ 1}$	$\text{Lepton } \eta \text{ 0}$	$\text{Lepton } \eta \text{ 1}$
$\text{Lepton } \eta \text{ 2}$	$\text{Lepton } \phi \text{ 0}$	$\text{Lepton } \phi \text{ 1}$
$\text{Lepton } \phi \text{ 2}$	$\text{Lepton } p_T \text{ 0}$	$\text{Lepton } p_T \text{ 1}$
$\text{Lepton } p_T \text{ 2}$	E_T^{miss}	$\min \Delta R(l_0)(\text{jet})$
$\min \Delta R(l_1)(\text{jet})$	$\min \Delta R(l_2)(\text{jet})$	$\min \Delta R(\text{Lepton})(\text{bjet})$
$mjj\text{Max frwdJet}$	$n\text{Jets}$	$n\text{Jets OR DL1r 60}$
$n\text{Jets OR DL1r 70}$	$n\text{Jets OR DL1r 85}$	topScore

Table 43: Input features used to distinguish signal and background events in the 3l channel.

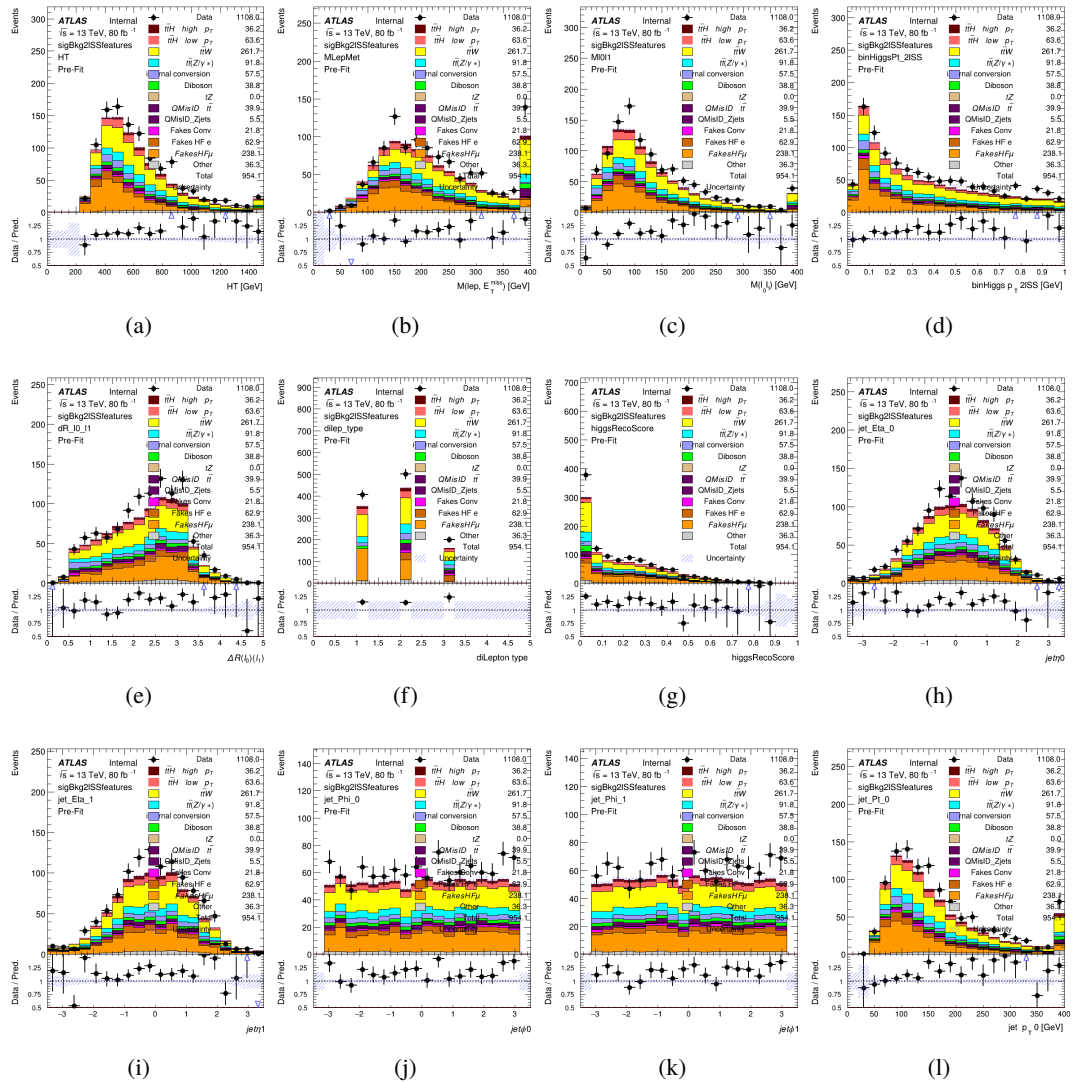


Figure 20.3:

1528

The BDTs are produced with a maximum tree depth of 6, using AUC as the target loss

1529 function.

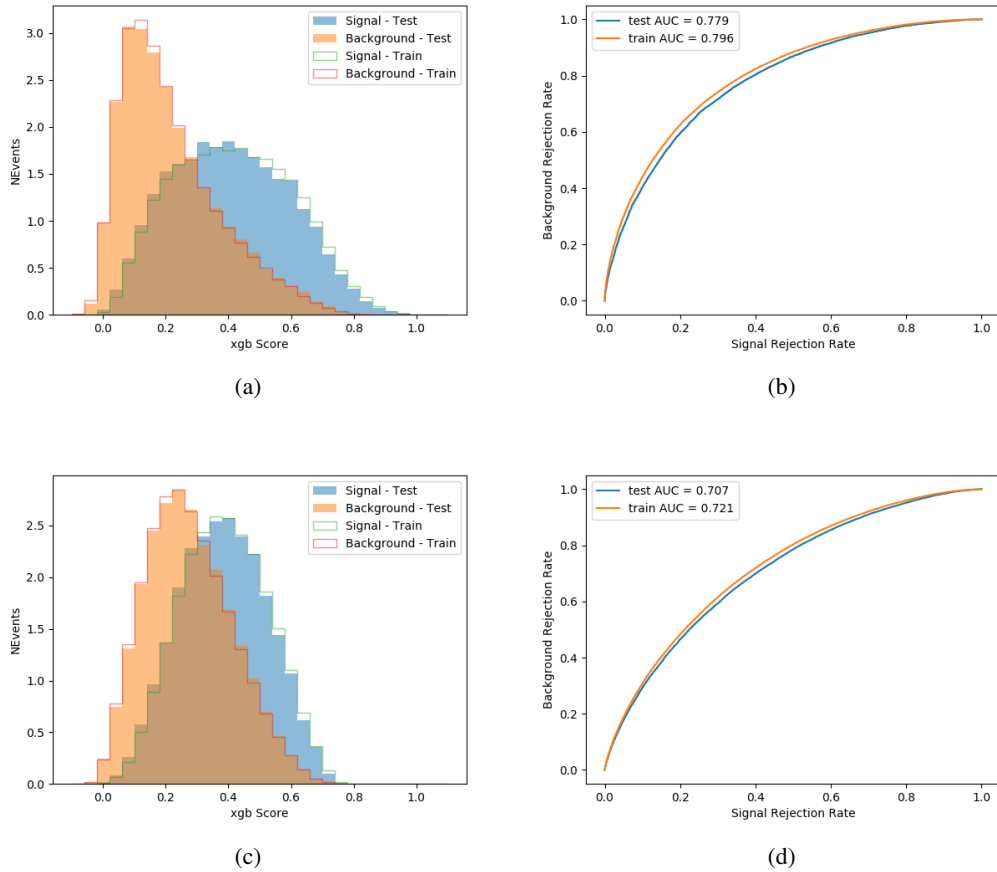


Figure 20.4:

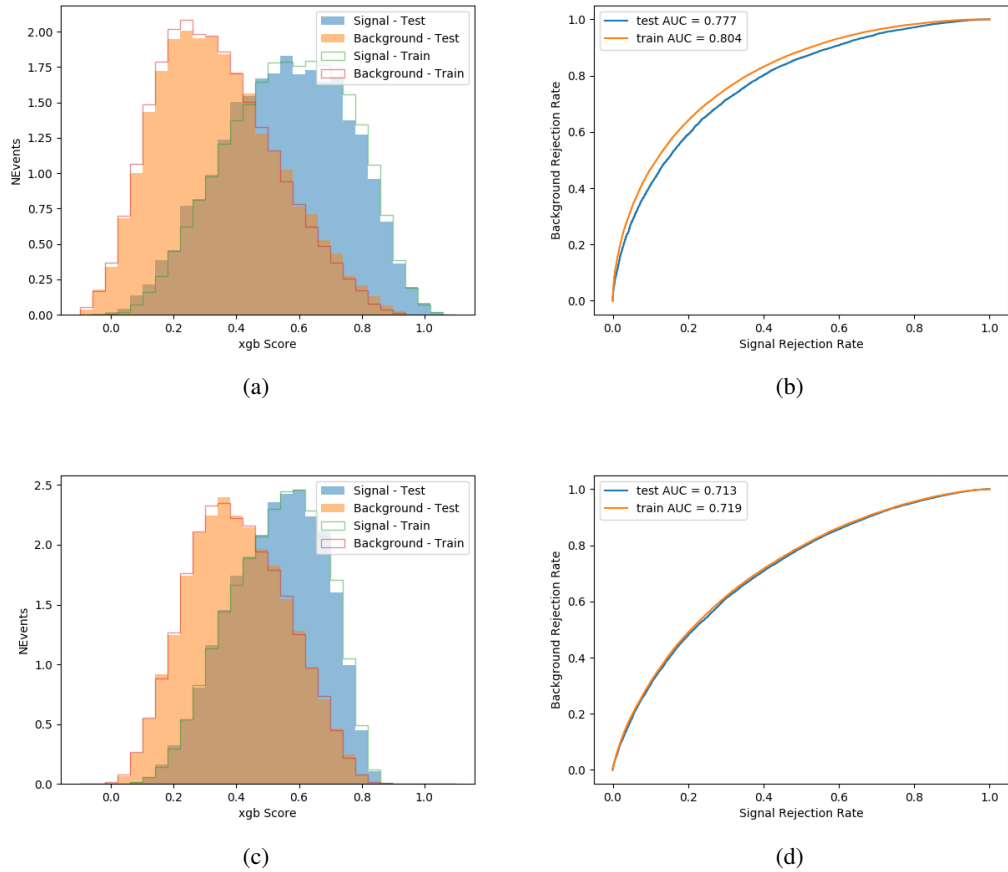


Figure 20.5:

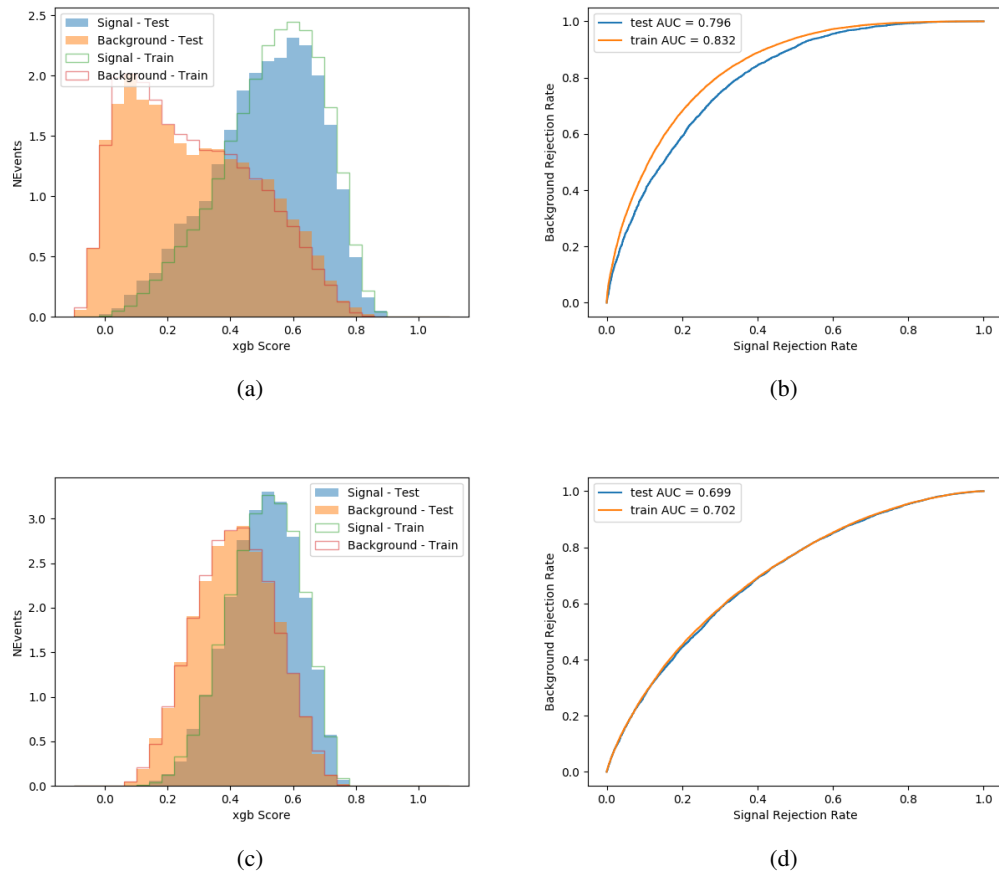


Figure 20.6:

1530

Output distributions of each MVA comparing MC prediction to data at 80 fb^{-1} are shown

1531

in Figure 20.2.

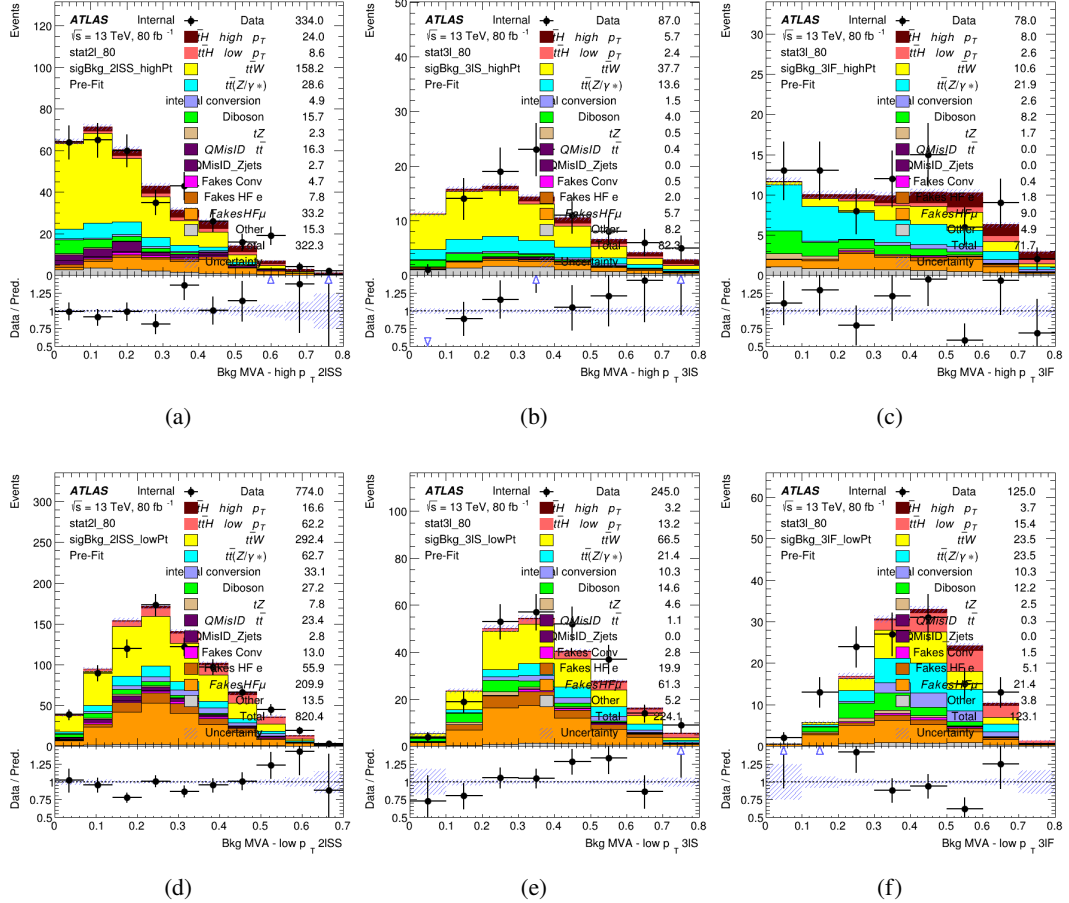


Figure 20.7: scores

1532 20.3 Signal Region Definitions

1533 Once pre-selection has been applied, channels are further refined based on the MVAs described
 1534 above. The output of the model described in Section 18.5 is used to separate the three channel
 1535 into two - Semi-leptonic and Fully-leptonic - based on the predicted decay mode of the Higgs
 1536 boson.

1537 For each event, depending on the channel as well as the predicted p_T of the Higgs derived
1538 from the algorithm described in Section 18.4, a cut on the appropriate background rejection
1539 algorithm is applied. The specific selection used, and the event yield in each channel after this
1540 selection has been applied, is summarized below.

1541 **20.3.1 2lSS**

1542 **20.3.2 3l – Semi – leptonic**

1543 **20.3.3 3l – Fully – leptonic**

1544 **21 Systematic Uncertainties**

1545 The systematic uncertainties that are considered are summarized in Table 46. These are imple-
1546 mented in the fit either as a normalization factors or as a shape variation or both in the signal
1547 and background estimations. The numerical impact of each of these uncertainties is outlined in
1548 section 22.

Table 44: Sources of systematic uncertainty considered in the analysis. Some of the systematic uncertainties are split into several components, as indicated by the number in the rightmost column.

Systematic uncertainty	Components
Luminosity	1
Pileup reweighting	1
Physics Objects	
Electron	6
Muon	15
Jet energy scale and resolution	28
Jet vertex fraction	1
Jet flavor tagging	131
E_T^{miss}	3
Total (Experimental)	186
Background Modeling	
Cross section	24
Renormalization and factorization scales	10
Parton shower and hadronization model	2
Shower tune	4
Total (Signal and background modeling)	40
Background Modeling	
Cross section	24
Renormalization and factorization scales	10
Parton shower and hadronization model	2
Shower tune	4
Total (Signal and background modeling)	40
Total (Overall)	226

¹⁵⁴⁹ The uncertainty in the combined 2015+2016 integrated luminosity is derived from a
¹⁵⁵⁰ calibration of the luminosity scale using x-y beam-separation scans performed in August 2015
¹⁵⁵¹ and May 2016 [29].

¹⁵⁵² The experimental uncertainties are related to the reconstruction and identification of light
¹⁵⁵³ leptons and b-tagging of jets, and to the reconstruction of E_T^{miss} . The TOTAL electron ID
¹⁵⁵⁴ correlation model is used, corresponding to 1 electron ID systematic. Electron ID is found to be

1555 a subleading systematic that is unconstrained by the fit, making it an appropriate choice for this
1556 analysis.

1557 The sources which contribute to the uncertainty in the jet energy scale [31] are decom-
1558 posed into uncorrelated components and treated as independent sources in the analysis. The
1559 CategoryReduction model is used to account for JES uncertainties, which decomposes the uncer-
1560 tainties into 30 nuisance parameters included in the fit. The SimpleJER model is used to account
1561 for jet energy resolution (JER) uncertainties, and 8 JER uncertainty components unclued as
1562 NPs in the fit.

1563 The uncertainties in the b-tagging efficiencies measured in dedicated calibration analyses
1564 [32] are also decomposed into uncorrelated components. The large number of components for
1565 b-tagging is due to the calibration of the distribution of the BDT discriminant.

1566 The systematic uncertainties associated with the signal and background processes are
1567 accounted for by varying the cross-section of each process within its uncertainty.

1568 The full list of systematic uncertainties considered in the analysis is summarized in Tables
1569 47, 48 and 49.

1570

Experimental Systematics on Leptons and E_T^{miss}			
Type	Description	Systematics Name	Application
Trigger			
Scale Factors	Trigger Efficiency	lepSFTrigTight_MU(EL)_SF_Trigger_STAT(SYST)	Event Weight
Muons			
Efficiencies	Reconstruction and Identification	lepSFObjTight_MU_SF_ID_STAT(SYST)	Event Weight
	Isolation	lepSFObjTight_MU_SF_Isol_STAT(SYST)	Event Weight
	Track To Vertex Association	lepSFObjTight_MU_SF_TTVA_STAT(SYST)	Event Weight
p_T Scale	p_T Scale	MUONS_SCALE	p_T Correction
Resolution	Inner Detector Energy Resolution	MUONS_ID	p_T Correction
	Muon Spectrometer Energy Resolution	MUONS_MS	p_T Correction
Electrons			
Efficiencies	Reconstruction	lepSFObjTight_EL_SF_ID	Event Weight
	Identification	lepSFObjTight_EL_SF_Reco	Event Weight
	Isolation	lepSFObjTight_EL_SF_Isol	Event Weight
Scale Factor	Energy Scale	EG_SCALE_ALL	Energy Correction
Resolution	Energy Resolution	EG_RESOLUTION_ALL	Energy Correction
E_T^{miss}			
Soft Tracks Terms	Resolution	MET_SoftTrk_ResoPerp	p_T Correction
	Resolution	MET_SoftTrk_ResoPara	p_T Correction
	Scale	MET_SoftTrk_ScaleUp	p_T Correction
	Scale	MET_SoftTrk_ScaleDown	p_T Correction

Table 45: Summary of experimental systematics considered for leptons and E_T^{miss} . Includes type, description, name of systematic as used in the fit, and mode of application. The mode of application indicates the systematic evaluation, e.g. as an overall event re-weighting (Event Weight) or rescaling (p_T Correction).

Experimental Systematics on Jets			
Type	Origin	Systematics Name	Application
Jet Vertex Tagger		JVT	Event Weight
Energy Scale	Calibration Method	JET_21NP_ JET_EffectiveNP_1-19	p _T Correction p _T Correction
	η inter-calibration	JET_EtaIntercalibration_Modelling JET_EtaIntercalibration_NonClosure JET_EtaIntercalibration_TotalStat	p _T Correction p _T Correction p _T Correction
	High p _T jets	JET_SingleParticle_HighPt	p _T Correction
	Pile-Up	JET_Pileup_OffsetNPV JET_Pileup_OffsetMu JET_Pileup_PtTerm JET_Pileup_RhoTopology	p _T Correction p _T Correction p _T Correction p _T Correction
	Non Closure	JET_PunchThrough_MC15	p _T Correction
	Flavour	JET_Flavor_Response JET_BJES_Response JET_Flavor_Composition	p _T Correction p _T Correction p _T Correction
Resolution		JET_JER_SINGLE_NP	Event Weight

Table 46: Jet systematics take into account effects of jets calibration method, η inter-calibration, high p_T jets, pile-up, and flavor response. They are all diagonalised into effective parameters.

Experimental Systematics on b-tagging		
Type	Origin	Systematic Name
Scale Factors	DL1r b-tagger efficiency on b originated jets in bins of η	DL1r_Continuous_EventWeight_B0-29
	DL1r b-tagger efficiency on c originated jets in bins of η	DL1r_Continuous_EventWeight_C0-19
	DL1r b-tagger efficiency on light flavoured originated jets in bins of η and p_T	DL1r_Continuous_EventWeight_Light0-79
	DL1r b-tagger extrapolation efficiency	DL1r_Continuous_EventWeight_extrapolation DL1r_Continuous_EventWeight_extrapolation_from_charm

Table 47: Summary of experimental systematics to be included for b-tagging of jets in the analysis, using the continuous DL1r tagging algorithm. All of the b-tagging related systematics are applied as event weights. From left: type, description, and the name of systematic used in the fit.

1571 As mentioned in Section ??, a normalization corrections and uncertainties on the estimates
 1572 of non-prompt leptons backgrounds are derived using data driven techniques, decribed in detail
 1573 in [5]. These are derived from a likelihood fit over various non-prompt enriched control regions,
 1574 targeting several sources of non-prompt light leptons separately: external conversion electrons,
 1575 internal conversion electrons, electrons from heavy flavor decays, and muons from heavy flavor
 1576 decays.

1577 The normalization factor and uncertainty applied to each source of non-prompt leptons is
 1578 summarized in Table ??

Processs	N
NF_e^{ExtCO}	1.70 ± 0.51
NF_e^{IntCO}	0.75 ± 0.26
NF_e^{HF}	1.09 ± 0.32
NF_{μ}^{HF}	1.28 ± 0.17

1579 In addition to those derived from the control regions, several additional uncertainties are
 1580 assigned to the non-prompt lepton background. An additional 25% uncertainty on material
 1581 conversions is assigned, based on the comparison between data and MC in a region where a
 1582 loose electron fails the photon conversion veto. A shape uncertainty of 15% (6%) is assigned to
 1583 the HF non-prompt electron (muon) background based on a comparison between data and MC
 1584 where the second leading electron (muon) is only required to be loose. As the contribution from
 1585 light non-prompt leptons is small, about 10% percent of the contribution from HF non-prompt
 1586 leptons, it is derived from the agreement between data and simulation in a LF enriched region at
 1587 low values of the non-prompt lepton BDT. The resulting uncertainty is 100%, and is taken to be
 1588 uncorrelated between internal and material conversions.

1589 Theoretical uncertainties applied to MC predictions, including cross section, PDF, and
 1590 scale uncertainties are taken from theory calculations for the predominate prompt backgrounds.
 1591 Following the nominal $t\bar{t}H - ML$ analysis, a 50% uncertainty is applied to Diboson to account
 1592 for the large uncertainty in estimating $VV +$ heavy flavor. The other “rare” background processes
 1593 - including tZ , rare top processes, $ttWW$, WtZ , VVV , $tHjb$ and WtH - are assigned an overall
 1594 50% normalization uncertainty as well. The theory uncertainties applied to the MC estimates
 1595 are summarized in Table 50.

Process	X-section [%]
t̄H (aMC@NLO+Pythia8)	QCD Scale: $^{+5.8}_{-9.2}$ PDF($+\alpha_S$): ± 3.6
t̄Z (aMC@NLO+Pythia8)	QCD Scale: $^{+9.6}_{-11.3}$ PDF($+\alpha_S$): ± 4
t̄W (aMC@NLO+Pythia8)	QCD Scale: $^{+12.9}_{-11.5}$ PDF($+\alpha_S$): ± 3.4
tHjb (aMC@NLO+Pythia8)	QCD Scale: $^{+6.5}_{-14.9}$ PDF($+\alpha_S$): ± 3.7
WtH (aMC@NLO+Pythia8)	QCD Scale: $^{+5.0}_{-6.7}$ PDF($+\alpha_S$): ± 6.3
VV (Sherpa 2.2.1)	± 50
t̄t	± 20
Others	± 50

Table 48: Summary of theoretical uncertainties for MC predictions in the analysis.

1596 Additional uncertainties to account for t̄W mismodelling are also applied. These include
 1597 a “Generator” uncertainty, based on a comparison between the nominal Sherpa 2.2.5 sample,
 1598 and the formerly used aMC@NLO sample, and an “Extra radiation” uncertainty, which includes
 1599 renormalisation and factorisation scale variations of the Sherpa 2.2.5 sample.

1600 22 Results

1601 A maximum likelihood fit is performed simultaneously over the reconstructed Higgs p_T spectrum
 1602 in the three signal regions, 2lSS, 3lS, and 3lF. The signal is split into high and low p_T samples,
 1603 based on whether the truth p_T of the Higgs is above or below 150 GeV. The parameters $\mu_{t\bar{t}Hhighp_T}$
 1604 and $\mu_{t\bar{t}Hlowp_T}$, where $\mu = \sigma_{\text{observed}}/\sigma_{SM}$, are extracted from the fit, signifying the difference

1605 between the observed value and the theory prediction. Unblinded results are shown for the 80
1606 fb^{-1} data set, as well as MC only projections of results using the full Run-2, 140 fb^{-1} dataset.

1607 As described in Section 21, there are 229 systematic uncertainties that are considered
1608 as NPs in the fit. These NPs are constrained by Gaussian or log-normal probability density
1609 functions. The latter are used for normalisation factors to ensure that they are always positive.
1610 The expected number of signal and background events are functions of the likelihood. The prior
1611 for each NP is added as a penalty term, decreasing the likelihood as it is shifted away from its
1612 nominal value.

1613 22.1 Results - 80 fb^{-1}

1614 As the data collected from 2015-2017 has been unblinded for $t\bar{t}H - \text{ML}$ channels, representing 80
1615 fb^{-1} , those events are unblinded. The predicted Higgs p_T spectrum is fit to data simultaneously
1616 in each of the three signal regions shown in Figure 22.1.

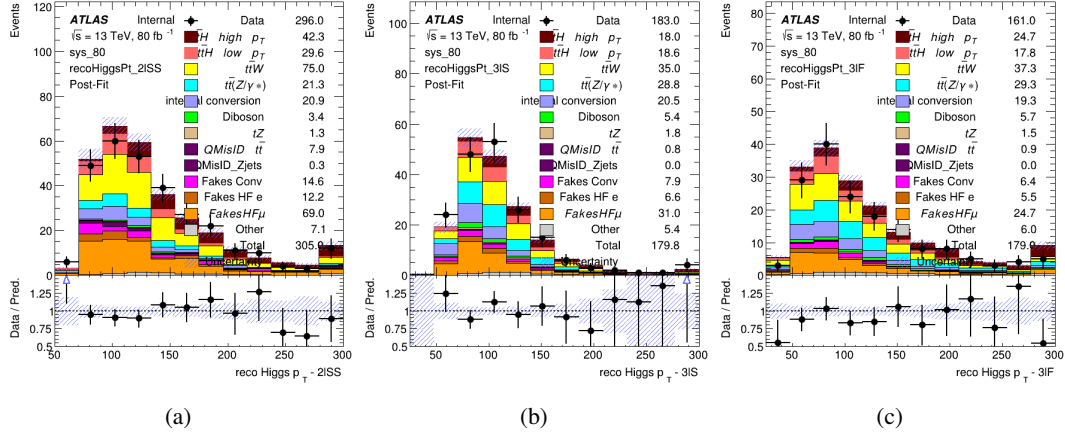


Figure 22.1: Post-fit distributions of the reconstructed Higgs p_T in the three signal regions, (a) 2ISS, (b) 3IS, and (c) 3IF, for 80 fb^{-1} of MC

1617

A post-fit summary of the fitted regions is shown in Figure 22.2.

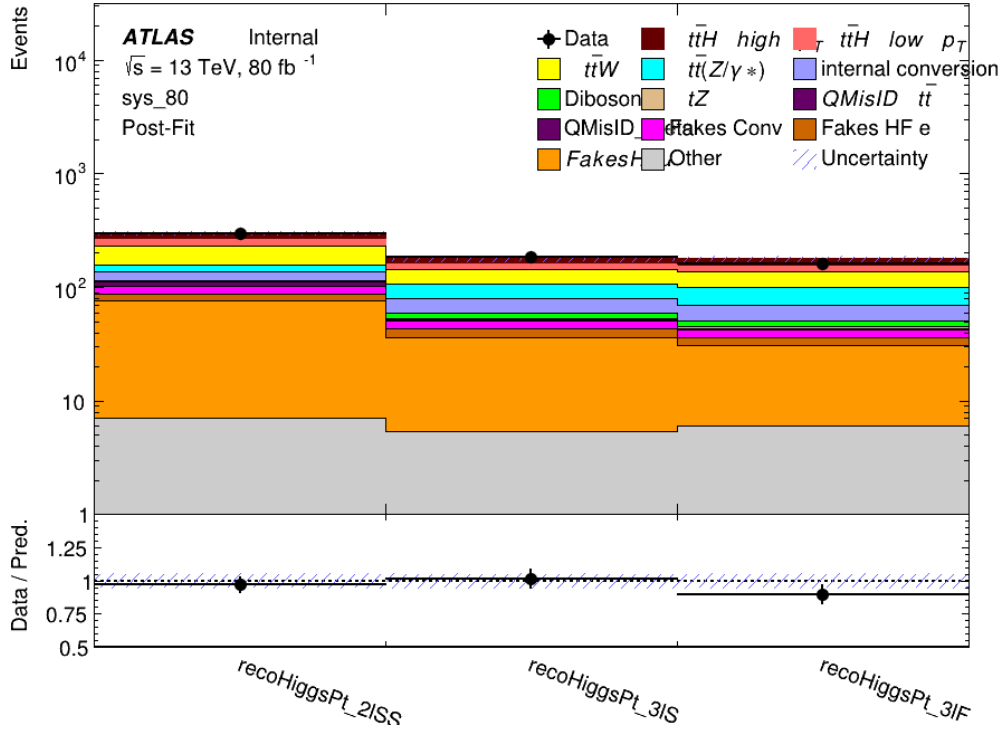


Figure 22.2: Post-fit summary of the yields in each signal region.

1618 The the measured μ values for high and low p_T Higgs production obtained from the fit
 1619 are shown in 51. A significance of 1.7σ is observed for $t\bar{t}H$ high p_T , and 2.1σ is measured for
 1620 $t\bar{t}H$ low p_T .

$$\mu_{t\bar{t}H \text{ high } p_T} = 2.1^{+0.62}_{-0.59}(\text{stat})^{+0.40}_{-0.43}(\text{sys})$$

$$\mu_{t\bar{t}H \text{ low } p_T} = 0.83^{+0.37}_{-0.37}(\text{stat})^{+0.48}_{-0.47}(\text{sys})$$

Table 49: Best fit μ values for $t\bar{t}H$ high p_T and $t\bar{t}H$ low p_T , where $\mu = \sigma_{\text{obs}}/\sigma_{\text{pred}}$

1621 The most prominent sources of systematic uncertainty, as measured by their impact on
 1622 $\mu_{t\bar{t}H \text{ high } p_T}$, are summarized in Table 52.

Uncertainty Source	$\Delta\mu$	
Jet Energy Scale	0.25	0.23
$t\bar{t}H$ cross-section (QCD Scale)	-0.11	0.21
ATLAS Luminosity	-0.13	0.14
Jet Flavor Tagging	0.14	0.13
$t\bar{t}W$ cross-section (QCD Scale)	-0.12	0.11
Higgs Branching Ratio	-0.1	0.11
$t\bar{t}H$ cross-section (PDF)	-0.07	0.08
Electron ID	-0.06	0.06
$t\bar{t}$ HF Muon Unc.	-0.05	0.06
$t\bar{t}Z$ cross-section (QCD Scale)	-0.05	0.05
Diboson cross-section	-0.05	0.05
HF Muon Shape - 3l	-0.04	0.04
Total Systematic Uncertainty	0.40	0.43

Table 50: Summary of the most significant sources of systematic uncertainty on the measurement of $t\bar{t}H$ high p_T .

1623 The ranking and impact of those nuisance parameters with the largest contribution to the
 1624 overall uncertainty is shown in Figure 22.3.

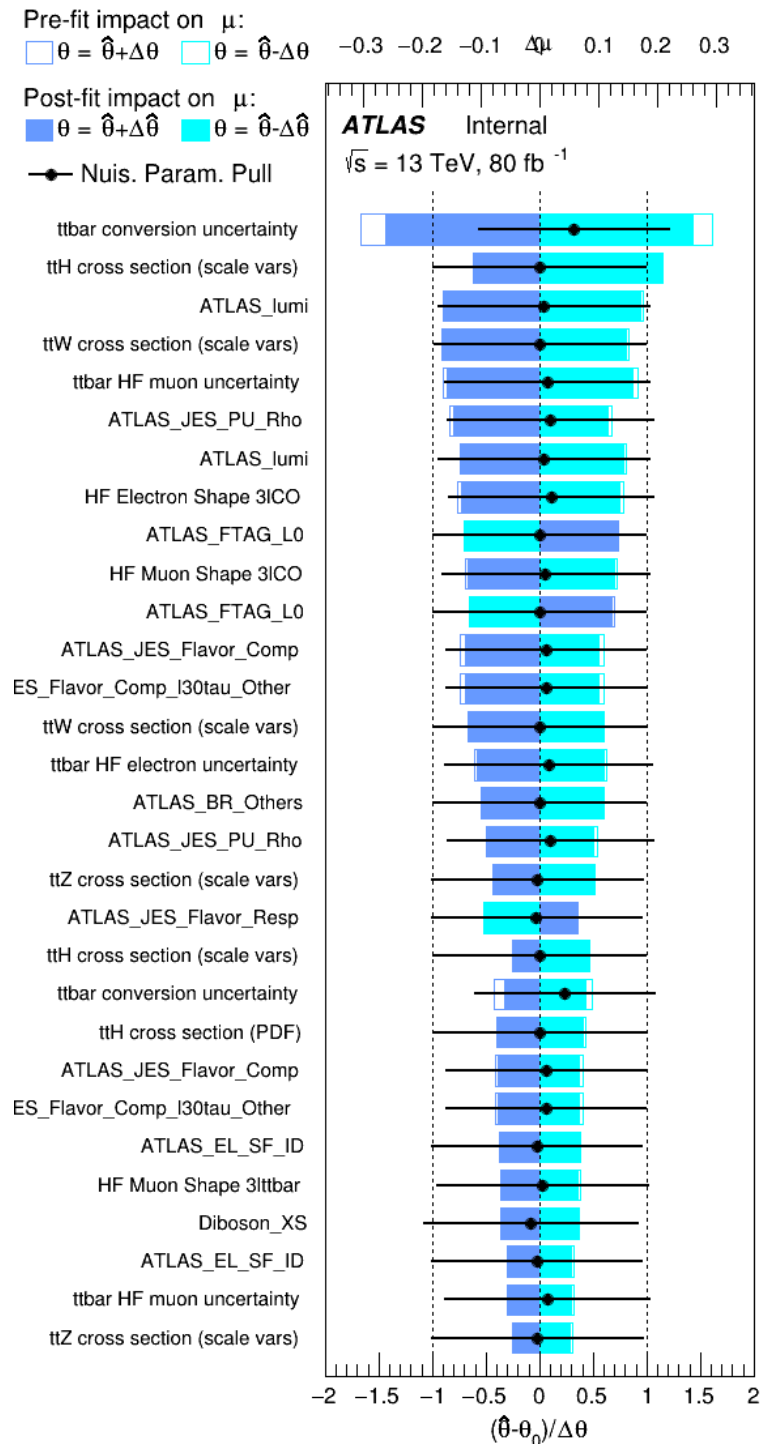


Figure 22.3: Impact of systematic uncertainties on the measurement of high p_T $t\bar{t}H$ events

1625

The background composition of each of the fit regions is shown in Figure 22.4.

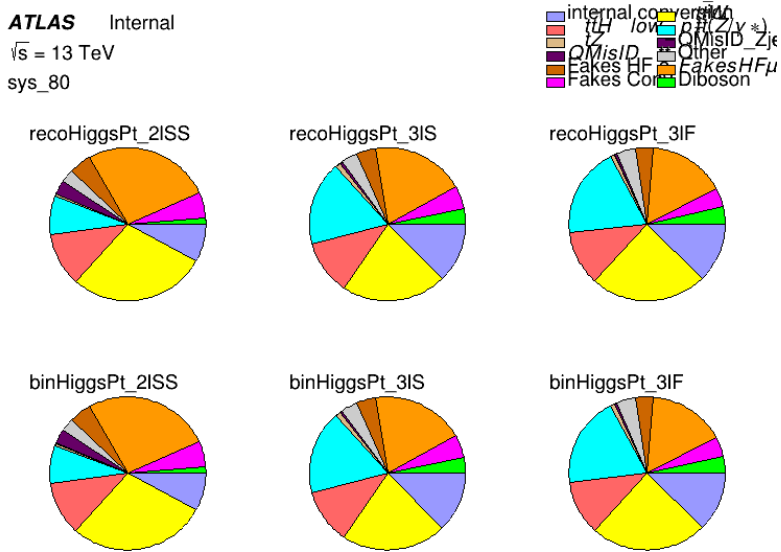


Figure 22.4: Background composition of the fit regions.

1626

22.2 Projected Results - 140 fb^{-1}

1627

As data collected in 2018 has not yet been unblinded for $t\bar{t}H - \text{ML}$ at the time of this note, data from that year remains blinded. Instead, an Asimov fit is performed - with the MC prediction being used both as the SM prediction as well as the data in the fit - in order to give expected results.

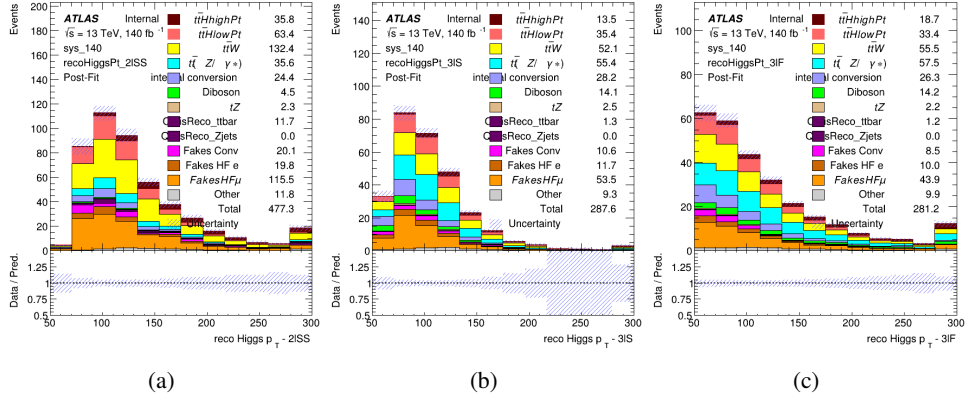


Figure 22.5: Blinded post-fit distributions of the reconstructed Higgs p_T in the three signal regions, (a) 2lSS, (b) 3lS, and (c) 3lF, for 140 fb^{-1} of data

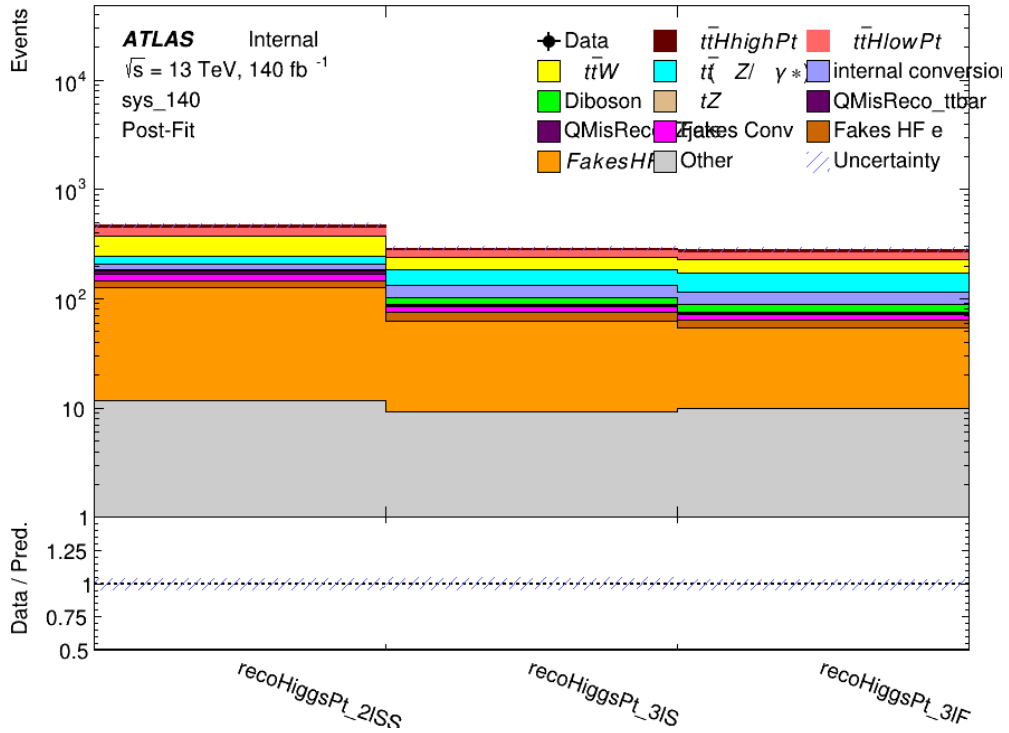


Figure 22.6: Post-fit summary of fit.

¹⁶³² shown in [53](#). A significance of 2.0σ is expected for $t\bar{t}H$ high p_T , and a projected significance

¹⁶³³ 2.3σ is extracted for $t\bar{t}H$ low p_T .

$$\mu_{t\bar{t}H \text{ high } p_T} = 1.00^{+0.45}_{-0.43} (\text{stat})^{+0.31}_{-0.31} (\text{sys})$$

$$\mu_{t\bar{t}H \text{ low } p_T} = 1.00^{+0.29}_{-0.30} (\text{stat})^{+0.47}_{-0.46} (\text{sys})$$

Table 51: Best fit μ values for $t\bar{t}H$ high p_T and $t\bar{t}H$ low p_T , where $\mu = \sigma_{\text{obs}}/\sigma_{\text{pred}}$

¹⁶³⁴ The most prominent sources of systematic uncertainty, as measured by their impact on

¹⁶³⁵ $\mu_{t\bar{t}H \text{ high } p_T}$, are summarized in Table [54](#).

Uncertainty Source	$\Delta\mu$	
Jet Energy Scale	0.2	0.18
$t\bar{t}W$ cross-section (QCD Scale)	-0.12	0.11
ATLAS Luminosity	-0.11	0.11
Jet Flavor Tagging	0.11	0.10
$t\bar{t}H$ cross-section (QCD Scale)	-0.06	0.06
Higgs Branching Ratio	-0.1	0.11
$t\bar{t}H$ cross-section (PDF)	-0.07	0.08
Electron ID	-0.05	0.05
$t\bar{t}$ HF Muon Unc.	-0.04	0.06
$t\bar{t}Z$ cross-section (QCD Scale)	-0.03	0.04
Diboson cross-section	-0.03	0.03
HF Muon Shape - 3l	-0.02	0.02
Total Systematic Uncertainty	0.31	0.31

Table 52: Summary of the most significant sources of systematic uncertainty on the measurement of $t\bar{t}H$ high p_T .

¹⁶³⁶ The ranking and impact of those nuisance parameters with the largest contribution to the

¹⁶³⁷ overall uncertainty is shown in Figure [22.7](#).

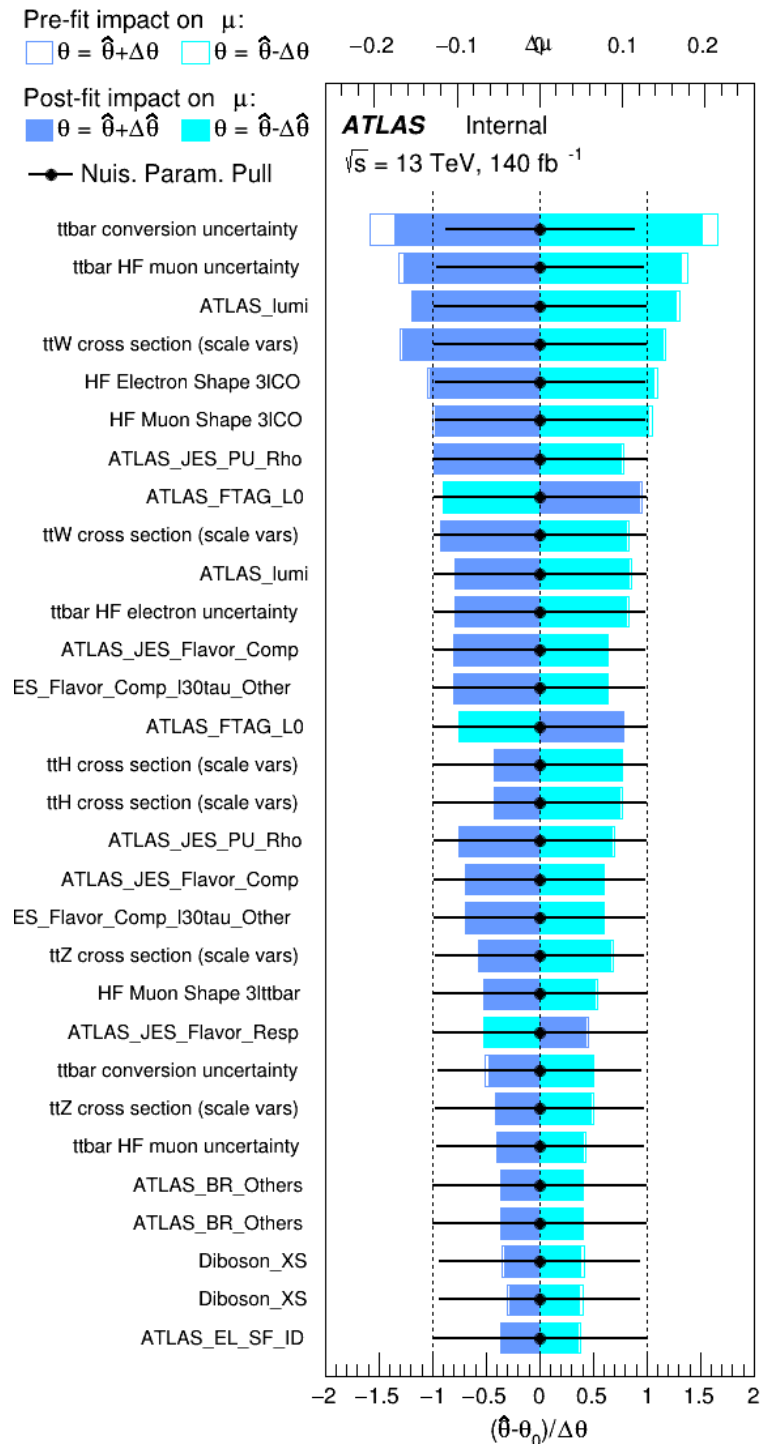


Figure 22.7: Impact of systematic uncertainties on the measurement of high p_T $t\bar{t}H$ events

1638

The background composition of each of the fit regions is shown in Figure 22.8.

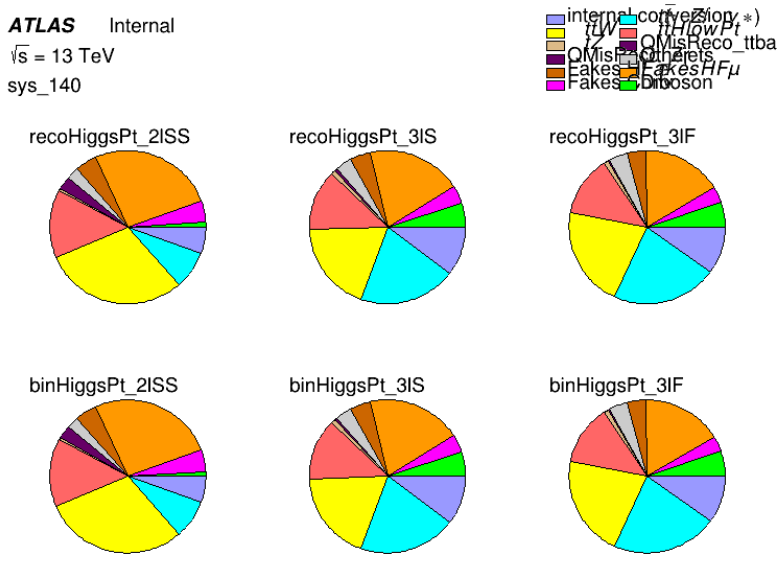


Figure 22.8: Background composition of the fit regions.

1639

Part VI

1640

Conclusion

1641 As search for the effects of dimension-six operators on $t\bar{t}H$ production is performed. An effective
 1642 field theory approached is used to parametrize the effects of high energy physics on the Higgs
 1643 momentum spectrum. The momentum spectrum is reconstructed using various MVA techniques,
 1644 and the limits on dimension-six operators are limited to X.

1645 References

- 1646 [1] R. Oerter, *The theory of almost everything : the Standard Model, the unsung triumph of*
1647 *modern physics*, Pi Press, 2006, ISBN: 978-0-13-236678-6.
- 1648 [2] P. W. Higgs, *Broken Symmetries and the Masses of Gauge Bosons*,
1649 Phys. Rev. Lett. 13 (Oct, 1964) 508-509 ().
- 1650 [3] J. Goldstone, A. Salam and S. Weinberg, *Broken Symmetries*,
1651 Phys. Rev. **127** (3 1962) 965,
1652 URL: <https://link.aps.org/doi/10.1103/PhysRev.127.965>.
- 1653 [4] J. Ellis, *Higgs Physics*,
1654 (2013) 117, 52 pages, 45 figures, Lectures presented at the ESHEP 2013 School of
1655 High-Energy Physics, to appear as part of the proceedings in a CERN Yellow Report,
1656 URL: <https://cds.cern.ch/record/1638469>.
- 1657 [5] *Evidence for the associated production of the Higgs boson and a top quark pair with the*
1658 *ATLAS detector*, tech. rep. ATLAS-CONF-2017-077, CERN, 2017,
1659 URL: <https://cds.cern.ch/record/2291405>.
- 1660 [6] A. M. Sirunyan et al., *Observation of $t\bar{t}H$ Production*,
1661 *Physical Review Letters* **120** (2018), ISSN: 1079-7114,
1662 URL: <http://dx.doi.org/10.1103/PhysRevLett.120.231801>.

- 1663 [7] B. Dumont, S. Fichet and G. von Gersdorff,
1664 *A Bayesian view of the Higgs sector with higher dimensional operators,*
1665 *Journal of High Energy Physics* **2013** (2013), ISSN: 1029-8479,
1666 URL: [http://dx.doi.org/10.1007/JHEP07\(2013\)065](http://dx.doi.org/10.1007/JHEP07(2013)065).
- 1667 [8] S. Banerjee, S. Mukhopadhyay and B. Mukhopadhyaya,
1668 *Higher dimensional operators and the LHC Higgs data: The role of modified kinematics,*
1669 *Physical Review D* **89** (2014), ISSN: 1550-2368,
1670 URL: <http://dx.doi.org/10.1103/PhysRevD.89.053010>.
- 1671 [9] M. Zinser, ‘The Large Hadron Collider’, *Search for New Heavy Charged Bosons and*
1672 *Measurement of High-Mass Drell-Yan Production in Proton—Proton Collisions,*
1673 Springer International Publishing, 2018 47, ISBN: 978-3-030-00650-1,
1674 URL: https://doi.org/10.1007/978-3-030-00650-1_4.
- 1675 [10] *Detector and Technology*, URL: <https://atlas.cern/discover/detector>.
- 1676 [11] M. Marjanovic, *ATLAS Tile calorimeter calibration and monitoring systems*, 2018.
- 1677 [12] M. Aaboud et al., *Observation of electroweak $W^\pm Z$ boson pair production in association*
1678 *with two jets in pp collisions at $\sqrt{s} = 13$ TeV with the ATLAS detector,*
1679 *Phys. Lett. B* **793** (2019) 469, arXiv: [1812.09740 \[hep-ex\]](https://arxiv.org/abs/1812.09740).
- 1680 [13] T. Gleisberg et al., *Event generation with SHERPA 1.1*, *JHEP* **02** (2009) 007,
1681 arXiv: [0811.4622 \[hep-ph\]](https://arxiv.org/abs/0811.4622).
- 1682 [14] R. D. Ball et al., *Parton distributions for the LHC Run II*, *JHEP* **04** (2015) 040,
1683 arXiv: [1410.8849 \[hep-ph\]](https://arxiv.org/abs/1410.8849).

- 1684 [15] H.-L. Lai et al., *New parton distributions for collider physics*,
 1685 Phys. Rev. D **82** (2010) 074024, arXiv: [1007.2241 \[hep-ph\]](https://arxiv.org/abs/1007.2241).
- 1686 [16] S. Frixione, G. Ridolfi and P. Nason,
 1687 *A positive-weight next-to-leading-order Monte Carlo for heavy flavour hadroproduction*,
 1688 JHEP **09** (2007) 126, arXiv: [0707.3088 \[hep-ph\]](https://arxiv.org/abs/0707.3088).
- 1689 [17] E. Re, *Single-top Wt-channel production matched with parton showers using the*
 1690 *POWHEG method*, Eur. Phys. J. C **71** (2011) 1547, arXiv: [1009.2450 \[hep-ph\]](https://arxiv.org/abs/1009.2450).
- 1691 [18] ATLAS Collaboration, *Electron efficiency measurements with the ATLAS detector using*
 1692 *the 2015 LHC proton–proton collision data*, ATLAS-CONF-2016-024, 2016,
 1693 URL: <https://cds.cern.ch/record/2157687>.
- 1694 [19] ATLAS Collaboration, *Measurement of the muon reconstruction performance of the*
 1695 *ATLAS detector using 2011 and 2012 LHC proton–proton collision data*,
 1696 Eur. Phys. J. C **74** (2014) 3130, arXiv: [1407.3935 \[hep-ex\]](https://arxiv.org/abs/1407.3935).
- 1697 [20] R. Narayan et al., *Measurement of the total and differential cross sections of a*
 1698 *top-quark-antiquark pair in association with a W boson in proton-proton collisions at a*
 1699 *centre-of-mass energy of 13 TeV with ATLAS detector at the Large Hadron Collider*,
 1700 tech. rep. ATL-COM-PHYS-2020-217, CERN, 2020,
 1701 URL: <https://cds.cern.ch/record/2712986>.
- 1702 [21] ATLAS Collaboration, *Jet Calibration and Systematic Uncertainties for Jets*
 1703 *Reconstructed in the ATLAS Detector at $\sqrt{s} = 13 \text{ TeV}$* , ATL-PHYS-PUB-2015-015,
 1704 2015, URL: <https://cds.cern.ch/record/2037613>.

- 1705 [22] ATLAS Collaboration,
 1706 *Selection of jets produced in 13 TeV proton–proton collisions with the ATLAS detector,*
 1707 ATLAS-CONF-2015-029, 2015, URL: <https://cds.cern.ch/record/2037702>.
- 1708 [23] ATLAS Collaboration, *Performance of pile-up mitigation techniques for jets in pp*
 1709 *collisions at $\sqrt{s} = 8$ TeV using the ATLAS detector*, *Eur. Phys. J. C* **76** (2016) 581,
 1710 arXiv: [1510.03823 \[hep-ex\]](https://arxiv.org/abs/1510.03823).
- 1711 [24] ATLAS Collaboration, *Performance of missing transverse momentum reconstruction*
 1712 *with the ATLAS detector in the first proton–proton collisions at $\sqrt{s} = 13$ TeV,*
 1713 ATL-PHYS-PUB-2015-027, 2015, URL: <https://cds.cern.ch/record/2037904>.
- 1714 [25] 2021, URL: https://twiki.cern.ch/twiki/bin/view/AtlasProtected/BTagCalibrationRecommendationsRelease21#Tools_for_Flavor_Tagging_Calibra.
- 1717 [26] P. S. A. Hoecker, *TMVA 4 Toolkit for Multivariate Data Analysis with ROOT*,
 1718 arXiv:physics/0703039 (2013).
- 1719 [27] F. Cardillo et al., *Measurement of the fiducial and differential cross-section of a top*
 1720 *quark pair in association with a Z boson at 13 TeV with the ATLAS detector*, (2019),
 1721 URL: <https://cds.cern.ch/record/2672207>.
- 1722 [28] T. Chen and C. Guestrin, ‘XGBoost: A Scalable Tree Boosting System’,
 1723 *Proceedings of the 22nd ACM SIGKDD International Conference on Knowledge*
 1724 *Discovery and Data Mining*, KDD ’16, ACM, 2016 785, ISBN: 978-1-4503-4232-2,
 1725 URL: <http://doi.acm.org/10.1145/2939672.2939785>.

- 1726 [29] ATLAS Collaboration, *Luminosity determination in pp collisions at $\sqrt{s} = 7 \text{ TeV}$ using*
1727 *the ATLAS detector at the LHC*, [Eur. Phys. J. C **71** \(2011\) 1630](#),
1728 arXiv: [1101.2185 \[hep-ex\]](#).
- 1729 [30] G. Avoni et al.,
1730 *The new LUCID-2 detector for luminosity measurement and monitoring in ATLAS*,
1731 [JINST **13** \(2018\) P07017](#).
- 1732 [31] G. Aad, T. Abajyan, B. Abbott and etal, *Jet energy resolution in proton-proton collisions*
1733 *at $\sqrt{s} = 7 \text{ TeV}$ recorded in 2010 with the ATLAS detector*,
1734 [The European Physical Journal C **73** \(2013\) 2306](#), ISSN: 1434-6052,
1735 URL: <https://doi.org/10.1140/epjc/s10052-013-2306-0>.
- 1736 [32] A. Collaboration, *Performance of b -jet identification in the ATLAS experiment*,
1737 [Journal of Instrumentation **11** \(2016\) P04008](#),
1738 URL: <http://stacks.iop.org/1748-0221/11/i=04/a=P04008>.
- 1739 [33] *Observation of the associated production of a top quark and a Z boson at 13 TeV with*
1740 *ATLAS*, (2020), URL: <https://cds.cern.ch/record/2722504>.

¹⁷⁴¹ **List of contributions**

¹⁷⁴²

¹⁷⁴³ **Appendices**

¹⁷⁴⁴ **.1 Non-prompt lepton MVA**

1745 A lepton MVA has been developed to better reject non-prompt leptons than standard cut
1746 based selections based upon impact parameter, isolation and PID. The name of this MVA is
1747 **PromptLeptonIso**. The full set of studies and detailed explanation can be found in [20].

1748 The decays of W and Z bosons are commonly selected by the identification of one or two
1749 electrons or muons. The negligible lifetimes of these bosons mean that the leptons produced in the
1750 decay originate from the interaction vertex and are thus labelled “prompt”. Analyses using these
1751 light leptons impose strict reconstruction quality, isolation and impact parameter requirements
1752 to remove “fake” leptons. A significant source of the fake light leptons are non-prompt leptons
1753 produced in decays of hadrons that contain bottom (b) or charm (c) quarks. Such hadrons
1754 typically have microscopically significant lifetimes that can be detected experimentally.

1755 These non-prompt leptons can also pass the tight selection criteria. In analyses that
1756 involve top (t) quarks, which decay almost exclusively into a W boson and a b quark, non-
1757 prompt leptons from the semileptonic decay of bottom and charm hadrons can be a significant
1758 source of background events. This is particularly the case in the selection of same-sign dilepton
1759 and multilepton final states.

1760 The main idea is to identify non-prompt light leptons using lifetime information associated
1761 with a track jet that matches the selected light lepton. This lifetime information is computed
1762 using tracks contained within the jet. Typically, lepton lifetime is determined using the impact
1763 parameter of the track reconstructed by the inner tracking detector which is matched to the recon-
1764 structed lepton. Using additional reconstructed charged particle tracks increases the precision of

1765 identifying the displaced decay vertex of bottom or charm hadrons that produced a non-prompt
 1766 light lepton. The MVA also includes information related to the isolation of the lepton to reject
 1767 non-prompt leptons.

1768 **PromptLeptonIso** is a gradient boosted BDT. The training of the BDT is performed on
 1769 leptons selected from the PowHEG+PYTHIA6 non-allhad $t\bar{t}$ MC sample. Eight variables are used
 1770 to train the BDT in order to discriminate between prompt and non-prompt leptons. The track
 1771 jets that are matched to the non-prompt leptons correspond to jets initiated by b or c quarks, and
 1772 may contain a displaced vertex. Consequently, three of the selected variables are used to identify
 1773 b-tag jets by standard ATLAS flavour tagging algorithms. Two variables use the relationship
 1774 between the track jet and lepton: the ratio of the lepton p_T with respect to the track jet p_T and
 1775 ΔR between the lepton and the track jet axis. Finally three additional variables test whether the
 1776 reconstructed lepton is isolated: the number of tracks collected by the track jet and the lepton
 1777 track and calorimeter isolation variables. Table 55 describes the variables used to train the BDT
 1778 algorithm. The choice of input variables has been extensively discussed with Egamma, Muon,
 1779 Tracking, and Flavour Tagging CP groups.

Variable	Description
N_{track} in track jet	Number of tracks collected by the track jet
$\text{IP2 log}(P_b/P_{\text{light}})$	Log-likelihood ratio between the b and light jet hypotheses with the IP2D algorithm
$\text{IP3 log}(P_b/P_{\text{light}})$	Log-likelihood ratio between the b and light jet hypotheses with the IP3D algorithm
$N_{\text{TrkAtVtx}} \text{ SV + JF}$	Number of tracks used in the secondary vertex found by the SV1 algorithm in addition to the number of tracks from secondary vertices found by the JetFitter algorithm with at least two tracks
$p_T^{\text{lepton}} / p_T^{\text{track jet}}$	The ratio of the lepton p_T and the track jet p_T
$\Delta R(\text{lepton}, \text{track jet})$	ΔR between the lepton and the track jet axis
$p_T^{\text{VarCone30}} / p_T$	Lepton track isolation, with track collecting radius of $\Delta R < 0.3$
$E_T^{\text{TopoCone30}} / p_T$	Lepton calorimeter isolation, with topological cluster collecting radius of $\Delta R < 0.3$

Table 53: A table of the variables used in the training of **PromptLeptonIso**.

1780 The output distribution of the BDT is shown in Figure .1.

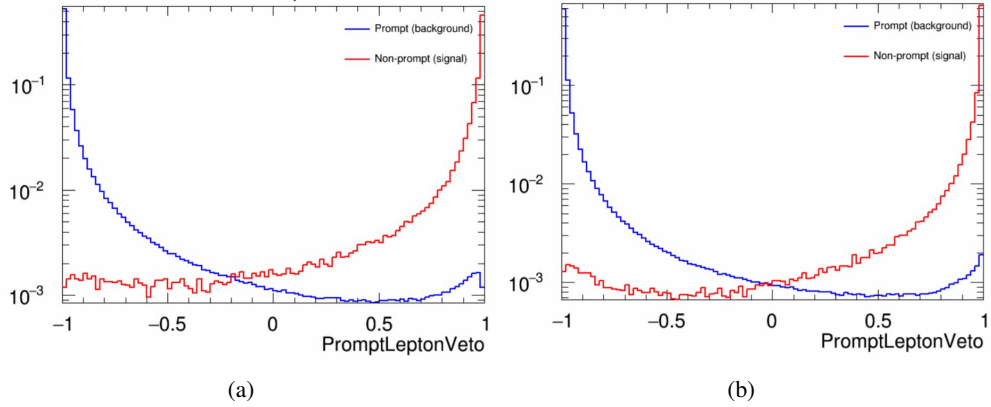


Figure .9: Distribution of the PLV BDT discriminant for (a) electrons and (b) muons

1781 The ROC curve for the BDT response, compared to the standard `FixedCutTight` WP, is
 1782 shown in figure .1, which shows a clear improvement when using this alternate training.

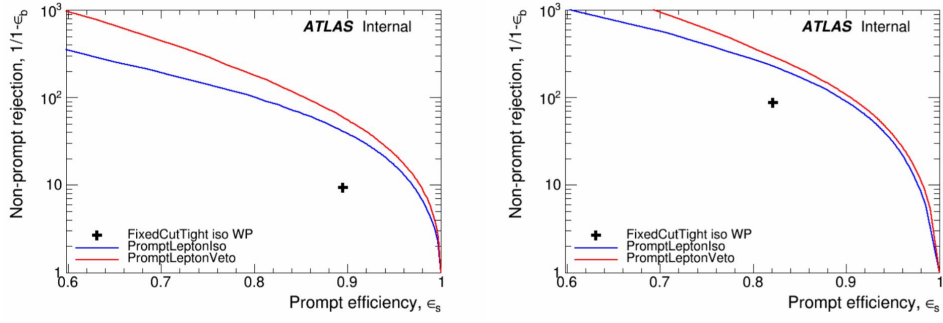


Figure .10: ROC curves for the PLV as well as the performance of the standard `FixedCutTight` WP for (left) electrons and (right) muons

1783 A cutoff value of -0.7 for electrons and -0.5 for muons are chosen as the WPs for this
 1784 MVA, based on an optimisation of S/\sqrt{B} performed in the preselection regions of the $t\bar{t}H - ML$
 1785 analysis, which have a signature similar to that of this analysis.

1786 The efficiency of the tight `PromptLeptonIso` working point is measured using the tag
1787 and probe method with $Z \rightarrow \ell^+ \ell^-$ events. Such calibration are performed by analysers from
1788 this analysis in communication with the Egamma and Muon combined performance groups. The
1789 scale factor are approximately 0.92 for $10 < p_T < 15$ GeV, and averaging at 0.98 to 0.99 for
1790 higher p_T leptons. An extra systematic is applied to muons within $\Delta R < 0.6$ of a calorimeter
1791 jet, since there is a strong dependence on the scale factor due to the presence of these jets. For
1792 electrons, the dominant systematics is coming from pile-up dependence. Overall the systematics
1793 are a maximum of 3% at low p_T and decreasing at a function of p_T .

¹⁷⁹⁴ **.2 Non-prompt CR Modelling**

1795 In order to further validate the modeling in each of the non-prompt CRs, additional
 1796 kinematic plots are made in the Z+jets CR and $t\bar{t}$ CR in each of the continuous b-tag regions,
 1797 after the correction factors detailed in Section 12.3 have been applied.

1798 In the case of the Z+jets CR, the p_T spectrum of the lepton originating from the W
 1799 candidate is shown, as this is the distribution used to extract the scale factor applied to Z+jets.
 1800 These plots are shown in Figures .11 and .12.

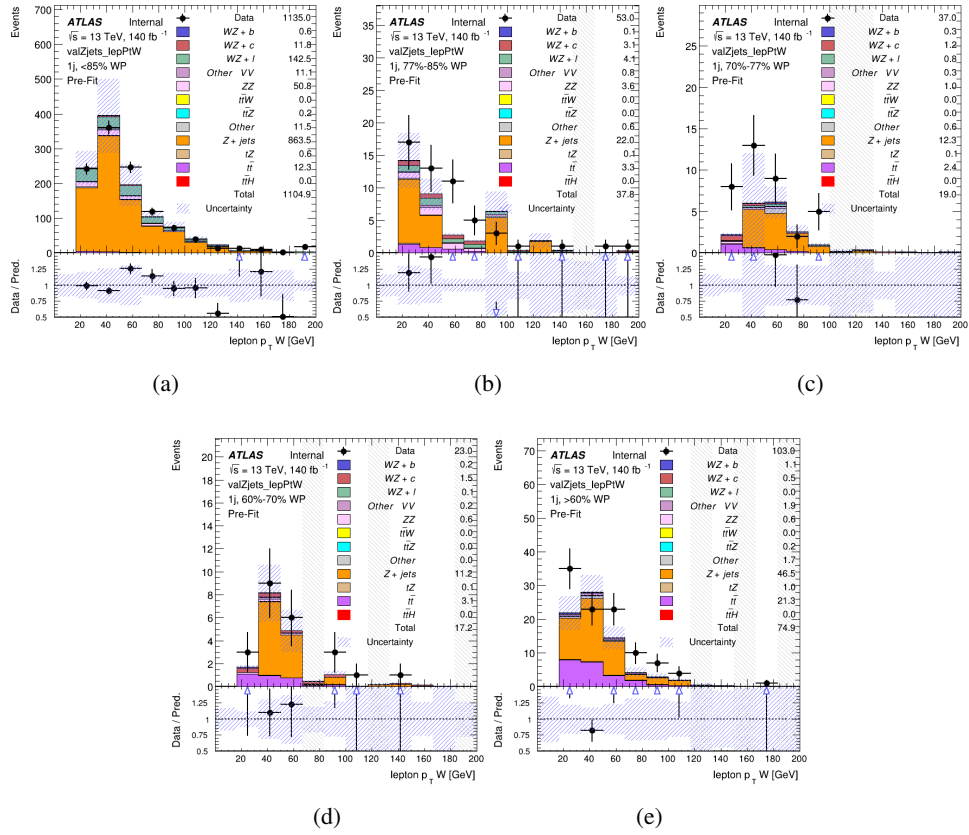


Figure .11: Comparisons between the data and MC distributions of the p_T of the lepton originating from the W-candidate in the Z+jets CR for each of the 1-jet b-tag working point regions

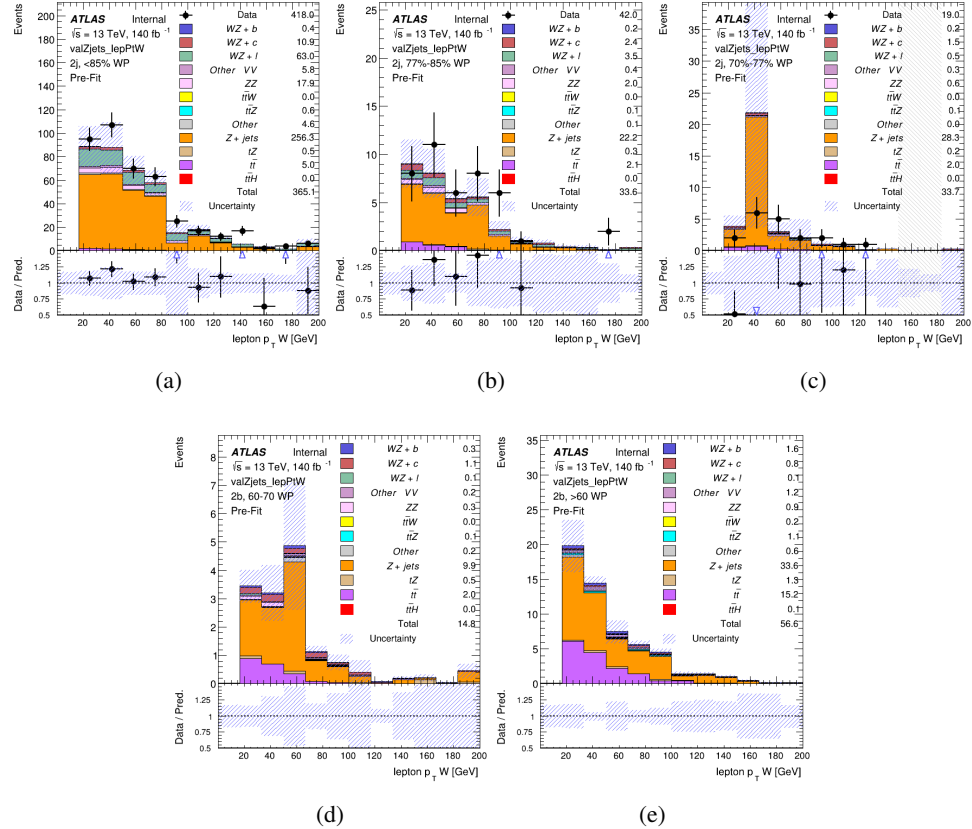


Figure .12: Comparisons between the data and MC distributions of the p_T of the lepton originating from the W-candidate in the Z+jets CR for each of the 2-jet b-tag working point regions

1801 The same is shown for the $t\bar{t}$ CR, but the p_T of the OS lepton is used instead as a
 1802 representation of the modeling, as the lepton from the W is not well defined for $t\bar{t}$ events. These
 1803 plots are shown in Figures .13 and .14.

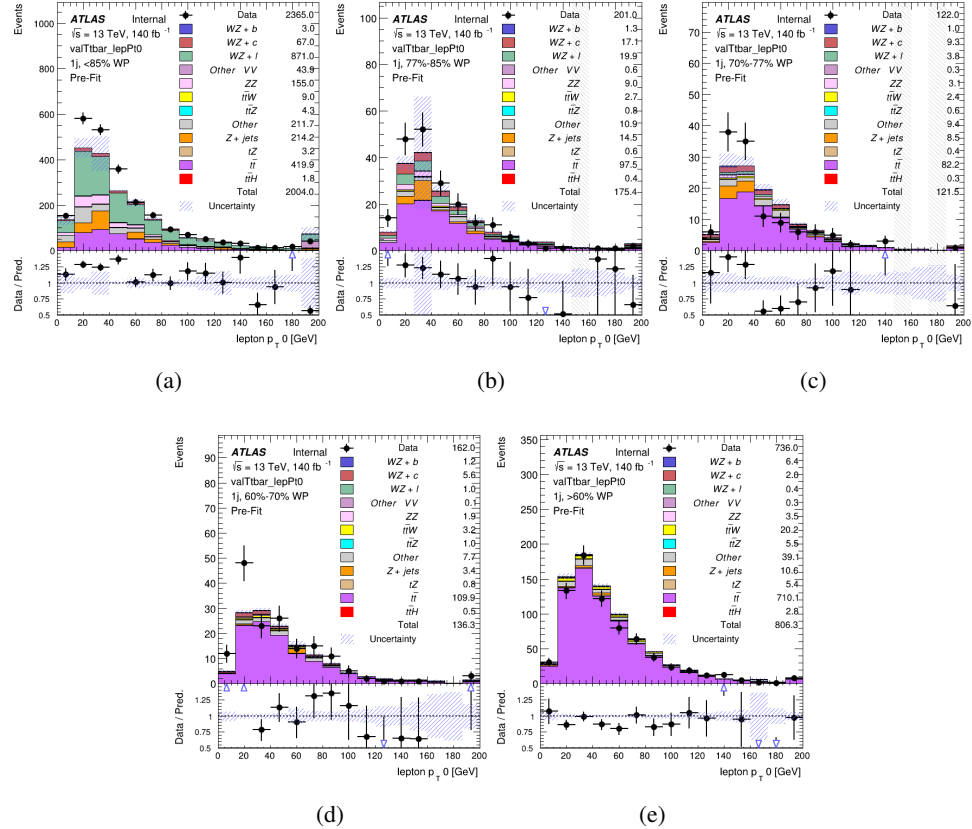


Figure .13: Comparisons between the data and MC distributions of the p_T of the OS lepton in the $t\bar{t}$ CR for each of the 1-jet b-tag working point regions

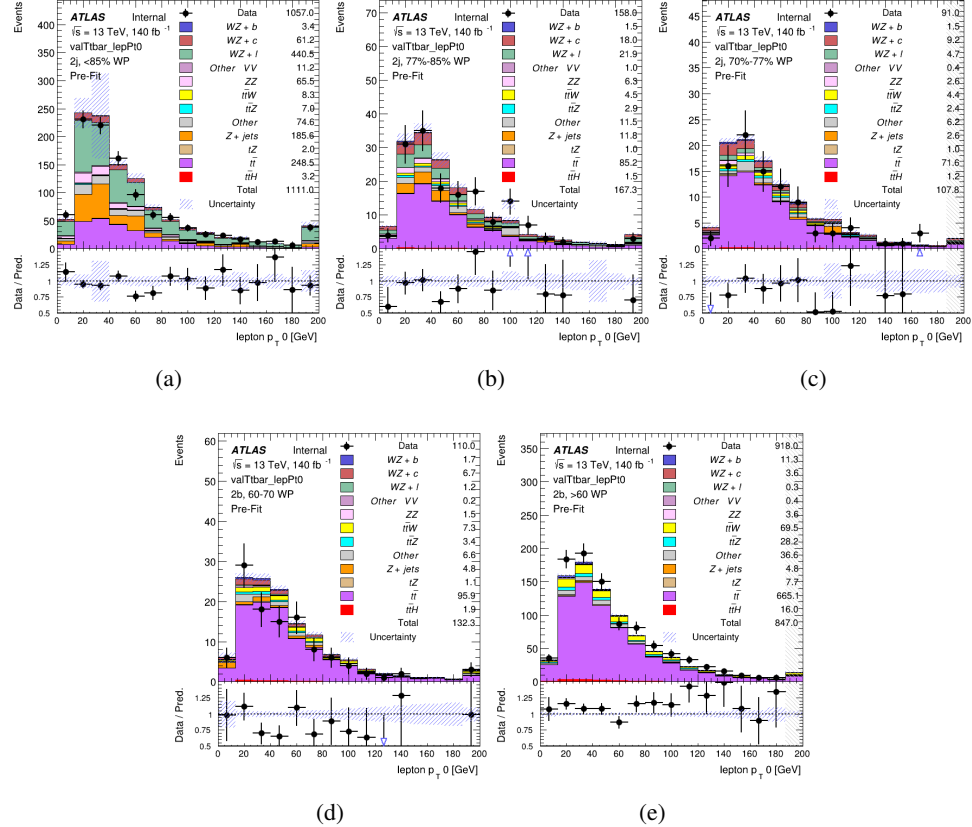


Figure 14: Comparisons between the data and MC distributions of the p_T of the OS lepton in the $t\bar{t}$ CR for each of the 2-jet b-tag working point regions

1804 .3 tZ Interference Studies

1805 Because it includes an on-shell Z boson as well as a b-jet and W from the top decay, tZ
1806 production represents an identical final state to WZ + b-jet. This implies the possibility of matrix
1807 level interference between these two processes not accounted for in the Monte Carlo simulations,
1808 which consider the two processes independently. Truth level studies are performed in order to
1809 estimate the impact of these interference effects.

1810 In order to estimate the matrix level interference effects between tZ and WZ + b-jet, two
1811 different sets of simulations are produced using MadGraph 5 [**Madgraph**] - one which simulates
1812 these two processes independently, and another where they are produced simultaneously, such
1813 that interference effects are present. These two sets of samples are then compared, and the
1814 difference between them can be taken to represent any interference effects.

1815 MadGraph simulations of 10,000 tZ and 10,000 WZ + b-jet events are produced, along
1816 with 20,000 events where both are present, in the fiducial region where three leptons and at least
1817 one jet are produced.

1818 A selection mimicking the preselection used in the main analysis is applied to the samples:
1819 The SS leptons are required to have $p_T > 20$ GeV, and > 10 GeV is required for the OS lepton.
1820 The associated b-jet is required to have $p_T > 25$ GeV, and all physics objects are required to fall
1821 in a range of $|\eta| < 2.5$.

1822 The kinematics of these samples after the selection has been applied are shown below:

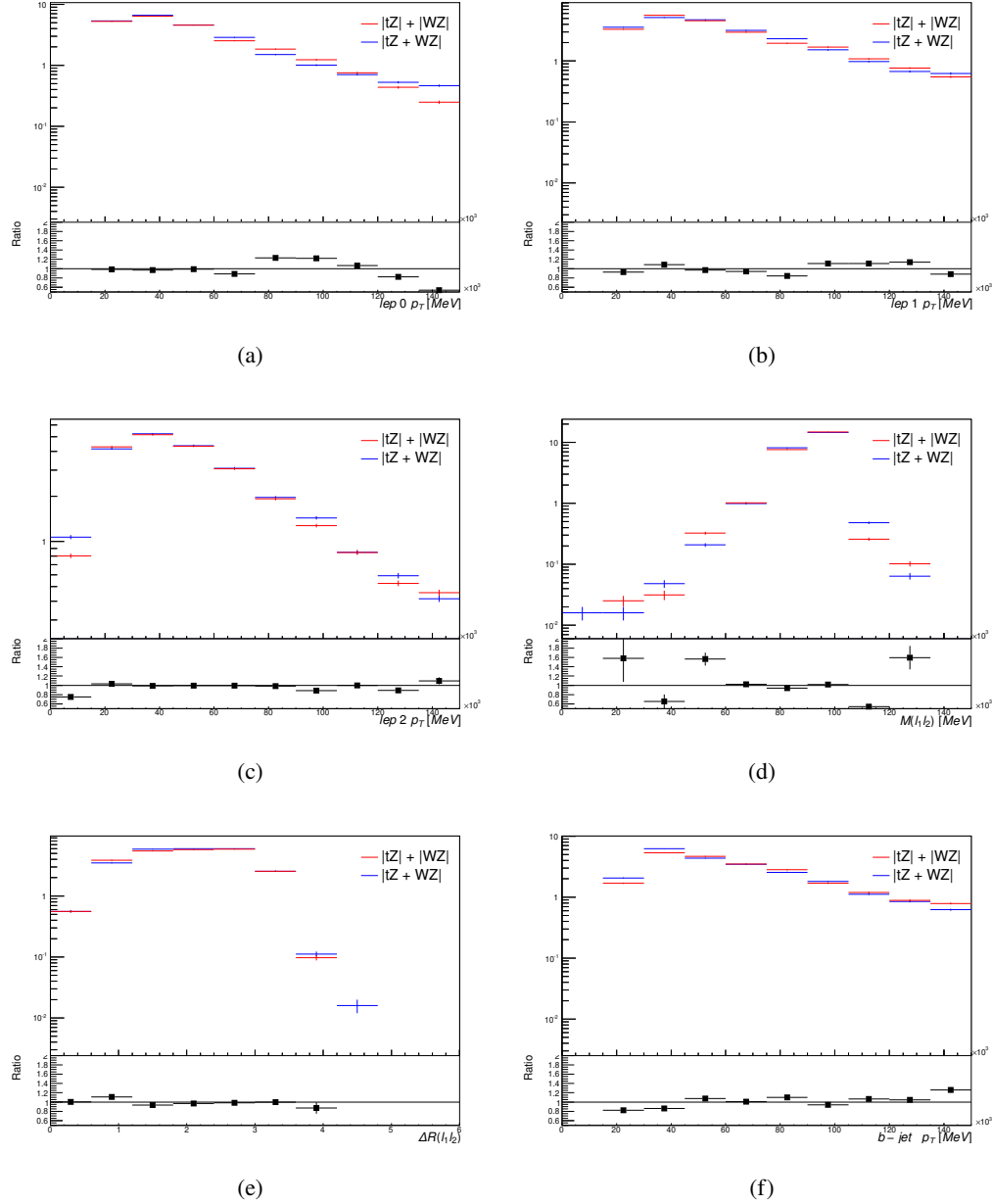


Figure .15: Comparisons between (a) the p_T of the lepton from the W, (b) and (c) show the p_T of the lepton from the Z, (d) the invariant mass of the Z-candidate, (e) ΔR of the leptons from the Z, and (f) the p_T of the b-jet, for WZ and tZ events generated with interference effects (blue) and without interference effects (red).

1823 The overall cross-section of the two methods agree within error, and no significant differ-
1824 ences in the kinematic distributions are seen. It is therefore concluded that interference effects
1825 do not significantly impact the results.

1826 **.4 Alternate tZ Inclusive Fit**

1827 **.4.1 tZ Inclusive Fit**

1828 While tZ is often considered as a distinct process from WZ + b, this could also be considered part
1829 of the signal. Alternate studies are performed where, using the same framework as the nominal
1830 analysis, a measurement of WZ + b is performed that includes tZ as part of WZ+b.

1831 Because of this change, the tZ CR is no longer necessary, and only the five pseudo-
1832 continuous b-tag regions are used in the fit. Further, systematics related to the tZ cross-section
1833 are removed from the fit, as they are now encompassed by the normalization measurement of
1834 WZ + b. All other systematic uncertainties are carried over from the nominal analysis.

1835 An expected WZ + b cross-section of $4.1^{+0.78}_{-0.74}(\text{stat})^{+0.53}_{-0.52}(\text{sys}) \text{ fb}$ is extracted from the fit,
1836 with an expected significance of 4.0σ .

1837 The impact of the predominate systematics are summarized in Table 56.

Uncertainty Source	$\Delta\mu$	
WZ + light cross-section	0.08	-0.08
Jet Energy Scale	-0.06	0.08
Luminosity	-0.05	0.06
WZ + charm cross-section	-0.04	0.05
Other Diboson + b cross-section	-0.04	0.04
WZ cross-section - QCD scale	-0.04	0.03
t̄t cross-section	-0.03	0.03
Jet Energy Resolution	-0.03	0.03
Flavor tagging	-0.03	0.03
Z+jets cross section	-0.02	0.02
Total Systematic Uncertainty	-0.15	0.16

Table 54: Summary of the most significant sources of systematic uncertainty on the measurement of WZ + b with exactly one associated jet.

1838 **.4.2 Floating tZ**

1839 In order to quantify the impact of the tZ uncertainty on the fit, an alternate fit strategy is used
1840 where the tZ normalization is allowed to float. This normalization factor replaces the cross-
1841 section uncertainty on tZ, and all other parameters of the fit remain the same.

1842 An uncertainty of 17% on the normalization of tZ is extracted from the fit, compared to a
1843 theory uncertainty of 15% applied to the tZ cross-section. The measured uncertainties on WZ
1844 remain the same.

1845 .5 DSID list

Data:

```
data15_13TeV.AllYear.physics_Main.PhysCont.DAOD_HIGG8D1.grp15_v01_p4134
data16_13TeV.AllYear.physics_Main.PhysCont.DAOD_HIGG8D1.grp16_v01_p4134
data17_13TeV.AllYear.physics_Main.PhysCont.DAOD_HIGG8D1.grp17_v01_p4134
data18_13TeV.AllYear.physics_Main.PhysCont.DAOD_HIGG8D1.grp18_v01_p4134
```

mc16a:

```
mc16_13TeV.361603.PowhegPy8EG_CT10nloME_AZNLOCTEQ6L1_ZZllll_mll4.deriv.DAOD_HIGG8D1.e4475_s3126_r9364_r9315_p4133
mc16_13TeV.361602.PowhegPy8EG_CT10nloME_AZNLOCTEQ6L1_WZlvvv_mll4.deriv.DAOD_HIGG8D1.e4054_s3126_r9364_r9315_p4133
mc16_13TeV.361604.PowhegPy8EG_CT10nloME_AZNLOCTEQ6L1_ZZvvll_mll4.deriv.DAOD_HIGG8D1.e4475_s3126_r9364_r9315_p4133
mc16_13TeV.361600.PowhegPy8EG_CT10nloME_AZNLOCTEQ6L1_WWlvvv.deriv.DAOD_HIGG8D1.e4616_s3126_r9364_r9315_p4133
mc16_13TeV.361605.PowhegPy8EG_CT10nloME_AZNLOCTEQ6L1_ZZvvvv_mll4.deriv.DAOD_HIGG8D1.e4054_s3126_s3136_r9364_r9315_p4133
mc16_13TeV.361601.PowhegPy8EG_CT10nloME_AZNLOCTEQ6L1_WZlVll_mll4.deriv.DAOD_HIGG8D1.e4475_s3126_r9364_r9315_p4133
mc16_13TeV.364286.Sherpa_222_NNPDF30NNLO_llvjj_ss_EW4.deriv.DAOD_HIGG8D1.e6055_e5984_s3126_r9364_r9315_p3983 mc16_13TeV.364285.Sherpa_222_NNPDF30NNLO_llvjj_EW6_OFPlus.deriv.DAOD_HIGG8D1.e7421_e5984_s3126_r9364_r9315_p4133
mc16_13TeV.364740.MGPy8EG_NNPDF30NLO_A14NNPDF23LO_lvlljj_EW6_SFPlus.deriv.DAOD_HIGG8D1.e7421_e5984_s3126_r9364_r9315_p4133
mc16_13TeV.364742.MGPy8EG_NNPDF30NLO_A14NNPDF23LO_lvlljj_EW6_SFPlus.deriv.DAOD_HIGG8D1.e7421_e5984_s3126_r9364_r9315_p4133
mc16_13TeV.364253.Sherpa_222_NNPDF30NNLO_llv.deriv.DAOD_HIGG8D1.e5916_s3126_r9364_r9315_p4133
mc16_13TeV.364250.Sherpa_222_NNPDF30NNLO_lll.deriv.DAOD_HIGG8D1.e5894_s3126_r9364_r9315_p4133
mc16_13TeV.364254.Sherpa_222_NNPDF30NNLO_llv.deriv.DAOD_HIGG8D1.e5916_s3126_r9364_r9315_p4133
mc16_13TeV.364255.Sherpa_222_NNPDF30NNLO_lvvv.deriv.DAOD_HIGG8D1.e5916_s3126_r9364_r9315_p4133
mc16_13TeV.410155.aMcAtNloPythia8EvtGen_MEN30NLO_A14N23LO_ttW.deriv.DAOD_HIGG8D1.e5070_s3126_r9364_r9315_p4133
mc16_13TeV.410156.aMcAtNloPythia8EvtGen_MEN30NLO_A14N23LO_ttZnunu.deriv.DAOD_HIGG8D1.e5070_s3126_r9364_r9315_p4133
mc16_13TeV.410157.aMcAtNloPythia8EvtGen_MEN30NLO_A14N23LO_ttZqq.deriv.DAOD_HIGG8D1.e5070_s3126_r9364_r9315_p4133
mc16_13TeV.410218.aMcAtNloPythia8EvtGen_MEN30NLO_A14N23LO_ttee.deriv.DAOD_HIGG8D1.e5070_s3126_r9364_r9315_p4133
mc16_13TeV.410219.aMcAtNloPythia8EvtGen_MEN30NLO_A14N23LO_ttmumu.deriv.DAOD_HIGG8D1.e5070_s3126_r9364_r9315_p4133
mc16_13TeV.410220.aMcAtNloPythia8EvtGen_MEN30NLO_A14N23LO_ttautau.deriv.DAOD_HIGG8D1.e5070_s3126_r9364_r9315_p4133
mc16_13TeV.412063.aMcAtNloPythia8EvtGen_tllq_NNPDF30_nf4_A14.deriv.DAOD_TOPQ1.e7054_e5984_s3126_r9364_r9315_p4174
mc16_13TeV.410276.aMcAtNloPythia8EvtGen_MEN30NLO_A14N23LO_ttee_mll_1_5.deriv.DAOD_HIGG8D1.e6087_e5984_s3126_r9364_r9315_p4133
mc16_13TeV.410277.aMcAtNloPythia8EvtGen_MEN30NLO_A14N23LO_ttmumu_mll_1_5.deriv.DAOD_HIGG8D1.e6087_e5984_s3126_r9364_r9315_p4133
mc16_13TeV.410278.aMcAtNloPythia8EvtGen_MEN30NLO_A14N23LO_ttautau_mll_1_5.deriv.DAOD_HIGG8D1.e6087_e5984_s3126_r9364_r9315_p4133
mc16_13TeV.410397.MadGraphPythia8EvtGen_ttbar_wbee_MEN30LO_A14N23LO.deriv.DAOD_HIGG8D1.e6086_e5984_s3126_r9364_r9315_p4133
```

mc16_13TeV.410398.MadGraphPythia8EvtGen_ttbar_wbmumu_MEN30LO_A14N23LO.deriv.DAOD_HIGG8D1.e6086_e5984_s3126_r9364_r9315_p4133
 mc16_13TeV.410399.MadGraphPythia8EvtGen_ttbar_wbtautau_MEN30LO_A14N23LO.deriv.DAOD_HIGG8D1.e6086_e5984_s3126_r9364_r9315_p4133
 mc16_13TeV.410658.PhPy8EG_A14_tchan_BW50_lept_top.deriv.DAOD_HIGG8D1.e6671_e5984_s3126_r9364_r9315_p4133
 mc16_13TeV.410659.PhPy8EG_A14_tchan_BW50_lept_antitop.deriv.DAOD_HIGG8D1.e6671_e5984_s3126_r9364_r9315_p4133
 mc16_13TeV.410644.PowhegPythia8EvtGen_A14_singletop_schan_lept_top.deriv.DAOD_HIGG8D1.e6527_e5984_s3126_r9364_r9315_p4133
 mc16_13TeV.410645.PowhegPythia8EvtGen_A14_singletop_schan_lept_antitop.deriv.DAOD_HIGG8D1.e6527_e5984_s3126_r9364_r9315_p4133
 mc16_13TeV.304014.MadGraphPythia8EvtGen_A14NNPDF23_3top_SM.deriv.DAOD_HIGG8D1.e4324_s3126_r9364_r9315_p4133
 mc16_13TeV.410080.MadGraphPythia8EvtGen_A14NNPDF23_4topSM.deriv.DAOD_HIGG8D1.e4111_s3126_r9364_r9315_p4133
 mc16_13TeV.410081.MadGraphPythia8EvtGen_A14NNPDF23_ttbarWW.deriv.DAOD_HIGG8D1.e4111_s3126_r9364_r9315_p4133
 mc16_13TeV.364100.Sherpa_221_NNPDF30NNLO_Zmumu_MAXHTPTV0_70_CVetoBVeto.deriv.DAOD_HIGG8D1.e5271_s3126_r9364_r9315_p4133
 mc16_13TeV.364101.Sherpa_221_NNPDF30NNLO_Zmumu_MAXHTPTV0_70_CFilterBVeto.deriv.DAOD_HIGG8D1.e5271_s3126_r9364_r9315_p4133
 mc16_13TeV.364102.Sherpa_221_NNPDF30NNLO_Zmumu_MAXHTPTV0_70_BFilter.deriv.DAOD_HIGG8D1.e5271_s3126_r9364_r9315_p4133
 mc16_13TeV.364103.Sherpa_221_NNPDF30NNLO_Zmumu_MAXHTPTV70_140_CVetoBVeto.deriv.DAOD_HIGG8D1.e5271_s3126_r9364_r9315_p4133
 mc16_13TeV.364104.Sherpa_221_NNPDF30NNLO_Zmumu_MAXHTPTV70_140_CFilterBVeto.deriv.DAOD_HIGG8D1.e5271_s3126_r9364_r9315_p4133
 mc16_13TeV.364106.Sherpa_221_NNPDF30NNLO_Zmumu_MAXHTPTV140_280_CVetoBVeto.deriv.DAOD_HIGG8D1.e5271_s3126_r9364_r9315_p4133
 mc16_13TeV.364107.Sherpa_221_NNPDF30NNLO_Zmumu_MAXHTPTV140_280_CFilterBVeto.deriv.DAOD_HIGG8D1.e5271_s3126_r9364_r9315_p4133
 mc16_13TeV.364108.Sherpa_221_NNPDF30NNLO_Zmumu_MAXHTPTV140_280_BFilter.deriv.DAOD_HIGG8D1.e5271_s3126_r9364_r9315_p4133
 mc16_13TeV.364109.Sherpa_221_NNPDF30NNLO_Zmumu_MAXHTPTV280_500_CVetoBVeto.deriv.DAOD_HIGG8D1.e5271_s3126_r9364_r9315_p4133
 mc16_13TeV.364110.Sherpa_221_NNPDF30NNLO_Zmumu_MAXHTPTV280_500_CFilterBVeto.deriv.DAOD_HIGG8D1.e5271_s3126_r9364_r9315_p4133
 mc16_13TeV.364111.Sherpa_221_NNPDF30NNLO_Zmumu_MAXHTPTV280_500_BFilter.deriv.DAOD_HIGG8D1.e5271_e5984_s3126_r9364_r9315_p4133
 mc16_13TeV.364111.Sherpa_221_NNPDF30NNLO_Zmumu_MAXHTPTV280_500_BFilter.deriv.DAOD_HIGG8D1.e5271_s3126_r9364_r9315_p4133
 mc16_13TeV.364112.Sherpa_221_NNPDF30NNLO_Zmumu_MAXHTPTV500_1000.deriv.DAOD_HIGG8D1.e5271_s3126_r9364_r9315_p4133
 mc16_13TeV.364113.Sherpa_221_NNPDF30NNLO_Zmumu_MAXHTPTV1000_E_CMS.deriv.DAOD_HIGG8D1.e5271_s3126_r9364_r9315_p4133
 mc16_13TeV.364114.Sherpa_221_NNPDF30NNLO_Zee_MAXHTPTV0_70_CVetoBVeto.deriv.DAOD_HIGG8D1.e5299_s3126_r9364_r9315_p4133
 mc16_13TeV.364115.Sherpa_221_NNPDF30NNLO_Zee_MAXHTPTV0_70_CFilterBVeto.deriv.DAOD_HIGG8D1.e5299_s3126_r9364_r9315_p4133
 mc16_13TeV.364116.Sherpa_221_NNPDF30NNLO_Zee_MAXHTPTV0_70_BFilter.deriv.DAOD_HIGG8D1.e5299_s3126_r9364_r9315_p4133
 mc16_13TeV.364117.Sherpa_221_NNPDF30NNLO_Zee_MAXHTPTV70_140_CVetoBVeto.deriv.DAOD_HIGG8D1.e5299_s3126_r9364_r9315_p4133
 mc16_13TeV.364118.Sherpa_221_NNPDF30NNLO_Zee_MAXHTPTV70_140_CFilterBVeto.deriv.DAOD_HIGG8D1.e5299_s3126_r9364_r9315_p4133
 mc16_13TeV.364119.Sherpa_221_NNPDF30NNLO_Zee_MAXHTPTV70_140_BFilter.deriv.DAOD_HIGG8D1.e5299_s3126_r9364_r9315_p4133
 mc16_13TeV.364120.Sherpa_221_NNPDF30NNLO_Zee_MAXHTPTV140_280_CVetoBVeto.deriv.DAOD_HIGG8D1.e5299_s3126_r9364_r9315_p4133
 mc16_13TeV.364121.Sherpa_221_NNPDF30NNLO_Zee_MAXHTPTV140_280_CFilterBVeto.deriv.DAOD_HIGG8D1.e5299_s3126_r9364_r9315_p4133

mc16_13TeV.364122.Sherpa_221_NNPDF30NNLO_Zee_MAXHTPTV140_280_BFilter.deriv.DAOD_HIGG8D1.e5299_s3126_r9364_r9315_p4133
 mc16_13TeV.364123.Sherpa_221_NNPDF30NNLO_Zee_MAXHTPTV280_500_CVetoBVeto.deriv.DAOD_HIGG8D1.e5299_s3126_r9364_r9315_p4133
 mc16_13TeV.364124.Sherpa_221_NNPDF30NNLO_Zee_MAXHTPTV280_500_CFilterBVeto.deriv.DAOD_HIGG8D1.e5299_s3126_r9364_r9315_p4133
 mc16_13TeV.364125.Sherpa_221_NNPDF30NNLO_Zee_MAXHTPTV280_500_BFilter.deriv.DAOD_HIGG8D1.e5299_s3126_r9364_r9315_p4133
 mc16_13TeV.364125.Sherpa_221_NNPDF30NNLO_Zee_MAXHTPTV280_500_BFilter.deriv.DAOD_HIGG8D1.e5299_e5984_s3126_r9364_r9315_p4133
 mc16_13TeV.364126.Sherpa_221_NNPDF30NNLO_Zee_MAXHTPTV500_1000.deriv.DAOD_HIGG8D1.e5299_s3126_r9364_r9315_p4133
 mc16_13TeV.364127.Sherpa_221_NNPDF30NNLO_Zee_MAXHTPTV1000_E_CMS.deriv.DAOD_HIGG8D1.e5299_s3126_r9364_r9315_p4133
 mc16_13TeV.364128.Sherpa_221_NNPDF30NNLO_Ztautau_MAXHTPTV0_70_CVetoBVeto.deriv.DAOD_HIGG8D1.e5307_s3126_r9364_r9315_p4133
 mc16_13TeV.364129.Sherpa_221_NNPDF30NNLO_Ztautau_MAXHTPTV0_70_CFilterBVeto.deriv.DAOD_HIGG8D1.e5307_s3126_r9364_r9315_p4133
 mc16_13TeV.364130.Sherpa_221_NNPDF30NNLO_Ztautau_MAXHTPTV0_70_BFilter.deriv.DAOD_HIGG8D1.e5307_s3126_r9364_r9315_p4133
 mc16_13TeV.364131.Sherpa_221_NNPDF30NNLO_Ztautau_MAXHTPTV70_140_CVetoBVeto.deriv.DAOD_HIGG8D1.e5307_s3126_r9364_r9315_p4133
 mc16_13TeV.364132.Sherpa_221_NNPDF30NNLO_Ztautau_MAXHTPTV70_140_CFilterBVeto.deriv.DAOD_HIGG8D1.e5307_s3126_r9364_r9315_p4133
 mc16_13TeV.364133.Sherpa_221_NNPDF30NNLO_Ztautau_MAXHTPTV70_140_BFilter.deriv.DAOD_HIGG8D1.e5307_s3126_r9364_r9315_p4133
 mc16_13TeV.364134.Sherpa_221_NNPDF30NNLO_Ztautau_MAXHTPTV140_280_CVetoBVeto.deriv.DAOD_HIGG8D1.e5307_s3126_r9364_r9315_p4133
 mc16_13TeV.364135.Sherpa_221_NNPDF30NNLO_Ztautau_MAXHTPTV140_280_CFilterBVeto.deriv.DAOD_HIGG8D1.e5307_s3126_r9364_r9315_p4133
 mc16_13TeV.364136.Sherpa_221_NNPDF30NNLO_Ztautau_MAXHTPTV140_280_BFilter.deriv.DAOD_HIGG8D1.e5307_s3126_r9364_r9315_p4133
 mc16_13TeV.364137.Sherpa_221_NNPDF30NNLO_Ztautau_MAXHTPTV280_500_CVetoBVeto.deriv.DAOD_HIGG8D1.e5307_e5984_s3126_r9364_r9315_p4133
 mc16_13TeV.364137.Sherpa_221_NNPDF30NNLO_Ztautau_MAXHTPTV280_500_CVetoBVeto.deriv.DAOD_HIGG8D1.e5307_s3126_r9364_r9315_p4133
 mc16_13TeV.364138.Sherpa_221_NNPDF30NNLO_Ztautau_MAXHTPTV280_500_CFilterBVeto.deriv.DAOD_HIGG8D1.e5313_s3126_r9364_r9315_p4133
 mc16_13TeV.364139.Sherpa_221_NNPDF30NNLO_Ztautau_MAXHTPTV280_500_BFilter.deriv.DAOD_HIGG8D1.e5313_s3126_r9364_r9315_p4133
 mc16_13TeV.364140.Sherpa_221_NNPDF30NNLO_Ztautau_MAXHTPTV500_1000.deriv.DAOD_HIGG8D1.e5307_s3126_r9364_r9315_p4133
 mc16_13TeV.364141.Sherpa_221_NNPDF30NNLO_Ztautau_MAXHTPTV1000_E_CMS.deriv.DAOD_HIGG8D1.e5307_s3126_r9364_r9315_p4133
 mc16_13TeV.364198.Sherpa_221_NN30NNLO_Zmm_Mll10_40_MAXHTPTV0_70_BVeto.deriv.DAOD_HIGG8D1.e5421_s3126_r9364_r9315_p4133
 mc16_13TeV.364199.Sherpa_221_NN30NNLO_Zmm_Mll10_40_MAXHTPTV0_70_BFilter.deriv.DAOD_HIGG8D1.e5421_s3126_r9364_r9315_p4133
 mc16_13TeV.364200.Sherpa_221_NN30NNLO_Zmm_Mll10_40_MAXHTPTV70_280_BVeto.deriv.DAOD_HIGG8D1.e5421_s3126_r9364_r9315_p4133
 mc16_13TeV.364201.Sherpa_221_NN30NNLO_Zmm_Mll10_40_MAXHTPTV70_280_BFilter.deriv.DAOD_HIGG8D1.e5421_s3126_r9364_r9315_p4133
 mc16_13TeV.364202.Sherpa_221_NN30NNLO_Zmm_Mll10_40_MAXHTPTV280_E_CMS_BVeto.deriv.DAOD_HIGG8D1.e5421_s3126_r9364_r9315_p4133
 mc16_13TeV.364203.Sherpa_221_NN30NNLO_Zmm_Mll10_40_MAXHTPTV280_E_CMS_BFilter.deriv.DAOD_HIGG8D1.e5421_s3126_r9364_r9315_p4133
 mc16_13TeV.364204.Sherpa_221_NN30NNLO_Zee_Mll10_40_MAXHTPTV0_70_BVeto.deriv.DAOD_HIGG8D1.e5421_s3126_r9364_r9315_p4133
 mc16_13TeV.364205.Sherpa_221_NN30NNLO_Zee_Mll10_40_MAXHTPTV0_70_BFilter.deriv.DAOD_HIGG8D1.e5421_s3126_r9364_r9315_p4133
 mc16_13TeV.364206.Sherpa_221_NN30NNLO_Zee_Mll10_40_MAXHTPTV70_280_BVeto.deriv.DAOD_HIGG8D1.e5421_s3126_r9364_r9315_p4133

mc16_13TeV.364207.Sherpa_221_NN30NNLO_Zee_Mll10_40_MAXHTPTV70_280_BFilter.deriv.DAOD_HIGG8D1.e5421_s3126_r9364_r9315_p4133
 mc16_13TeV.364208.Sherpa_221_NN30NNLO_Zee_Mll10_40_MAXHTPTV280_E_CMS_BVeto.deriv.DAOD_HIGG8D1.e5421_s3126_r9364_r9315_p4133
 mc16_13TeV.364209.Sherpa_221_NN30NNLO_Zee_Mll10_40_MAXHTPTV280_E_CMS_BFilter.deriv.DAOD_HIGG8D1.e5421_s3126_r9364_r9315_p4133
 mc16_13TeV.364210.Sherpa_221_NN30NNLO_Ztt_Mll10_40_MAXHTPTV0_70_BVeto.deriv.DAOD_HIGG8D1.e5421_s3126_r9364_r9315_p4133
 mc16_13TeV.364211.Sherpa_221_NN30NNLO_Ztt_Mll10_40_MAXHTPTV0_70_BFilter.deriv.DAOD_HIGG8D1.e5421_s3126_r9364_r9315_p4133
 mc16_13TeV.364212.Sherpa_221_NN30NNLO_Ztt_Mll10_40_MAXHTPTV70_280_BVeto.deriv.DAOD_HIGG8D1.e5421_s3126_r9364_r9315_p4133
 mc16_13TeV.364213.Sherpa_221_NN30NNLO_Ztt_Mll10_40_MAXHTPTV70_280_BFilter.deriv.DAOD_HIGG8D1.e5421_s3126_r9364_r9315_p4133
 mc16_13TeV.364214.Sherpa_221_NN30NNLO_Ztt_Mll10_40_MAXHTPTV280_E_CMS_BVeto.deriv.DAOD_HIGG8D1.e5421_s3126_r9364_r9315_p4133
 mc16_13TeV.364215.Sherpa_221_NN30NNLO_Ztt_Mll10_40_MAXHTPTV280_E_CMS_BFilter.deriv.DAOD_HIGG8D1.e5421_s3126_r9364_r9315_p4133
 mc16_13TeV.364156.Sherpa_221_NNPDF30NNLO_Wmunu_MAXHTPTV0_70_CVetoBVeto.deriv.DAOD_HIGG8D1.e5340_s3126_r9364_r9315_p4133
 mc16_13TeV.364157.Sherpa_221_NNPDF30NNLO_Wmunu_MAXHTPTV0_70_CFilterBVeto.deriv.DAOD_HIGG8D1.e5340_s3126_r9364_r9315_p4133
 mc16_13TeV.364157.Sherpa_221_NNPDF30NNLO_Wmunu_MAXHTPTV0_70_CFilterBVeto.deriv.DAOD_HIGG8D1.e5340_e5984_s3126_r9364_r9315_p4133
 mc16_13TeV.364158.Sherpa_221_NNPDF30NNLO_Wmunu_MAXHTPTV0_70_BFilter.deriv.DAOD_HIGG8D1.e5340_s3126_r9364_r9315_p4133
 mc16_13TeV.364159.Sherpa_221_NNPDF30NNLO_Wmunu_MAXHTPTV70_140_CVetoBVeto.deriv.DAOD_HIGG8D1.e5340_s3126_r9364_r9315_p4133
 mc16_13TeV.364160.Sherpa_221_NNPDF30NNLO_Wmunu_MAXHTPTV70_140_CFilterBVeto.deriv.DAOD_HIGG8D1.e5340_s3126_r9364_r9315_p4133
 mc16_13TeV.364161.Sherpa_221_NNPDF30NNLO_Wmunu_MAXHTPTV70_140_BFilter.deriv.DAOD_HIGG8D1.e5340_s3126_r9364_r9315_p4133
 mc16_13TeV.364162.Sherpa_221_NNPDF30NNLO_Wmunu_MAXHTPTV140_280_CVetoBVeto.deriv.DAOD_HIGG8D1.e5340_s3126_r9364_r9315_p4133
 mc16_13TeV.364163.Sherpa_221_NNPDF30NNLO_Wmunu_MAXHTPTV140_280_CFilterBVeto.deriv.DAOD_HIGG8D1.e5340_s3126_r9364_r9315_p4133
 mc16_13TeV.364163.Sherpa_221_NNPDF30NNLO_Wmunu_MAXHTPTV140_280_CFilterBVeto.deriv.DAOD_HIGG8D1.e5340_e5984_s3126_s3136_r9364_r9315_p4133
 mc16_13TeV.364164.Sherpa_221_NNPDF30NNLO_Wmunu_MAXHTPTV140_280_BFilter.deriv.DAOD_HIGG8D1.e5340_s3126_r9364_r9315_p4133
 mc16_13TeV.364165.Sherpa_221_NNPDF30NNLO_Wmunu_MAXHTPTV280_500_CVetoBVeto.deriv.DAOD_HIGG8D1.e5340_s3126_r9364_r9315_p4133
 mc16_13TeV.364166.Sherpa_221_NNPDF30NNLO_Wmunu_MAXHTPTV280_500_CFilterBVeto.deriv.DAOD_HIGG8D1.e5340_s3126_r9364_r9315_p4133
 mc16_13TeV.364167.Sherpa_221_NNPDF30NNLO_Wmunu_MAXHTPTV280_500_BFilter.deriv.DAOD_HIGG8D1.e5340_e5984_s3126_r9364_r9315_p4133
 mc16_13TeV.364167.Sherpa_221_NNPDF30NNLO_Wmunu_MAXHTPTV280_500_BFilter.deriv.DAOD_HIGG8D1.e5340_s3126_r9364_r9315_p4133
 mc16_13TeV.364168.Sherpa_221_NNPDF30NNLO_Wmunu_MAXHTPTV500_1000.deriv.DAOD_HIGG8D1.e5340_s3126_r9364_r9315_p4133
 mc16_13TeV.364169.Sherpa_221_NNPDF30NNLO_Wmunu_MAXHTPTV1000_E_CMS.deriv.DAOD_HIGG8D1.e5340_s3126_r9364_r9315_p4133
 mc16_13TeV.364170.Sherpa_221_NNPDF30NNLO_Wenu_MAXHTPTV0_70_CVetoBVeto.deriv.DAOD_HIGG8D1.e5340_s3126_r9364_r9315_p4133
 mc16_13TeV.364171.Sherpa_221_NNPDF30NNLO_Wenu_MAXHTPTV0_70_CFilterBVeto.deriv.DAOD_HIGG8D1.e5340_e5984_s3126_r9364_r9315_p4133
 mc16_13TeV.364171.Sherpa_221_NNPDF30NNLO_Wenu_MAXHTPTV0_70_CFilterBVeto.deriv.DAOD_HIGG8D1.e5340_s3126_r9364_r9315_p4133
 mc16_13TeV.364172.Sherpa_221_NNPDF30NNLO_Wenu_MAXHTPTV0_70_BFilter.deriv.DAOD_HIGG8D1.e5340_s3126_r9364_r9315_p4133
 mc16_13TeV.364173.Sherpa_221_NNPDF30NNLO_Wenu_MAXHTPTV70_140_CVetoBVeto.deriv.DAOD_HIGG8D1.e5340_s3126_r9364_r9315_p4133

mc16_13TeV.364174.Sherpa_221_NNPDF30NNLO_Wenu_MAXHTPTV70_140_CFilterBVeto.deriv.DAOD_HIGG8D1.e5340_s3126_r9364_r9315_p4133
 mc16_13TeV.364175.Sherpa_221_NNPDF30NNLO_Wenu_MAXHTPTV70_140_BFilter.deriv.DAOD_HIGG8D1.e5340_e5984_s3126_s3136_r9364_r9315_p4133
 mc16_13TeV.364175.Sherpa_221_NNPDF30NNLO_Wenu_MAXHTPTV70_140_BFilter.deriv.DAOD_HIGG8D1.e5340_s3126_r9364_r9315_p4133
 mc16_13TeV.364176.Sherpa_221_NNPDF30NNLO_Wenu_MAXHTPTV140_280_CVetoBVeto.deriv.DAOD_HIGG8D1.e5340_s3126_r9364_r9315_p4133
 mc16_13TeV.364177.Sherpa_221_NNPDF30NNLO_Wenu_MAXHTPTV140_280_CFilterBVeto.deriv.DAOD_HIGG8D1.e5340_s3126_r9364_r9315_p4133
 mc16_13TeV.364177.Sherpa_221_NNPDF30NNLO_Wenu_MAXHTPTV140_280_CFilterBVeto.deriv.DAOD_HIGG8D1.e5340_e5984_s3126_s3136_r9364_r9315_p4133
 mc16_13TeV.364178.Sherpa_221_NNPDF30NNLO_Wenu_MAXHTPTV140_280_BFilter.deriv.DAOD_HIGG8D1.e5340_s3126_r9364_r9315_p4133
 mc16_13TeV.364179.Sherpa_221_NNPDF30NNLO_Wenu_MAXHTPTV280_500_CVetoBVeto.deriv.DAOD_HIGG8D1.e5340_s3126_r9364_r9315_p4133
 mc16_13TeV.364180.Sherpa_221_NNPDF30NNLO_Wenu_MAXHTPTV280_500_CFilterBVeto.deriv.DAOD_HIGG8D1.e5340_s3126_r9364_r9315_p4133
 mc16_13TeV.364181.Sherpa_221_NNPDF30NNLO_Wenu_MAXHTPTV280_500_BFilter.deriv.DAOD_HIGG8D1.e5340_e5984_s3126_r9364_r9315_p4133
 mc16_13TeV.364181.Sherpa_221_NNPDF30NNLO_Wenu_MAXHTPTV280_500_BFilter.deriv.DAOD_HIGG8D1.e5340_s3126_r9364_r9315_p4133
 mc16_13TeV.364182.Sherpa_221_NNPDF30NNLO_Wenu_MAXHTPTV500_1000.deriv.DAOD_HIGG8D1.e5340_s3126_r9364_r9315_p4133
 mc16_13TeV.364183.Sherpa_221_NNPDF30NNLO_Wenu_MAXHTPTV1000_E_CMS.deriv.DAOD_HIGG8D1.e5340_s3126_r9364_r9315_p4133
 mc16_13TeV.364184.Sherpa_221_NNPDF30NNLO_Wtaunu_MAXHTPTV0_70_CVetoBVeto.deriv.DAOD_HIGG8D1.e5340_s3126_r9364_r9315_p4133
 mc16_13TeV.364185.Sherpa_221_NNPDF30NNLO_Wtaunu_MAXHTPTV0_70_CFilterBVeto.deriv.DAOD_HIGG8D1.e5340_e5984_s3126_r9364_r9315_p4133
 mc16_13TeV.364185.Sherpa_221_NNPDF30NNLO_Wtaunu_MAXHTPTV0_70_CFilterBVeto.deriv.DAOD_HIGG8D1.e5340_s3126_r9364_r9315_p4133
 mc16_13TeV.364186.Sherpa_221_NNPDF30NNLO_Wtaunu_MAXHTPTV0_70_BFilter.deriv.DAOD_HIGG8D1.e5340_s3126_r9364_r9315_p4133
 mc16_13TeV.364187.Sherpa_221_NNPDF30NNLO_Wtaunu_MAXHTPTV70_140_CVetoBVeto.deriv.DAOD_HIGG8D1.e5340_s3126_r9364_r9315_p4133
 mc16_13TeV.364188.Sherpa_221_NNPDF30NNLO_Wtaunu_MAXHTPTV70_140_CFilterBVeto.deriv.DAOD_HIGG8D1.e5340_s3126_r9364_r9315_p4133
 mc16_13TeV.364189.Sherpa_221_NNPDF30NNLO_Wtaunu_MAXHTPTV70_140_BFilter.deriv.DAOD_HIGG8D1.e5340_s3126_r9364_r9315_p4133
 mc16_13TeV.364190.Sherpa_221_NNPDF30NNLO_Wtaunu_MAXHTPTV140_280_CVetoBVeto.deriv.DAOD_HIGG8D1.e5340_e5984_s3126_r9364_r9315_p4133
 mc16_13TeV.364190.Sherpa_221_NNPDF30NNLO_Wtaunu_MAXHTPTV140_280_CVetoBVeto.deriv.DAOD_HIGG8D1.e5340_s3126_r9364_r9315_p4133
 mc16_13TeV.364191.Sherpa_221_NNPDF30NNLO_Wtaunu_MAXHTPTV140_280_CFilterBVeto.deriv.DAOD_HIGG8D1.e5340_s3126_r9364_r9315_p4133
 mc16_13TeV.364191.Sherpa_221_NNPDF30NNLO_Wtaunu_MAXHTPTV140_280_CFilterBVeto.deriv.DAOD_HIGG8D1.e5340_e5984_s3126_s3136_r9364_r9315_p4133
 mc16_13TeV.364192.Sherpa_221_NNPDF30NNLO_Wtaunu_MAXHTPTV140_280_BFilter.deriv.DAOD_HIGG8D1.e5340_s3126_r9364_r9315_p4133
 mc16_13TeV.364193.Sherpa_221_NNPDF30NNLO_Wtaunu_MAXHTPTV280_500_CVetoBVeto.deriv.DAOD_HIGG8D1.e5340_s3126_r9364_r9315_p4133
 mc16_13TeV.364193.Sherpa_221_NNPDF30NNLO_Wtaunu_MAXHTPTV280_500_CVetoBVeto.deriv.DAOD_HIGG8D1.e5340_e5984_s3126_s3136_r9364_r9315_p4133
 mc16_13TeV.364194.Sherpa_221_NNPDF30NNLO_Wtaunu_MAXHTPTV280_500_CFilterBVeto.deriv.DAOD_HIGG8D1.e5340_e5984_s3126_s3136_r9364_r9315_p4133
 mc16_13TeV.364195.Sherpa_221_NNPDF30NNLO_Wtaunu_MAXHTPTV280_500_BFilter.deriv.DAOD_HIGG8D1.e5340_s3126_r9364_r9315_p4133
 mc16_13TeV.364196.Sherpa_221_NNPDF30NNLO_Wtaunu_MAXHTPTV500_1000.deriv.DAOD_HIGG8D1.e5340_s3126_r9364_r9315_p4133

mc16_13TeV.364197.Sherpa_221_NNPDF30NNLO_Wtaunu_MAXHTPTV1000_E_CMS.deriv.DAOD_HIGG8D1.e5340_s3126_r9364_r9315_p4133
 mc16_13TeV.364500.Sherpa_222_NNPDF30NNLO_eegamma_pty_7_15.deriv.DAOD_HIGG8D1.e5928_e5984_s3126_r9364_r9315_p4133
 mc16_13TeV.364501.Sherpa_222_NNPDF30NNLO_eegamma_pty_15_35.deriv.DAOD_HIGG8D1.e5928_e5984_s3126_r9364_r9315_p4133
 mc16_13TeV.364502.Sherpa_222_NNPDF30NNLO_eegamma_pty_35_70.deriv.DAOD_HIGG8D1.e5928_e5984_s3126_r9364_r9315_p4133
 mc16_13TeV.364503.Sherpa_222_NNPDF30NNLO_eegamma_pty_70_140.deriv.DAOD_HIGG8D1.e5928_e5984_s3126_r9364_r9315_p4133
 mc16_13TeV.364504.Sherpa_222_NNPDF30NNLO_eegamma_pty_140_E_CMS.deriv.DAOD_HIGG8D1.e5928_e5984_s3126_r9364_r9315_p4133
 mc16_13TeV.364505.Sherpa_222_NNPDF30NNLO_mumugamma_pty_7_15.deriv.DAOD_HIGG8D1.e5928_e5984_s3126_r9364_r9315_p4133
 mc16_13TeV.364506.Sherpa_222_NNPDF30NNLO_mumugamma_pty_15_35.deriv.DAOD_HIGG8D1.e5988_e5984_s3126_r9364_r9315_p4133
 mc16_13TeV.364507.Sherpa_222_NNPDF30NNLO_mumugamma_pty_35_70.deriv.DAOD_HIGG8D1.e5928_e5984_s3126_r9364_r9315_p4133
 mc16_13TeV.364508.Sherpa_222_NNPDF30NNLO_mumugamma_pty_70_140.deriv.DAOD_HIGG8D1.e5928_e5984_s3126_r9364_r9315_p4133
 mc16_13TeV.364509.Sherpa_222_NNPDF30NNLO_mumugamma_pty_140_E_CMS.deriv.DAOD_HIGG8D1.e5928_e5984_s3126_r9364_r9315_p4133
 mc16_13TeV.364510.Sherpa_222_NNPDF30NNLO_tautaugamma_pty_7_15.deriv.DAOD_HIGG8D1.e5928_s3126_r9364_r9315_p4133
 mc16_13TeV.364511.Sherpa_222_NNPDF30NNLO_tautaugamma_pty_15_35.deriv.DAOD_HIGG8D1.e5928_s3126_r9364_r9315_p4133
 mc16_13TeV.364512.Sherpa_222_NNPDF30NNLO_tautaugamma_pty_35_70.deriv.DAOD_HIGG8D1.e5928_s3126_r9364_r9315_p4133
 mc16_13TeV.364513.Sherpa_222_NNPDF30NNLO_tautaugamma_pty_70_140.deriv.DAOD_HIGG8D1.e5982_s3126_r9364_r9315_p4133
 mc16_13TeV.364514.Sherpa_222_NNPDF30NNLO_tautaugamma_pty_140_E_CMS.deriv.DAOD_HIGG8D1.e5928_s3126_r9364_r9315_p4133
 mc16_13TeV.364521.Sherpa_222_NNPDF30NNLO_enugamma_pty_7_15.deriv.DAOD_HIGG8D1.e5928_s3126_r9364_r9315_p4133
 mc16_13TeV.364522.Sherpa_222_NNPDF30NNLO_enugamma_pty_15_35.deriv.DAOD_HIGG8D1.e5928_s3126_r9364_r9315_p4133
 mc16_13TeV.364523.Sherpa_222_NNPDF30NNLO_enugamma_pty_35_70.deriv.DAOD_HIGG8D1.e5928_s3126_r9364_r9315_p4133
 mc16_13TeV.364524.Sherpa_222_NNPDF30NNLO_enugamma_pty_70_140.deriv.DAOD_HIGG8D1.e5928_s3126_r9364_r9315_p4133
 mc16_13TeV.364525.Sherpa_222_NNPDF30NNLO_enugamma_pty_140_E_CMS.deriv.DAOD_HIGG8D1.e5928_s3126_r9364_r9315_p4133
 mc16_13TeV.364526.Sherpa_222_NNPDF30NNLO_munugamma_pty_7_15.deriv.DAOD_HIGG8D1.e5928_s3126_r9364_r9315_p4133
 mc16_13TeV.364527.Sherpa_222_NNPDF30NNLO_munugamma_pty_15_35.deriv.DAOD_HIGG8D1.e5928_s3126_r9364_r9315_p4133
 mc16_13TeV.364528.Sherpa_222_NNPDF30NNLO_munugamma_pty_35_70.deriv.DAOD_HIGG8D1.e5928_s3126_r9364_r9315_p4133
 mc16_13TeV.364529.Sherpa_222_NNPDF30NNLO_munugamma_pty_70_140.deriv.DAOD_HIGG8D1.e5928_s3126_r9364_r9315_p4133
 mc16_13TeV.364530.Sherpa_222_NNPDF30NNLO_munugamma_pty_140_E_CMS.deriv.DAOD_HIGG8D1.e5928_s3126_r9364_r9315_p4133
 mc16_13TeV.364530.Sherpa_222_NNPDF30NNLO_munugamma_pty_140_E_CMS.deriv.DAOD_HIGG8D1.e5928_e5984_s3126_r9364_r9315_p4133
 mc16_13TeV.364531.Sherpa_222_NNPDF30NNLO_taunugamma_pty_7_15.deriv.DAOD_HIGG8D1.e5928_s3126_r9364_r9315_p4133
 mc16_13TeV.364532.Sherpa_222_NNPDF30NNLO_taunugamma_pty_15_35.deriv.DAOD_HIGG8D1.e5928_s3126_r9364_r9315_p4133
 mc16_13TeV.364533.Sherpa_222_NNPDF30NNLO_taunugamma_pty_35_70.deriv.DAOD_HIGG8D1.e5928_s3126_r9364_r9315_p4133

mc16_13TeV.364534.Sherpa_222_NNPDF30NNLO_taunugamma_pty_70_140.deriv.DAOD_HIGG8D1.e5928_s3126_r9364_r9315_p4133
 mc16_13TeV.364535.Sherpa_222_NNPDF30NNLO_taunugamma_pty_140_E_CMS.deriv.DAOD_HIGG8D1.e5928_s3126_r9364_r9315_p4133
 mc16_13TeV.364535.Sherpa_222_NNPDF30NNLO_taunugamma_pty_140_E_CMS.deriv.DAOD_HIGG8D1.e5928_e5984_s3126_r9364_r9315_p4133
 mc16_13TeV.410560.MadGraphPythia8EvtGen_A14_tZ_4fl_tchan_noAllHad.deriv.DAOD_HIGG8D1.e5803_s3126_r9364_r9315_p4133
 mc16_13TeV.410013.PowhegPythiaEvtGen_P2012_Wt_inclusive_top.deriv.DAOD_HIGG8D1.e3753_s3126_r9364_r9315_p4133
 mc16_13TeV.410014.PowhegPythiaEvtGen_P2012_Wt_inclusive_antitop.deriv.DAOD_HIGG8D1.e3753_s3126_r9364_r9315_p4133
 mc16_13TeV.410408.aMcAtNloPythia8EvtGen_tWZ_Ztoll_minDR1.deriv.DAOD_HIGG8D1.e6423_e5984_s3126_r9364_r9315_p4133
 mc16_13TeV.364242.Sherpa_222_NNPDF30NNLO_WWW_3l3v_EW6.deriv.DAOD_HIGG8D1.e5887_s3126_r9364_r9315_p4133
 mc16_13TeV.364243.Sherpa_222_NNPDF30NNLO_WWZ_4l2v_EW6.deriv.DAOD_HIGG8D1.e5887_s3126_r9364_r9315_p4133
 mc16_13TeV.364244.Sherpa_222_NNPDF30NNLO_WWZ_2l4v_EW6.deriv.DAOD_HIGG8D1.e5887_s3126_r9364_r9315_p4133
 mc16_13TeV.364245.Sherpa_222_NNPDF30NNLO_WZZ_5l1v_EW6.deriv.DAOD_HIGG8D1.e5887_s3126_r9364_r9315_p4133
 mc16_13TeV.364246.Sherpa_222_NNPDF30NNLO_WZZ_3l3v_EW6.deriv.DAOD_HIGG8D1.e5887_s3126_r9364_r9315_p4133
 mc16_13TeV.364247.Sherpa_222_NNPDF30NNLO_ZZZ_6l0v_EW6.deriv.DAOD_HIGG8D1.e5887_s3126_r9364_r9315_p4133
 mc16_13TeV.364248.Sherpa_222_NNPDF30NNLO_ZZZ_4l2v_EW6.deriv.DAOD_HIGG8D1.e5887_s3126_r9364_r9315_p4133
 mc16_13TeV.364249.Sherpa_222_NNPDF30NNLO_ZZZ_2l4v_EW6.deriv.DAOD_HIGG8D1.e5887_s3126_r9364_r9315_p4133
 mc16_13TeV.342284.Pythia8EvtGen_A14NNPDF23LO_WH125_inc.deriv.DAOD_HIGG8D1.e4246_s3126_r9364_r9315_p4133
 mc16_13TeV.342285.Pythia8EvtGen_A14NNPDF23LO_ZH125_inc.deriv.DAOD_HIGG8D1.e4246_s3126_r9364_r9315_p4133
 mc16_13TeV.341998.aMcAtNloHppEG_UEEE5_CTEQ6L1_CT10ME_tWH125_gamgam_yt_plus1.deriv.DAOD_HIGG8D1.e4394_e5984_s3126_r9364_r9315_p4133
 mc16_13TeV.410389.MadGraphPythia8EvtGen_A14NNPDF23_ttgamma_nonallhadronic.deriv.DAOD_HIGG8D1.e6155_e5984_s3126_r9364_r9315_p4133
 mc16_13TeV.410470.PhPy8EG_A14_ttbar_hdamp258p75_nonallhad.deriv.DAOD_HIGG8D1.e6337_e5984_s3126_r9364_r9315_p4133
 mc16_13TeV.410472.PhPy8EG_A14_ttbar_hdamp258p75_dil.deriv.DAOD_HIGG8D1.e6348_e5984_s3126_r9364_r9315_p4133
 mc16_13TeV.346343.PhPy8EG_A14NNPDF23_NNPDF30ME_ttH125_allhad.deriv.DAOD_HIGG8D1.e7148_e5984_s3126_r9364_r9315_p4133
 mc16_13TeV.346344.PhPy8EG_A14NNPDF23_NNPDF30ME_ttH125_semilep.deriv.DAOD_HIGG8D1.e7148_e5984_s3126_r9364_r9315_p4133
 mc16_13TeV.346345.PhPy8EG_A14NNPDF23_NNPDF30ME_ttH125_dilep.deriv.DAOD_HIGG8D1.e7148_e5984_s3126_r9364_r9315_p4133

mc16d:

mc16_13TeV.364253.Sherpa_222_NNPDF30NNLO_lllv.deriv.DAOD_HIGG8D1.e5916_e5984_s3126_r10201_r10210_p4133
 mc16_13TeV.364250.Sherpa_222_NNPDF30NNLO_llll.deriv.DAOD_HIGG8D1.e5894_e5984_s3126_r10201_r10210_p4133
 mc16_13TeV.364254.Sherpa_222_NNPDF30NNLO_llvv.deriv.DAOD_HIGG8D1.e5916_e5984_s3126_r10201_r10210_p4133
 mc16_13TeV.364255.Sherpa_222_NNPDF30NNLO_lvvv.deriv.DAOD_HIGG8D1.e5916_e5984_s3126_r10201_r10210_p4133
 mc16_13TeV.410155.aMcAtNloPythia8EvtGen_MEN30NLO_A14N23LO_ttW.deriv.DAOD_HIGG8D1.e5070_e5984_s3126_r10201_r10210_p4133

mc16_13TeV.410156.aMcAtNloPythia8EvtGen_MEN30NLO_A14N23LO_ttZnunu.deriv.DAOD_HIGG8D1.e5070_e5984_s3126_r10201_r10210_p4133
 mc16_13TeV.410157.aMcAtNloPythia8EvtGen_MEN30NLO_A14N23LO_ttZqq.deriv.DAOD_HIGG8D1.e5070_e5984_s3126_r10201_r10210_p4133
 mc16_13TeV.410218.aMcAtNloPythia8EvtGen_MEN30NLO_A14N23LO_ttee.deriv.DAOD_HIGG8D1.e5070_e5984_s3126_r10201_r10210_p4133
 mc16_13TeV.410219.aMcAtNloPythia8EvtGen_MEN30NLO_A14N23LO_ttmumu.deriv.DAOD_HIGG8D1.e5070_e5984_s3126_r10201_r10210_p4133
 mc16_13TeV.410220.aMcAtNloPythia8EvtGen_MEN30NLO_A14N23LO_ttautau.deriv.DAOD_HIGG8D1.e5070_e5984_s3126_r10201_r10210_p4133
 mc16_13TeV.410276.aMcAtNloPythia8EvtGen_MEN30NLO_A14N23LO_ttee_mll_1_5.deriv.DAOD_HIGG8D1.e6087_e5984_s3126_r10201_r10210_p4133
 mc16_13TeV.410277.aMcAtNloPythia8EvtGen_MEN30NLO_A14N23LO_ttmumu_mll_1_5.deriv.DAOD_HIGG8D1.e6087_e5984_s3126_r10201_r10210_p4133
 mc16_13TeV.410278.aMcAtNloPythia8EvtGen_MEN30NLO_A14N23LO_ttautau_mll_1_5.deriv.DAOD_HIGG8D1.e6087_e5984_s3126_r10201_r10210_p4133
 mc16_13TeV.410397.MadGraphPythia8EvtGen_ttbar_wbee_MEN30LO_A14N23LO.deriv.DAOD_HIGG8D1.e6086_e5984_s3126_r10201_r10210_p4133
 mc16_13TeV.410398.MadGraphPythia8EvtGen_ttbar_wbmumu_MEN30LO_A14N23LO.deriv.DAOD_HIGG8D1.e6086_e5984_s3126_r10201_r10210_p4133
 mc16_13TeV.410399.MadGraphPythia8EvtGen_ttbar_wbttau_MEN30LO_A14N23LO.deriv.DAOD_HIGG8D1.e6086_e5984_s3126_r10201_r10210_p4133
 mc16_13TeV.410658.PhPy8EG_A14_tchan_BW50_lept_top.deriv.DAOD_HIGG8D1.e6671_e5984_s3126_r10201_r10210_p4133
 mc16_13TeV.410659.PhPy8EG_A14_tchan_BW50_lept_antitop.deriv.DAOD_HIGG8D1.e6671_e5984_s3126_r10201_r10210_p4133
 mc16_13TeV.410644.PowhegPythia8EvtGen_A14_singletop_schan_lept_top.deriv.DAOD_HIGG8D1.e6527_e5984_s3126_r10201_r10210_p4133
 mc16_13TeV.410645.PowhegPythia8EvtGen_A14_singletop_schan_lept_antitop.deriv.DAOD_HIGG8D1.e6527_s3126_r10201_r10210_p4133
 mc16_13TeV.412063.aMcAtNloPythia8EvtGen_tllq_NNPDF30_nf4_A14.deriv.DAOD_TOPQ1.e7054_e5984_s3126_r10201_r10210_p4174
 mc16_13TeV.304014.MadGraphPythia8EvtGen_A14NNPDF23_3top_SM.deriv.DAOD_HIGG8D1.e4324_e5984_s3126_r10201_r10210_p4133
 mc16_13TeV.410080.MadGraphPythia8EvtGen_A14NNPDF23_4topSM.deriv.DAOD_HIGG8D1.e4111_e5984_s3126_r10201_r10210_p4133
 mc16_13TeV.410081.MadGraphPythia8EvtGen_A14NNPDF23_ttbarWW.deriv.DAOD_HIGG8D1.e4111_e5984_s3126_r10201_r10210_p4133
 mc16_13TeV.364100.Sherpa_221_NNPDF30NNLO_Zmumu_MAXHTPTV0_70_CVetoBVeto.deriv.DAOD_HIGG8D1.e5271_s3126_r10201_r10210_p4133
 mc16_13TeV.364101.Sherpa_221_NNPDF30NNLO_Zmumu_MAXHTPTV0_70_CFfilterBVeto.deriv.DAOD_HIGG8D1.e5271_s3126_r10201_r10210_p4133
 mc16_13TeV.364101.Sherpa_221_NNPDF30NNLO_Zmumu_MAXHTPTV0_70_CFfilterBVeto.deriv.DAOD_HIGG8D1.e5271_e5984_s3126_r10201_r10210_p4133
 mc16_13TeV.364102.Sherpa_221_NNPDF30NNLO_Zmumu_MAXHTPTV0_70_BFilter.deriv.DAOD_HIGG8D1.e5271_s3126_r10201_r10210_p4133
 mc16_13TeV.364103.Sherpa_221_NNPDF30NNLO_Zmumu_MAXHTPTV70_140_CVetoBVeto.deriv.DAOD_HIGG8D1.e5271_s3126_r10201_r10210_p4133
 mc16_13TeV.364104.Sherpa_221_NNPDF30NNLO_Zmumu_MAXHTPTV70_140_CFfilterBVeto.deriv.DAOD_HIGG8D1.e5271_s3126_r10201_r10210_p4133
 mc16_13TeV.364106.Sherpa_221_NNPDF30NNLO_Zmumu_MAXHTPTV140_280_CVetoBVeto.deriv.DAOD_HIGG8D1.e5271_s3126_r10201_r10210_p4133
 mc16_13TeV.364107.Sherpa_221_NNPDF30NNLO_Zmumu_MAXHTPTV140_280_CFfilterBVeto.deriv.DAOD_HIGG8D1.e5271_s3126_r10201_r10210_p4133
 mc16_13TeV.364108.Sherpa_221_NNPDF30NNLO_Zmumu_MAXHTPTV140_280_BFilter.deriv.DAOD_HIGG8D1.e5271_e5984_s3126_r10201_r10210_p4133
 mc16_13TeV.364109.Sherpa_221_NNPDF30NNLO_Zmumu_MAXHTPTV280_500_CVetoBVeto.deriv.DAOD_HIGG8D1.e5271_e5984_s3126_r10201_r10210_p4133
 mc16_13TeV.364109.Sherpa_221_NNPDF30NNLO_Zmumu_MAXHTPTV280_500_CVetoBVeto.deriv.DAOD_HIGG8D1.e5271_s3126_r10201_r10210_p4133

mc16_13TeV.364110.Sherpa_221_NNPDF30NNLO_Zmumu_MAXHTPTV280_500_CFilterBVeto.deriv.DAOD_HIGG8D1.e5271_s3126_r10201_r10210_p4133
 mc16_13TeV.364111.Sherpa_221_NNPDF30NNLO_Zmumu_MAXHTPTV280_500_BFilter.deriv.DAOD_HIGG8D1.e5271_e5984_s3126_r10201_r10210_p4133
 mc16_13TeV.364111.Sherpa_221_NNPDF30NNLO_Zmumu_MAXHTPTV280_500_BFilter.deriv.DAOD_HIGG8D1.e5271_s3126_r10201_r10210_p4133
 mc16_13TeV.364112.Sherpa_221_NNPDF30NNLO_Zmumu_MAXHTPTV500_1000.deriv.DAOD_HIGG8D1.e5271_e5984_s3126_r10201_r10210_p4133
 mc16_13TeV.364112.Sherpa_221_NNPDF30NNLO_Zmumu_MAXHTPTV500_1000.deriv.DAOD_HIGG8D1.e5271_s3126_r10201_r10210_p4133
 mc16_13TeV.364113.Sherpa_221_NNPDF30NNLO_Zmumu_MAXHTPTV1000_E_CMS.deriv.DAOD_HIGG8D1.e5271_s3126_r10201_r10210_p4133
 mc16_13TeV.364114.Sherpa_221_NNPDF30NNLO_Zee_MAXHTPTV0_70_CVetoBVeto.deriv.DAOD_HIGG8D1.e5299_s3126_r10201_r10210_p4133
 mc16_13TeV.364115.Sherpa_221_NNPDF30NNLO_Zee_MAXHTPTV0_70_CFilterBVeto.deriv.DAOD_HIGG8D1.e5299_e5984_s3126_r10201_r10210_p4133
 mc16_13TeV.364116.Sherpa_221_NNPDF30NNLO_Zee_MAXHTPTV0_70_BFilter.deriv.DAOD_HIGG8D1.e5299_e5984_s3126_r10201_r10210_p4133
 mc16_13TeV.364117.Sherpa_221_NNPDF30NNLO_Zee_MAXHTPTV70_140_CVetoBVeto.deriv.DAOD_HIGG8D1.e5299_e5984_s3126_r10201_r10210_p4133
 mc16_13TeV.364118.Sherpa_221_NNPDF30NNLO_Zee_MAXHTPTV70_140_CFilterBVeto.deriv.DAOD_HIGG8D1.e5299_e5984_s3126_r10201_r10210_p4133
 mc16_13TeV.364119.Sherpa_221_NNPDF30NNLO_Zee_MAXHTPTV70_140_BFilter.deriv.DAOD_HIGG8D1.e5299_e5984_s3126_r10201_r10210_p4133
 mc16_13TeV.364120.Sherpa_221_NNPDF30NNLO_Zee_MAXHTPTV140_280_CVetoBVeto.deriv.DAOD_HIGG8D1.e5299_e5984_s3126_r10201_r10210_p4133
 mc16_13TeV.364121.Sherpa_221_NNPDF30NNLO_Zee_MAXHTPTV140_280_CFilterBVeto.deriv.DAOD_HIGG8D1.e5299_e5984_s3126_r10201_r10210_p4133
 mc16_13TeV.364122.Sherpa_221_NNPDF30NNLO_Zee_MAXHTPTV140_280_BFilter.deriv.DAOD_HIGG8D1.e5299_e5984_s3126_r10201_r10210_p4133
 mc16_13TeV.364123.Sherpa_221_NNPDF30NNLO_Zee_MAXHTPTV280_500_CVetoBVeto.deriv.DAOD_HIGG8D1.e5299_e5984_s3126_r10201_r10210_p4133
 mc16_13TeV.364124.Sherpa_221_NNPDF30NNLO_Zee_MAXHTPTV280_500_CFilterBVeto.deriv.DAOD_HIGG8D1.e5299_e5984_s3126_r10201_r10210_p4133
 mc16_13TeV.364125.Sherpa_221_NNPDF30NNLO_Zee_MAXHTPTV280_500_BFilter.deriv.DAOD_HIGG8D1.e5299_e5984_s3126_r10201_r10210_p4133
 mc16_13TeV.364126.Sherpa_221_NNPDF30NNLO_Zee_MAXHTPTV500_1000.deriv.DAOD_HIGG8D1.e5299_e5984_s3126_r10201_r10210_p4133
 mc16_13TeV.364127.Sherpa_221_NNPDF30NNLO_Zee_MAXHTPTV1000_E_CMS.deriv.DAOD_HIGG8D1.e5299_e5984_s3126_r10201_r10210_p4133
 mc16_13TeV.364128.Sherpa_221_NNPDF30NNLO_Ztautau_MAXHTPTV0_70_CVetoBVeto.deriv.DAOD_HIGG8D1.e5307_e5984_s3126_r10201_r10210_p4133
 mc16_13TeV.364129.Sherpa_221_NNPDF30NNLO_Ztautau_MAXHTPTV0_70_CFilterBVeto.deriv.DAOD_HIGG8D1.e5307_e5984_s3126_r10201_r10210_p4133
 mc16_13TeV.364130.Sherpa_221_NNPDF30NNLO_Ztautau_MAXHTPTV0_70_BFilter.deriv.DAOD_HIGG8D1.e5307_e5984_s3126_r10201_r10210_p4133
 mc16_13TeV.364131.Sherpa_221_NNPDF30NNLO_Ztautau_MAXHTPTV70_140_CVetoBVeto.deriv.DAOD_HIGG8D1.e5307_e5984_s3126_r10201_r10210_p4133
 mc16_13TeV.364132.Sherpa_221_NNPDF30NNLO_Ztautau_MAXHTPTV70_140_CFilterBVeto.deriv.DAOD_HIGG8D1.e5307_e5984_s3126_r10201_r10210_p4133
 mc16_13TeV.364133.Sherpa_221_NNPDF30NNLO_Ztautau_MAXHTPTV70_140_BFilter.deriv.DAOD_HIGG8D1.e5307_e5984_s3126_r10201_r10210_p4133
 mc16_13TeV.364134.Sherpa_221_NNPDF30NNLO_Ztautau_MAXHTPTV140_280_CVetoBVeto.deriv.DAOD_HIGG8D1.e5307_e5984_s3126_r10201_r10210_p4133
 mc16_13TeV.364135.Sherpa_221_NNPDF30NNLO_Ztautau_MAXHTPTV140_280_CFilterBVeto.deriv.DAOD_HIGG8D1.e5307_e5984_s3126_r10201_r10210_p4133
 mc16_13TeV.364136.Sherpa_221_NNPDF30NNLO_Ztautau_MAXHTPTV140_280_BFilter.deriv.DAOD_HIGG8D1.e5307_e5984_s3126_r10201_r10210_p4133
 mc16_13TeV.364137.Sherpa_221_NNPDF30NNLO_Ztautau_MAXHTPTV280_500_CVetoBVeto.deriv.DAOD_HIGG8D1.e5307_e5984_s3126_r10201_r10210_p4133
 mc16_13TeV.364138.Sherpa_221_NNPDF30NNLO_Ztautau_MAXHTPTV280_500_CFilterBVeto.deriv.DAOD_HIGG8D1.e5313_e5984_s3126_r10201_r10210_p4133

mc16_13TeV.364139.Sherpa_221_NNPDF30NNLO_Ztautau_MAXHTPTV280_500_BFilter.deriv.DAOD_HIGG8D1.e5313_e5984_s3126_r10201_r10210_p4133
 mc16_13TeV.364140.Sherpa_221_NNPDF30NNLO_Ztautau_MAXHTPTV500_1000.deriv.DAOD_HIGG8D1.e5307_e5984_s3126_r10201_r10210_p4133
 mc16_13TeV.364141.Sherpa_221_NNPDF30NNLO_Ztautau_MAXHTPTV1000_E_CMS.deriv.DAOD_HIGG8D1.e5307_e5984_s3126_r10201_r10210_p4133
 mc16_13TeV.364198.Sherpa_221_NN30NNLO_Zmm_Mll10_40_MAXHTPTV0_70_BVeto.deriv.DAOD_HIGG8D1.e5421_e5984_s3126_r10201_r10210_p4133
 mc16_13TeV.364199.Sherpa_221_NN30NNLO_Zmm_Mll10_40_MAXHTPTV0_70_BFilter.deriv.DAOD_HIGG8D1.e5421_e5984_s3126_r10201_r10210_p4133
 mc16_13TeV.364200.Sherpa_221_NN30NNLO_Zmm_Mll10_40_MAXHTPTV70_280_BVeto.deriv.DAOD_HIGG8D1.e5421_e5984_s3126_r10201_r10210_p4133
 mc16_13TeV.364201.Sherpa_221_NN30NNLO_Zmm_Mll10_40_MAXHTPTV70_280_BFilter.deriv.DAOD_HIGG8D1.e5421_e5984_s3126_r10201_r10210_p4133
 mc16_13TeV.364202.Sherpa_221_NN30NNLO_Zmm_Mll10_40_MAXHTPTV280_E_CMS_BVeto.deriv.DAOD_HIGG8D1.e5421_e5984_s3126_r10201_r10210_p4133
 mc16_13TeV.364203.Sherpa_221_NN30NNLO_Zmm_Mll10_40_MAXHTPTV280_E_CMS_BFilter.deriv.DAOD_HIGG8D1.e5421_e5984_s3126_r10201_r10210_p4133
 mc16_13TeV.364204.Sherpa_221_NN30NNLO_Zee_Mll10_40_MAXHTPTV0_70_BVeto.deriv.DAOD_HIGG8D1.e5421_e5984_s3126_r10201_r10210_p4133
 mc16_13TeV.364205.Sherpa_221_NN30NNLO_Zee_Mll10_40_MAXHTPTV0_70_BFilter.deriv.DAOD_HIGG8D1.e5421_e5984_s3126_r10201_r10210_p4133
 mc16_13TeV.364206.Sherpa_221_NN30NNLO_Zee_Mll10_40_MAXHTPTV70_280_BVeto.deriv.DAOD_HIGG8D1.e5421_e5984_s3126_r10201_r10210_p4133
 mc16_13TeV.364207.Sherpa_221_NN30NNLO_Zee_Mll10_40_MAXHTPTV70_280_BFilter.deriv.DAOD_HIGG8D1.e5421_e5984_s3126_r10201_r10210_p4133
 mc16_13TeV.364208.Sherpa_221_NN30NNLO_Zee_Mll10_40_MAXHTPTV280_E_CMS_BVeto.deriv.DAOD_HIGG8D1.e5421_e5984_s3126_r10201_r10210_p4133
 mc16_13TeV.364209.Sherpa_221_NN30NNLO_Zee_Mll10_40_MAXHTPTV280_E_CMS_BFilter.deriv.DAOD_HIGG8D1.e5421_e5984_s3126_r10201_r10210_p4133
 mc16_13TeV.364210.Sherpa_221_NN30NNLO_Ztt_Mll10_40_MAXHTPTV0_70_BVeto.deriv.DAOD_HIGG8D1.e5421_e5984_s3126_r10201_r10210_p4133
 mc16_13TeV.364211.Sherpa_221_NN30NNLO_Ztt_Mll10_40_MAXHTPTV0_70_BFilter.deriv.DAOD_HIGG8D1.e5421_e5984_s3126_r10201_r10210_p4133
 mc16_13TeV.364212.Sherpa_221_NN30NNLO_Ztt_Mll10_40_MAXHTPTV70_280_BVeto.deriv.DAOD_HIGG8D1.e5421_e5984_s3126_r10201_r10210_p4133
 mc16_13TeV.364213.Sherpa_221_NN30NNLO_Ztt_Mll10_40_MAXHTPTV70_280_BFilter.deriv.DAOD_HIGG8D1.e5421_e5984_s3126_r10201_r10210_p4133
 mc16_13TeV.364214.Sherpa_221_NN30NNLO_Ztt_Mll10_40_MAXHTPTV280_E_CMS_BVeto.deriv.DAOD_HIGG8D1.e5421_e5984_s3126_r10201_r10210_p4133
 mc16_13TeV.364215.Sherpa_221_NN30NNLO_Ztt_Mll10_40_MAXHTPTV280_E_CMS_BFilter.deriv.DAOD_HIGG8D1.e5421_e5984_s3126_r10201_r10210_p4133
 mc16_13TeV.364156.Sherpa_221_NNPDF30NNLO_Wmunu_MAXHTPTV0_70_CVetoBVeto.deriv.DAOD_HIGG8D1.e5340_s3126_r10201_r10210_p4133
 mc16_13TeV.364156.Sherpa_221_NNPDF30NNLO_Wmunu_MAXHTPTV0_70_CVetoBVeto.deriv.DAOD_HIGG8D1.e5340_e5984_s3126_s3136_r10201_r10210_p4133
 mc16_13TeV.364157.Sherpa_221_NNPDF30NNLO_Wmunu_MAXHTPTV0_70_CFilterBVeto.deriv.DAOD_HIGG8D1.e5340_e5984_s3126_s3136_r10201_r10210_p4133
 mc16_13TeV.364157.Sherpa_221_NNPDF30NNLO_Wmunu_MAXHTPTV0_70_CFilterBVeto.deriv.DAOD_HIGG8D1.e5340_s3126_r10201_r10210_p4133
 mc16_13TeV.364158.Sherpa_221_NNPDF30NNLO_Wmunu_MAXHTPTV0_70_BFilter.deriv.DAOD_HIGG8D1.e5340_e5984_s3126_s3136_r10201_r10210_p4133
 mc16_13TeV.364158.Sherpa_221_NNPDF30NNLO_Wmunu_MAXHTPTV0_70_BFilter.deriv.DAOD_HIGG8D1.e5340_s3126_r10201_r10210_p4133
 mc16_13TeV.364159.Sherpa_221_NNPDF30NNLO_Wmunu_MAXHTPTV70_140_CVetoBVeto.deriv.DAOD_HIGG8D1.e5340_s3126_r10201_r10210_p4133
 mc16_13TeV.364159.Sherpa_221_NNPDF30NNLO_Wmunu_MAXHTPTV70_140_CVetoBVeto.deriv.DAOD_HIGG8D1.e5340_e5984_s3126_r10201_r10210_p4133
 mc16_13TeV.364159.Sherpa_221_NNPDF30NNLO_Wmunu_MAXHTPTV70_140_CVetoBVeto.deriv.DAOD_HIGG8D1.e5340_e5984_s3126_s3136_r10201_r10210_p4133

mc16_13TeV.364160.Sherpa_221_NNPDF30NNLO_Wmunu_MAXHTPTV70_140_CFilterBVeto.deriv.DAOD_HIGG8D1.e5340_e5984_s3126_r10201_r10210_p4133
 mc16_13TeV.364160.Sherpa_221_NNPDF30NNLO_Wmunu_MAXHTPTV70_140_CFilterBVeto.deriv.DAOD_HIGG8D1.e5340_s3126_r10201_r10210_p4133
 mc16_13TeV.364161.Sherpa_221_NNPDF30NNLO_Wmunu_MAXHTPTV70_140_BFilter.deriv.DAOD_HIGG8D1.e5340_s3126_r10201_r10210_p4133
 mc16_13TeV.364161.Sherpa_221_NNPDF30NNLO_Wmunu_MAXHTPTV70_140_BFilter.deriv.DAOD_HIGG8D1.e5340_e5984_s3126_s3136_r10201_r10210_p4133
 mc16_13TeV.364162.Sherpa_221_NNPDF30NNLO_Wmunu_MAXHTPTV140_280_CVetoBVeto.deriv.DAOD_HIGG8D1.e5340_s3126_r10201_r10210_p4133
 mc16_13TeV.364162.Sherpa_221_NNPDF30NNLO_Wmunu_MAXHTPTV140_280_CVetoBVeto.deriv.DAOD_HIGG8D1.e5340_e5984_s3126_s3136_r10201_r10210_p4133
 mc16_13TeV.364163.Sherpa_221_NNPDF30NNLO_Wmunu_MAXHTPTV140_280_CFilterBVeto.deriv.DAOD_HIGG8D1.e5340_s3126_r10201_r10210_p4133
 mc16_13TeV.364163.Sherpa_221_NNPDF30NNLO_Wmunu_MAXHTPTV140_280_CFilterBVeto.deriv.DAOD_HIGG8D1.e5340_e5984_s3126_s3136_r10201_r10210_p4133
 mc16_13TeV.364163.Sherpa_221_NNPDF30NNLO_Wmunu_MAXHTPTV140_280_CFilterBVeto.deriv.DAOD_HIGG8D1.e5340_e5984_s3126_r10201_r10210_p4133
 mc16_13TeV.364164.Sherpa_221_NNPDF30NNLO_Wmunu_MAXHTPTV140_280_BFilter.deriv.DAOD_HIGG8D1.e5340_s3126_r10201_r10210_p4133
 mc16_13TeV.364164.Sherpa_221_NNPDF30NNLO_Wmunu_MAXHTPTV140_280_BFilter.deriv.DAOD_HIGG8D1.e5340_e5984_s3126_s3136_r10201_r10210_p4133
 mc16_13TeV.364165.Sherpa_221_NNPDF30NNLO_Wmunu_MAXHTPTV280_500_CVetoBVeto.deriv.DAOD_HIGG8D1.e5340_e5984_s3126_r10201_r10210_p4133
 mc16_13TeV.364166.Sherpa_221_NNPDF30NNLO_Wmunu_MAXHTPTV280_500_CFilterBVeto.deriv.DAOD_HIGG8D1.e5340_s3126_r10201_r10210_p4133
 mc16_13TeV.364166.Sherpa_221_NNPDF30NNLO_Wmunu_MAXHTPTV280_500_CFilterBVeto.deriv.DAOD_HIGG8D1.e5340_e5984_s3126_s3136_r10201_r10210_p4133
 mc16_13TeV.364167.Sherpa_221_NNPDF30NNLO_Wmunu_MAXHTPTV280_500_BFilter.deriv.DAOD_HIGG8D1.e5340_s3126_r10201_r10210_p4133
 mc16_13TeV.364167.Sherpa_221_NNPDF30NNLO_Wmunu_MAXHTPTV280_500_BFilter.deriv.DAOD_HIGG8D1.e5340_e5984_s3126_r10201_r10210_p4133
 mc16_13TeV.364168.Sherpa_221_NNPDF30NNLO_Wmunu_MAXHTPTV500_1000.deriv.DAOD_HIGG8D1.e5340_s3126_r10201_r10210_p4133
 mc16_13TeV.364168.Sherpa_221_NNPDF30NNLO_Wmunu_MAXHTPTV500_1000.deriv.DAOD_HIGG8D1.e5340_e5984_s3126_s3136_r10201_r10210_p4133
 mc16_13TeV.364169.Sherpa_221_NNPDF30NNLO_Wmunu_MAXHTPTV1000_E_CMS.deriv.DAOD_HIGG8D1.e5340_s3126_r10201_r10210_p4133
 mc16_13TeV.364169.Sherpa_221_NNPDF30NNLO_Wmunu_MAXHTPTV1000_E_CMS.deriv.DAOD_HIGG8D1.e5340_e5984_s3126_s3136_r10201_r10210_p4133
 mc16_13TeV.364170.Sherpa_221_NNPDF30NNLO_Wenu_MAXHTPTV0_70_CVetoBVeto.deriv.DAOD_HIGG8D1.e5340_e5984_s3126_s3136_r10201_r10210_p4133
 mc16_13TeV.364170.Sherpa_221_NNPDF30NNLO_Wenu_MAXHTPTV0_70_CVetoBVeto.deriv.DAOD_HIGG8D1.e5340_s3126_r10201_r10210_p4133
 mc16_13TeV.364171.Sherpa_221_NNPDF30NNLO_Wenu_MAXHTPTV0_70_CFilterBVeto.deriv.DAOD_HIGG8D1.e5340_e5984_s3126_r10201_r10210_p4133
 mc16_13TeV.364171.Sherpa_221_NNPDF30NNLO_Wenu_MAXHTPTV0_70_CFilterBVeto.deriv.DAOD_HIGG8D1.e5340_s3126_r10201_r10210_p4133
 mc16_13TeV.364171.Sherpa_221_NNPDF30NNLO_Wenu_MAXHTPTV0_70_CFilterBVeto.deriv.DAOD_HIGG8D1.e5340_e5984_s3126_s3136_r10201_r10210_p4133
 mc16_13TeV.364172.Sherpa_221_NNPDF30NNLO_Wenu_MAXHTPTV0_70_BFilter.deriv.DAOD_HIGG8D1.e5340_e5984_s3126_s3136_r10201_r10210_p4133
 mc16_13TeV.364172.Sherpa_221_NNPDF30NNLO_Wenu_MAXHTPTV0_70_BFilter.deriv.DAOD_HIGG8D1.e5340_e5984_s3126_r10201_r10210_p4133
 mc16_13TeV.364173.Sherpa_221_NNPDF30NNLO_Wenu_MAXHTPTV70_140_CVetoBVeto.deriv.DAOD_HIGG8D1.e5340_s3126_r10201_r10210_p4133
 mc16_13TeV.364173.Sherpa_221_NNPDF30NNLO_Wenu_MAXHTPTV70_140_CVetoBVeto.deriv.DAOD_HIGG8D1.e5340_e5984_s3126_r10201_r10210_p4133

mc16_13TeV.364174.Sherpa_221_NNPDF30NNLO_Wenu_MAXHTPTV70_140_CFilterBVeto.deriv.DAOD_HIGG8D1.e5340_s3126_r10201_r10210_p4133
 mc16_13TeV.364174.Sherpa_221_NNPDF30NNLO_Wenu_MAXHTPTV70_140_CFilterBVeto.deriv.DAOD_HIGG8D1.e5340_e5984_s3126_r10201_r10210_p4133
 mc16_13TeV.364175.Sherpa_221_NNPDF30NNLO_Wenu_MAXHTPTV70_140_BFilter.deriv.DAOD_HIGG8D1.e5340_e5984_s3126_r10201_r10210_p4133
 mc16_13TeV.364175.Sherpa_221_NNPDF30NNLO_Wenu_MAXHTPTV70_140_BFilter.deriv.DAOD_HIGG8D1.e5340_e5984_s3126_s3136_r10201_r10210_p4133
 mc16_13TeV.364175.Sherpa_221_NNPDF30NNLO_Wenu_MAXHTPTV70_140_BFilter.deriv.DAOD_HIGG8D1.e5340_s3126_r10201_r10210_p4133
 mc16_13TeV.364176.Sherpa_221_NNPDF30NNLO_Wenu_MAXHTPTV140_280_CVetoBVeto.deriv.DAOD_HIGG8D1.e5340_e5984_s3126_s3136_r10201_r10210_p4133
 mc16_13TeV.364176.Sherpa_221_NNPDF30NNLO_Wenu_MAXHTPTV140_280_CVetoBVeto.deriv.DAOD_HIGG8D1.e5340_s3126_r10201_r10210_p4133
 mc16_13TeV.364177.Sherpa_221_NNPDF30NNLO_Wenu_MAXHTPTV140_280_CFilterBVeto.deriv.DAOD_HIGG8D1.e5340_s3126_r10201_r10210_p4133
 mc16_13TeV.364177.Sherpa_221_NNPDF30NNLO_Wenu_MAXHTPTV140_280_CFilterBVeto.deriv.DAOD_HIGG8D1.e5340_e5984_s3126_s3136_r10201_r10210_p4133
 mc16_13TeV.364177.Sherpa_221_NNPDF30NNLO_Wenu_MAXHTPTV140_280_CFilterBVeto.deriv.DAOD_HIGG8D1.e5340_e5984_s3126_s3136_r10201_r10210_p4133
 mc16_13TeV.364177.Sherpa_221_NNPDF30NNLO_Wenu_MAXHTPTV140_280_CFilterBVeto.deriv.DAOD_HIGG8D1.e5340_e5984_s3126_r10201_r10210_p4133
 mc16_13TeV.364178.Sherpa_221_NNPDF30NNLO_Wenu_MAXHTPTV140_280_BFilter.deriv.DAOD_HIGG8D1.e5340_s3126_r10201_r10210_p4133
 mc16_13TeV.364179.Sherpa_221_NNPDF30NNLO_Wenu_MAXHTPTV280_500_CVetoBVeto.deriv.DAOD_HIGG8D1.e5340_s3126_r10201_r10210_p4133
 mc16_13TeV.364179.Sherpa_221_NNPDF30NNLO_Wenu_MAXHTPTV280_500_CVetoBVeto.deriv.DAOD_HIGG8D1.e5340_e5984_s3126_r10201_r10210_p4133
 mc16_13TeV.364180.Sherpa_221_NNPDF30NNLO_Wenu_MAXHTPTV280_500_CFilterBVeto.deriv.DAOD_HIGG8D1.e5340_e5984_s3126_s3136_r10201_r10210_p4133
 mc16_13TeV.364180.Sherpa_221_NNPDF30NNLO_Wenu_MAXHTPTV280_500_CFilterBVeto.deriv.DAOD_HIGG8D1.e5340_s3126_r10201_r10210_p4133
 mc16_13TeV.364181.Sherpa_221_NNPDF30NNLO_Wenu_MAXHTPTV280_500_BFilter.deriv.DAOD_HIGG8D1.e5340_e5984_s3126_r10201_r10210_p4133
 mc16_13TeV.364181.Sherpa_221_NNPDF30NNLO_Wenu_MAXHTPTV280_500_BFilter.deriv.DAOD_HIGG8D1.e5340_s3126_r10201_r10210_p4133
 mc16_13TeV.364182.Sherpa_221_NNPDF30NNLO_Wenu_MAXHTPTV500_1000.deriv.DAOD_HIGG8D1.e5340_s3126_r10201_r10210_p4133
 mc16_13TeV.364182.Sherpa_221_NNPDF30NNLO_Wenu_MAXHTPTV500_1000.deriv.DAOD_HIGG8D1.e5340_e5984_s3126_s3136_r10201_r10210_p4133
 mc16_13TeV.364183.Sherpa_221_NNPDF30NNLO_Wenu_MAXHTPTV1000_E_CMS.deriv.DAOD_HIGG8D1.e5340_e5984_s3126_r10201_r10210_p4133
 mc16_13TeV.364184.Sherpa_221_NNPDF30NNLO_Wtaunu_MAXHTPTV0_70_CVetoBVeto.deriv.DAOD_HIGG8D1.e5340_e5984_s3126_r10201_r10210_p4133
 mc16_13TeV.364184.Sherpa_221_NNPDF30NNLO_Wtaunu_MAXHTPTV0_70_CVetoBVeto.deriv.DAOD_HIGG8D1.e5340_s3126_r10201_r10210_p4133
 mc16_13TeV.364185.Sherpa_221_NNPDF30NNLO_Wtaunu_MAXHTPTV0_70_CFilterBVeto.deriv.DAOD_HIGG8D1.e5340_e5984_s3126_r10201_r10210_p4133
 mc16_13TeV.364186.Sherpa_221_NNPDF30NNLO_Wtaunu_MAXHTPTV0_70_BFilter.deriv.DAOD_HIGG8D1.e5340_e5984_s3126_r10201_r10210_p4133
 mc16_13TeV.364187.Sherpa_221_NNPDF30NNLO_Wtaunu_MAXHTPTV70_140_CVetoBVeto.deriv.DAOD_HIGG8D1.e5340_e5984_s3126_r10201_r10210_p4133
 mc16_13TeV.364188.Sherpa_221_NNPDF30NNLO_Wtaunu_MAXHTPTV70_140_CFilterBVeto.deriv.DAOD_HIGG8D1.e5340_e5984_s3126_r10201_r10210_p4133
 mc16_13TeV.364189.Sherpa_221_NNPDF30NNLO_Wtaunu_MAXHTPTV70_140_BFilter.deriv.DAOD_HIGG8D1.e5340_s3126_r10201_r10210_p4133
 mc16_13TeV.364190.Sherpa_221_NNPDF30NNLO_Wtaunu_MAXHTPTV140_280_CVetoBVeto.deriv.DAOD_HIGG8D1.e5340_s3126_r10201_r10210_p4133
 mc16_13TeV.364190.Sherpa_221_NNPDF30NNLO_Wtaunu_MAXHTPTV140_280_CVetoBVeto.deriv.DAOD_HIGG8D1.e5340_e5984_s3126_s3136_r10201_r10210_p4133

mc16_13TeV.364191.Sherpa_221_NNPDF30NNLO_Wtaunu_MAXHTPTV140_280_CFilterBVeto.deriv.DAOD_HIGG8D1.e5340_e5984_s3126_s3136_r10201_r10210_p4133
 mc16_13TeV.364191.Sherpa_221_NNPDF30NNLO_Wtaunu_MAXHTPTV140_280_CFilterBVeto.deriv.DAOD_HIGG8D1.e5340_s3126_r10201_r10210_p4133
 mc16_13TeV.364192.Sherpa_221_NNPDF30NNLO_Wtaunu_MAXHTPTV140_280_BFilter.deriv.DAOD_HIGG8D1.e5340_e5984_s3126_r10201_r10210_p4133
 mc16_13TeV.364193.Sherpa_221_NNPDF30NNLO_Wtaunu_MAXHTPTV280_500_CVetoBVeto.deriv.DAOD_HIGG8D1.e5340_e5984_s3126_r10201_r10210_p4133
 mc16_13TeV.364193.Sherpa_221_NNPDF30NNLO_Wtaunu_MAXHTPTV280_500_CVetoBVeto.deriv.DAOD_HIGG8D1.e5340_e5984_s3126_s3136_r10201_r10210_p4133
 mc16_13TeV.364194.Sherpa_221_NNPDF30NNLO_Wtaunu_MAXHTPTV280_500_CFilterBVeto.deriv.DAOD_HIGG8D1.e5340_e5984_s3126_r10201_r10210_p4133
 mc16_13TeV.364194.Sherpa_221_NNPDF30NNLO_Wtaunu_MAXHTPTV280_500_CFilterBVeto.deriv.DAOD_HIGG8D1.e5340_s3126_r10201_r10210_p4133
 mc16_13TeV.364194.Sherpa_221_NNPDF30NNLO_Wtaunu_MAXHTPTV280_500_BFilter.deriv.DAOD_HIGG8D1.e5340_e5984_s3126_r10201_r10210_p4133
 mc16_13TeV.364194.Sherpa_221_NNPDF30NNLO_Wtaunu_MAXHTPTV280_500_BFilter.deriv.DAOD_HIGG8D1.e5340_s3126_s3136_r10201_r10210_p4133
 mc16_13TeV.364195.Sherpa_221_NNPDF30NNLO_Wtaunu_MAXHTPTV280_500_BFilter.deriv.DAOD_HIGG8D1.e5340_e5984_s3126_r10201_r10210_p4133
 mc16_13TeV.364195.Sherpa_221_NNPDF30NNLO_Wtaunu_MAXHTPTV280_500_BFilter.deriv.DAOD_HIGG8D1.e5340_s3126_r10201_r10210_p4133
 mc16_13TeV.364196.Sherpa_221_NNPDF30NNLO_Wtaunu_MAXHTPTV500_1000.deriv.DAOD_HIGG8D1.e5340_e5984_s3126_s3136_r10201_r10210_p4133
 mc16_13TeV.364196.Sherpa_221_NNPDF30NNLO_Wtaunu_MAXHTPTV500_1000.deriv.DAOD_HIGG8D1.e5340_s3126_r10201_r10210_p4133
 mc16_13TeV.364197.Sherpa_221_NNPDF30NNLO_Wtaunu_MAXHTPTV1000_E_CMS.deriv.DAOD_HIGG8D1.e5340_e5984_s3126_r10201_r10210_p4133
 mc16_13TeV.364500.Sherpa_222_NNPDF30NNLO_eegamma_pty_7_15.deriv.DAOD_HIGG8D1.e5928_e5984_s3126_r10201_r10210_p4133
 mc16_13TeV.364501.Sherpa_222_NNPDF30NNLO_eegamma_pty_15_35.deriv.DAOD_HIGG8D1.e5928_e5984_s3126_r10201_r10210_p4133
 mc16_13TeV.364502.Sherpa_222_NNPDF30NNLO_eegamma_pty_35_70.deriv.DAOD_HIGG8D1.e5928_e5984_s3126_r10201_r10210_p4133
 mc16_13TeV.364503.Sherpa_222_NNPDF30NNLO_eegamma_pty_70_140.deriv.DAOD_HIGG8D1.e5928_e5984_s3126_r10201_r10210_p4133
 mc16_13TeV.364504.Sherpa_222_NNPDF30NNLO_eegamma_pty_140_E_CMS.deriv.DAOD_HIGG8D1.e5928_e5984_s3126_r10201_r10210_p4133
 mc16_13TeV.364505.Sherpa_222_NNPDF30NNLO_mumugamma_pty_7_15.deriv.DAOD_HIGG8D1.e5928_e5984_s3126_r10201_r10210_p4133
 mc16_13TeV.364506.Sherpa_222_NNPDF30NNLO_mumugamma_pty_15_35.deriv.DAOD_HIGG8D1.e5928_e5984_s3126_r10201_r10210_p4133
 mc16_13TeV.364507.Sherpa_222_NNPDF30NNLO_mumugamma_pty_35_70.deriv.DAOD_HIGG8D1.e5928_e5984_s3126_r10201_r10210_p4133
 mc16_13TeV.364508.Sherpa_222_NNPDF30NNLO_mumugamma_pty_70_140.deriv.DAOD_HIGG8D1.e5928_e5984_s3126_r10201_r10210_p4133
 mc16_13TeV.364509.Sherpa_222_NNPDF30NNLO_mumugamma_pty_140_E_CMS.deriv.DAOD_HIGG8D1.e5928_e5984_s3126_r10201_r10210_p4133
 mc16_13TeV.364510.Sherpa_222_NNPDF30NNLO_tautaugamma_pty_7_15.deriv.DAOD_HIGG8D1.e5928_e5984_s3126_r10201_r10210_p4133
 mc16_13TeV.364511.Sherpa_222_NNPDF30NNLO_tautaugamma_pty_15_35.deriv.DAOD_HIGG8D1.e5928_e5984_s3126_r10201_r10210_p4133
 mc16_13TeV.364512.Sherpa_222_NNPDF30NNLO_tautaugamma_pty_35_70.deriv.DAOD_HIGG8D1.e5928_e5984_s3126_r10201_r10210_p4133
 mc16_13TeV.364513.Sherpa_222_NNPDF30NNLO_tautaugamma_pty_70_140.deriv.DAOD_HIGG8D1.e5982_e5984_s3126_r10201_r10210_p4133
 mc16_13TeV.364513.Sherpa_222_NNPDF30NNLO_tautaugamma_pty_70_140.deriv.DAOD_HIGG8D1.e5928_e5984_s3126_r10201_r10210_p4133
 mc16_13TeV.364514.Sherpa_222_NNPDF30NNLO_tautaugamma_pty_140_E_CMS.deriv.DAOD_HIGG8D1.e5928_e5984_s3126_r10201_r10210_p4133
 mc16_13TeV.364521.Sherpa_222_NNPDF30NNLO_enugamma_pty_7_15.deriv.DAOD_HIGG8D1.e5928_e5984_s3126_r10201_r10210_p4133
 mc16_13TeV.364522.Sherpa_222_NNPDF30NNLO_enugamma_pty_15_35.deriv.DAOD_HIGG8D1.e5928_e5984_s3126_r10201_r10210_p4133

mc16_13TeV.364523.Sherpa_222_NNPDF30NNLO_enugamma_pty_35_70.deriv.DAOD_HIGG8D1.e5928_e5984_s3126_r10201_r10210_p4133
 mc16_13TeV.364524.Sherpa_222_NNPDF30NNLO_enugamma_pty_70_140.deriv.DAOD_HIGG8D1.e5928_e5984_s3126_r10201_r10210_p4133
 mc16_13TeV.364525.Sherpa_222_NNPDF30NNLO_enugamma_pty_140_E_CMS.deriv.DAOD_HIGG8D1.e5928_e5984_s3126_r10201_r10210_p4133
 mc16_13TeV.364526.Sherpa_222_NNPDF30NNLO_munugamma_pty_7_15.deriv.DAOD_HIGG8D1.e5928_e5984_s3126_r10201_r10210_p4133
 mc16_13TeV.364527.Sherpa_222_NNPDF30NNLO_munugamma_pty_15_35.deriv.DAOD_HIGG8D1.e5928_e5984_s3126_r10201_r10210_p4133
 mc16_13TeV.364528.Sherpa_222_NNPDF30NNLO_munugamma_pty_35_70.deriv.DAOD_HIGG8D1.e5928_e5984_s3126_r10201_r10210_p4133
 mc16_13TeV.364529.Sherpa_222_NNPDF30NNLO_munugamma_pty_70_140.deriv.DAOD_HIGG8D1.e5928_e5984_s3126_r10201_r10210_p4133
 mc16_13TeV.364530.Sherpa_222_NNPDF30NNLO_munugamma_pty_140_E_CMS.deriv.DAOD_HIGG8D1.e5928_e5984_s3126_r10201_r10210_p4133
 mc16_13TeV.364531.Sherpa_222_NNPDF30NNLO_taunugamma_pty_7_15.deriv.DAOD_HIGG8D1.e5928_e5984_s3126_r10201_r10210_p4133
 mc16_13TeV.364532.Sherpa_222_NNPDF30NNLO_taunugamma_pty_15_35.deriv.DAOD_HIGG8D1.e5928_e5984_s3126_r10201_r10210_p4133
 mc16_13TeV.364533.Sherpa_222_NNPDF30NNLO_taunugamma_pty_35_70.deriv.DAOD_HIGG8D1.e5928_e5984_s3126_r10201_r10210_p4133
 mc16_13TeV.364534.Sherpa_222_NNPDF30NNLO_taunugamma_pty_70_140.deriv.DAOD_HIGG8D1.e5928_e5984_s3126_r10201_r10210_p4133
 mc16_13TeV.364535.Sherpa_222_NNPDF30NNLO_taunugamma_pty_140_E_CMS.deriv.DAOD_HIGG8D1.e5928_e5984_s3126_r10201_r10210_p4133
 mc16_13TeV.410560.MadGraphPythia8EvtGen_A14_tZ_4fl_tchan_noAllHad.deriv.DAOD_HIGG8D1.e5803_e5984_s3126_r10201_r10210_p4133
 mc16_13TeV.410013.PowhegPythiaEvtGen_P2012_Wt_inclusive_top.deriv.DAOD_HIGG8D1.e3753_s3126_r10201_r10210_p4133
 mc16_13TeV.410014.PowhegPythiaEvtGen_P2012_Wt_inclusive_antitop.deriv.DAOD_HIGG8D1.e3753_s3126_r10201_r10210_p4133
 mc16_13TeV.410408.aMcAtNloPythia8EvtGen_tWZ_Ztoll_minDR1.deriv.DAOD_HIGG8D1.e6423_e5984_s3126_r10201_r10210_p4133
 mc16_13TeV.364242.Sherpa_222_NNPDF30NNLO_WWW_3l3v_EW6.deriv.DAOD_HIGG8D1.e5887_e5984_s3126_r10201_r10210_p4133
 mc16_13TeV.364243.Sherpa_222_NNPDF30NNLO_WWZ_4l2v_EW6.deriv.DAOD_HIGG8D1.e5887_e5984_s3126_r10201_r10210_p4133
 mc16_13TeV.364244.Sherpa_222_NNPDF30NNLO_WWZ_2l4v_EW6.deriv.DAOD_HIGG8D1.e5887_e5984_s3126_r10201_r10210_p4133
 mc16_13TeV.364245.Sherpa_222_NNPDF30NNLO_WZZ_5l1v_EW6.deriv.DAOD_HIGG8D1.e5887_e5984_s3126_r10201_r10210_p4133
 mc16_13TeV.364246.Sherpa_222_NNPDF30NNLO_WZZ_3l3v_EW6.deriv.DAOD_HIGG8D1.e5887_e5984_s3126_r10201_r10210_p4133
 mc16_13TeV.364247.Sherpa_222_NNPDF30NNLO_ZZZ_6l0v_EW6.deriv.DAOD_HIGG8D1.e5887_e5984_s3126_r10201_r10210_p4133
 mc16_13TeV.364248.Sherpa_222_NNPDF30NNLO_ZZZ_4l2v_EW6.deriv.DAOD_HIGG8D1.e5887_e5984_s3126_r10201_r10210_p4133
 mc16_13TeV.364249.Sherpa_222_NNPDF30NNLO_ZZZ_2l4v_EW6.deriv.DAOD_HIGG8D1.e5887_e5984_s3126_r10201_r10210_p4133
 mc16_13TeV.342284.Pythia8EvtGen_A14NNPDF23LO_WH125_inc.deriv.DAOD_HIGG8D1.e4246_e5984_s3126_r10201_r10210_p4133
 mc16_13TeV.342285.Pythia8EvtGen_A14NNPDF23LO_ZH125_inc.deriv.DAOD_HIGG8D1.e4246_e5984_s3126_r10201_r10210_p4133
 mc16_13TeV.341998.aMcAtNloHppEG_UEEE5_CTEQ6L1_CT10ME_tWH125_gamgam_yt_plus1.deriv.DAOD_HIGG8D1.e4394_e5984_s3126_r10201_r10210_p4133
 mc16_13TeV.410470.PhPy8EG_A14_ttbar_hdamp258p75_nonallhad.deriv.DAOD_HIGG8D1.e6337_e5984_s3126_r10201_r10210_p4133
 mc16_13TeV.410472.PhPy8EG_A14_ttbar_hdamp258p75_dil.deriv.DAOD_HIGG8D1.e6348_e5984_s3126_r10201_r10210_p4133
 mc16_13TeV.346343.PhPy8EG_A14NNPDF23_NNPDF30ME_ttH125_allhad.deriv.DAOD_HIGG8D1.e7148_e5984_s3126_r10201_r10210_p4133

mc16_13TeV.346344.PhPy8EG_A14NNPDF23_NNPDF30ME_ttH125_semilep.deriv.DAOD_HIGG8D1.e7148_e5984_a875_r10201_r10210_p4133

mc16_13TeV.346345.PhPy8EG_A14NNPDF23_NNPDF30ME_ttH125_dilep.deriv.DAOD_HIGG8D1.e7148_e5984_a875_r10201_r10210_p4133

mc16e:

mc16_13TeV.361605.PowhegPy8EG_CT10nloME_AZNLOCTEQ6L1_ZZvvvv_mll4.deriv.DAOD_HIGG8D1.e4054_e5984_s3126_r10724_r10726_p4133

mc16_13TeV.361602.PowhegPy8EG_CT10nloME_AZNLOCTEQ6L1_WZlvvv_mll4.deriv.DAOD_HIGG8D1.e4054_e5984_s3126_r10724_r10726_p4133

mc16_13TeV.361601.PowhegPy8EG_CT10nloME_AZNLOCTEQ6L1_WZlvl_l_mll4.deriv.DAOD_HIGG8D1.e4475_e5984_s3126_r10724_r10726_p4133

mc16_13TeV.361600.PowhegPy8EG_CT10nloME_AZNLOCTEQ6L1_WWlvvv.deriv.DAOD_HIGG8D1.e4616_e5984_s3126_r10724_r10726_p4133

mc16_13TeV.361603.PowhegPy8EG_CT10nloME_AZNLOCTEQ6L1_ZZllll_mll4.deriv.DAOD_HIGG8D1.e4475_e5984_s3126_r10724_r10726_p4133

mc16_13TeV.361604.PowhegPy8EG_CT10nloME_AZNLOCTEQ6L1_ZZvvll_mll4.deriv.DAOD_HIGG8D1.e4475_e5984_s3126_r10724_r10726_p4133

mc16_13TeV.364288.Sherpa_222_NNPDF30NNLO_llll_lowMllPtComplement.deriv.DAOD_HIGG8D1.e6096_s3126_r10724_p3983 mc16_13TeV.364287.Sherpa_222_NNPDF

mc16_13TeV.364285.Sherpa_222_NNPDF30NNLO_llvjj_EW6.deriv.DAOD_HIGG8D1.e6055_e5984_s3126_r10724_r10726_p3983

mc16_13TeV.364284.Sherpa_222_NNPDF30NNLO_llvjj_EW6.deriv.DAOD_HIGG8D1.e6055_s3126_r10724_p3983

mc16_13TeV.364283.Sherpa_222_NNPDF30NNLO_lllljj_EW6.deriv.DAOD_HIGG8D1.e6055_s3126_r10724_p3983

mc16_13TeV.364739.MGPy8EG_NNPDF30NLO_A14NNPDF23LO_lvlljjEW6_OFMinus.deriv.DAOD_HIGG8D1.e7421_e5984_s3126_r10724_r10726_p4133

mc16_13TeV.364742.MGPy8EG_NNPDF30NLO_A14NNPDF23LO_lvlljjEW6_SFPlus.deriv.DAOD_HIGG8D1.e7421_e5984_s3126_r10724_r10726_p4133

mc16_13TeV.364740.MGPy8EG_NNPDF30NLO_A14NNPDF23LO_lvlljjEW6_OFPlus.deriv.DAOD_HIGG8D1.e7421_e5984_s3126_r10724_r10726_p4133

mc16_13TeV.364741.MGPy8EG_NNPDF30NLO_A14NNPDF23LO_lvlljjEW6_SFMinus.deriv.DAOD_HIGG8D1.e7421_e5984_s3126_r10724_r10726_p4133

mc16_13TeV.364253.Sherpa_222_NNPDF30NNLO_llv.deriv.DAOD_HIGG8D1.e5916_e5984_s3126_r10724_r10726_p4133

mc16_13TeV.364250.Sherpa_222_NNPDF30NNLO_llll.deriv.DAOD_HIGG8D1.e5894_e5984_s3126_r10724_r10726_p4133

mc16_13TeV.364254.Sherpa_222_NNPDF30NNLO_llv.deriv.DAOD_HIGG8D1.e5916_e5984_s3126_r10724_r10726_p4133

mc16_13TeV.364255.Sherpa_222_NNPDF30NNLO_lvvv.deriv.DAOD_HIGG8D1.e5916_e5984_s3126_r10724_r10726_p4133

mc16_13TeV.410155.aMcAtNloPythia8EvtGen_MEN30NLO_A14N23LO_ttW.deriv.DAOD_HIGG8D1.e5070_e5984_s3126_r10724_r10726_p4133

mc16_13TeV.410156.aMcAtNloPythia8EvtGen_MEN30NLO_A14N23LO_ttZnuuu.deriv.DAOD_HIGG8D1.e5070_e5984_s3126_r10724_r10726_p4133

mc16_13TeV.410157.aMcAtNloPythia8EvtGen_MEN30NLO_A14N23LO_ttZqq.deriv.DAOD_HIGG8D1.e5070_e5984_s3126_r10724_r10726_p4133

mc16_13TeV.410218.aMcAtNloPythia8EvtGen_MEN30NLO_A14N23LO_ttee.deriv.DAOD_HIGG8D1.e5070_e5984_s3126_r10724_r10726_p4133

mc16_13TeV.410219.aMcAtNloPythia8EvtGen_MEN30NLO_A14N23LO_ttmumu.deriv.DAOD_HIGG8D1.e5070_e5984_s3126_r10724_r10726_p4133

mc16_13TeV.410220.aMcAtNloPythia8EvtGen_MEN30NLO_A14N23LO_ttautau.deriv.DAOD_HIGG8D1.e5070_e5984_s3126_r10724_r10726_p4133

mc16_13TeV.410276.aMcAtNloPythia8EvtGen_MEN30NLO_A14N23LO_ttee_mll_1_5.deriv.DAOD_HIGG8D1.e6087_e5984_s3126_r10724_r10726_p4133

mc16_13TeV.410277.aMcAtNloPythia8EvtGen_MEN30NLO_A14N23LO_ttmumu_mll_1_5.deriv.DAOD_HIGG8D1.e6087_e5984_s3126_r10724_r10726_p4133

mc16_13TeV.410278.aMcAtNloPythia8EvtGen_MEN30NLO_A14N23LO_ttautau_mll_1_5.deriv.DAOD_HIGG8D1.e6087_e5984_s3126_r10724_r10726_p4133

mc16_13TeV.410397.MadGraphPythia8EvtGen_ttbar_wbee_MEN30LO_A14N23LO.deriv.DAOD_HIGG8D1.e6086_e5984_s3126_r10724_r10726_p4133
 mc16_13TeV.410398.MadGraphPythia8EvtGen_ttbar_wbmumu_MEN30LO_A14N23LO.deriv.DAOD_HIGG8D1.e6086_e5984_s3126_r10724_r10726_p4133
 mc16_13TeV.410399.MadGraphPythia8EvtGen_ttbar_wbttau_MEN30LO_A14N23LO.deriv.DAOD_HIGG8D1.e6086_e5984_s3126_r10724_r10726_p4133
 mc16_13TeV.410658.PhPy8EG_A14_tchan_BW50_lept_top.deriv.DAOD_HIGG8D1.e6671_e5984_s3126_s3136_r10724_r10726_p4133
 mc16_13TeV.410659.PhPy8EG_A14_tchan_BW50_lept_antitop.deriv.DAOD_HIGG8D1.e6671_e5984_s3126_s3136_r10724_r10726_p4133
 mc16_13TeV.410644.PowhegPythia8EvtGen_A14_singletop_schan_lept_top.deriv.DAOD_HIGG8D1.e6527_e5984_s3126_r10724_r10726_p4133
 mc16_13TeV.410645.PowhegPythia8EvtGen_A14_singletop_schan_lept_antitop.deriv.DAOD_HIGG8D1.e6527_e5984_s3126_r10724_r10726_p4133
 mc16_13TeV.412063.aMcAtNloPythia8EvtGen_llq_NNPDF30_nf4_A14.deriv.DAOD_TOPQ1.e7054_e5984_s3126_r10724_r10726_p4174
 mc16_13TeV.304014.MadGraphPythia8EvtGen_A14NNPDF23_3top_SM.deriv.DAOD_HIGG8D1.e4324_e5984_s3126_r10724_r10726_p4133
 mc16_13TeV.410080.MadGraphPythia8EvtGen_A14NNPDF23_4topSM.deriv.DAOD_HIGG8D1.e4111_e5984_s3126_r10724_r10726_p4133
 mc16_13TeV.410081.MadGraphPythia8EvtGen_A14NNPDF23_ttbarWW.deriv.DAOD_HIGG8D1.e4111_e5984_s3126_r10724_r10726_p4133
 mc16_13TeV.364100.Sherpa_221_NNPDF30NNLO_Zmumu_MAXHTPTV0_70_CVetoBVeto.deriv.DAOD_HIGG8D1.e5271_e5984_s3126_s3136_r10724_r10726_p4133
 mc16_13TeV.364100.Sherpa_221_NNPDF30NNLO_Zmumu_MAXHTPTV0_70_CVetoBVeto.deriv.DAOD_HIGG8D1.e5271_e5984_s3126_r10724_r10726_p4133
 mc16_13TeV.364101.Sherpa_221_NNPDF30NNLO_Zmumu_MAXHTPTV0_70_CFilterBVeto.deriv.DAOD_HIGG8D1.e5271_e5984_s3126_r10724_r10726_p4133
 mc16_13TeV.364102.Sherpa_221_NNPDF30NNLO_Zmumu_MAXHTPTV0_70_BFilter.deriv.DAOD_HIGG8D1.e5271_e5984_s3126_s3136_r10724_r10726_p4133
 mc16_13TeV.364102.Sherpa_221_NNPDF30NNLO_Zmumu_MAXHTPTV0_70_BFilter.deriv.DAOD_HIGG8D1.e5271_e5984_s3126_r10724_r10726_p4133
 mc16_13TeV.364103.Sherpa_221_NNPDF30NNLO_Zmumu_MAXHTPTV70_140_CVetoBVeto.deriv.DAOD_HIGG8D1.e5271_e5984_s3126_r10724_r10726_p4133
 mc16_13TeV.364103.Sherpa_221_NNPDF30NNLO_Zmumu_MAXHTPTV70_140_CVetoBVeto.deriv.DAOD_HIGG8D1.e5271_e5984_s3126_s3136_r10724_r10726_p4133
 mc16_13TeV.364104.Sherpa_221_NNPDF30NNLO_Zmumu_MAXHTPTV70_140_CFilterBVeto.deriv.DAOD_HIGG8D1.e5271_e5984_s3126_r10724_r10726_p4133
 mc16_13TeV.364104.Sherpa_221_NNPDF30NNLO_Zmumu_MAXHTPTV70_140_CFilterBVeto.deriv.DAOD_HIGG8D1.e5271_e5984_s3126_s3136_r10724_r10726_p4133
 mc16_13TeV.364106.Sherpa_221_NNPDF30NNLO_Zmumu_MAXHTPTV140_280_CVetoBVeto.deriv.DAOD_HIGG8D1.e5271_e5984_s3126_s3136_r10724_r10726_p4133
 mc16_13TeV.364107.Sherpa_221_NNPDF30NNLO_Zmumu_MAXHTPTV140_280_CFilterBVeto.deriv.DAOD_HIGG8D1.e5271_e5984_s3126_r10724_r10726_p4133
 mc16_13TeV.364107.Sherpa_221_NNPDF30NNLO_Zmumu_MAXHTPTV140_280_CFilterBVeto.deriv.DAOD_HIGG8D1.e5271_e5984_s3126_s3136_r10724_r10726_p4133
 mc16_13TeV.364108.Sherpa_221_NNPDF30NNLO_Zmumu_MAXHTPTV140_280_BFilter.deriv.DAOD_HIGG8D1.e5271_e5984_s3126_r10724_r10726_p4133
 mc16_13TeV.364109.Sherpa_221_NNPDF30NNLO_Zmumu_MAXHTPTV280_500_CVetoBVeto.deriv.DAOD_HIGG8D1.e5271_e5984_s3126_r10724_r10726_p4133
 mc16_13TeV.364110.Sherpa_221_NNPDF30NNLO_Zmumu_MAXHTPTV280_500_CFilterBVeto.deriv.DAOD_HIGG8D1.e5271_e5984_s3126_r10724_r10726_p4133
 mc16_13TeV.364110.Sherpa_221_NNPDF30NNLO_Zmumu_MAXHTPTV280_500_CFilterBVeto.deriv.DAOD_HIGG8D1.e5271_e5984_s3126_s3136_r10724_r10726_p4133
 mc16_13TeV.364111.Sherpa_221_NNPDF30NNLO_Zmumu_MAXHTPTV280_500_BFilter.deriv.DAOD_HIGG8D1.e5271_e5984_s3126_s3136_r10724_r10726_p4133
 mc16_13TeV.364111.Sherpa_221_NNPDF30NNLO_Zmumu_MAXHTPTV280_500_BFilter.deriv.DAOD_HIGG8D1.e5271_e5984_s3126_r10724_r10726_p4133
 mc16_13TeV.364112.Sherpa_221_NNPDF30NNLO_Zmumu_MAXHTPTV500_1000.deriv.DAOD_HIGG8D1.e5271_e5984_s3126_r10724_r10726_p4133

mc16_13TeV.364113.Sherpa_221_NNPDF30NNLO_Zmumu_MAXHTPTV1000_E_CMS.deriv.DAOD_HIGG8D1.e5271_e5984_s3126_r10724_r10726_p4133
 mc16_13TeV.364113.Sherpa_221_NNPDF30NNLO_Zmumu_MAXHTPTV1000_E_CMS.deriv.DAOD_HIGG8D1.e5271_e5984_s3126_s3136_r10724_r10726_p4133
 mc16_13TeV.364114.Sherpa_221_NNPDF30NNLO_Zee_MAXHTPTV0_70_CVetoBVeto.deriv.DAOD_HIGG8D1.e5299_e5984_s3126_s3136_r10724_r10726_p4133
 mc16_13TeV.364114.Sherpa_221_NNPDF30NNLO_Zee_MAXHTPTV0_70_CVetoBVeto.deriv.DAOD_HIGG8D1.e5299_e5984_s3126_r10724_r10726_p4133
 mc16_13TeV.364115.Sherpa_221_NNPDF30NNLO_Zee_MAXHTPTV0_70_CFilterBVeto.deriv.DAOD_HIGG8D1.e5299_e5984_s3126_s3136_r10724_r10726_p4133
 mc16_13TeV.364115.Sherpa_221_NNPDF30NNLO_Zee_MAXHTPTV0_70_CFilterBVeto.deriv.DAOD_HIGG8D1.e5299_e5984_s3126_r10724_r10726_p4133
 mc16_13TeV.364116.Sherpa_221_NNPDF30NNLO_Zee_MAXHTPTV0_70_BFilter.deriv.DAOD_HIGG8D1.e5299_e5984_s3126_r10724_r10726_p4133
 mc16_13TeV.364117.Sherpa_221_NNPDF30NNLO_Zee_MAXHTPTV70_140_CVetoBVeto.deriv.DAOD_HIGG8D1.e5299_e5984_s3126_s3136_r10724_r10726_p4133
 mc16_13TeV.364117.Sherpa_221_NNPDF30NNLO_Zee_MAXHTPTV70_140_CVetoBVeto.deriv.DAOD_HIGG8D1.e5299_e5984_s3126_r10724_r10726_p4133
 mc16_13TeV.364118.Sherpa_221_NNPDF30NNLO_Zee_MAXHTPTV70_140_CFilterBVeto.deriv.DAOD_HIGG8D1.e5299_e5984_s3126_s3136_r10724_r10726_p4133
 mc16_13TeV.364118.Sherpa_221_NNPDF30NNLO_Zee_MAXHTPTV70_140_CFilterBVeto.deriv.DAOD_HIGG8D1.e5299_e5984_s3126_r10724_r10726_p4133
 mc16_13TeV.364119.Sherpa_221_NNPDF30NNLO_Zee_MAXHTPTV70_140_BFilter.deriv.DAOD_HIGG8D1.e5299_e5984_s3126_r10724_r10726_p4133
 mc16_13TeV.364120.Sherpa_221_NNPDF30NNLO_Zee_MAXHTPTV140_280_CVetoBVeto.deriv.DAOD_HIGG8D1.e5299_e5984_s3126_r10724_r10726_p4133
 mc16_13TeV.364121.Sherpa_221_NNPDF30NNLO_Zee_MAXHTPTV140_280_CFilterBVeto.deriv.DAOD_HIGG8D1.e5299_e5984_s3126_r10724_r10726_p4133
 mc16_13TeV.364122.Sherpa_221_NNPDF30NNLO_Zee_MAXHTPTV140_280_BFilter.deriv.DAOD_HIGG8D1.e5299_e5984_s3126_s3136_r10724_r10726_p4133
 mc16_13TeV.364122.Sherpa_221_NNPDF30NNLO_Zee_MAXHTPTV140_280_BFilter.deriv.DAOD_HIGG8D1.e5299_e5984_s3126_r10724_r10726_p4133
 mc16_13TeV.364123.Sherpa_221_NNPDF30NNLO_Zee_MAXHTPTV280_500_CVetoBVeto.deriv.DAOD_HIGG8D1.e5299_e5984_s3126_r10724_r10726_p4133
 mc16_13TeV.364124.Sherpa_221_NNPDF30NNLO_Zee_MAXHTPTV280_500_CFilterBVeto.deriv.DAOD_HIGG8D1.e5299_e5984_s3126_r10724_r10726_p4133
 mc16_13TeV.364125.Sherpa_221_NNPDF30NNLO_Zee_MAXHTPTV280_500_BFilter.deriv.DAOD_HIGG8D1.e5299_e5984_s3126_s3136_r10724_r10726_p4133
 mc16_13TeV.364125.Sherpa_221_NNPDF30NNLO_Zee_MAXHTPTV280_500_BFilter.deriv.DAOD_HIGG8D1.e5299_e5984_s3126_r10724_r10726_p4133
 mc16_13TeV.364126.Sherpa_221_NNPDF30NNLO_Zee_MAXHTPTV500_1000.deriv.DAOD_HIGG8D1.e5299_e5984_s3126_r10724_r10726_p4133
 mc16_13TeV.364126.Sherpa_221_NNPDF30NNLO_Zee_MAXHTPTV500_1000.deriv.DAOD_HIGG8D1.e5299_e5984_s3126_s3136_r10724_r10726_p4133
 mc16_13TeV.364127.Sherpa_221_NNPDF30NNLO_Zee_MAXHTPTV1000_E_CMS.deriv.DAOD_HIGG8D1.e5299_e5984_s3126_s3136_r10724_r10726_p4133
 mc16_13TeV.364127.Sherpa_221_NNPDF30NNLO_Zee_MAXHTPTV1000_E_CMS.deriv.DAOD_HIGG8D1.e5299_e5984_s3126_r10724_r10726_p4133
 mc16_13TeV.364128.Sherpa_221_NNPDF30NNLO_Ztautau_MAXHTPTV0_70_CVetoBVeto.deriv.DAOD_HIGG8D1.e5307_e5984_s3126_s3136_r10724_r10726_p4133
 mc16_13TeV.364128.Sherpa_221_NNPDF30NNLO_Ztautau_MAXHTPTV0_70_CVetoBVeto.deriv.DAOD_HIGG8D1.e5307_e5984_s3126_r10724_r10726_p4133
 mc16_13TeV.364129.Sherpa_221_NNPDF30NNLO_Ztautau_MAXHTPTV0_70_CFilterBVeto.deriv.DAOD_HIGG8D1.e5307_e5984_s3126_r10724_r10726_p4133
 mc16_13TeV.364129.Sherpa_221_NNPDF30NNLO_Ztautau_MAXHTPTV0_70_CFilterBVeto.deriv.DAOD_HIGG8D1.e5307_e5984_s3126_s3136_r10724_r10726_p4133
 mc16_13TeV.364130.Sherpa_221_NNPDF30NNLO_Ztautau_MAXHTPTV0_70_BFilter.deriv.DAOD_HIGG8D1.e5307_e5984_s3126_s3136_r10724_r10726_p4133
 mc16_13TeV.364130.Sherpa_221_NNPDF30NNLO_Ztautau_MAXHTPTV0_70_BFilter.deriv.DAOD_HIGG8D1.e5307_e5984_s3126_r10724_r10726_p4133
 mc16_13TeV.364131.Sherpa_221_NNPDF30NNLO_Ztautau_MAXHTPTV70_140_CVetoBVeto.deriv.DAOD_HIGG8D1.e5307_e5984_s3126_r10724_r10726_p4133

mc16_13TeV.364132.Sherpa_221_NNPDF30NNLO_Ztautau_MAXHTPTV70_140_CFilterBVeto.deriv.DAOD_HIGG8D1.e5307_e5984_s3126_r10724_r10726_p4133
 mc16_13TeV.364132.Sherpa_221_NNPDF30NNLO_Ztautau_MAXHTPTV70_140_CFilterBVeto.deriv.DAOD_HIGG8D1.e5307_e5984_s3126_s3136_r10724_r10726_p4133
 mc16_13TeV.364133.Sherpa_221_NNPDF30NNLO_Ztautau_MAXHTPTV70_140_BFilter.deriv.DAOD_HIGG8D1.e5307_e5984_s3126_r10724_r10726_p4133
 mc16_13TeV.364134.Sherpa_221_NNPDF30NNLO_Ztautau_MAXHTPTV140_280_CVetoBVeto.deriv.DAOD_HIGG8D1.e5307_e5984_s3126_r10724_r10726_p4133
 mc16_13TeV.364135.Sherpa_221_NNPDF30NNLO_Ztautau_MAXHTPTV140_280_CFilterBVeto.deriv.DAOD_HIGG8D1.e5307_e5984_s3126_r10724_r10726_p4133
 mc16_13TeV.364135.Sherpa_221_NNPDF30NNLO_Ztautau_MAXHTPTV140_280_CFilterBVeto.deriv.DAOD_HIGG8D1.e5307_e5984_s3126_s3136_r10724_r10726_p4133
 mc16_13TeV.364136.Sherpa_221_NNPDF30NNLO_Ztautau_MAXHTPTV140_280_BFilter.deriv.DAOD_HIGG8D1.e5307_e5984_s3126_r10724_r10726_p4133
 mc16_13TeV.364137.Sherpa_221_NNPDF30NNLO_Ztautau_MAXHTPTV280_500_CVetoBVeto.deriv.DAOD_HIGG8D1.e5307_e5984_s3126_r10724_r10726_p4133
 mc16_13TeV.364138.Sherpa_221_NNPDF30NNLO_Ztautau_MAXHTPTV280_500_CFilterBVeto.deriv.DAOD_HIGG8D1.e5313_e5984_s3126_s3136_r10724_r10726_p4133
 mc16_13TeV.364138.Sherpa_221_NNPDF30NNLO_Ztautau_MAXHTPTV280_500_CFilterBVeto.deriv.DAOD_HIGG8D1.e5313_e5984_s3126_r10724_r10726_p4133
 mc16_13TeV.364139.Sherpa_221_NNPDF30NNLO_Ztautau_MAXHTPTV280_500_BFilter.deriv.DAOD_HIGG8D1.e5313_e5984_s3126_r10724_r10726_p4133
 mc16_13TeV.364139.Sherpa_221_NNPDF30NNLO_Ztautau_MAXHTPTV280_500_BFilter.deriv.DAOD_HIGG8D1.e5313_e5984_s3126_s3136_r10724_r10726_p4133
 mc16_13TeV.364140.Sherpa_221_NNPDF30NNLO_Ztautau_MAXHTPTV500_1000.deriv.DAOD_HIGG8D1.e5307_e5984_s3126_r10724_r10726_p4133
 mc16_13TeV.364140.Sherpa_221_NNPDF30NNLO_Ztautau_MAXHTPTV500_1000.deriv.DAOD_HIGG8D1.e5307_e5984_s3126_s3136_r10724_r10726_p4133
 mc16_13TeV.364141.Sherpa_221_NNPDF30NNLO_Ztautau_MAXHTPTV1000_E_CMS.deriv.DAOD_HIGG8D1.e5307_e5984_s3126_s3136_r10724_r10726_p4133
 mc16_13TeV.364141.Sherpa_221_NNPDF30NNLO_Ztautau_MAXHTPTV1000_E_CMS.deriv.DAOD_HIGG8D1.e5307_e5984_s3126_r10724_r10726_p4133
 mc16_13TeV.364198.Sherpa_221_NN30NNLO_Zmm_Mll10_40_MAXHTPTV0_70_BVeto.deriv.DAOD_HIGG8D1.e5421_e5984_s3126_r10724_r10726_p4133
 mc16_13TeV.364199.Sherpa_221_NN30NNLO_Zmm_Mll10_40_MAXHTPTV0_70_BFilter.deriv.DAOD_HIGG8D1.e5421_e5984_s3126_r10724_r10726_p4133
 mc16_13TeV.364200.Sherpa_221_NN30NNLO_Zmm_Mll10_40_MAXHTPTV70_280_BVeto.deriv.DAOD_HIGG8D1.e5421_e5984_s3126_r10724_r10726_p4133
 mc16_13TeV.364201.Sherpa_221_NN30NNLO_Zmm_Mll10_40_MAXHTPTV70_280_BFilter.deriv.DAOD_HIGG8D1.e5421_e5984_s3126_r10724_r10726_p4133
 mc16_13TeV.364202.Sherpa_221_NN30NNLO_Zmm_Mll10_40_MAXHTPTV280_E_CMS_BVeto.deriv.DAOD_HIGG8D1.e5421_e5984_s3126_r10724_r10726_p4133
 mc16_13TeV.364203.Sherpa_221_NN30NNLO_Zmm_Mll10_40_MAXHTPTV280_E_CMS_BFilter.deriv.DAOD_HIGG8D1.e5421_e5984_s3126_r10724_r10726_p4133
 mc16_13TeV.364204.Sherpa_221_NN30NNLO_Zee_Mll10_40_MAXHTPTV0_70_BVeto.deriv.DAOD_HIGG8D1.e5421_e5984_s3126_r10724_r10726_p4133
 mc16_13TeV.364205.Sherpa_221_NN30NNLO_Zee_Mll10_40_MAXHTPTV0_70_BFilter.deriv.DAOD_HIGG8D1.e5421_e5984_s3126_r10724_r10726_p4133
 mc16_13TeV.364206.Sherpa_221_NN30NNLO_Zee_Mll10_40_MAXHTPTV70_280_BVeto.deriv.DAOD_HIGG8D1.e5421_e5984_s3126_r10724_r10726_p4133
 mc16_13TeV.364207.Sherpa_221_NN30NNLO_Zee_Mll10_40_MAXHTPTV70_280_BFilter.deriv.DAOD_HIGG8D1.e5421_e5984_s3126_r10724_r10726_p4133
 mc16_13TeV.364208.Sherpa_221_NN30NNLO_Zee_Mll10_40_MAXHTPTV280_E_CMS_BVeto.deriv.DAOD_HIGG8D1.e5421_e5984_s3126_r10724_r10726_p4133
 mc16_13TeV.364209.Sherpa_221_NN30NNLO_Zee_Mll10_40_MAXHTPTV280_E_CMS_BFilter.deriv.DAOD_HIGG8D1.e5421_e5984_s3126_r10724_r10726_p4133
 mc16_13TeV.364210.Sherpa_221_NN30NNLO_Ztt_Mll10_40_MAXHTPTV0_70_BVeto.deriv.DAOD_HIGG8D1.e5421_e5984_s3126_r10724_r10726_p4133
 mc16_13TeV.364211.Sherpa_221_NN30NNLO_Ztt_Mll10_40_MAXHTPTV0_70_BFilter.deriv.DAOD_HIGG8D1.e5421_e5984_s3126_r10724_r10726_p4133
 mc16_13TeV.364212.Sherpa_221_NN30NNLO_Ztt_Mll10_40_MAXHTPTV70_280_BVeto.deriv.DAOD_HIGG8D1.e5421_e5984_s3126_r10724_r10726_p4133

mc16_13TeV.364213.Sherpa_221_NN30NNLO_Ztt_Mll10_40_MAXHTPTV70_280_BFilter.deriv.DAOD_HIGG8D1.e5421_e5984_s3126_r10724_r10726_p4133
 mc16_13TeV.364214.Sherpa_221_NN30NNLO_Ztt_Mll10_40_MAXHTPTV280_E_CMS_BVeto.deriv.DAOD_HIGG8D1.e5421_e5984_s3126_r10724_r10726_p4133
 mc16_13TeV.364215.Sherpa_221_NN30NNLO_Ztt_Mll10_40_MAXHTPTV280_E_CMS_BFilter.deriv.DAOD_HIGG8D1.e5421_e5984_s3126_r10724_r10726_p4133
 mc16_13TeV.364156.Sherpa_221_NNPDF30NNLO_Wmunu_MAXHTPTV0_70_CVetoBVeto.deriv.DAOD_HIGG8D1.e5340_e5984_s3126_r10724_r10726_p4133
 mc16_13TeV.364157.Sherpa_221_NNPDF30NNLO_Wmunu_MAXHTPTV0_70_CFilterBVeto.deriv.DAOD_HIGG8D1.e5340_e5984_s3126_r10724_r10726_p4133
 mc16_13TeV.364158.Sherpa_221_NNPDF30NNLO_Wmunu_MAXHTPTV0_70_BFilter.deriv.DAOD_HIGG8D1.e5340_e5984_s3126_s3136_r10724_r10726_p4133
 mc16_13TeV.364158.Sherpa_221_NNPDF30NNLO_Wmunu_MAXHTPTV0_70_BFilter.deriv.DAOD_HIGG8D1.e5340_e5984_s3126_r10724_r10726_p4133
 mc16_13TeV.364159.Sherpa_221_NNPDF30NNLO_Wmunu_MAXHTPTV70_140_CVetoBVeto.deriv.DAOD_HIGG8D1.e5340_e5984_s3126_s3136_r10724_r10726_p4133
 mc16_13TeV.364160.Sherpa_221_NNPDF30NNLO_Wmunu_MAXHTPTV70_140_CFilterBVeto.deriv.DAOD_HIGG8D1.e5340_e5984_s3126_s3136_r10724_r10726_p4133
 mc16_13TeV.364160.Sherpa_221_NNPDF30NNLO_Wmunu_MAXHTPTV70_140_CFilterBVeto.deriv.DAOD_HIGG8D1.e5340_e5984_s3126_r10724_r10726_p4133
 mc16_13TeV.364161.Sherpa_221_NNPDF30NNLO_Wmunu_MAXHTPTV70_140_BFilter.deriv.DAOD_HIGG8D1.e5340_e5984_s3126_r10724_r10726_p4133
 mc16_13TeV.364162.Sherpa_221_NNPDF30NNLO_Wmunu_MAXHTPTV140_280_CVetoBVeto.deriv.DAOD_HIGG8D1.e5340_e5984_s3126_r10724_r10726_p4133
 mc16_13TeV.364163.Sherpa_221_NNPDF30NNLO_Wmunu_MAXHTPTV140_280_CFilterBVeto.deriv.DAOD_HIGG8D1.e5340_e5984_s3126_s3136_r10724_r10726_p4133
 mc16_13TeV.364163.Sherpa_221_NNPDF30NNLO_Wmunu_MAXHTPTV140_280_CFilterBVeto.deriv.DAOD_HIGG8D1.e5340_e5984_s3126_r10724_r10726_p4133
 mc16_13TeV.364164.Sherpa_221_NNPDF30NNLO_Wmunu_MAXHTPTV140_280_BFilter.deriv.DAOD_HIGG8D1.e5340_e5984_s3126_r10724_r10726_p4133
 mc16_13TeV.364165.Sherpa_221_NNPDF30NNLO_Wmunu_MAXHTPTV280_500_CVetoBVeto.deriv.DAOD_HIGG8D1.e5340_e5984_s3126_r10724_r10726_p4133
 mc16_13TeV.364165.Sherpa_221_NNPDF30NNLO_Wmunu_MAXHTPTV280_500_CVetoBVeto.deriv.DAOD_HIGG8D1.e5340_e5984_s3126_s3136_r10724_r10726_p4133
 mc16_13TeV.364166.Sherpa_221_NNPDF30NNLO_Wmunu_MAXHTPTV280_500_CFilterBVeto.deriv.DAOD_HIGG8D1.e5340_e5984_s3126_s3136_r10724_r10726_p4133
 mc16_13TeV.364166.Sherpa_221_NNPDF30NNLO_Wmunu_MAXHTPTV280_500_CFilterBVeto.deriv.DAOD_HIGG8D1.e5340_e5984_s3126_r10724_r10726_p4133
 mc16_13TeV.364167.Sherpa_221_NNPDF30NNLO_Wmunu_MAXHTPTV280_500_BFilter.deriv.DAOD_HIGG8D1.e5340_e5984_s3126_r10724_r10726_p4133
 mc16_13TeV.364167.Sherpa_221_NNPDF30NNLO_Wmunu_MAXHTPTV280_500_BFilter.deriv.DAOD_HIGG8D1.e5340_e5984_s3126_s3136_r10724_r10726_p4133
 mc16_13TeV.364168.Sherpa_221_NNPDF30NNLO_Wmunu_MAXHTPTV500_1000.deriv.DAOD_HIGG8D1.e5340_e5984_s3126_r10724_r10726_p4133
 mc16_13TeV.364168.Sherpa_221_NNPDF30NNLO_Wmunu_MAXHTPTV500_1000.deriv.DAOD_HIGG8D1.e5340_e5984_s3126_s3136_r10724_r10726_p4133
 mc16_13TeV.364169.Sherpa_221_NNPDF30NNLO_Wmunu_MAXHTPTV1000_E_CMS.deriv.DAOD_HIGG8D1.e5340_e5984_s3126_s3136_r10724_r10726_p4133
 mc16_13TeV.364169.Sherpa_221_NNPDF30NNLO_Wmunu_MAXHTPTV1000_E_CMS.deriv.DAOD_HIGG8D1.e5340_e5984_s3126_r10724_r10726_p4133
 mc16_13TeV.364170.Sherpa_221_NNPDF30NNLO_Wenu_MAXHTPTV0_70_CVetoBVeto.deriv.DAOD_HIGG8D1.e5340_e5984_s3126_r10724_r10726_p4133
 mc16_13TeV.364171.Sherpa_221_NNPDF30NNLO_Wenu_MAXHTPTV0_70_CFilterBVeto.deriv.DAOD_HIGG8D1.e5340_e5984_s3126_r10724_r10726_p4133
 mc16_13TeV.364172.Sherpa_221_NNPDF30NNLO_Wenu_MAXHTPTV0_70_BFilter.deriv.DAOD_HIGG8D1.e5340_e5984_s3126_r10724_r10726_p4133
 mc16_13TeV.364173.Sherpa_221_NNPDF30NNLO_Wenu_MAXHTPTV70_140_CVetoBVeto.deriv.DAOD_HIGG8D1.e5340_e5984_s3126_s3136_r10724_r10726_p4133
 mc16_13TeV.364174.Sherpa_221_NNPDF30NNLO_Wenu_MAXHTPTV70_140_CFilterBVeto.deriv.DAOD_HIGG8D1.e5340_e5984_s3126_r10724_r10726_p4133
 mc16_13TeV.364175.Sherpa_221_NNPDF30NNLO_Wenu_MAXHTPTV70_140_BFilter.deriv.DAOD_HIGG8D1.e5340_e5984_s3126_s3136_r10724_r10726_p4133

mc16_13TeV.364176.Sherpa_221_NNPDF30NNLO_Wenu_MAXHTPTV140_280_CVetoBVeto.deriv.DAOD_HIGG8D1.e5340_e5984_s3126_r10724_r10726_p4133
 mc16_13TeV.364177.Sherpa_221_NNPDF30NNLO_Wenu_MAXHTPTV140_280_CFilterBVeto.deriv.DAOD_HIGG8D1.e5340_e5984_s3126_r10724_r10726_p4133
 mc16_13TeV.364177.Sherpa_221_NNPDF30NNLO_Wenu_MAXHTPTV140_280_CFilterBVeto.deriv.DAOD_HIGG8D1.e5340_e5984_s3126_s3136_r10724_r10726_p4133
 mc16_13TeV.364178.Sherpa_221_NNPDF30NNLO_Wenu_MAXHTPTV140_280_BFilter.deriv.DAOD_HIGG8D1.e5340_e5984_s3126_r10724_r10726_p4133
 mc16_13TeV.364179.Sherpa_221_NNPDF30NNLO_Wenu_MAXHTPTV280_500_CVetoBVeto.deriv.DAOD_HIGG8D1.e5340_e5984_s3126_r10724_r10726_p4133
 mc16_13TeV.364179.Sherpa_221_NNPDF30NNLO_Wenu_MAXHTPTV280_500_CVetoBVeto.deriv.DAOD_HIGG8D1.e5340_e5984_s3126_s3136_r10724_r10726_p4133
 mc16_13TeV.364180.Sherpa_221_NNPDF30NNLO_Wenu_MAXHTPTV280_500_CFilterBVeto.deriv.DAOD_HIGG8D1.e5340_e5984_s3126_s3136_r10724_r10726_p4133
 mc16_13TeV.364180.Sherpa_221_NNPDF30NNLO_Wenu_MAXHTPTV280_500_CFilterBVeto.deriv.DAOD_HIGG8D1.e5340_e5984_s3126_r10724_r10726_p4133
 mc16_13TeV.364181.Sherpa_221_NNPDF30NNLO_Wenu_MAXHTPTV280_500_BFilter.deriv.DAOD_HIGG8D1.e5340_e5984_s3126_s3136_r10724_r10726_p4133
 mc16_13TeV.364181.Sherpa_221_NNPDF30NNLO_Wenu_MAXHTPTV280_500_BFilter.deriv.DAOD_HIGG8D1.e5340_e5984_s3126_r10724_r10726_p4133
 mc16_13TeV.364182.Sherpa_221_NNPDF30NNLO_Wenu_MAXHTPTV500_1000.deriv.DAOD_HIGG8D1.e5340_e5984_s3126_s3136_r10724_r10726_p4133
 mc16_13TeV.364182.Sherpa_221_NNPDF30NNLO_Wenu_MAXHTPTV500_1000.deriv.DAOD_HIGG8D1.e5340_e5984_s3126_r10724_r10726_p4133
 mc16_13TeV.364183.Sherpa_221_NNPDF30NNLO_Wenu_MAXHTPTV1000_E_CMS.deriv.DAOD_HIGG8D1.e5340_e5984_s3126_r10724_r10726_p4133
 mc16_13TeV.364183.Sherpa_221_NNPDF30NNLO_Wenu_MAXHTPTV1000_E_CMS.deriv.DAOD_HIGG8D1.e5340_e5984_s3126_s3136_r10724_r10726_p4133
 mc16_13TeV.364184.Sherpa_221_NNPDF30NNLO_Wtaunu_MAXHTPTV0_70_CVetoBVeto.deriv.DAOD_HIGG8D1.e5340_e5984_s3126_r10724_r10726_p4133
 mc16_13TeV.364185.Sherpa_221_NNPDF30NNLO_Wtaunu_MAXHTPTV0_70_CFilterBVeto.deriv.DAOD_HIGG8D1.e5340_e5984_s3126_r10724_r10726_p4133
 mc16_13TeV.364186.Sherpa_221_NNPDF30NNLO_Wtaunu_MAXHTPTV0_70_BFilter.deriv.DAOD_HIGG8D1.e5340_e5984_s3126_s3136_r10724_r10726_p4133
 mc16_13TeV.364186.Sherpa_221_NNPDF30NNLO_Wtaunu_MAXHTPTV0_70_BFilter.deriv.DAOD_HIGG8D1.e5340_e5984_s3126_r10724_r10726_p4133
 mc16_13TeV.364187.Sherpa_221_NNPDF30NNLO_Wtaunu_MAXHTPTV70_140_CVetoBVeto.deriv.DAOD_HIGG8D1.e5340_e5984_s3126_r10724_r10726_p4133
 mc16_13TeV.364188.Sherpa_221_NNPDF30NNLO_Wtaunu_MAXHTPTV70_140_CFilterBVeto.deriv.DAOD_HIGG8D1.e5340_e5984_s3126_r10724_r10726_p4133
 mc16_13TeV.364189.Sherpa_221_NNPDF30NNLO_Wtaunu_MAXHTPTV70_140_BFilter.deriv.DAOD_HIGG8D1.e5340_e5984_s3126_r10724_r10726_p4133
 mc16_13TeV.364189.Sherpa_221_NNPDF30NNLO_Wtaunu_MAXHTPTV70_140_BFilter.deriv.DAOD_HIGG8D1.e5340_e5984_s3126_s3136_r10724_r10726_p4133
 mc16_13TeV.364190.Sherpa_221_NNPDF30NNLO_Wtaunu_MAXHTPTV140_280_CVetoBVeto.deriv.DAOD_HIGG8D1.e5340_e5984_s3126_r10724_r10726_p4133
 mc16_13TeV.364190.Sherpa_221_NNPDF30NNLO_Wtaunu_MAXHTPTV140_280_CVetoBVeto.deriv.DAOD_HIGG8D1.e5340_e5984_s3126_s3136_r10724_r10726_p4133
 mc16_13TeV.364191.Sherpa_221_NNPDF30NNLO_Wtaunu_MAXHTPTV140_280_CFilterBVeto.deriv.DAOD_HIGG8D1.e5340_e5984_s3126_r10724_r10726_p4133
 mc16_13TeV.364191.Sherpa_221_NNPDF30NNLO_Wtaunu_MAXHTPTV140_280_CFilterBVeto.deriv.DAOD_HIGG8D1.e5340_e5984_s3126_s3136_r10724_r10726_p4133
 mc16_13TeV.364192.Sherpa_221_NNPDF30NNLO_Wtaunu_MAXHTPTV140_280_BFilter.deriv.DAOD_HIGG8D1.e5340_e5984_s3126_s3136_r10724_r10726_p4133
 mc16_13TeV.364192.Sherpa_221_NNPDF30NNLO_Wtaunu_MAXHTPTV140_280_BFilter.deriv.DAOD_HIGG8D1.e5340_e5984_s3126_r10724_r10726_p4133
 mc16_13TeV.364193.Sherpa_221_NNPDF30NNLO_Wtaunu_MAXHTPTV280_500_CVetoBVeto.deriv.DAOD_HIGG8D1.e5340_e5984_s3126_r10724_r10726_p4133
 mc16_13TeV.364193.Sherpa_221_NNPDF30NNLO_Wtaunu_MAXHTPTV280_500_CVetoBVeto.deriv.DAOD_HIGG8D1.e5340_e5984_s3126_s3136_r10724_r10726_p4133
 mc16_13TeV.364194.Sherpa_221_NNPDF30NNLO_Wtaunu_MAXHTPTV280_500_CFilterBVeto.deriv.DAOD_HIGG8D1.e5340_e5984_s3126_s3136_r10724_r10726_p4133

mc16_13TeV.364194.Sherpa_221_NNPDF30NNLO_Wtaunu_MAXHTPTV280_500_CFilterBVeto.deriv.DAOD_HIGG8D1.e5340_e5984_s3126_r10724_r10726_p4133
 mc16_13TeV.364195.Sherpa_221_NNPDF30NNLO_Wtaunu_MAXHTPTV280_500_BFilter.deriv.DAOD_HIGG8D1.e5340_e5984_s3126_s3136_r10724_r10726_p4133
 mc16_13TeV.364195.Sherpa_221_NNPDF30NNLO_Wtaunu_MAXHTPTV280_500_BFilter.deriv.DAOD_HIGG8D1.e5340_e5984_s3126_r10724_r10726_p4133
 mc16_13TeV.364196.Sherpa_221_NNPDF30NNLO_Wtaunu_MAXHTPTV500_1000.deriv.DAOD_HIGG8D1.e5340_e5984_s3126_s3136_r10724_r10726_p4133
 mc16_13TeV.364196.Sherpa_221_NNPDF30NNLO_Wtaunu_MAXHTPTV500_1000.deriv.DAOD_HIGG8D1.e5340_e5984_s3126_r10724_r10726_p4133
 mc16_13TeV.364197.Sherpa_221_NNPDF30NNLO_Wtaunu_MAXHTPTV1000_E_CMS.deriv.DAOD_HIGG8D1.e5340_e5984_s3126_s3136_r10724_r10726_p4133
 mc16_13TeV.364197.Sherpa_221_NNPDF30NNLO_Wtaunu_MAXHTPTV1000_E_CMS.deriv.DAOD_HIGG8D1.e5340_e5984_s3126_r10724_r10726_p4133
 mc16_13TeV.364500.Sherpa_222_NNPDF30NNLO_eegamma_pty_7_15.deriv.DAOD_HIGG8D1.e5928_e5984_s3126_r10724_r10726_p4133
 mc16_13TeV.364501.Sherpa_222_NNPDF30NNLO_eegamma_pty_15_35.deriv.DAOD_HIGG8D1.e5928_e5984_s3126_r10724_r10726_p4133
 mc16_13TeV.364502.Sherpa_222_NNPDF30NNLO_eegamma_pty_35_70.deriv.DAOD_HIGG8D1.e5928_e5984_s3126_r10724_r10726_p4133
 mc16_13TeV.364503.Sherpa_222_NNPDF30NNLO_eegamma_pty_70_140.deriv.DAOD_HIGG8D1.e5928_e5984_s3126_r10724_r10726_p4133
 mc16_13TeV.364504.Sherpa_222_NNPDF30NNLO_eegamma_pty_140_E_CMS.deriv.DAOD_HIGG8D1.e5928_e5984_s3126_r10724_r10726_p4133
 mc16_13TeV.364505.Sherpa_222_NNPDF30NNLO_mumugamma_pty_7_15.deriv.DAOD_HIGG8D1.e5928_e5984_s3126_r10724_r10726_p4133
 mc16_13TeV.364506.Sherpa_222_NNPDF30NNLO_mumugamma_pty_15_35.deriv.DAOD_HIGG8D1.e5928_e5984_s3126_r10724_r10726_p4133
 mc16_13TeV.364507.Sherpa_222_NNPDF30NNLO_mumugamma_pty_35_70.deriv.DAOD_HIGG8D1.e5928_e5984_s3126_r10724_r10726_p4133
 mc16_13TeV.364508.Sherpa_222_NNPDF30NNLO_mumugamma_pty_70_140.deriv.DAOD_HIGG8D1.e5928_e5984_s3126_r10724_r10726_p4133
 mc16_13TeV.364509.Sherpa_222_NNPDF30NNLO_mumugamma_pty_140_E_CMS.deriv.DAOD_HIGG8D1.e5928_e5984_s3126_r10724_r10726_p4133
 mc16_13TeV.364511.Sherpa_222_NNPDF30NNLO_tautaugamma_pty_15_35.deriv.DAOD_HIGG8D1.e5928_e5984_s3126_r10724_r10726_p4133
 mc16_13TeV.364512.Sherpa_222_NNPDF30NNLO_tautaugamma_pty_35_70.deriv.DAOD_HIGG8D1.e5928_e5984_s3126_r10724_r10726_p4133
 mc16_13TeV.364513.Sherpa_222_NNPDF30NNLO_tautaugamma_pty_70_140.deriv.DAOD_HIGG8D1.e5982_e5984_s3126_r10724_r10726_p4133
 mc16_13TeV.364514.Sherpa_222_NNPDF30NNLO_tautaugamma_pty_140_E_CMS.deriv.DAOD_HIGG8D1.e5928_e5984_s3126_r10724_r10726_p4133
 mc16_13TeV.364522.Sherpa_222_NNPDF30NNLO_enugamma_pty_15_35.deriv.DAOD_HIGG8D1.e5928_e5984_s3126_r10724_r10726_p4133
 mc16_13TeV.364523.Sherpa_222_NNPDF30NNLO_enugamma_pty_35_70.deriv.DAOD_HIGG8D1.e5928_e5984_s3126_r10724_r10726_p4133
 mc16_13TeV.364524.Sherpa_222_NNPDF30NNLO_enugamma_pty_70_140.deriv.DAOD_HIGG8D1.e5928_e5984_s3126_r10724_r10726_p4133
 mc16_13TeV.364525.Sherpa_222_NNPDF30NNLO_enugamma_pty_140_E_CMS.deriv.DAOD_HIGG8D1.e5928_e5984_s3126_r10724_r10726_p4133
 mc16_13TeV.364527.Sherpa_222_NNPDF30NNLO_munugamma_pty_15_35.deriv.DAOD_HIGG8D1.e5928_e5984_s3126_r10724_r10726_p4133
 mc16_13TeV.364528.Sherpa_222_NNPDF30NNLO_munugamma_pty_35_70.deriv.DAOD_HIGG8D1.e5928_e5984_s3126_r10724_r10726_p4133
 mc16_13TeV.364529.Sherpa_222_NNPDF30NNLO_munugamma_pty_70_140.deriv.DAOD_HIGG8D1.e5928_e5984_s3126_r10724_r10726_p4133
 mc16_13TeV.364530.Sherpa_222_NNPDF30NNLO_munugamma_pty_140_E_CMS.deriv.DAOD_HIGG8D1.e5928_e5984_s3126_r10724_r10726_p4133
 mc16_13TeV.364532.Sherpa_222_NNPDF30NNLO_taunugamma_pty_15_35.deriv.DAOD_HIGG8D1.e5928_e5984_s3126_r10724_r10726_p4133
 mc16_13TeV.364533.Sherpa_222_NNPDF30NNLO_taunugamma_pty_35_70.deriv.DAOD_HIGG8D1.e5928_e5984_s3126_r10724_r10726_p4133

mc16_13TeV.364534.Sherpa_222_NNPDF30NNLO_taunugamma_pty_70_140.deriv.DAOD_HIGG8D1.e5928_e5984_s3126_r10724_r10726_p4133
mc16_13TeV.364535.Sherpa_222_NNPDF30NNLO_taunugamma_pty_140_E_CMS.deriv.DAOD_HIGG8D1.e5928_e5984_s3126_r10724_r10726_p4133
mc16_13TeV.410560.MadGraphPythia8EvtGen_A14_tZ_4fl_tchan_noAllHad.deriv.DAOD_HIGG8D1.e5803_e5984_s3126_r10724_r10726_p4133
mc16_13TeV.410408.aMcAtNloPythia8EvtGen_tWZ_Ztoll_minDR1.deriv.DAOD_HIGG8D1.e6423_e5984_s3126_r10724_r10726_p4133
mc16_13TeV.364242.Sherpa_222_NNPDF30NNLO_WWW_3l3v_EW6.deriv.DAOD_HIGG8D1.e5887_e5984_s3126_r10724_r10726_p4133
mc16_13TeV.364243.Sherpa_222_NNPDF30NNLO_WWZ_4l2v_EW6.deriv.DAOD_HIGG8D1.e5887_e5984_s3126_r10724_r10726_p4133
mc16_13TeV.364244.Sherpa_222_NNPDF30NNLO_WWZ_2l4v_EW6.deriv.DAOD_HIGG8D1.e5887_e5984_s3126_r10724_r10726_p4133
mc16_13TeV.364245.Sherpa_222_NNPDF30NNLO_WZZ_5l1v_EW6.deriv.DAOD_HIGG8D1.e5887_e5984_s3126_r10724_r10726_p4133
mc16_13TeV.364246.Sherpa_222_NNPDF30NNLO_WZZ_3l3v_EW6.deriv.DAOD_HIGG8D1.e5887_e5984_s3126_r10724_r10726_p4133
mc16_13TeV.364247.Sherpa_222_NNPDF30NNLO_ZZZ_6l0v_EW6.deriv.DAOD_HIGG8D1.e5887_e5984_s3126_r10724_r10726_p4133
mc16_13TeV.364248.Sherpa_222_NNPDF30NNLO_ZZZ_4l2v_EW6.deriv.DAOD_HIGG8D1.e5887_e5984_s3126_r10724_r10726_p4133
mc16_13TeV.364249.Sherpa_222_NNPDF30NNLO_ZZZ_2l4v_EW6.deriv.DAOD_HIGG8D1.e5887_e5984_s3126_r10724_r10726_p4133
mc16_13TeV.342284.Pythia8EvtGen_A14NNPDF23LO_WH125_inc.deriv.DAOD_HIGG8D1.e4246_e5984_s3126_r10724_r10726_p4133
mc16_13TeV.342285.Pythia8EvtGen_A14NNPDF23LO_ZH125_inc.deriv.DAOD_HIGG8D1.e4246_e5984_s3126_r10724_r10726_p4133
mc16_13TeV.341998.aMcAtNloHppEG_UEEE5_CTEQ6L1_CT10ME_tWH125_gamgam_yt_plus1.deriv.DAOD_HIGG8D1.e4394_e5984_s3126_r10724_r10726_p4133
mc16_13TeV.410389.MadGraphPythia8EvtGen_A14NNPDF23_ttgamma_nonallhadronic.deriv.DAOD_HIGG8D1.e6155_e5984_s3126_r10724_r10726_p4133
mc16_13TeV.410470.PhPy8EG_A14_ttbar_hdamp258p75_nonallhad.deriv.DAOD_HIGG8D1.e6337_e5984_s3126_r10724_r10726_p4133
mc16_13TeV.410472.PhPy8EG_A14_ttbar_hdamp258p75_dil.deriv.DAOD_HIGG8D1.e6348_e5984_s3126_r10724_r10726_p4133
mc16_13TeV.346343.PhPy8EG_A14NNPDF23_NNPDF30ME_ttH125_allhad.deriv.DAOD_HIGG8D1.e7148_e5984_s3126_r10724_r10726_p4133
mc16_13TeV.346343.PhPy8EG_A14NNPDF23_NNPDF30ME_ttH125_allhad.deriv.DAOD_HIGG8D1.e7148_e5984_a875_r10724_r10726_p4133
mc16_13TeV.346344.PhPy8EG_A14NNPDF23_NNPDF30ME_ttH125_semilep.deriv.DAOD_HIGG8D1.e7148_e5984_a875_r10724_r10726_p4133
mc16_13TeV.346344.PhPy8EG_A14NNPDF23_NNPDF30ME_ttH125_semilep.deriv.DAOD_HIGG8D1.e7148_e5984_s3126_r10724_r10726_p4133
mc16_13TeV.346345.PhPy8EG_A14NNPDF23_NNPDF30ME_ttH125_dilep.deriv.DAOD_HIGG8D1.e7148_e5984_a875_r10724_r10726_p4133
mc16_13TeV.346345.PhPy8EG_A14NNPDF23_NNPDF30ME_ttH125_dilep.deriv.DAOD_HIGG8D1.e7148_e5984_s3126_r10724_r10726_p4133

1846 A Machine Learning Models

1847 The following section provides details of the various MVAs as well as a few studies performed
1848 in support of this analysis, exploring alternate decisions and strategies.

1849 A.1 Higgs Reconstruction Models**1850 A.1.1 b-jet Identification Features - 2lSS**

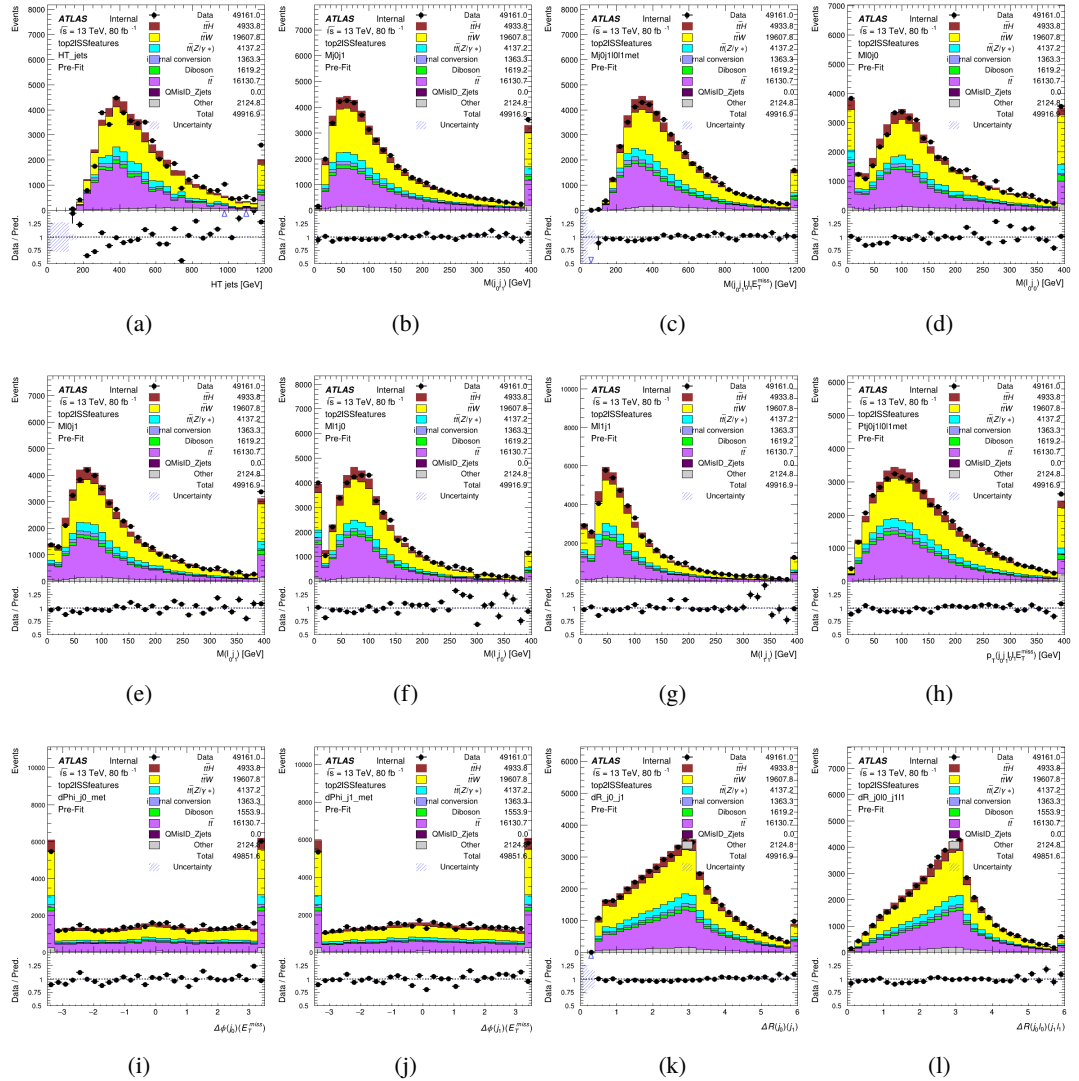


Figure A.1: Input features for top2lSS

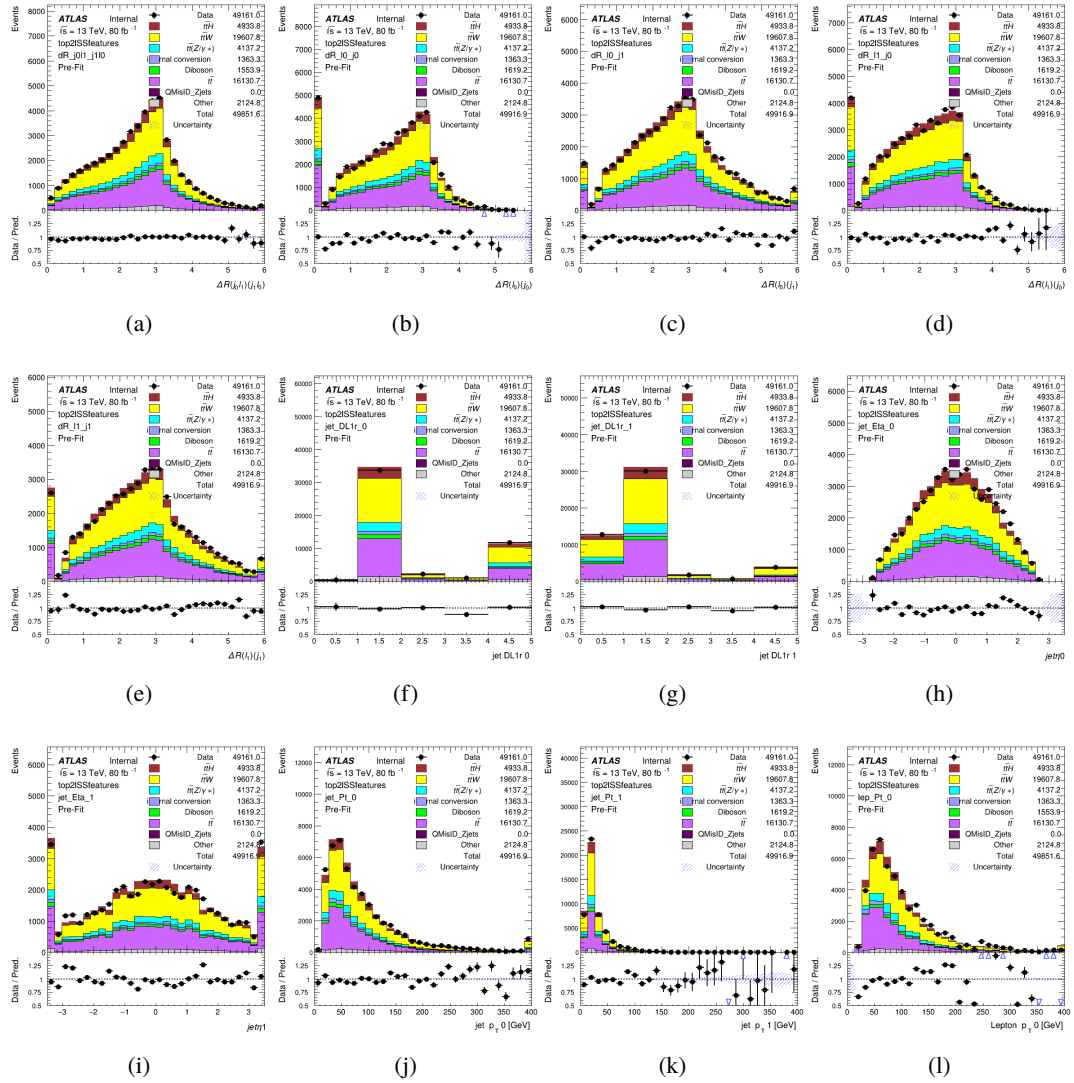


Figure A.2: Input features for top2lSS

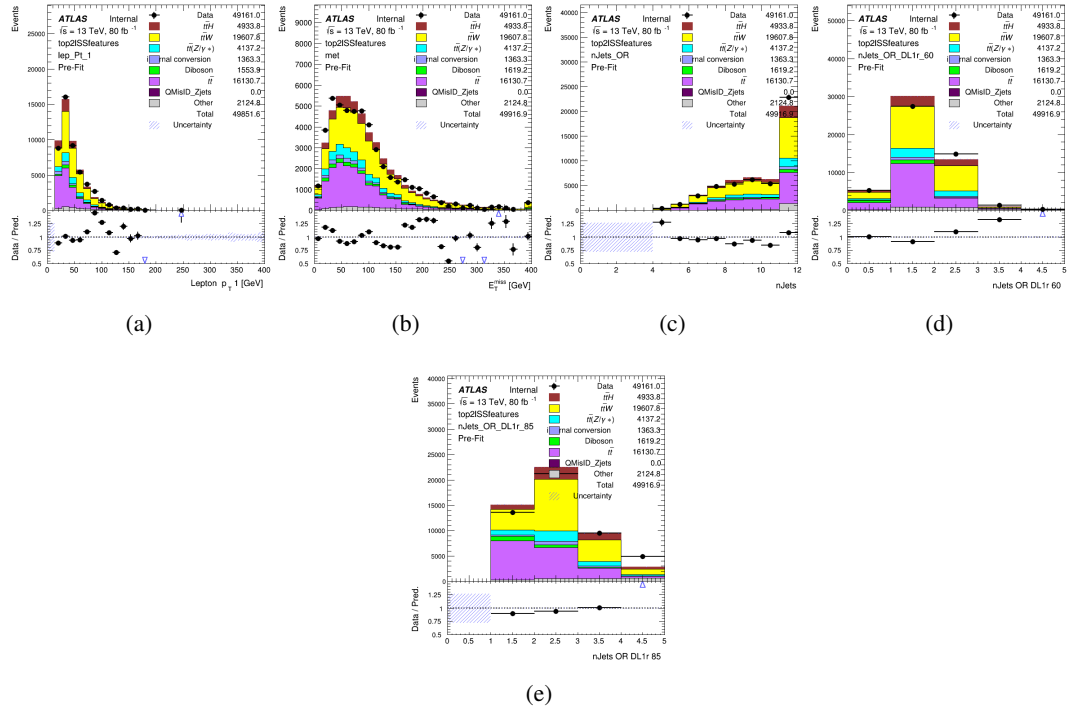


Figure A.3: Input features for top2ISS

1851 **A.1.2 b-jet Identification Features - 3l**

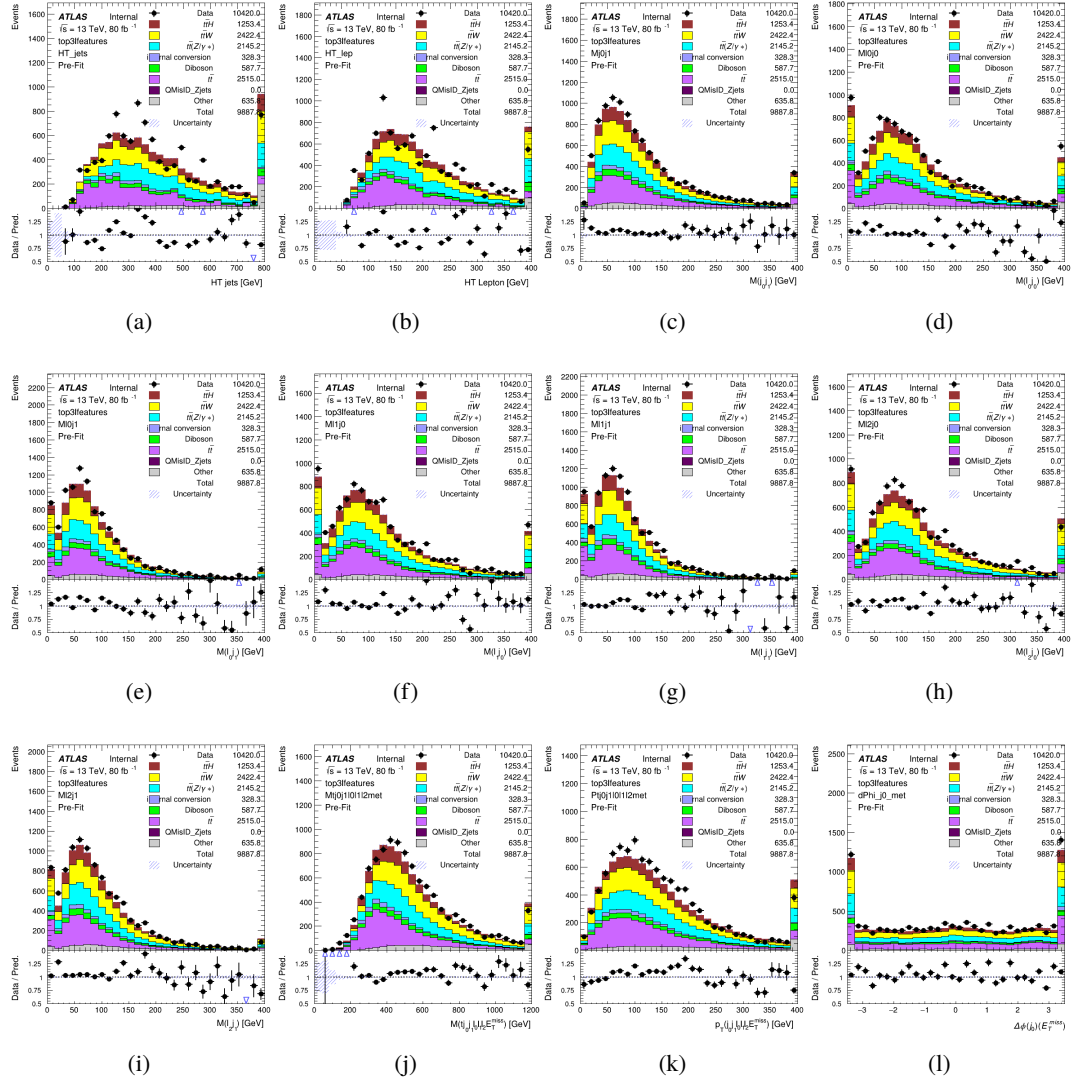


Figure A.4: Input features for top31

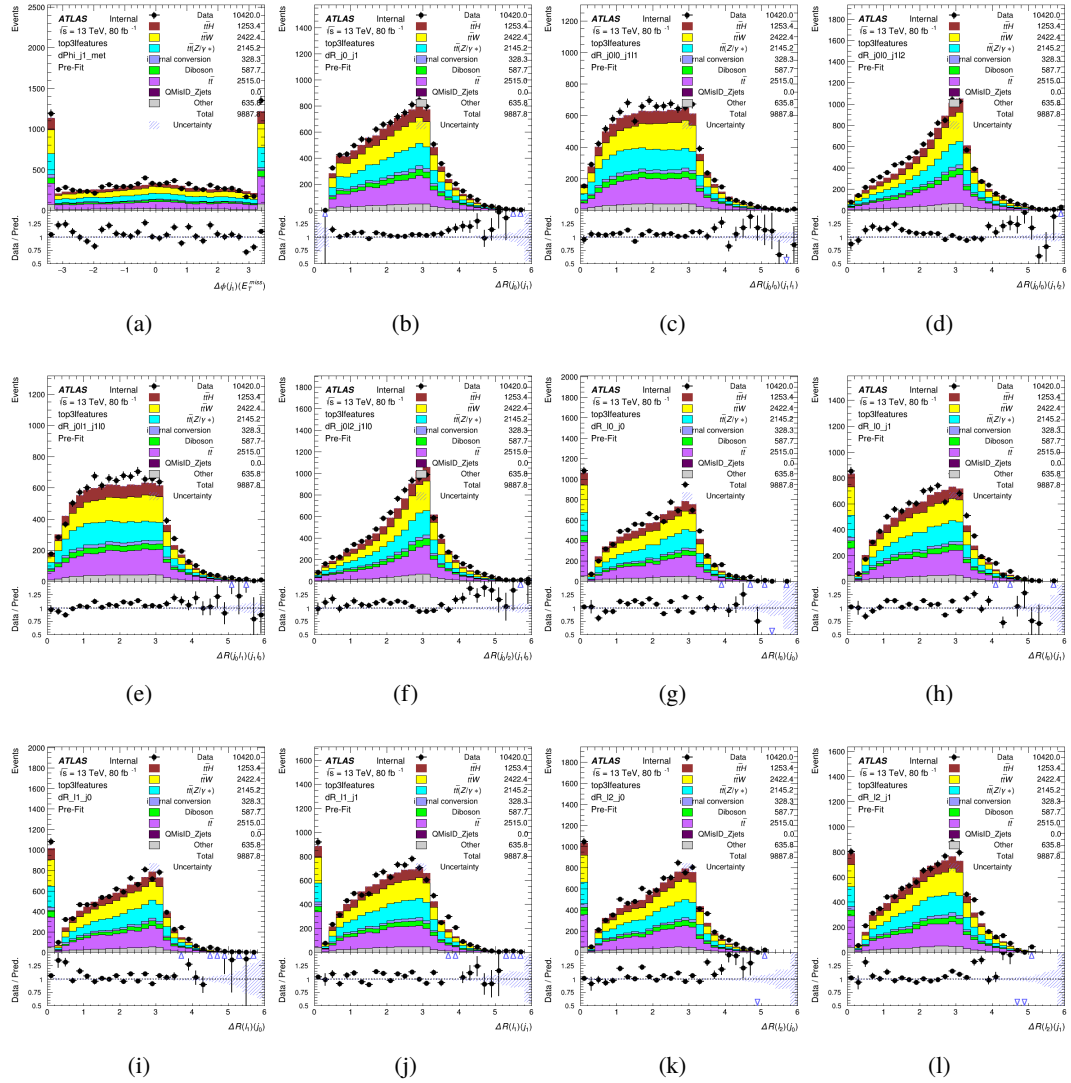


Figure A.5: Input features for top31

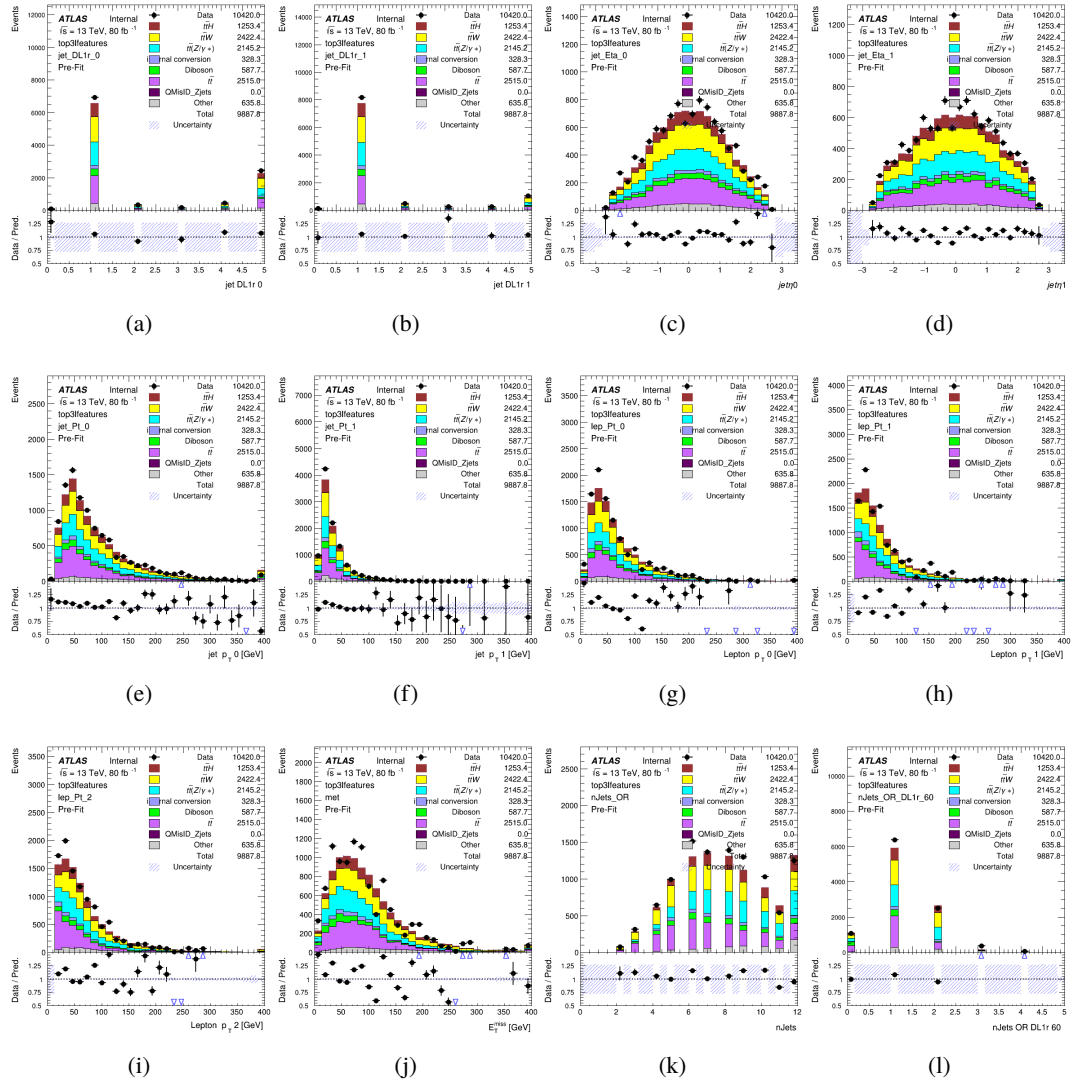
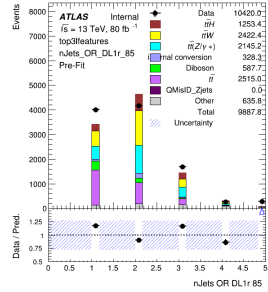


Figure A.6: Input features for top31



(a)

Figure A.7: Input features for top31

1852 **A.1.3 Higgs Reconstruction Features - 2lSS**

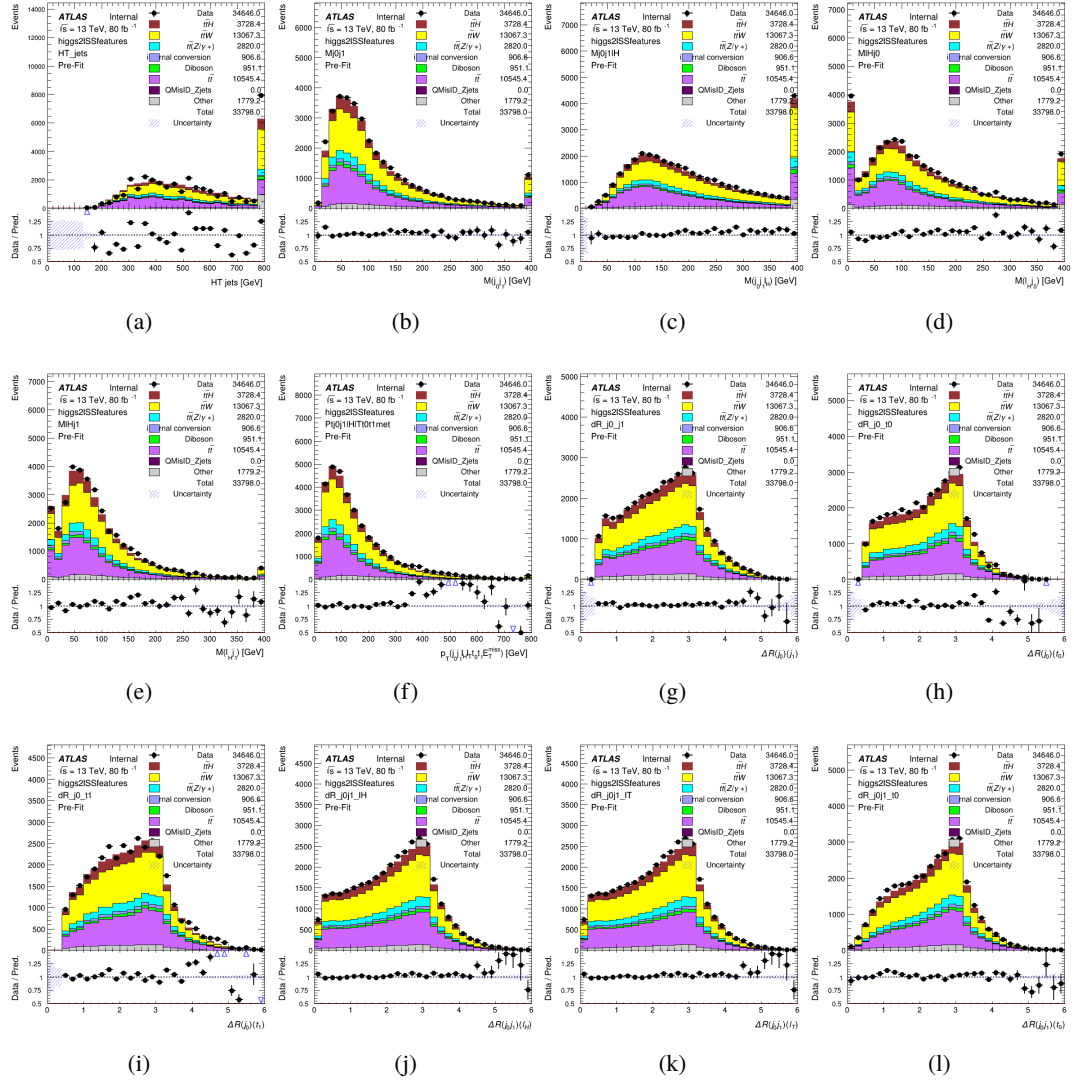


Figure A.8: Input features for higgs2lSS

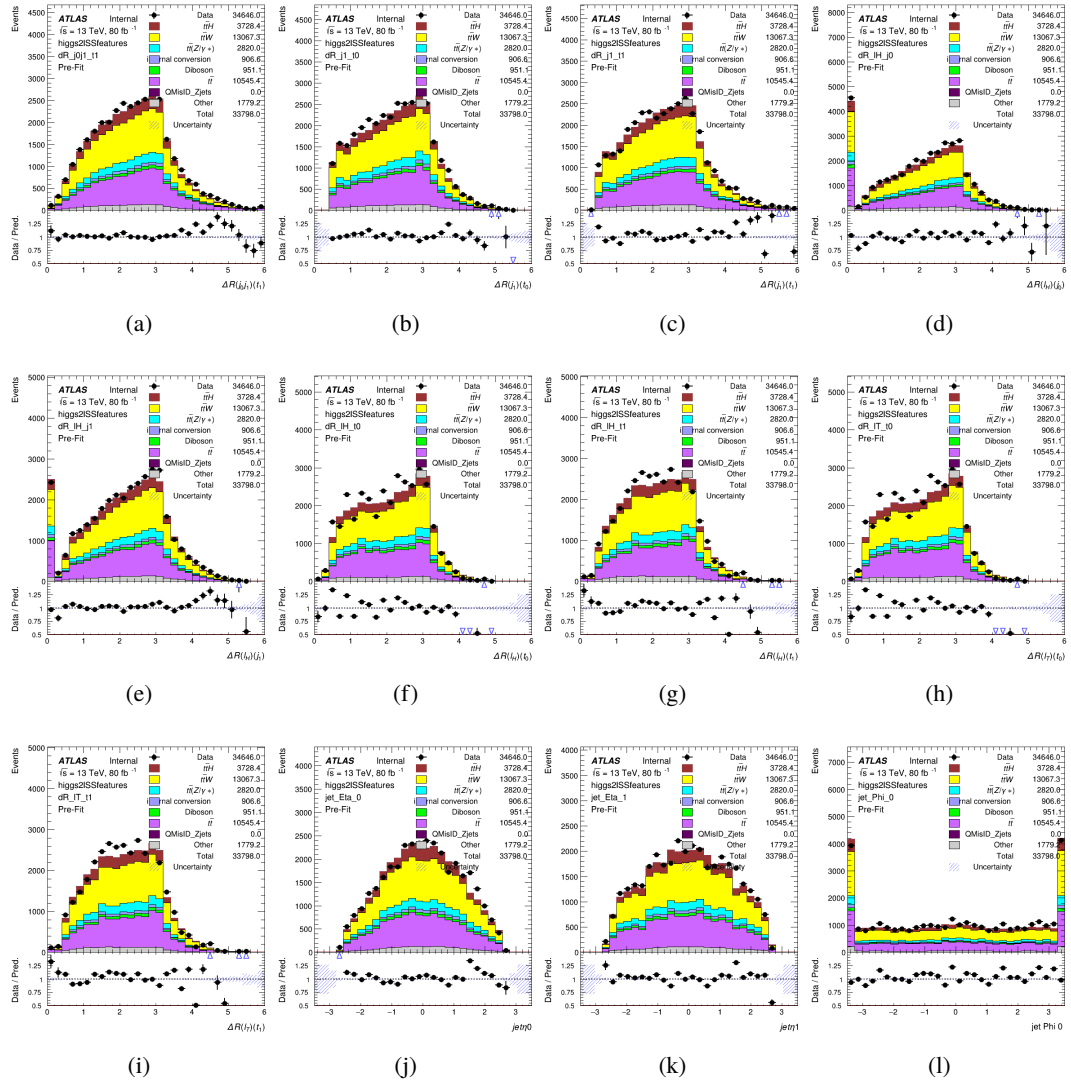


Figure A.9: Input features for higgs2lSS

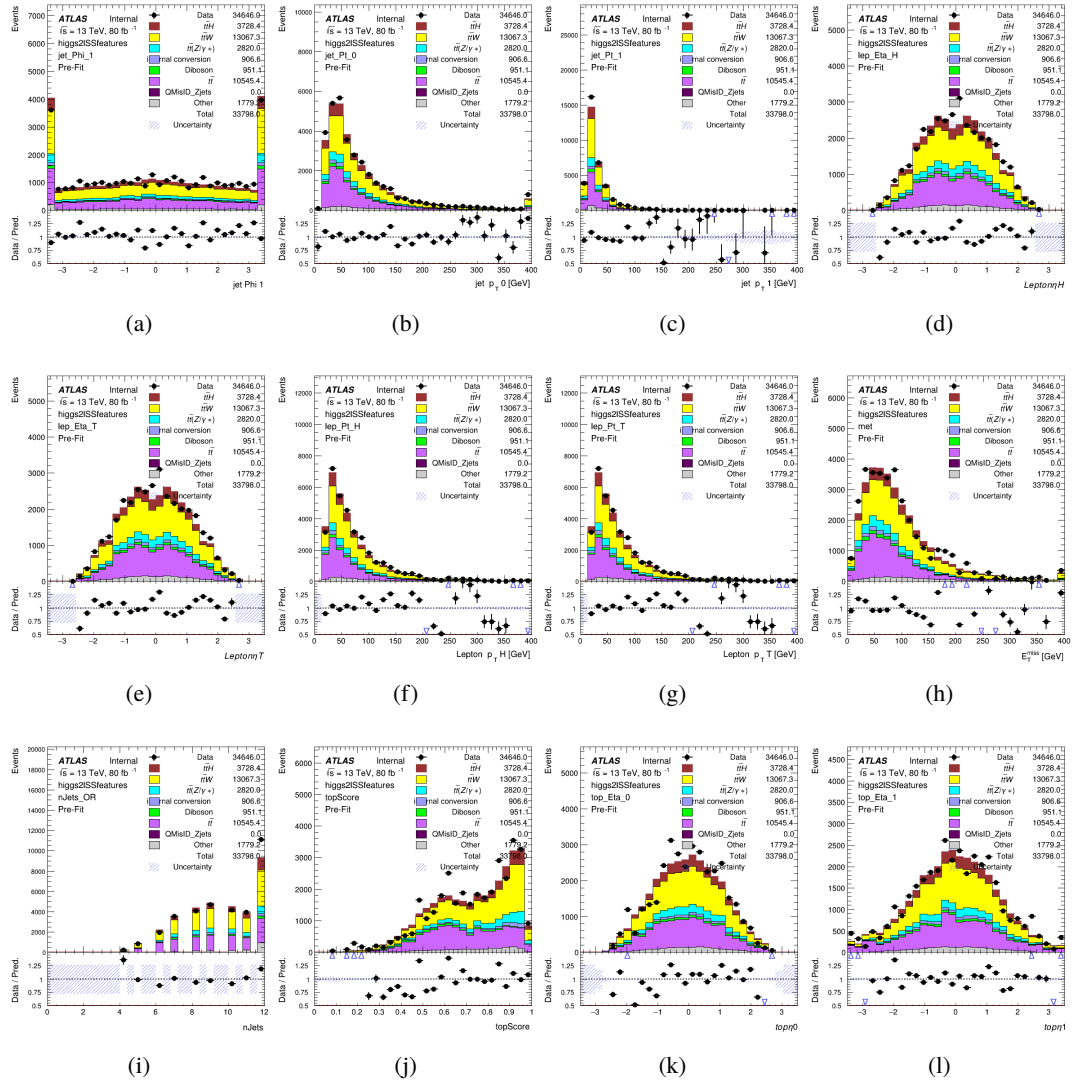


Figure A.10: Input features for higgs2IS

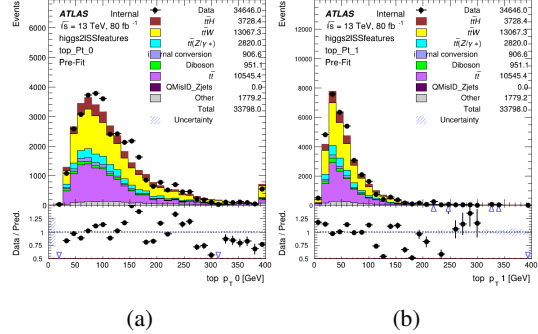


Figure A.11: Input features for higgs2lSS

1853 **A.1.4 Higgs Reconstruction Features - 3lS**

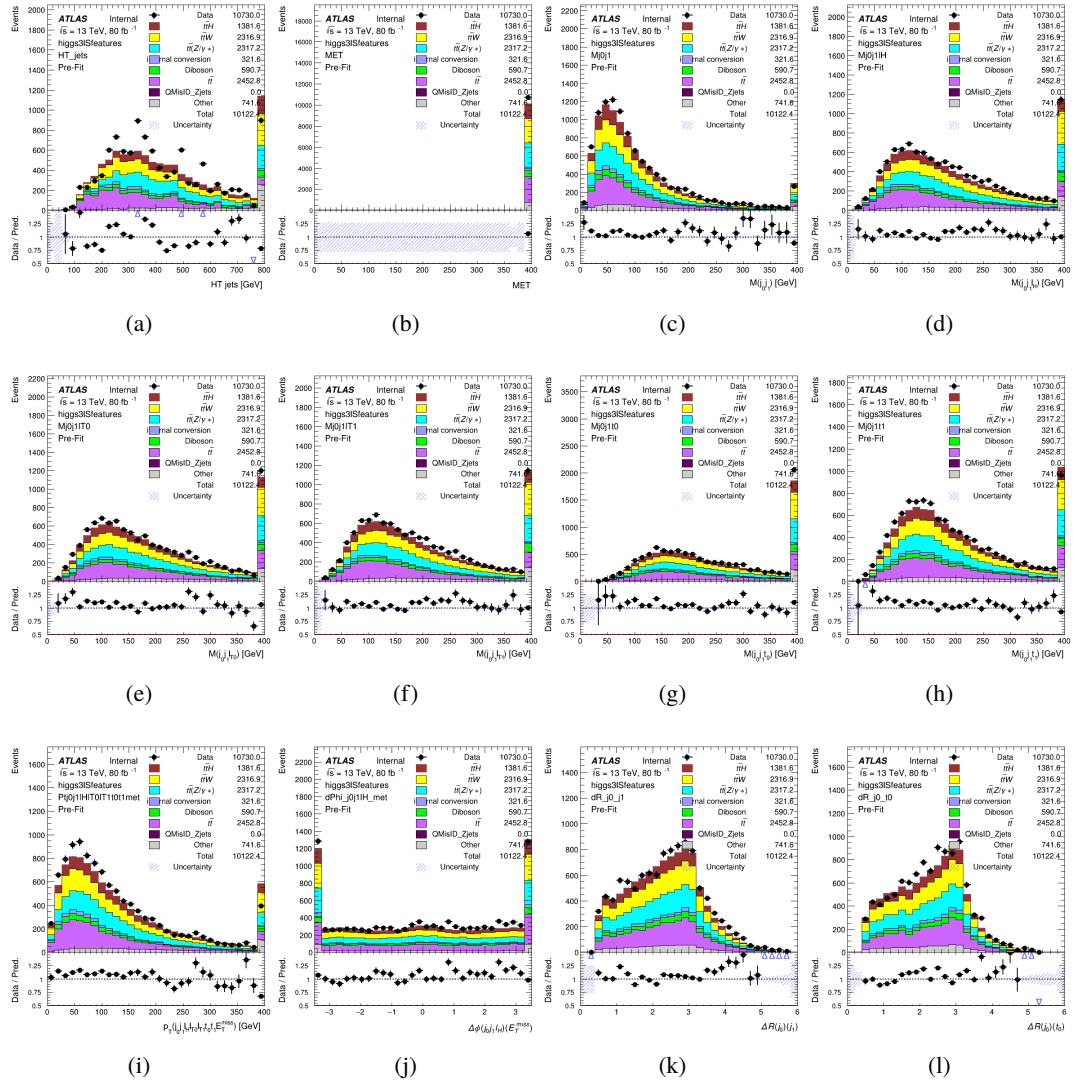


Figure A.12: Input features for higgs3IS

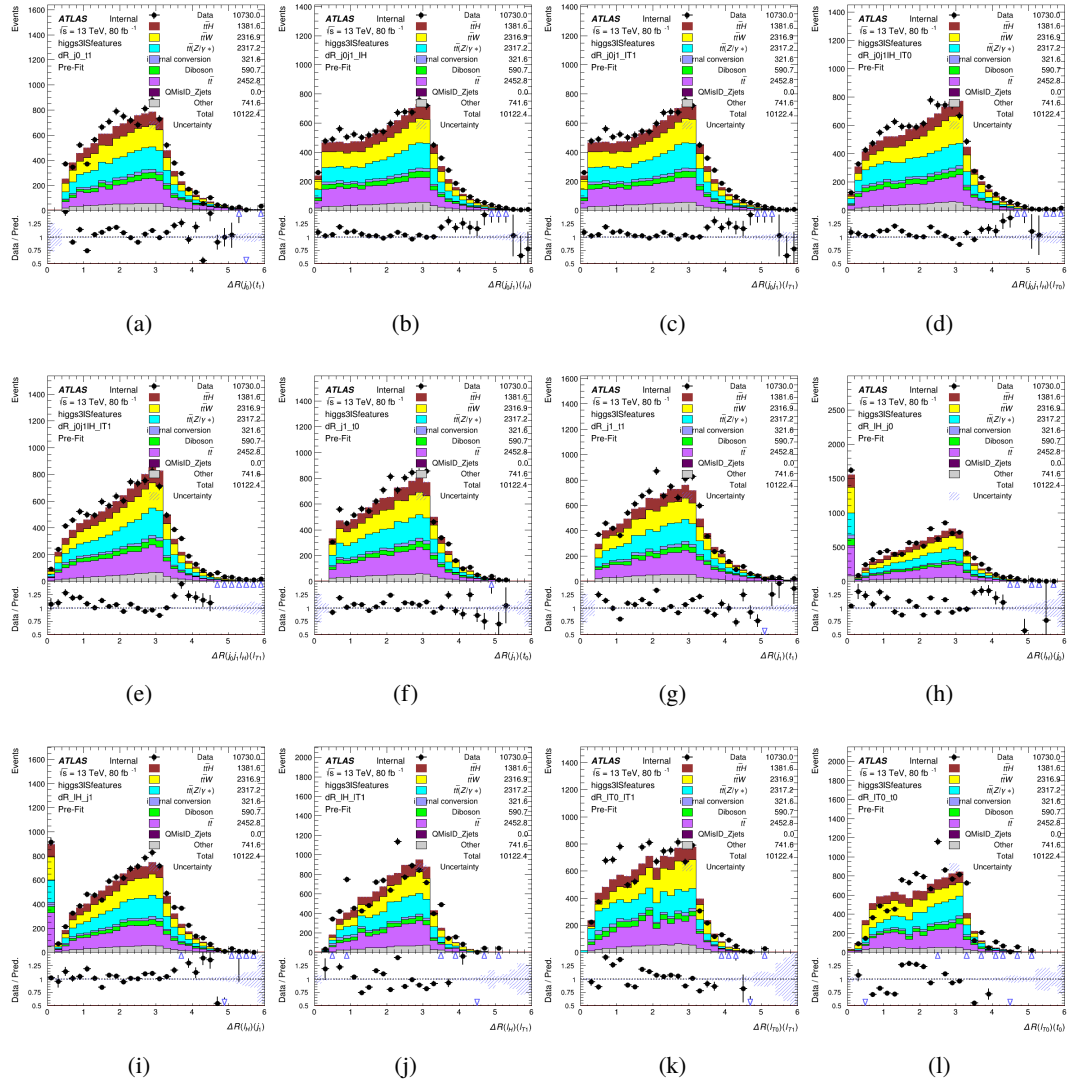


Figure A.13: Input features for higgs3IS

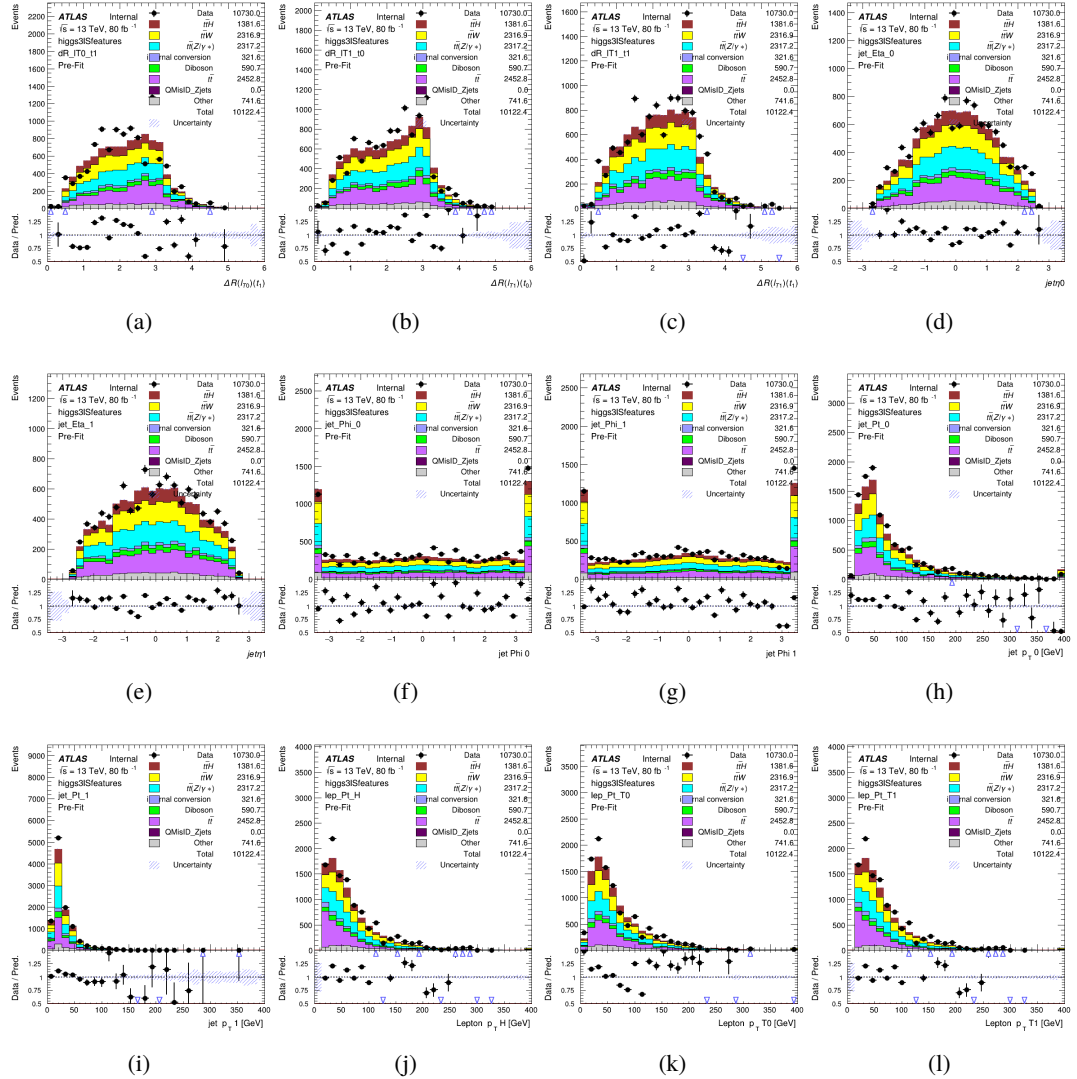


Figure A.14: Input features for higgs3IS

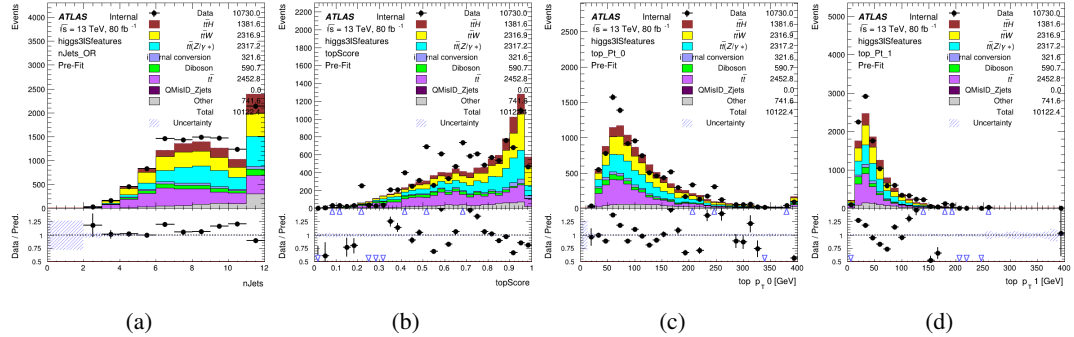


Figure A.15: Input features for higgs3IS

1854 **A.1.5 Higgs Reconstruction Features - 3lF**

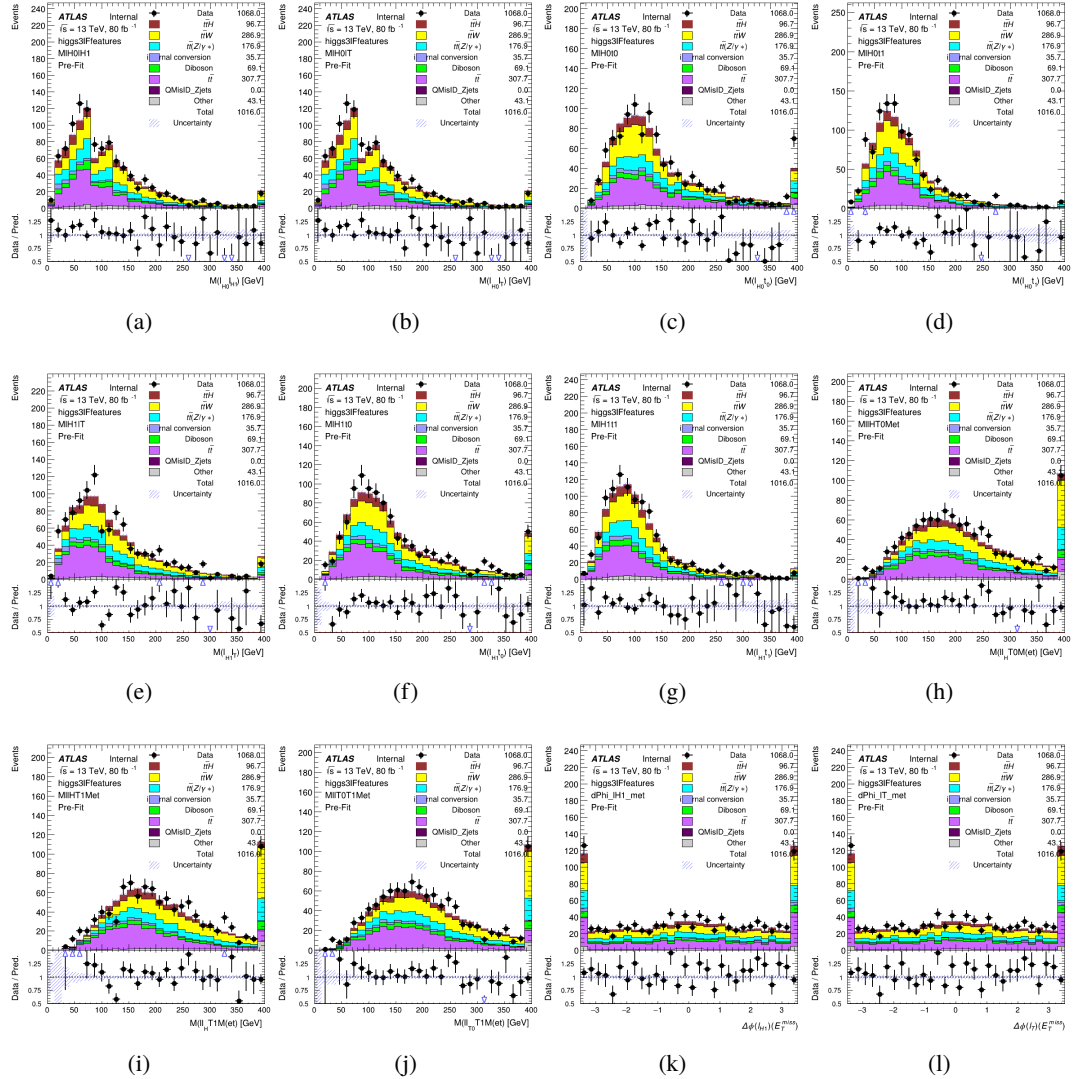


Figure A.16: Input features for higgs3IF

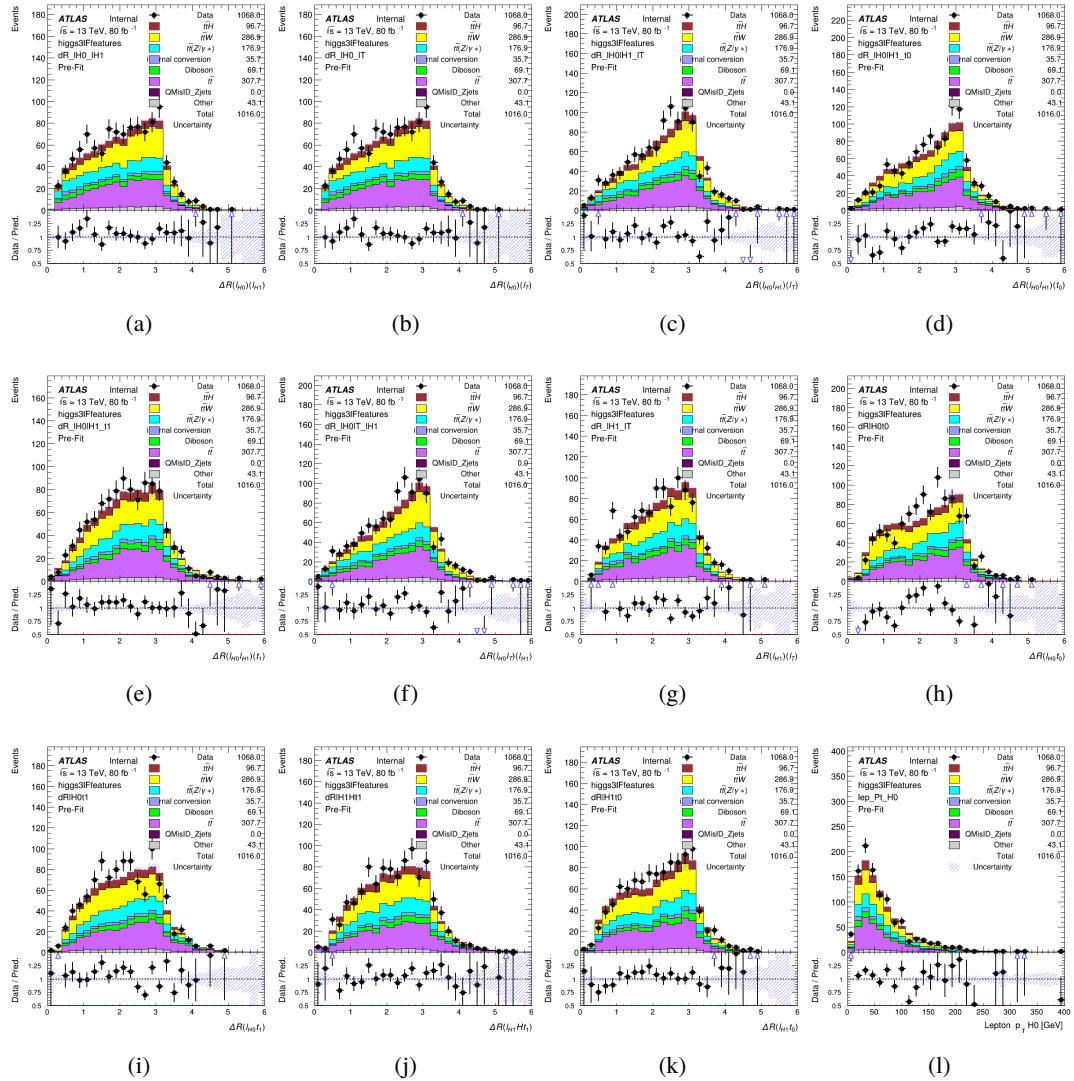


Figure A.17: Input features for higgs3lF

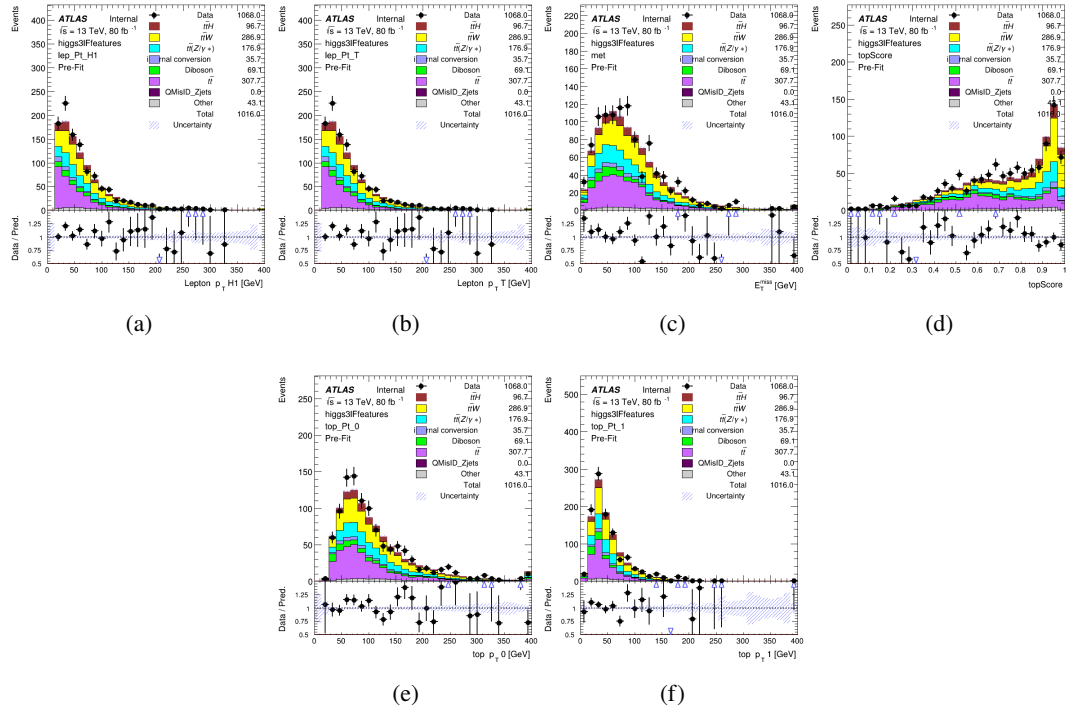
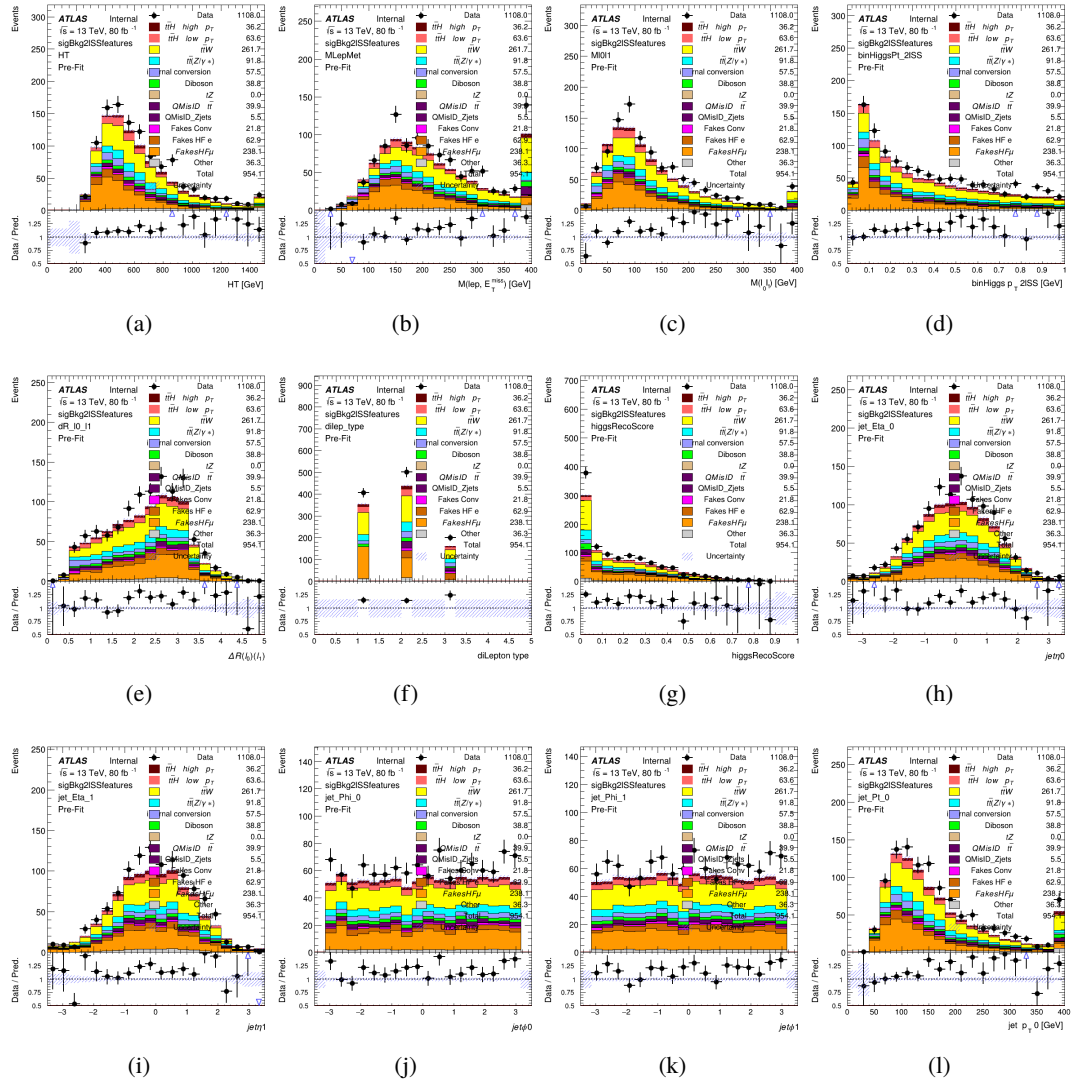
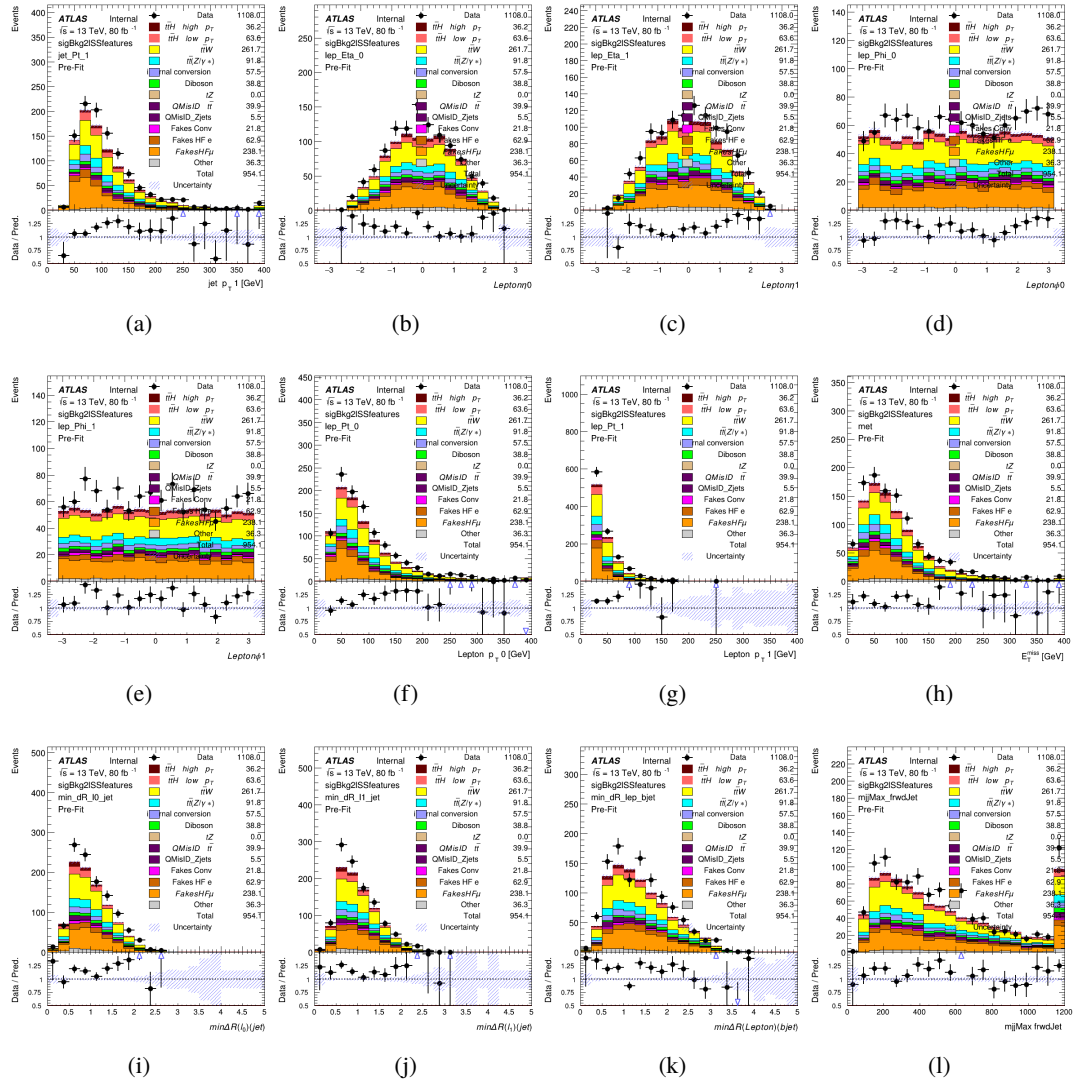


Figure A.18: Input features for higgs3lF

1855 **A.2 Background Rejection MVAs**

1856 **A.2.1 Background Rejection MVA Features - 2lSS**

Figure A.19: Input features for `sigBkg2lSS`

Figure A.20: Input features for `sigBkg2lSS`

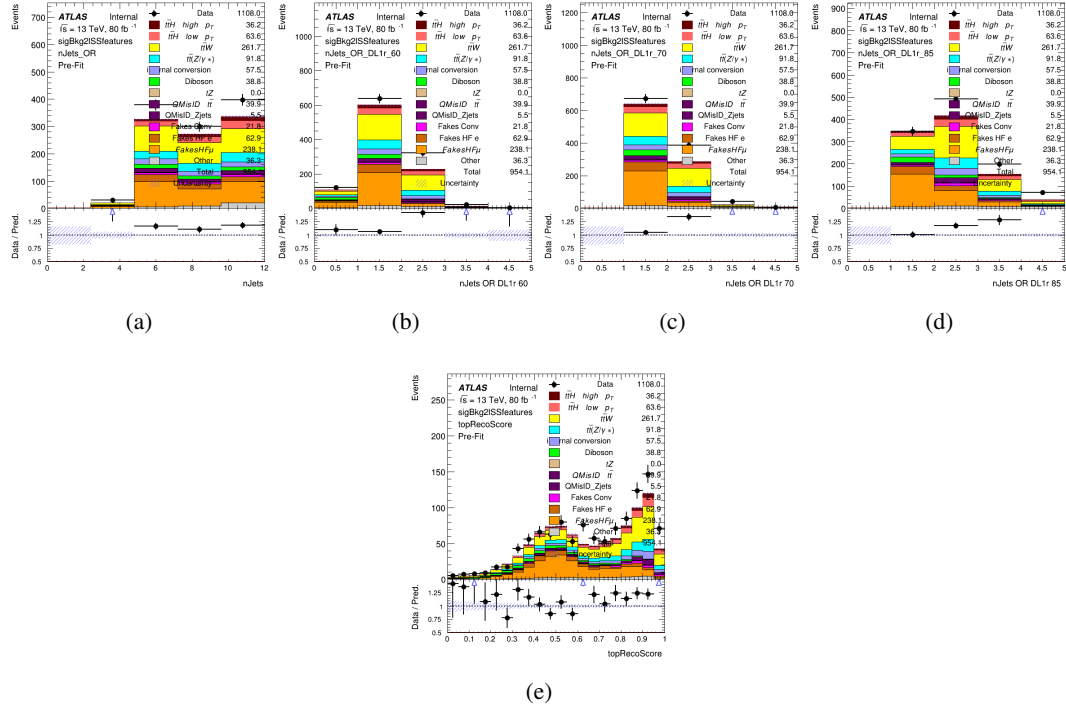


Figure A.21: Input features for sigBkg2lSS

1857 **A.2.2 Background Rejection MVA Features - 3l**

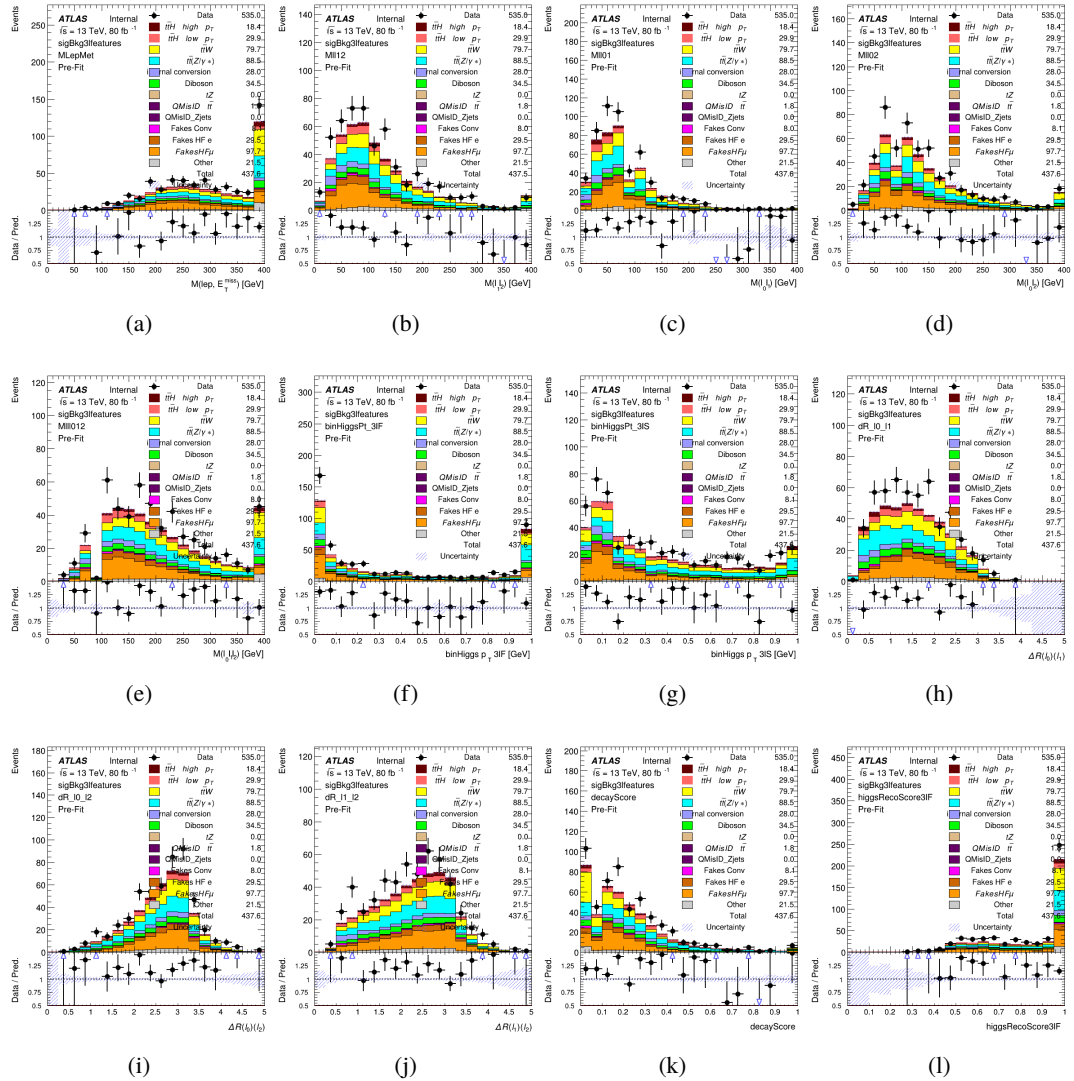


Figure A.22: Input features for sigBkg3l

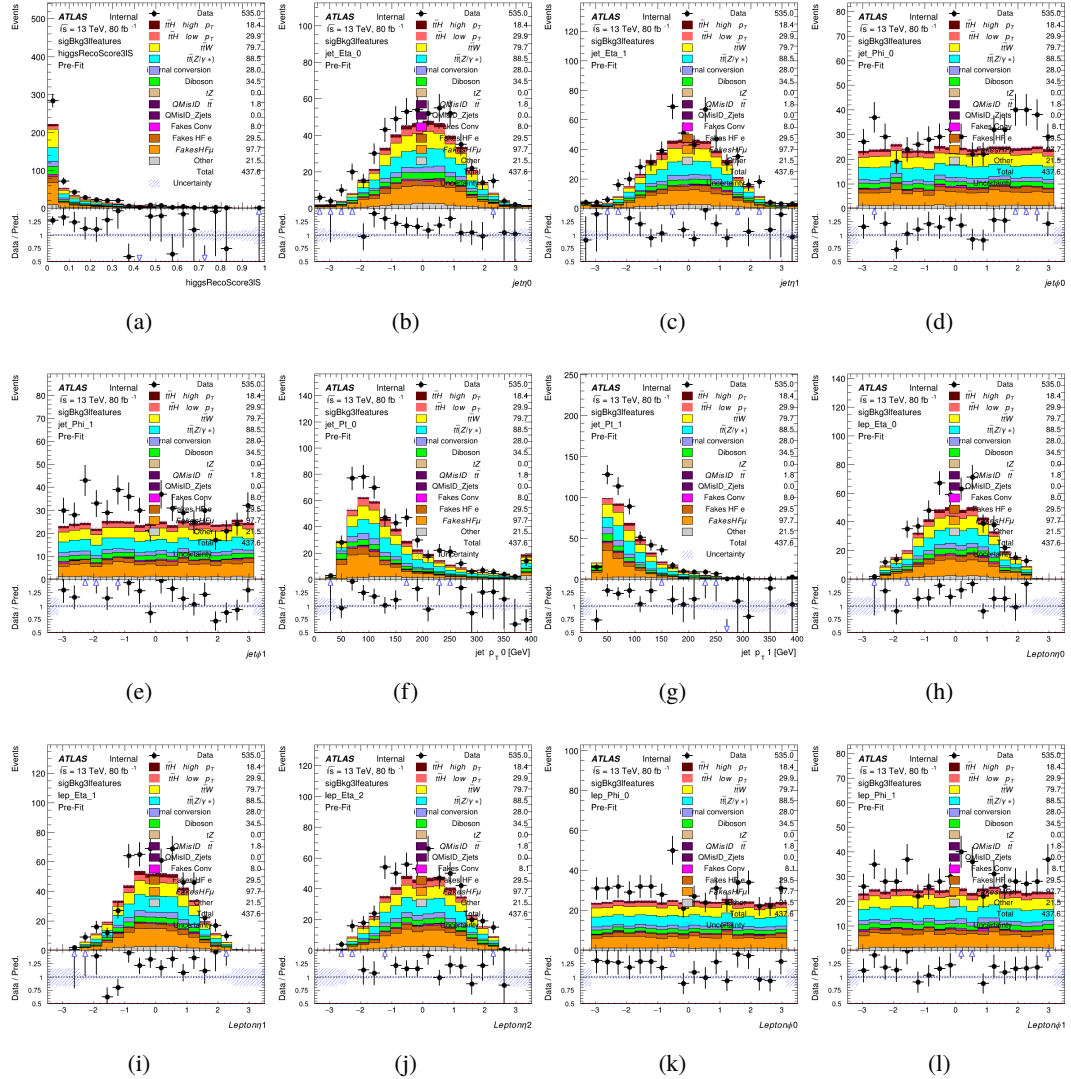


Figure A.23: Input features for sigBkg3l

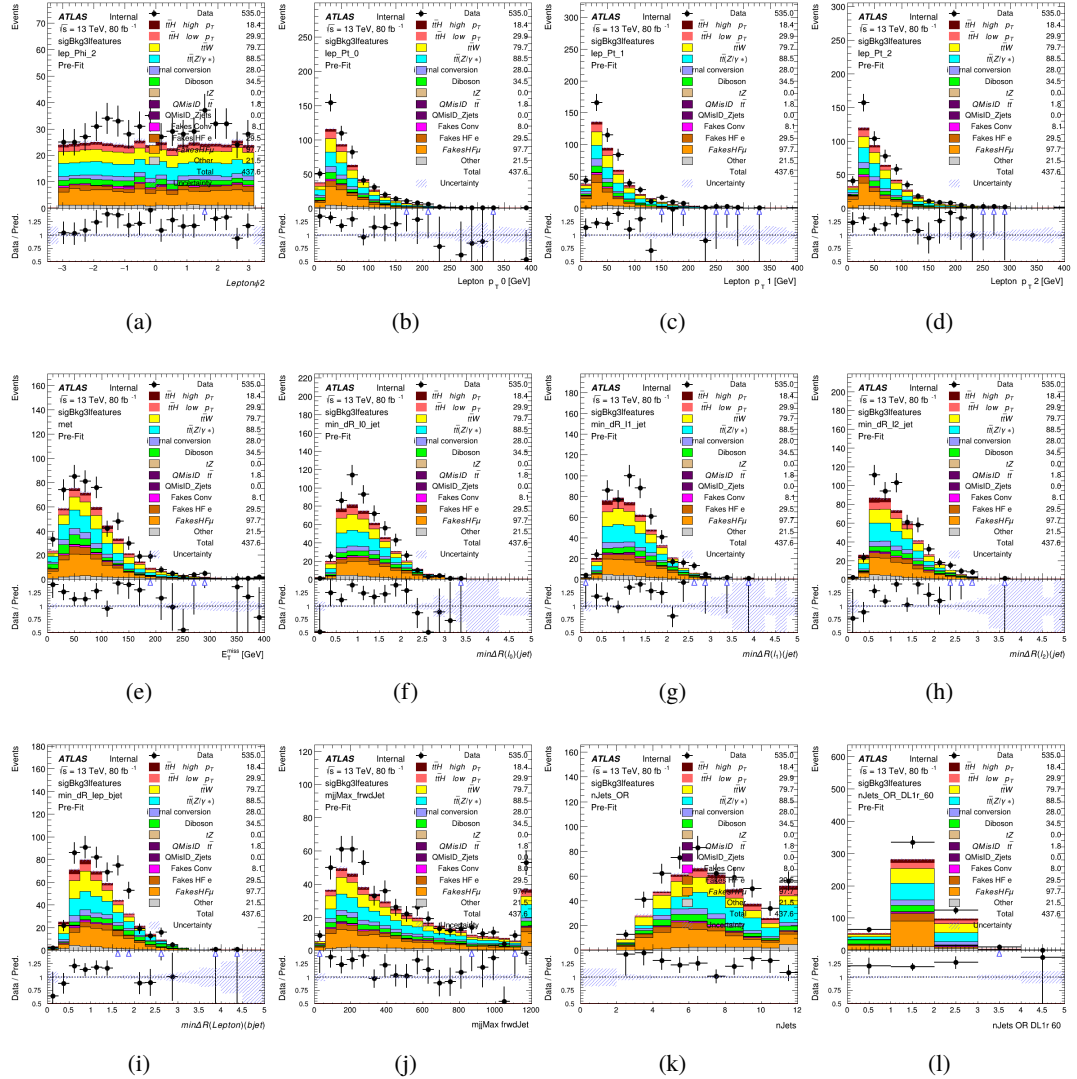


Figure A.24: Input features for sigBkg3l

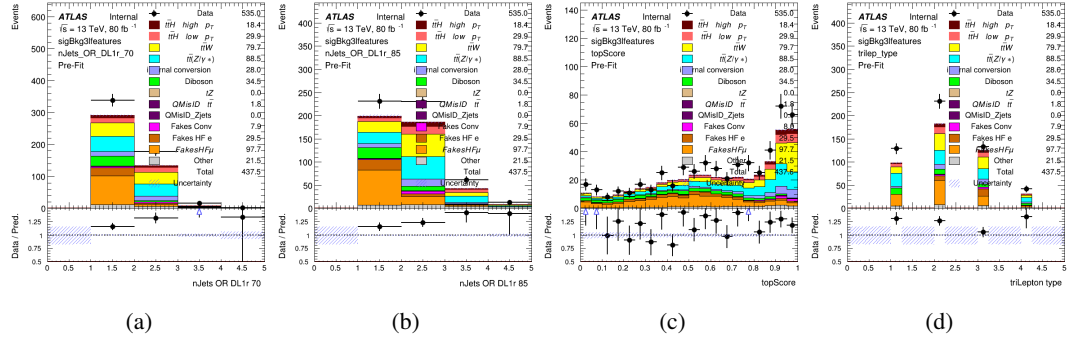


Figure A.25: Input features for sigBkg3l

1858 A.3 Alternate b-jet Identification Algorithm

1859 The nominal analysis reconstructs the b-jets by considering different combinations of jets, and
 1860 asking a neural network to determine whether each combination consists of b-jets from top quark
 1861 decays. An alternate approach would be to give the neural network about all of the jets in an event
 1862 at once, and train it to select which two are most likely to be the b-jets from top decay. It was
 1863 hypothesized that this could perform better than considering each combination independently, as
 1864 the neural network could consider the event as a whole. While this is not found to be the case,
 1865 these studies are documented here as a point of interest and comparison.

1866 For these studies, the kinematics of the 10 highest p_T jets in each event are used for
 1867 training. This includes the vast majority of truth b-jets. Specifically the p_T , η , ϕ , E , and DL1r
 1868 score of each jet are used. For events with fewer than 10 jets, these values are substituted with 0.
 1869 The p_T , η , ϕ , and E of the leptons and E_T^{miss} are included as well. Categorical cross entropy is
 1870 used as the loss function.

Table 56: Accuracy of the NN in identifying b-jets from tops in 2lSS events for the alternate categorical method compared to the nominal method.

Channel	Categorical	Nominal
2lSS	70.6%	73.9%
3l	76.1%	79.8%

1871 **A.4 Binary Classification of the Higgs p_T**

1872 A two bin fit of the Higgs momentum is used because statistics are insufficient for any finer
 1873 resolution. This means separating high and low p_T events is sufficient for this analysis. As
 1874 such, rather than attempting the reconstruct the full Higgs p_T spectrum, a binary classification
 1875 approach is explored.

1876 A model is built to determine whether $t\bar{t}H$ events include a high p_T (>150 GeV) or low
 1877 p_T (<150 GeV) Higgs Boson. While this is now a classification model, it uses the same input
 1878 features described in section 18.4. Binary crossentropy is used as the loss function.

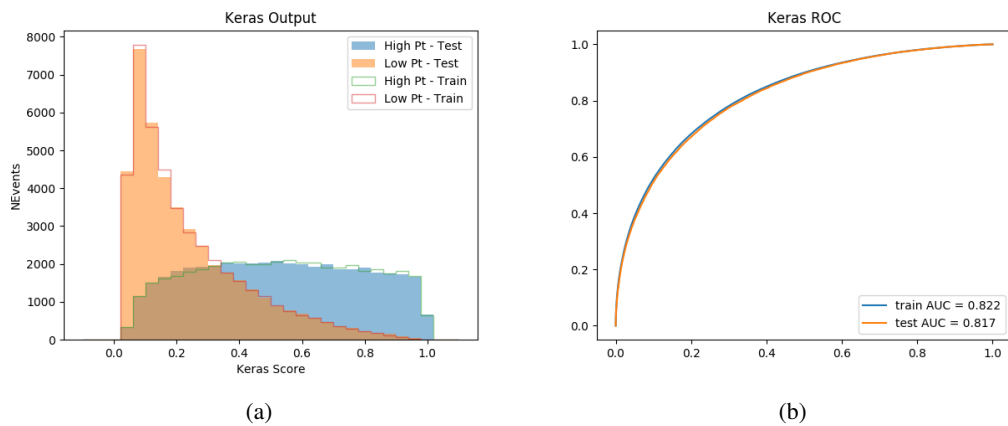


Figure A.26:

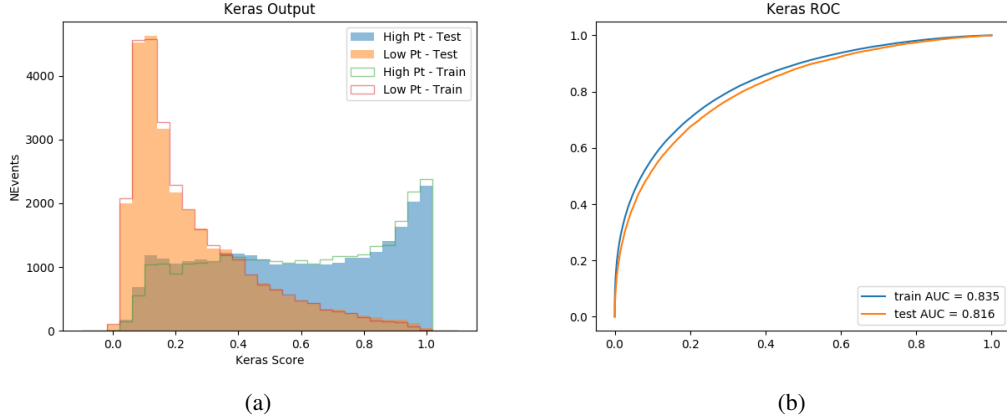


Figure A.27:

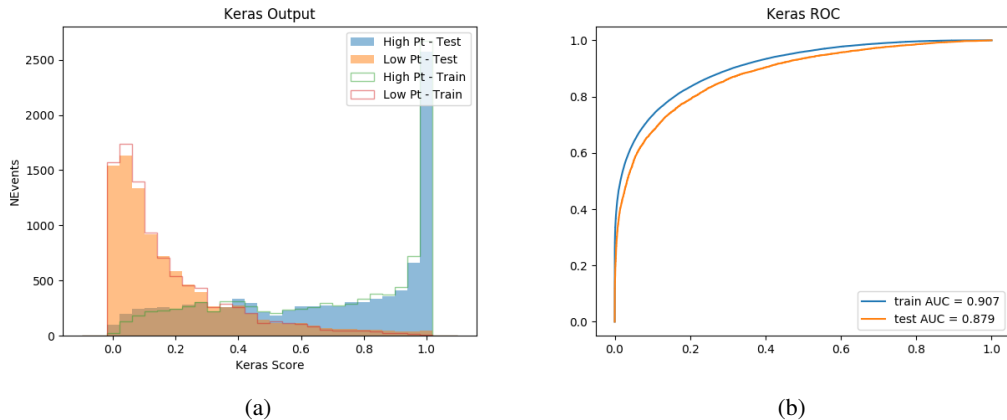


Figure A.28:

1879 A.5 Impact of Alternative Jet Selection

1880 A relatively low p_T threshold of 15 GeV is used to determine jet candidates, as the jets originating
 1881 from the Higgs decay are found to fall between 15 and 25 GeV a large fraction of the time. The
 1882 impact of different jet p_T cuts on our ability to reconstruct the Higgs p_T is explored here. The

1883 performance of the Higgs p_T prediction models is evaluated for jet p_T cuts of 10, 15, 20, and 25

1884 GeV.

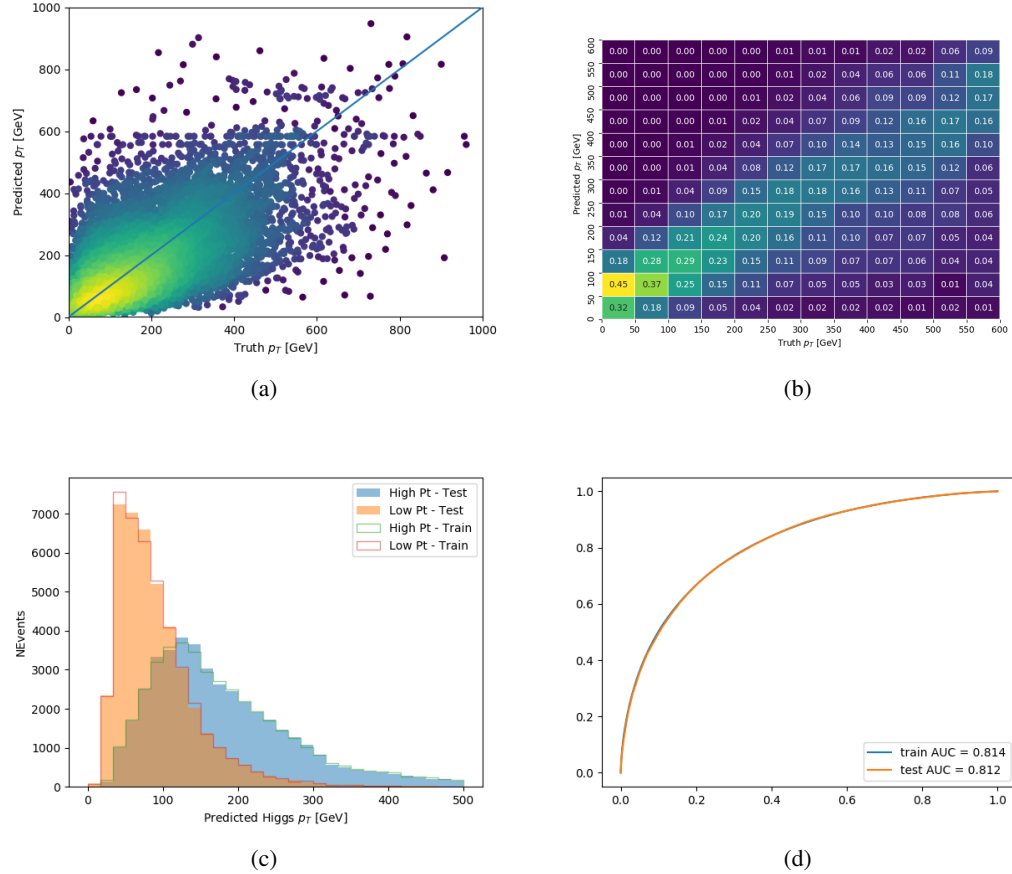


Figure A.29:

1885 **B**